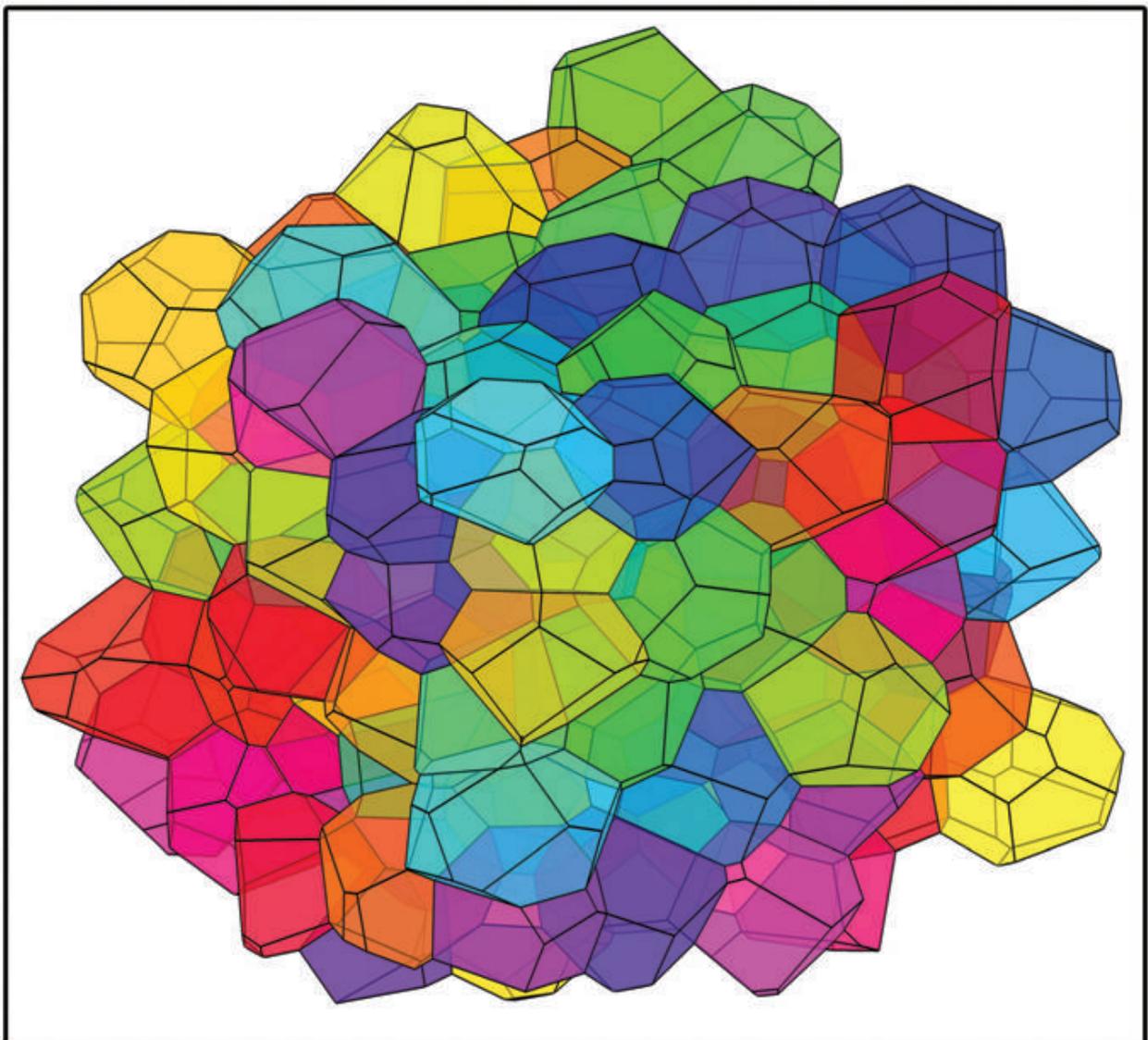


2D and 3D Grain Growth Modeling and Simulation

Luis Antonio Barrales Mora



2D and 3D Grain Growth Modeling and Simulation

**Von der Fakultät für Georessourcen und Materialtechnik der
Rheinisch-Westfälischen Technischen Hochschule Aachen**

Zur Erlangung des akademischen Grades eines
Doktors der Ingenieurwissenschaften

genehmigte Dissertation

vorgelegt von

**Maestro en Ciencias
Luis Antonio Barrales Mora**

aus Mexiko Stadt

Berichter: PD Dr. rer. nat. Volker Mohles
Univ.-Prof. Dr.rer.nat. Günter Gottstein

Tag der mündlichen Prüfung: 16. Juni 2008

Bibliografische Information der Deutschen Nationalbibliothek

Die Deutsche Nationalbibliothek verzeichnet diese Publikation in der Deutschen Nationalbibliografie; detaillierte bibliografische Daten sind im Internet über <http://dnb.ddb.de> abrufbar.

1. Aufl. - Göttingen : Cuvillier, 2008

Zugl.: (TH) Aachen , Univ., Diss., 2008

978-3-86727-684-9

© CUVILLIER VERLAG, Göttingen 2008

Nonnenstieg 8, 37075 Göttingen

Telefon: 0551-54724-0

Telefax: 0551-54724-21

www.cuvillier.de

Alle Rechte vorbehalten. Ohne ausdrückliche Genehmigung des Verlages ist es nicht gestattet, das Buch oder Teile daraus auf fotomechanischem Weg (Fotokopie, Mikrokopie) zu vervielfältigen.

1. Auflage, 2008

Gedruckt auf säurefreiem Papier

978-3-86727-684-9

Acknowledgements

I would like to thank Prof. Dr. Günter Gottstein for giving me the opportunity to work at the Institute of Physical Metallurgy and Metal Physics (IMM) of the RWTH-Aachen University. For his support, encouragement and trust I am deeply grateful.

I would also like to thank Dr. Volker Mohles leader of the Simulation research group of the IMM for his support since the very first day. His friendly encouragement and accurate advice made definitely my work easier. I am also very grateful to Prof. Dr. Dmitri A. Molodov and Prof. Dr. Lazar S. Shvindlerman for valuable discussions and suggestions that only improved this dissertation.

To my dear friends and colleagues I only have words of gratitude, to Carmen Schäfer, Emmanuel Jannot, Talal Al Samman, Dirk Kirch, Vladimir Ivanov, Peter Konijnenberg and Juan Manuel Salgado López, thank you very much.

Finally, I would like to express my most sincere gratitude to my loving family. I am, in particular, very grateful to my parents, Hugo Barrales Alvarez and Marisela Mora Muñoz for their love and support during all these years. As well, I would like to thank my wife, Viridiana Lumbreras Ledesma, for her patience (bearing me) and unconditional love and support.

List of Symbols

Latin Alphabet

A	area
a	grain size
b	burgers vector
c_{vac}	vacancy concentration
D	mean grain size; domain; dislocation spacing
D_0	diffusion pre-exponential factor
D_f	drag factor
D_m	diffusion coefficient for atomic jumps through the grain boundary; mean grain size
d_{max}	maximal attainable grain size
d_p	mean diameter of precipitates
E	energy
E_c	energy of the dislocation core
E_{coh}	cohesive energy
E_d	energy of an edge dislocation
e	number of edges in a topological network
$e(D)$	length of the triple lines of a domain
F	force
f	number of faces in a topological network; second-phase volume fraction
f_i	force of the i -th element
G	Gibbs potential
G_m	free energy of migration
g	number of grains in a topological network; free energy functional
H	magnetic field strength
K	proportionality constant
k	Boltzmann constant
L	boundary length
$L(D)$	mean width of a domain
M	Mobility

m_0	grain boundary mobility pre-exponential factor
m_{eff}	effective vertex mobility
m_{gb}	grain boundary mobility
m_{qp}	quadruple junction mobility
$m_{tj,tl}$	triple junction/line mobility
N	total number of atoms
n	grain growth exponent; normal vector to the boundary plane (bold); topological class
\vec{n}	normal vector to the grain boundary
P, ρ	driving force
$\rho_{i,j}$	partition site or the Voronoi diagram
ρ_m	mean magnetic driving force
Q_m	activation energy
q	quaternion
R	grain radius; kinetic energy functional
R_{th}	threshold radius
\bar{R}	mean grain radius
r_0	radius of the dislocation core
r_e	cutoff distance for the calculation of the interatomic potential
\vec{r}	vectorial radius of curvature
S	surface
\dot{S}	Surface rate of change
\vec{s}	length parametric vector
T	temperature; line tension
T_m	melting point
t	time; translation vector (bold)
\vec{t}	tangential vector to the grain boundary
\vec{u}	unit vector
V	volume; Voronoi region/polygon
V_{tj}	triple junction velocity
V_{qp}	quadruple point velocity
\dot{V}	volume rate of change
v	number of vertices in a topological network; velocity
v_x	velocity in the x-direction

Greek Alphabet

α	dihedral angle used in the Herring equation; constant of proportionality between grain diameter and curvature; complementary angle used for the calculation of the effect of quadruple junctions on grain boundary migration; depth of the potential well used in the calculation of the interatomic potential
β	turning angle
Γ	atomic jump frequency
γ	grain boundary energy
γ^l	line tension
γ^s	surface energy
ε	cutoff length for the triggering of the topological transformation
η	order parameter used in the phase field method
θ	rotation angle; mis- and disorientation angle; angle between the c-axis and magnetic field; angle between grain boundaries at the tip of the triple junctions and between triple lines at the tip of quadruple junctions
θ_∞	equilibrium angle for infinite mobility of grain boundary junctions
κ	curvature
$A_{tj,tl}$	parameter which describes the influence of a finite triple line mobility on grain boundary evolution
A_{qp}	parameter which describes the influence of a finite quadruple point mobility on grain boundary evolution
μ	shear modulus
μ_0	vacuum permeability of the free space
ξ	geometrical factor relating grain size and mean curvature
Σ	Density of the coincidence lattice
σ	standard deviation
ν	attack frequency; Poisson ratio; potential energy functional
ν_D	Debye frequency
φ	grain boundary inclination angle
Φ	second sequential rotation along an axis of the coordinate system for the composition of a general rotation according to the Euler theorem

- φ_1 first sequential rotation along an axis of the coordinate system for the composition of a general rotation according to the Euler theorem
- φ_2 third sequential rotation along an axis for the composition of a general rotation according to the Euler theorem
- X magnetic susceptibility
- Ω atomic volume

Preface

The properties of metallic materials are directly related to the kind, amount and distribution of lattice defects (dislocations, grain boundaries, etc.) that the material contains. In fact, the microstructure of a material can be defined as the collection of all thermodynamics non-equilibrium lattice defects [1]. The simultaneous occurrence of these defects in different quantities and qualities leads to a constellation of diverse microstructures, each of them with different properties. The key for the design of modern materials is the precise control of their microstructure. This task is achieved by the materials scientist by making use of different methods and techniques, from the apparently simple change in chemical composition to the use of complex processes (e.g. thermomechanical treatments, CVD, ECAP, etc). It is evident that the understanding of the underlying physics behind the phenomena governing these processes is fundamental for good accomplishment of this important task. Nowadays, concepts like **Materials Design**, **Grain Boundary Engineering**, etc. have become part of the normal language for the materials science researcher, emphasizing the importance of the microstructure control.

The heat treatment of metallic materials is one of the most used methods for the modification of the microstructure, especially when used in connection with plastic deformation. During this stage of the processing, the change in the mechanical properties of the material is principally aimed. For this purpose, three different phenomena are utilized: recrystallization, recovery and grain growth. Recrystallization is defined as the substitution of an existing deformed grain structure by a new dislocation-free structure. This is carried out by the formation and migration of high angle grain boundaries driven by the stored energy of deformation. Recovery, on the other hand, corresponds to all annealing processes that imply the annihilation and rearrangement of dislocations [2]. The final phenomenon is the grain growth which is defined as the collective motion of the grain boundaries driven by the reduction of the boundary area. Grain growth occurs immediately after the completion of the recrystallization and takes place when the deformed structure has completely been substituted by the new dislocation-free structure.

Despite having been largely studied, grain growth is still not completely understood. The complexity of the process arises from the diverse factors that affect the phenomenon. Due to the high complexity of the phenomenon, its abstraction is necessary. The process of abstraction consists in the replacement of the *real world* by a model, which properly describes the occurring phenomena in the *reality* [4].

Modeling and **Simulation** are nowadays essential tools that help to understand physical phenomena by providing solutions to setups which cannot be experimentally realized, explanation to experimental observations and validation of theoretical considerations. The present dissertation is dedicated to the simulation of grain growth and related phenomena by means of the **Vertex-Model**.

Contents

Acknowledgements	i
List of Symbols	ii
Preface	vi
1. Grain Growth	1
1.1 Introduction	1
1.2 Grain Boundaries	1
1.2.1 Low Angle Grain Boundaries	3
1.2.2 High Angle Grain Boundaries	5
1.2.3 Grain Boundary Energy	6
1.3 Grain Boundary Motion	9
1.3.1 Fundamentals	9
1.3.2 Driving Forces for the Grain Boundary Motion	11
1.4 Normal Grain Growth	11
1.4.1 Fundamentals and Topological Aspects of Grain Growth	12
1.4.2 Grain Growth Kinetics	15
1.4.3 Grain Growth Inhibition	15
1.4.3.1 Free-Surface Induced Inhibition	16
1.4.3.2 Solute Induced Inhibition	17
1.4.3.3 Particle Induced Inhibition	18
1.4.4 Abnormal Grain Growth	19
2. Grain Growth Modeling and Simulation	22
2.1 Introduction	22
2.2 Modeling and Simulation	22
2.3 Grain Growth Models	24
2.3.1 Monte Carlo Potts Model	24
2.3.2 Phase Field Model	25
2.3.3 Vertex Model	26
2.4 Simulation Model – A Vertex Model Approach –	27
2.4.1 Equations of Motion	28
2.4.2 Topological Transformations	30
2.5 Validation of the Model	33
2.5.1 Grain Growth kinetics	33
2.5.2 Comparison with the von Neumann–Mullins Relation	34
2.5.3 Grain Size Distribution	36
3. Influence of a Magnetic Field on Grain Growth	39
3.1 Introduction	39
3.2 The Magnetic Driving Force	39
3.3 Texture Evolution in Magnetically Annealed Titanium	41
3.4 Computer Simulations	42

3.4.1 Texture and Microstructure Evolution	43
3.4.2 Influence of a Magnetic Field on Grain Growth Kinetics	46
Von Neumann-Mullins Relation during Magnetic Annealing	47
3.5 Magnetic Annealing in a Sample with Randomly Oriented Grains	48
3.5.1 Orientation Distribution and Simulation Details	50
3.5.2 Texture Evolution	51
3.5.3 Grain Fraction Evolution	53
3.5.4 Effect of the Magnetic Field on Grain Size Distribution and Topologic Arrangement of the Grains	54
4. The Vertex Model, Grain Boundary Junctions and Grain Boundary Migration	57
4.1 Introduction	57
4.2 Grain Boundary Systems with Triple Junctions	58
4.3 Triple Junction Motion	59
4.3.1 Grain Boundary Shape and its Correlation with the Steady-state Motion of a Tricrystalline System	59
4.3.2 Effect of a Finite Triple Junction Mobility on the Evolution of a Multigranular System ($n>6$)	62
4.3.3 Validation and Verification of the Equations for the Effect of a Finite Triple Junction Mobility on the Evolution of a Grain Boundary System	63
4.3.4 Effect of a Finite Triple Junction Mobility on the Evolution of a 2D Polycrystal	69
4.4 Grain Boundary Motion and Dependency of the Boundary Energy on Inclination Angle	71
4.4.1 Modifications of the Vertex Model for the Consideration of the Inclination Dependency	71
4.4.2 Case of Study – Faceting of $\langle 100 \rangle$ Tilt Grain Boundaries	73
4.4.2.1 Molecular-Static Simulations	74
4.4.2.2 Vertex-Model Simulations of Grain Boundary Migration	76
5. 3D Grain Growth Vertex Model	79
5.1 Introduction	79
5.2 3D Vertex Model	79
5.2.1 Microstructure Generation	79
5.2.2 Discretization of the Grain Boundaries	82
5.2.3 Equation of Motion	84
5.2.4 Topological Transformations	85
6. Grain Boundary Junctions Revisited	93
6.1 Introduction	93
6.2 Three-sided Grain Configuration	93
6.2.1 3D Vertex Simulations	94
6.3 Steady-state Quadruple Junction Motion	95
6.3.1 Equations of Motion	96
6.3.2 Effect on Grain Microstructure Evolution	99

6.4 Effect of a Finite Triple Line Mobility on the Evolution of a 3D Grain Assembly	103
6.4.1 Effect on Grain Microstructure Evolution	104
6.5 Comparison with Theoretical Predictions	105
6.5.1 Analytical Description of the Volume Rate of Change	105
6.5.2 Comparison of the simulation Results with the MacPherson-Srolovitz Equation	106
6.5.3 The Effect of a Finite Quadruple Junction Mobility on the MacPherson-Srolovitz Equation	109
7. Summary	112
Abstract	115
Zusammenfassung	116
References	117
A. Details of the Simulation Program	122
A.1 Programming	122
A.2 Curvature Determination from Local Geometry	123
B. On Quaternions, Rotations, Orientations and Disorientations	125
B.1 Orientations, Rotations and Quaternions	125
B.2 Mis- and Disorientations	127
B.3 Random Orientations	129

Chapter 1

Grain Growth

1.1 Introduction

Grain growth is a widely investigated phenomenon in materials science. It influences a large variety of physical and mechanical properties of polycrystalline materials. Grain growth is the result of the collective migration of the grain boundaries and consequence of the necessary topological decay (decrease of the topological and structural elements of the microstructure) that takes place when the average volume of the grains increases. During grain growth both events occur simultaneously, making it a very complex phenomenon. The main driving force for the migration of grain boundaries during grain growth is the area of the boundaries, however, other sources can contribute to the driving force and hence influence grain growth as well. Such sources can be given by a gradient of any intensive thermodynamic variable, for example, temperature, pressure, density of defects, density of energy, etc. In the present chapter, the phenomenology of grain growth will be introduced.

1.2 Grain Boundaries

A polycrystal, as its name indicates, is conformed by many different crystals. Each crystal consists of an ordered three-dimensional arrangement of atoms, which repeats itself, thoroughly the volume of the crystal. These crystals are also known as grains or crystallites. Because each crystal may possess a different orientation, an interface must be formed between two crystals with different orientations when they come into contact. This interface is called grain boundary.

A grain boundary is a very complex structure; its mathematical description requires four parameters in the two-dimensional case and eight parameters in the three-dimensional one. These eight parameters can be discriminated in five macroscopic and three microscopic parameters. The macroscopic parameters are respectively, three Euler angles ($\varphi_1, \Phi, \varphi_2$) which describe the specific orientation difference between adjacent crystals to the grain boundary and two parameters describing the spatial orientation of the grain boundary by means of the normal unit vector to the grain boundary plane $\mathbf{n}=(n_1, n_2, n_3)$ with regard to one of the adjacent grains. The other three microscopic parameters are given by the three components of the translation vector $\mathbf{t}=(t_1, t_2, t_3)$ of the displacement of one crystal with respect to the other. The intrinsic properties of the grain boundary depend on the eight parameters. In particular, the mobility and the grain boundary energy are predominantly sensitive to them.

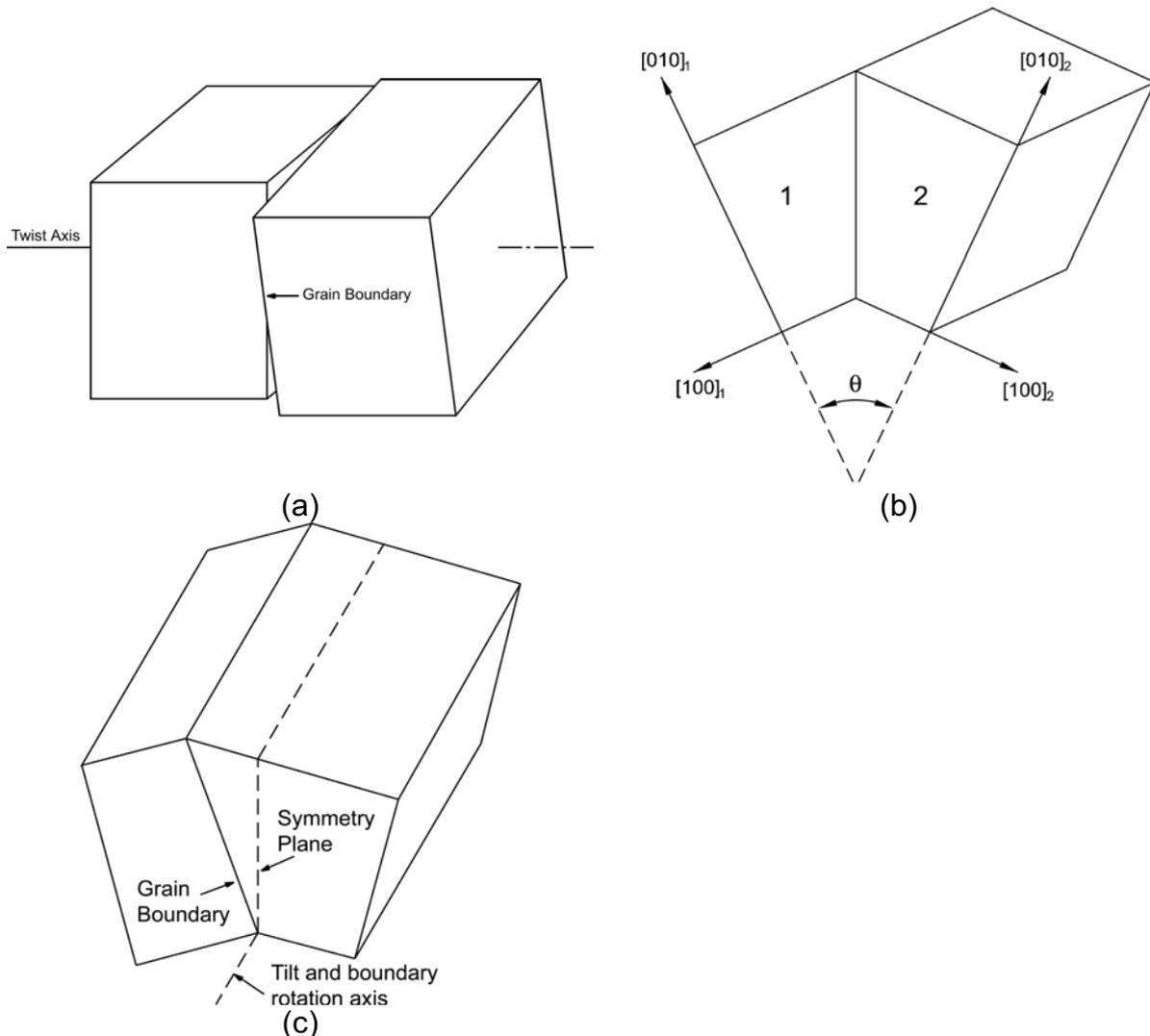


Figure 1.1. Types of grain boundaries. (a) Twist grain boundary, (b) symmetrical tilt grain boundary, (c) asymmetrical tilt grain boundary [2].

There are different kinds of grain boundaries. The easiest way to discriminate grain boundaries is to use the orientation relationship existing between neighboring crystallites. If a common origin is assumed, this relationship is reduced to a pure rotation, which can be defined in terms of a crystallographic axis $\langle hkl \rangle$ or a vector $[uvw]$ and an angle of rotation θ . The grain boundary can now be defined using the necessary rotation to bring one of the neighboring crystallites into the orientation of the other. For example, if the grain boundary plane is perpendicular to the rotation axis, the grain boundary is referred to as a pure *twist* grain boundary (Fig. 1.1a). In contrast, if the grain boundary plane is parallel to the rotation axis, the boundary is referred to as a pure *tilt* grain boundary (Fig. 1.1b). In the case of the twist grain boundary it should be noted that the grain boundary plane is unambiguous and does not depend on the rotation angle θ , however, for the tilt grain boundaries there is not unique grain boundary plane because there is an infinite number of possible planes parallel to a given direction. The simplest type of grain boundary is the symmetrical tilt grain boundary whose boundary plane mirrors the crystallographic direction of the adjacent crystallites. All other tilt grain boundaries are identified as *asymmetrical tilt grain boundaries* (Fig. 1.1c).

1.2.1 Low Angle Grain Boundaries

Depending on the magnitude of the rotation angle θ between adjacent crystals is also possible to distinguish two different kinds of grain boundaries: **Low Angle Grain Boundaries (LAGB)** and **High Angle Grain Boundaries (HAGB)**.

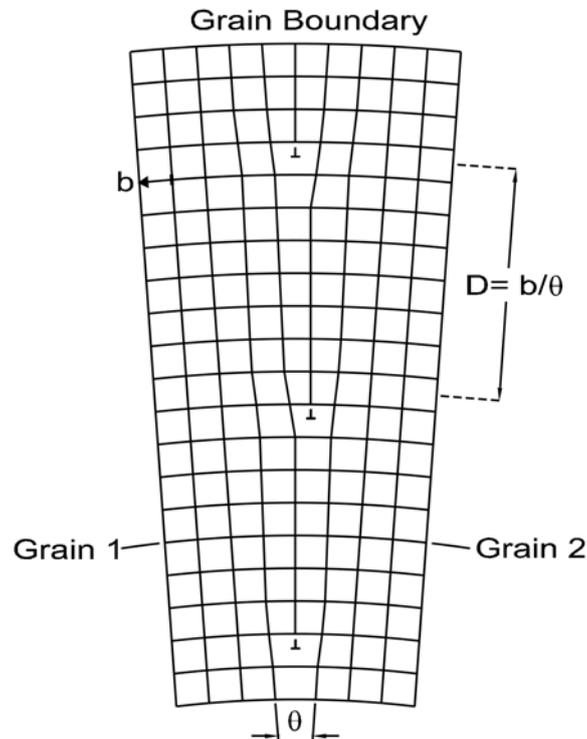


Figure 1.2. The dislocation model of a symmetrical low angle grain boundary.

A LAGB is an interface between two crystallites whose spatial orientation with respect to each other does not differ largely. This condition is reflected, precisely, in the rotation angle θ . If this angle does not exceed 15° , it is normally assumed that the grain boundary corresponds to a LAGB. A LAGB is completely comprised of a periodic set of crystal dislocations. In figure 1.2, the structure of a symmetrical low angle tilt grain boundary is shown. Such grain boundary consists of one set of edge dislocations with the same Burgers vector b . The number of dislocations per unit length in the grain boundary, $1/D$, increases with the misorientation angle θ

$$\frac{1}{D} = \frac{2\sin(\theta/2)}{b} \approx \frac{\theta}{b}. \quad (1.1)$$

In contrast, the structure of an asymmetrical grain boundary is more complex, it requires at least two sets of non-parallel edge dislocations to be constructed (Fig. 1.3). It should be noted that the grain boundary starts as a symmetrical tilt grain boundary but the increasing deviation from this configuration makes it necessary to introduce a new set of dislocations. The number of dislocations of this second set increases with increasing deviation, while the number of dislocations of the first set decreases. This situation leads to a point where the grain boundary is completely composed by dislocations of the second set. At this point the grain boundary is again

a symmetrical tilt grain boundary but perpendicular to the original grain boundary. The number of dislocations of each set can be calculated. The number of dislocations of the first set with Burgers vectors b_1 and of the second set with Burgers vector b_2 is given by

$$\frac{1}{D_1} = \frac{b_1}{\theta \cos \varphi} \quad (1.2)$$

and by

$$\frac{1}{D_2} = \frac{b_2}{\theta \sin \varphi} \quad (1.3)$$

respectively.

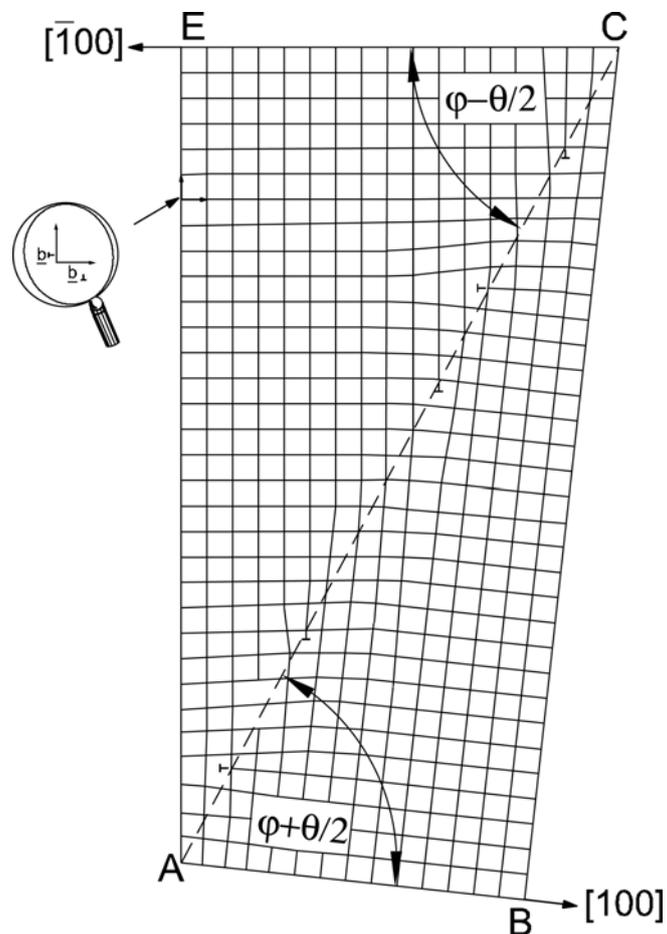


Figure 1.3. Asymmetrical tilt low angle grain boundary [4].

The case of the low angle twist boundaries is very similar to the previous one; the only difference is that screw dislocations (Fig. 1.4) now comprise the grain boundary. These grain boundaries always require at least two sets of screw dislocations because only under this condition a rotation is generated (a single set of screw dislocation leads only to a shear deformation).

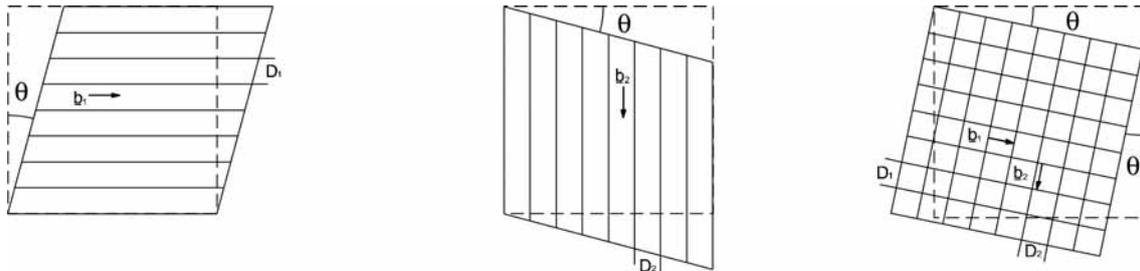


Figure 1.4. Dislocation model for a low angle twist grain boundary [2], a single set of screw dislocations lead to a shear, a second set is necessary for a rotation.

1.2.2 High Angle Grain Boundaries

For higher rotation angles ($\theta > 15^\circ$), the dislocation model fails to describe properly the structure of the grain boundary. It can be seen from Eq. (1.1), that the number of dislocations per unit length increases with the rotation angle. However, for this equation, it is supposed that the distance between dislocations is so large that the influence of the dislocations cores can be neglected. Nevertheless, for $\theta > 15^\circ$ the distance between dislocations reaches the range of the dislocation core radius, the dislocation cores then start to overlap and the dislocations lose their identity as individual lattice defects. Grain boundaries with rotation angles higher than 15° are called *high angle grain boundaries*. The modern understanding of the structure of these grain boundaries is still based on dislocations models of low angle grain boundaries.

The positions of the atoms of a perfect crystal are determined by the minimum of the Free Energy, the atoms will always occupy those positions that lead to this energetic state of the crystal. For the description of the structure of a high angle grain boundary, we can assume that the atoms in the grain boundary try to lie in these ideal positions (low energetic positions). If we take now two crystals with different spatial orientations and superpose them, it is possible to observe that some atoms of both crystals have the same positions; these points are referred to as coincidence sites. Due to the periodicity of the crystal lattices of both grains, the coincidence sites show also periodicity. In fact, the coincidence sites build also a lattice, which is called the **Coincidence Site Lattice (CSL)** (Fig. 1.5a). If we compare the density of a CSL with respect to the density of crystal lattice, it is possible to define the parameter Σ as follows [5]

$$\Sigma = \frac{\text{volume of elementary cell of CSL}}{\text{volume of elementary cell of crystal lattice}}. \quad (1.4)$$

This parameter defines how similar the CSL and the crystal lattice are. The larger the value of Σ is, the smaller is the number of coincidence sites in the grain boundary and vice versa. For example, a grain boundary with $\Sigma=1$, can be found, if we consider a grain boundary which is supposedly formed between two crystals with exactly the same spatial orientation, small deviations in the orientation of one of the crystals need to be compensated by the introduction of dislocations. Even with the introduction of dislocations the grain boundary can still be considered to possess an $\Sigma=1$ since all lattice nodes, except those of the dislocation cores, are in coincidence sites. Incidentally, this grain boundary corresponds to a LAGB.

Geometrically, high angle grain boundaries can be treated as small deviations from a nearest CSL. As in the case of LAGB, deviations from the CSL need to be compensated by lines of dislocations in between regions of undistorted CSL. These dislocations are called **Secondary Grain Boundary Dislocations (SGBD)** and the boundary between them is the perfect CSL boundary generated by the periodic arrangement of primary lattice dislocations. Burgers vector of SGBD is a translation vector of the **Displacement Shift Complete lattice (DSC-lattice)** (Fig. 1.5b). As a result, the DSC lattice is the coarsest grid, which contains all lattice points of both crystal lattices.

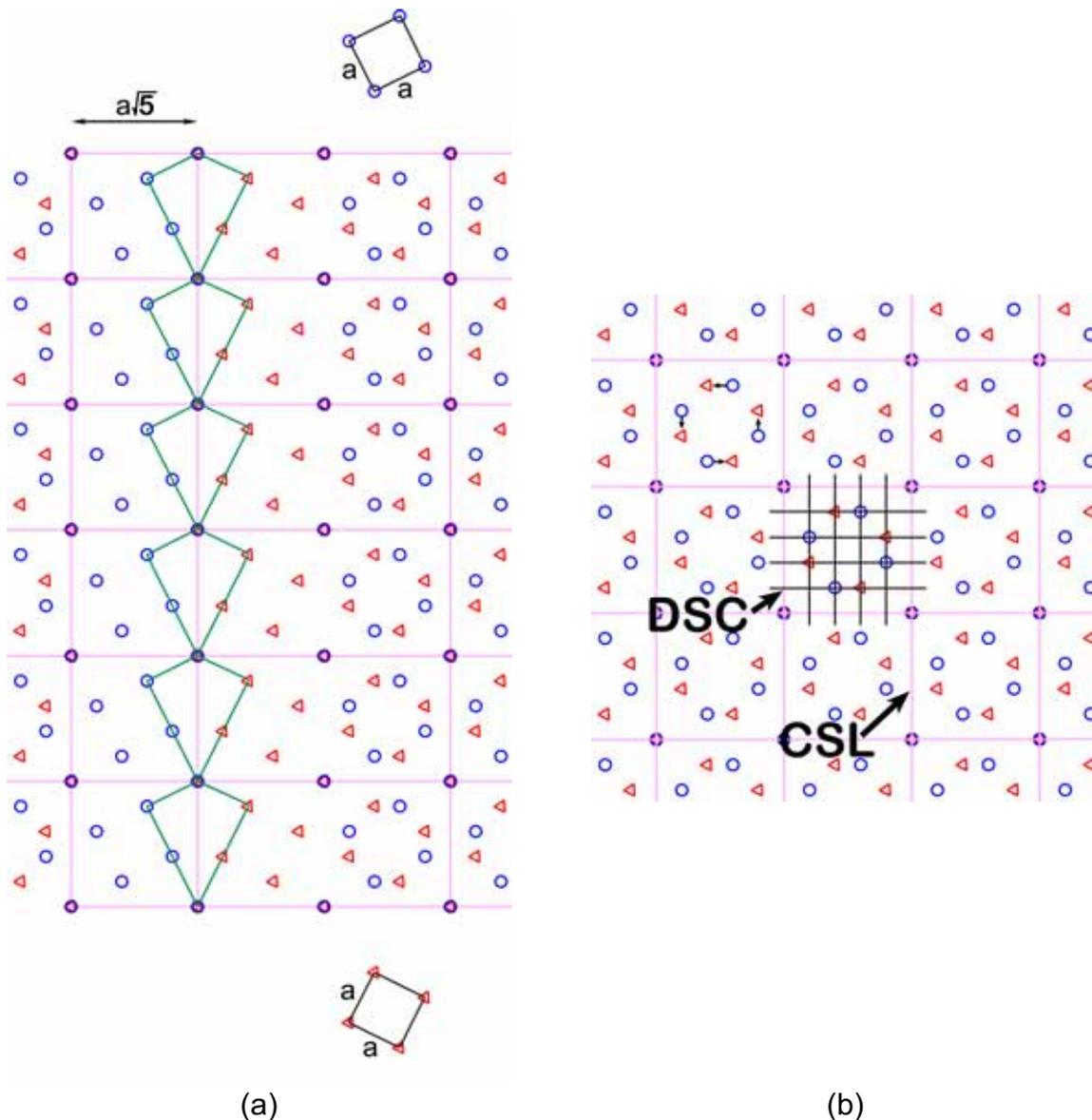


Figure 1.5. (a) Coincidence site lattice of a $36.9^\circ \langle 110 \rangle (\Sigma 5)$ grain boundary in a cubic crystal lattice. (b) Displacement Shift Complete Lattice and Coincidence Site Lattice.

1.2.3 Grain Boundary Energy

The grain boundary energy is a function of all eight parameters describing a grain boundary. Only five of these eight parameters can be influenced, namely, the orientation relationship and the inclination of the grain boundary. The dependency of

the grain boundary energy on inclination for a constant orientation relationship (i.e., constant misorientation) can be described by the Wulff-Plot (Fig. 1.6) [6].

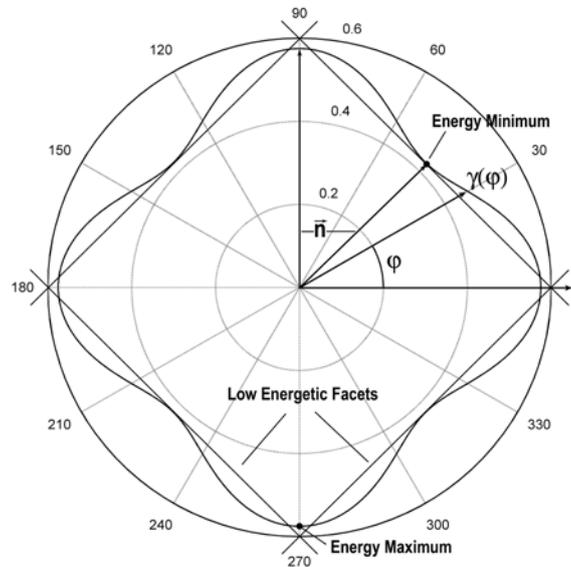


Figure 1.6. Two-dimensional Wulff-Plot shows the dependency of the grain boundary energy on inclination angle φ .

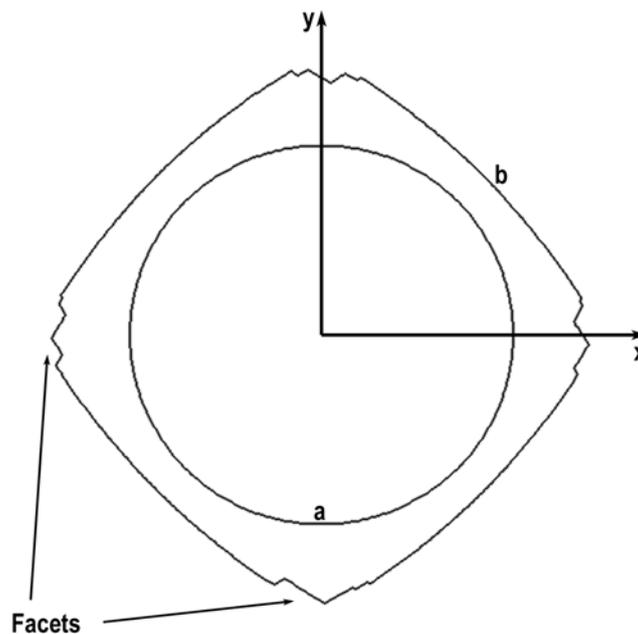


Figure 1.7. Simulated shape of the grain boundary of an island-grain for two different dependencies of the energy with the inclination is shown. For grain (a) no dependency is assumed, the shape of the grain boundary resembles a perfect circle. For (b) the function shown in Fig. 1.6 is assumed, the grain boundary, in this case, presents facets, which correspond to the low energetic positions ($\varphi \approx 45^\circ$).

The Wulff-Plot describes the grain boundary energy γ as a function of the inclination angle φ in polar coordinates and is related with the physical grain boundary through the normal vector \vec{n} . The shape of the grain boundary depends also strongly on the inclination. If the Wulff-Plot reveals positions, where the grain boundary energy is considerably low, then the grain boundary will tend to assume these positions (Fig. 1.7). It is possible to observe in Fig. 1.7 that the grain boundary (b) is composed only by facets that correspond to the low energetic positions of the Wulff-Plot of Fig. 1.6.

The high energetic position (near $\varphi=0^\circ, 90^\circ$) are broken down in small low energetic facets.

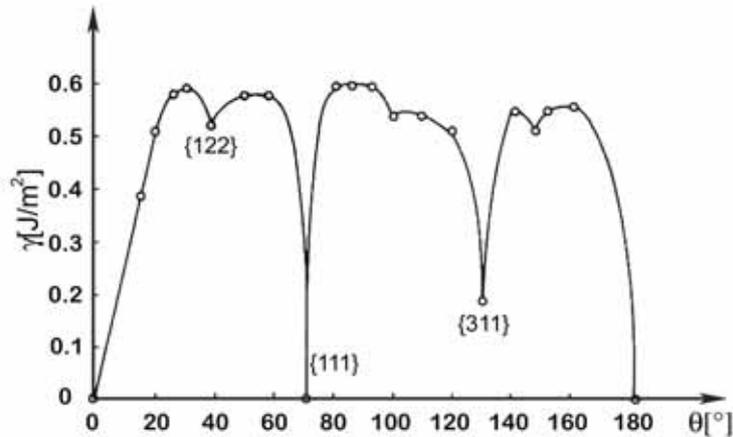


Figure 1.8. Grain boundary energy of an asymmetrical $\langle 110 \rangle$ tilt boundary as a function of tilt angle [7].

The grain boundary energy also depends on the orientation relationship existing between the adjacent crystallites to the grain boundary. In a previous section, we used the orientation relationship to differentiate LAGB from HAGB. As the LAGB are made up of dislocations the energy can be calculated using dislocations theory and therefore the free energy of a LAGB can be calculated exactly. The stress field of a dislocation in an infinite periodic arrangement is confined to a range in the order of the dislocation spacing, D [8]. The energy of an edge dislocation per unit length in an elastically isotropic material is given by

$$E_d = \frac{\mu b^2}{4\pi(1-\nu)} \ln \frac{D}{r_0} + E_c, \quad (1.5)$$

where ν is the Poisson ratio, μ is the shear modulus, $r_0 \approx b$ is the radius of the dislocation core and E_c is the energy of the dislocation core. Finally, the energy per unit area of a symmetrical tilt grain boundary as a function of the misorientation angle θ is given by

$$\gamma_b = \frac{\theta}{b} \left[\frac{\mu b^2}{4\pi(1-\nu)} \ln \frac{1}{\theta} + E_c \right] = \theta(A - B \ln \theta), \quad (1.6)$$

where $A = E_d/b$ and $B = \mu b/4\pi(1-\nu)$.

The free energy of a HAGB cannot be calculated using the previous equation because, as stated in a precedent section, the dislocation model fails in describing a HAGB due to the superposition of the dislocation cores. Nowadays, the best method to determine the free energy of general high angle grain boundaries is the use of computer simulations, in particular, molecular dynamics (MD). The energy of high angle grain boundaries is hardly dependent on the misorientation angle, as seen in figure 1.8. Fig. 1.8 shows the energy of a symmetrical $\langle 110 \rangle$ grain boundary in Al as a function of the misorientation angle. The presence of sharp minima (cusps) corresponds to special orientation relationships, which lead to particular low energetic boundaries. For example, the orientation relationship $70.5^\circ \langle 110 \rangle$, which

coincides with the coherent twin grain boundary, has a particular low energy. Also, when in both crystals a $\{311\}$ plane lies parallel to the grain boundary a cusp in the grain boundary energy will appear.

1.3 Grain Boundary Motion

1.3.1 Fundamentals

There is no unified theory of grain boundary migration. Almost all theoretical attempts try to describe grain boundary migration in the basis of the simple rate theory of atoms crossing the grain boundary with grain net energy. Grain boundary motion is reduced to the diffusive motion of atoms across the grain boundary [9]. It is assumed that the boundary is narrow enough to be crossed by a single atomic jump and also that the boundary is displaced by the diameter of an atom b every time when a jump occurs. Under these assumptions the velocity of the grain boundary reads

$$v = b(\Gamma_+ - \Gamma_-), \quad (1.7)$$

where Γ_+ and Γ_- are the jump frequencies in opposite directions to the grain boundary. If there is no difference in free energy between the neighboring crystals $\Gamma_+ - \Gamma_- = 0$ and the boundary will remain static. In contrast, when the free energies of the crystals are different a driving force P for the motion of the grain boundary appears as

$$P = -\frac{dG}{dV}, \quad (1.8)$$

this causes that every atom of volume $\Omega \approx b^3$ gains the free energy Pb^3 when jumps to the growing grain, in the opposite direction the atom must increase the Free Energy by the same quantity Pb^3 . Figure 1.9 shows schematically the variation of the Free Energy across the grain boundary. Correspondingly, the velocity of the grain boundary can now be expressed in terms of the thermally activated diffusional jumps from the shrinking grain to the other as follows

$$v = b \left[v_+ e^{\left(-\frac{G_m^+}{kT}\right)} - v_- e^{\left(-\frac{G_m^+ + Pb^3}{kT}\right)} \right] \quad (1.9)$$

If the attack frequencies $v_+ = v_- = v \approx v_D$, which is the Debye frequency, and also if the free energy of the migration G_m is the same in both directions, Eq. (1.7) can be rewritten as

$$v = b v_D c_{vac} \cdot e^{\left(-\frac{G_m}{kT}\right)} \left[1 - e^{\left(-\frac{Pb^3}{kT}\right)} \right], \quad (1.10)$$

since the jump of the atoms is only possible through the vacancies of the grain boundary, the vacancy concentration c_{vac} at the grain boundary must be considered.

In all practical cases, including recrystallization in heavily deformed metals, it can be considered that $Pb^3 \ll kT$ and, therefore

$$e^{\left(-\frac{Pb^3}{kT}\right)} \cong 1 - \frac{Pb^3}{kT}, \quad (1.11)$$

which leads to

$$v = \frac{b^4 v_D c_{vac}}{kT} e^{-\frac{G_m}{kT}} \cdot P \equiv m_{gb} \cdot P, \quad (1.12)$$

where m_{gb} is the grain boundary mobility. The relation between grain boundary mobility and the atomic jumps through the grain boundary with an activation energy Q_m is given by the Nernst-Einstein equation

$$m_{gb} = \frac{b^2 D_m}{kT} = \frac{b^2 D_0}{kT} e^{\left(-\frac{Q_m}{kT}\right)} = m_0 e^{\left(-\frac{Q_m}{kT}\right)}, \quad (1.13)$$

where D_m is the diffusion coefficient for the atomic jumps through the grain boundary, D_0 is the diffusion pre-exponential factor. Respectively, m_0 is the pre-exponential factor of the grain boundary mobility. It can be noted that if c_{vac} is not thermally activated, $Q_m = G_m$.

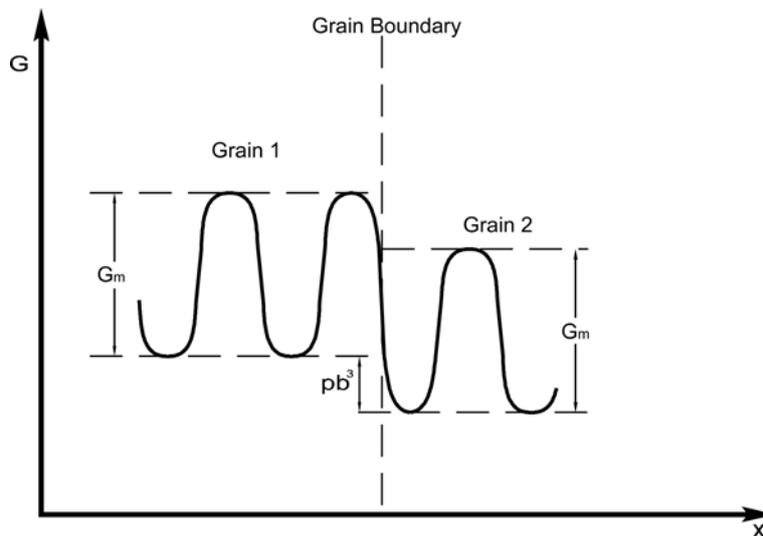


Figure 1.9. The free energy of a moving atom changes by the driving force Pb^3 when it crosses the boundary. G_m is the free energy barrier for the bulk diffusion [9].

1.3.2 Driving Forces for the Boundary Migration

A driving force for the migration of a grain boundary appears as a necessity of the system to reduce the total free energy. There are diverse sources for the driving forces, in principle, a gradient of any intensive thermodynamic variable leads to a driving force, for example, a gradient of temperature, pressure, density of defects, density of energy, etc. For the grain growth, the most relevant source for the driving force is the energy $\gamma \cdot A$ in the area A of the grain boundaries. Nevertheless, it cannot be excluded that other driving forces can occur at the same time affecting the evolution of the grain growth. Table 1.1 shows some possible driving forces for the grain boundary motion and their range of magnitude.

Source	Equation	Approx. Values	Estimated Driving Force (MPa)
Stored deformation energy	$\frac{1}{2} \rho \mu b^2$	$\rho \approx 10^{15} m^{-2}$ $\mu b^2 / 2 \approx 10^{-8} Jm^{-2}$	~ 10
Grain Boundary Energy	$\frac{2\gamma_{gb}}{R}$	$\gamma_{gb} \approx 0.5 Jm^{-2}$ $R \approx 10^{-4} m$	$\sim 10^{-2}$
Surface Energy	$\frac{2\Delta\gamma^s}{h}$	$h \approx 10^{-3} m$ $\Delta\gamma^s \approx 0.1 Jm^{-2}$	$\sim 10^{-4}$
Chemical Driving Force	$R(T_1 - T_0)c_0 \ln c_0$	5%Ag in Cu at 300°C	$\sim 10^2$
Magnetic Field	$\frac{\mu_0 H^2 \Delta\chi}{2} (\cos^2 \theta_1 - \cos^2 \theta_2)$	$H = 10^7 Am^{-1}$ $\Delta\chi \approx 1.8 \times 10^{-7}$	$\sim 10^{-4}$
Elastic Energy	$\frac{\tau^2}{2} \left(\frac{1}{E_1} - \frac{1}{E_2} \right)$	$\tau \approx 10 MPa$ $E_1, E_2 \approx 10^5 MPa$	$\sim 10^{-4}$
Temperature Gradient	$\frac{\Delta S \cdot 2\lambda \nabla T}{\Omega_a}$	$\Delta S \approx 8 \times 10^3 JK^{-1} mol^{-1}$ $\nabla T \approx 10^4 Km^{-1}$ $2\lambda \approx 5 \times 10^{-10} m$ $\Omega_a \approx 10 cm^3 mol^{-1}$	$\sim 10^{-5}$

1.4 Normal Grain Growth

In previous sections, the most important parameters that affect grain growth have been described. The definitions of grain boundary, grain boundary energy and grain boundary mobility were necessary because the evolution of the grain boundary is intrinsically related to the migration of the grain boundary. In the current section, the fundamental aspects of the grain growth will be explained.

1.4.1 Fundamentals and Topological Aspects Grain Growth

A polycrystal is composed of an arrangement of grains. The grains can be described by polyhedra (Fig. 1.10), whose faces, edges and vertices act as junctions of the polycrystal (faces=grain boundaries, edges=triple lines and vertices=quadruple junctions) and together with the grains form a topological network with well defined properties. In fact, the general formulation for such space network is given by the Euler formula for the unbounded state [10]:

$$e + g = f + v, \quad (1.14)$$

where e is the number of edges or triple lines, g the number of grains, f the number of grain boundaries and v the number of quadruple junctions. Under the assumption that all the grain boundaries have the same energy, the number of triple lines is double the number of quadruple junctions and the formulation reduces to

$$g + v = f. \quad (1.15)$$

For any grain of the assembly with a definite number of faces, the number of quadruple junctions of this grain is one less than the number of its grain boundaries and the number of triple lines is the double of the quadruple junctions

$$v + f = e + 1. \quad (1.16)$$

All these topological properties of the polycrystal are very relevant for the grain growth, as we will see subsequently.

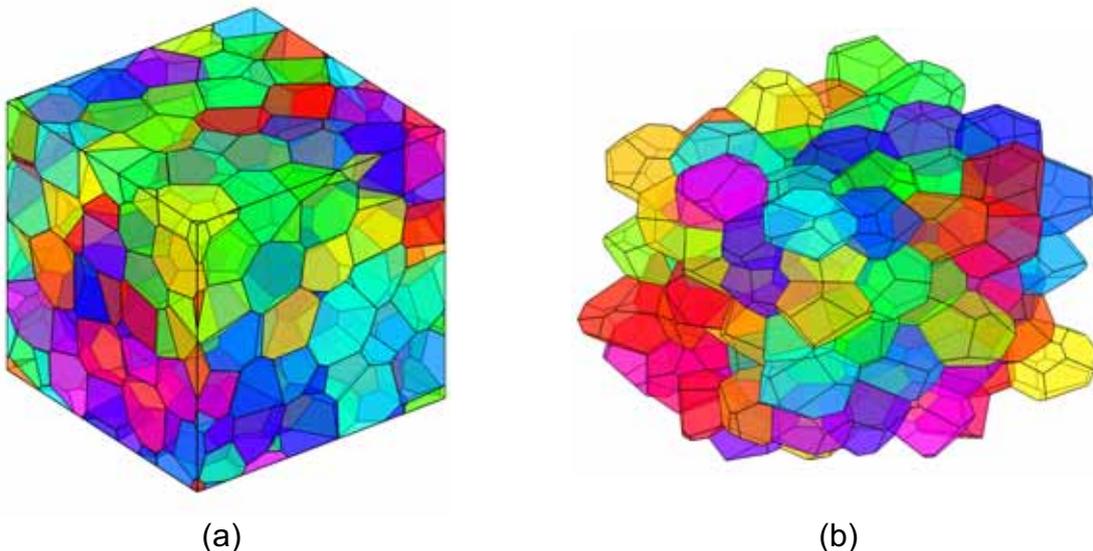


Figure 1.10. A polycrystal is an assembly of grains, (a) shows a three dimensional microstructure, the faces of the containing box cut the polycrystal forming two-dimensional sections of the polycrystal, (b) shows the same microstructure without a limiting box, the polyhedral nature of the grains can be better observed, the faces, edges and vertices of the polyhedra come into contact forming the junctions of the polycrystal.

Strictly speaking, the grains can be considered as polyhedra with curved faces. The shape of the grains, and thus the curvature of their grain boundaries, is result of the necessity of completely filling the space and the energetic equilibrium at triple lines

and quadruple junctions. The mathematical treatment of this three-dimensional problem is very complex. However, it is possible to use a two-dimensional model in order to understand the relationship between the shape of the grain boundaries and the needed topology to fill the space.

In the 2-dimensional case, the equilibrium of the arrangement of grain boundaries is only possible if all the grains have a hexagonal shape (Fig.1.11a). In this case, all the grain boundaries will be straight because at the triple junctions (intersection of a triple line with the plane) the grain boundaries meet at the equilibrium angle. In order for the surface tensions at the triple junctions to be in equilibrium, it must be valid

$$\frac{\gamma_{gb1}}{\sin \alpha_1} = \frac{\gamma_{gb2}}{\sin \alpha_2} = \frac{\gamma_{gb3}}{\sin \alpha_3}. \quad (1.17)$$

If the surfaces tensions of the three meeting grain boundaries are equal then the equilibrium angle must be 120° , but in case of anisotropy of the surface tensions ($\gamma_{gb1} \neq \gamma_{gb2} \neq \gamma_{gb3}$) the dihedral angles will have different values. This is commonly observed in multiphase material, for example, considering a triple junction in an α - β -brass formed by the grain boundaries between two α grains and one β grain, the dihedral angle corresponding to the β grain will be of 95° [11]. In the three dimensional case, it would be possible to fill completely the space and at the same time to have flat grain boundaries only if three grains meet at the triple lines with an angle of 120° and if four grains meet at the quadruple junctions with an angle of 109.47° . However, at quadruple junctions the equilibrium cannot be achieved.

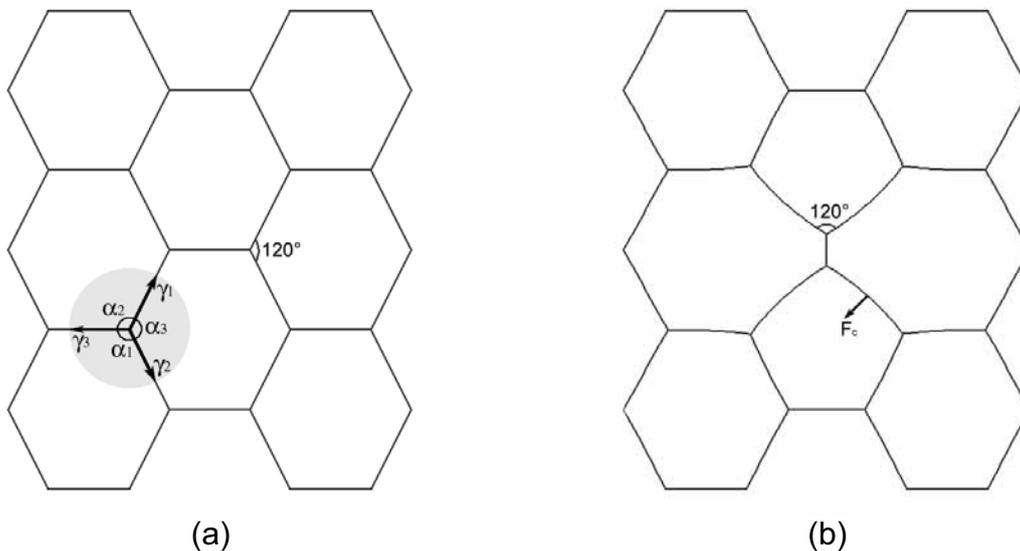


Figure 1.11. (a) A completely equilibrated two-dimensional microstructure can only be achieved by grains with a hexagonal shape. The equilibrium of forces at the triple junctions can also be seen (highlighted), (b) four grains without hexagonal shape introduce the imbalance in the microstructure making necessary the curvature of some grain boundaries in order to maintain the equilibrium at triple junctions. Due to the curvature a driving force F_c for the migration of the grain boundary appears.

A real polycrystal, something what one can find in a metallographic investigation, is not formed exclusively by hexagonal grains but by a constellation of grains with different shapes, sizes and number of sides. The simple presence of one grain with less or more than six sides makes it impossible to fulfill the equilibrium of the surface tensions at the triple junctions by using only straight grain boundaries, therefore the

condition given in Eq. (1.17) can only be satisfied if the grain boundaries are curved, as seen in figure 1.11b. The dihedral angles between the grain boundaries are still close to 120° degrees but the grain boundaries present now a considerable curvature. This curvature causes a driving force for the boundary migration. The force is applied at every point on the grain boundary in the direction normal to the grain boundary (local radius of curvature), as seen in Fig. 1.11b.

The migration of the grain boundary has principally two consequences: the first is the loss of equilibrium at triple junctions, which in turn causes the migration of the triple junction and the second is the result of the combination of the migration of the grain boundaries and the triple junctions.

The successive combination of both migrations leads to the eventual disappearance of the grain boundaries. This disappearance causes the change of the topology in the polycrystal, from Eq. (1.14)-(1.16) we can see that all the structural elements of the microstructure are topologically related. For instance, when a 3D polycrystal loses a triangular grain boundary, the number of quadruple junctions would be reduced by one and the number of triple lines would be reduced by two.

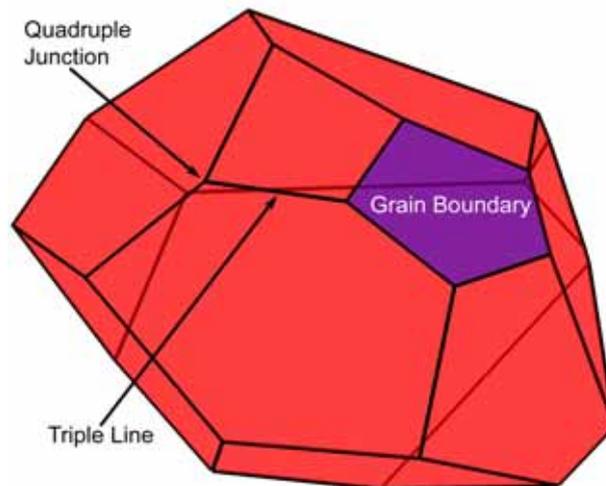


Figure 1.12. An arbitrary 14-sided grain, a grain boundary, a triple line and a quadruple junction are indicated.

Grain growth is, in fact, a topological process. For increase in the average grain volume, it is necessary that the number of grains in the body should diminish. This is a process of topological decay [12]. The average number of grain boundaries per grain in a polycrystal is about 14 (Fig. 1.12) and, correspondingly, 24 quadruple junctions and 36 triple lines. The random collapsing of 13 triangular grain boundaries in the polycrystal is equivalent to the reduction of one average fourteen-sided grain to a single sided grain, which is completely unstable and will collapse spontaneously under the driving force of the surface tension. The collapsing of a triangular grain boundary also destroys the triple lines shared with other grains. Due to this, new triangular grain boundaries are created out of former grain boundaries with multiple triple lines. The repetition of this process constitutes grain growth since the proportion of grain boundaries must be kept constant in the polycrystal. The detailed topological transformations, which take place during grain growth will be explain in detail in a further chapter.

1.4.2 Grain Growth Kinetics

The increase of the mean grain size with time during isothermal annealing can be easily described using an empiric equation [13-15]. Under the assumption that the mean curvature radius R of the grain boundary is proportional to the mean grain diameter D and that the mean grain boundary velocity is proportional to the change with time of the mean grain diameter (dD/dt), one can write:

$$\frac{dD}{dt} = mK_1 \frac{\gamma_{gb}}{D}, \quad (1.18)$$

where m is the grain boundary mobility, γ_{gb} is the grain boundary energy and K_1 is a geometrical constant relating the proportionality of R with D . Given that K_1 does not change with time Eq. (1.18) can be directly integrated

$$D^2 - D_0^2 = K_2 t \quad (1.19)$$

where D_0 is the mean grain size for $t=0$. If $D \gg D_0$, it is possible to simplify Eq. (1.19) even further:

$$D \cong Kt^n \quad (1.20)$$

n is known as the grain growth exponent. Theoretically, the mean grain size should increase with the square root of the time ($n=0.5$). However, this exponent has been found only in extremely pure metals near to the melting point. In metals of commercial purity, the value of n falls normally in the range of 0.2-0.3, depending on the purity, temperature and texture. For example, in table 1.2, the grain growth exponents for an alloy Cu-30%Zn at different temperatures are shown [16], as seen in this table, under some conditions higher exponents than 0.5 can be found.

Table 1.2	
Grain Growth Exponents for a Cu-30%Zn Alloy	
T (°C)	n
500	0.35
600	0.38
700	0.44
800	0.48
850	0.6

1.4.3 Grain Growth Inhibition

During grain growth, the free energy of the system decreases due to the elimination of the grain boundaries of the consumed grains, ideally grain growth should continue until any grain boundary is left, because only a single crystal can achieve the perfect thermodynamic stability, associated with the lowest possible internal energy of the system. Nevertheless, normal grain growth usually stops long before the polycrystal becomes a single crystal, indicating the existence of a maximal attainable grain size.

The nature of the phenomenon provides an intrinsic limitation to the growth of the crystals. The increase of the grain size necessarily implies the reduction of the grain boundary area per unit volume. Because the latter is the driving force for the grain boundary migration, the remaining driving force is reduced for further grain growth. Therefore, the increase of the grain size decreases with time and becomes zero when there is not enough driving force to sustain further growth. The minimal necessary driving force for the boundary migration depends on various factors like temperature, chemical composition, texture, size of the sample, etc.

1.4.3.1 Free Surface Induced Inhibition

It is well known that grain growth can be suppressed near to the surface of a metal. Beck and co-workers [14] found that the grain growth rate in strip samples was slower than expected and that the grain growth was completely inhibited when the grain size reached approximately the thickness of the sample.

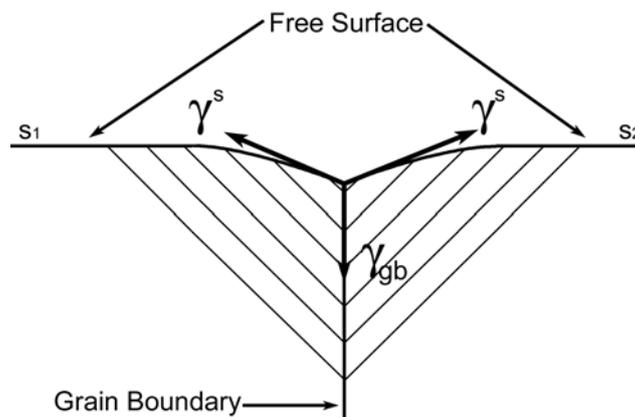


Figure 1.13. The equilibrium of forces of the grain boundary and surface tensions leads to the formation of a groove.

The inhibition of the grain growth in this case can be explained from the fact that when a grain boundary adjoins the free surface the equilibrium of the grain boundary and surface tensions needs to be reestablished. This leads to the formation of a thermal groove along the grain boundary (Fig. 1.13), which needs to be overcome in order for the grain boundary to move. The displacement of this element requires the mass transport and consequently energy dissipation, which makes it a dragging force for the grain boundary migration. The corresponding dragging force p_R is given by [9]

$$p_R = -\frac{\gamma_{gb}^2}{h\gamma^s}, \quad (1.21)$$

where h is the sample thickness and γ^s is the surface energy. This force causes that the grains with grain boundaries adjoining the free surface decrease their growing velocity. For samples with a mean grain size much smaller than its smallest dimension, thermal grooving has practically no influence, because the grain growth kinetics are determined mainly by the growing grains in the bulk, however, as the grain size increases and more grains come into contact with the surface, the drag becomes more and more effective until the grain growth ceases completely. This

occurs when the mean grain size is approximately two times bigger than the smallest dimension of the sample.

1.4.3.2 Solute Induced Inhibition

In this first case, the inhibition of the grain growth arose from the physical size of the sample. However, the chemistry of the material also plays an important role. In solid solution alloys it has been reported [16- 20] that grain growth is inhibited due to the influence of the solute atoms [21-23]. When the boundary migrates, the segregated atoms will attempt to remain in the boundary, this will cause that the boundary migrates at the velocity of the slowly moving impurities.

The problem is, however, more complex because the concentration distribution of the solute atoms is also altered by the grain boundary motion. In a stationary grain boundary the solute atoms are supposed to be symmetrically distributed about the central line of it. Once the grain boundary starts to move, the solute atoms cannot retain the same position, which leads to an asymmetric solute atom distribution.

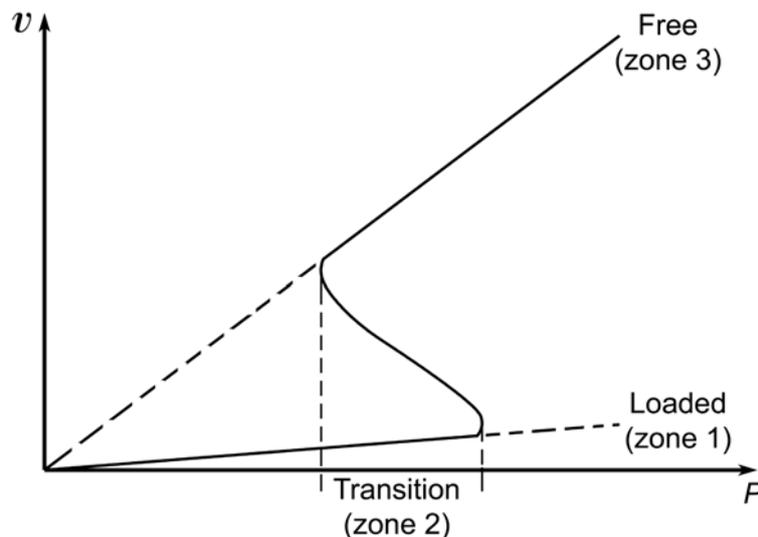


Figure 1.14. Dependence of the grain boundary migration rate on driving force in the presence of impurity drag. The transition from the loaded to the free boundary and vice versa occurs discontinuously.

The dragging force exerted on the grain boundary is a function of the asymmetry of the solute distribution, which is, in turn, dependent on the boundary velocity. It can be said that there are three zones of velocity dependence. The first one takes place when the boundary initiates its movement: as the velocity of the boundary increases from zero, the asymmetry of the solute distribution becomes more pronounced and therefore the drag effect increases as well. The second zone is the transition from the loaded to a free grain boundary. This zone is characterized by a very rapid increase of the velocity with increasing driving force (Fig. 1.14). Within this zone, the grain boundary can reach suddenly both, zone 1 or zone 3. Finally, the third zone corresponds to the movement of a boundary free from the cloud of impurity atoms [9].

Most of the experimental evidence suggests that grain growth kinetics are principally dominated by the movement of grain boundaries in the first zone [17,24], i.e. the

grain boundaries of the polycrystal do not reach the necessary velocity to break away from the impurity cloud. The linear relationship of the velocity with the driving force in both zones 1 and 3 guarantees a growth exponent of 0.5. This means that deviations of the exponent from this value cannot be explained on the basis of solute drag. The only possibility for this is that the boundary migration during grain growth takes place predominantly in the transition zone where the mobility is dependent on the velocity, which violates the suppositions of Eq. (1.8). The probability of the latter to happen is, however, very low. Another explanation to the deviation of n from 0.5, in this kind of alloys, was suggested by Grey and Higgins [17], who proposed the existence of a dragging force due to clusters of atoms which are unable to diffuse with the grain boundary. If the net driving force falls to the dragging force of the clusters, the grain growth will cease. This concept is somehow similar to the Zener pinning because also predicts a limiting grain size.

1.4.3.3 Particle Induced Inhibition

In the presence of second phase particles, the grain growth will be also inhibited. In this case, as outlined previously, grain growth will only take place until a determined maximal grain size is attained. The drag due to the particles can be explained physically by the attraction force between particles and grain boundaries which, in turn, is due to the reduction of the total boundary area which occurs when a grain boundary comes into contact with a particle. The detachment of the grain boundary from the particle significantly increases the total interfacial energy of the system. For this reason, the detachment will only occur if the total energy released by the boundary migration is enough to supply the increase in interfacial energy, for the particle, and at the same time to reduce the total free energy of the system [26].

The magnitude of the dragging force, and therefore the maximal achievable grain size, depends on the quantity and size of the second phase particles. This force is given by [25]

$$p_R = -3\gamma_{gb} \frac{f}{d_p}, \quad (1.22)$$

where f is the volume fraction of the second phase and d_p is the diameter of the precipitates.

During grain growth the total grain boundary area decreases gradually. Since the boundary area is the driving force for the grain boundary migration, grain growth will stop when the total remaining potential energy for the migration does not provide the necessary driving force for the detachment of the grain boundaries from the particles. It is possible to calculate the maximal grain size if we consider that, the grain growth ceases when the driving force and the dragging force come to an equilibrium i.e. $p = p_r$:

$$\frac{2\gamma_{gb}}{\alpha \cdot d} = 3\gamma_{gb} \frac{f}{d_p}, \quad (1.23)$$

where α is a proportionality constant between the curvature radius of the boundary and the grain diameter. With this, we can determine the maximal grain size as follows:

$$d_{\max} = \frac{2}{3\alpha} \cdot \frac{d_p}{f}. \quad (1.24)$$

The grain sizes calculated with Eq. (1.24) are normally bigger than those determined experimentally. This is due to the simplifications used for the assessment of Eq. (1.24).

1.4.4 Abnormal Grain Growth

Abnormal grain growth unlike normal grain growth is characterized by the excessive growth of a relatively small number of grains while the rest remains unaltered until they are consumed. Due to its nature, this phenomenon has been also called, “grain coarsening”, “exaggerated grain growth”, “discontinuous grain growth” and also “secondary recrystallization” [26]. At this point, it is important to remark that despite the apparent similarities between abnormal grain growth and recrystallization, they are completely different phenomena. The most important difference and probably the decisive one is the nature of the driving force. While for recrystallization the driving force is the stored energy of the deformation, for the abnormal grain growth it is still the reduction of the boundary area in a *deformation-free* polycrystal (in some circumstances, however, the surface energy can also play a role).

Two conditions have been found to be necessary for the onset of abnormal grain growth. The first is that the normal grain growth must be kinetically inhibited and the second is that certain grains must have an advantage to grow further. Since the inhibition of the normal grain growth is a pre-requisite for the abnormal growth to occur, it is normally considered that the main factors which lead to this phenomenon are second-phase particles and surface effects.

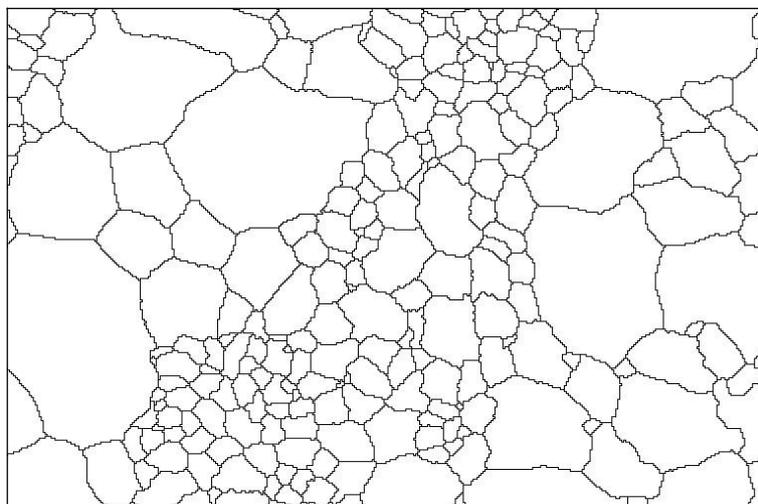


Figure 1.15. Abnormal grain growth in an Al-4%Cu alloy annealed at a temperature close to the melting point. The image was obtained by means of orientation microscopy in a quasi-2D sample. The mapping shows the excessive growth of some grains [28].

We have seen previously that the presence of second-phase particles inhibit the grain growth and limit the maximal achievable grain size. However, under certain conditions the second-phase particles can lead to abnormal grain growth. For example, it has been found in aluminum-copper alloys [27] that the annealing, near to the temperature where the copper enters into solid solution, inhibits the normal grain growth but leads to the development of abnormal grain growth. This occurs because the distribution in size and space of the particles in the matrix is not homogeneous and hence, it is possible that in some places of the sample the particles dissolve allowing local grain growth while the rest of the matrix is still pinned by the particles. Some grains near of the particle-free region may have a clear advantage for their growth promoting the abnormal growth of these favored grains.

Another mechanism for the stagnation of the grain growth arises from the finite size of the sample, as seen in section 1.4.3.1. There is enough experimental evidence [29-31] showing that abnormal grain growth can take place in thin films or in sheets where the grain size has reached a similar size than the sheet/film thickness.

For latter case, Dunn and Walter [29] found that the driving force for the abnormal grain growth was the difference in surface energies $\Delta\gamma^s = \gamma^{s_2} - \gamma^{s_1}$ (Fig. 1.11) of the two adjacent free surfaces to the grain boundary (in figure 1.11 denoted by s_1 and s_2). In turn, this difference comes from the dependency of the surface energy on the orientation. The driving force for the boundary migration is:

$$p_s = \frac{2\Delta\gamma^s}{h}. \quad (1.25)$$

In order for the grain boundary to move, the velocity of the grain boundary can be calculated from the difference between the driving force and the drag term due to the thermal groove (Eq. (1.21))

$$v = m_{gb}(p_s - p_R) = \frac{m_{gb}}{h} \left(2\Delta\gamma^s - \frac{\gamma_{gb}^2}{\gamma^s} \right). \quad (1.26)$$

Because the grain boundary needs to overcome the dragging force, it is possible to define a criterion and establish the required conditions for abnormal grain growth to occur. For this, the subsequent relation must be fulfilled [32]

$$2\Delta\gamma^s > \frac{\gamma_{gb}^2}{\gamma^s} \quad (1.27)$$

or

$$\frac{\Delta\gamma^s}{\gamma^s} > c \left(\frac{\gamma_{gb}}{\gamma^s} \right)^2 \quad (1.28)$$

where c is a constant. Mullins [33] considered that a value of about $\Delta\gamma^s/\gamma^s=0.03$ is sufficient to initiate the boundary migration of a typical HAGB without the contribution

of the component of the grain boundary energy, which leads to the abnormal grain growth of the grains with an energetic advantage.

Chapter 2

Grain Growth Modeling and Simulation

2.1 Introduction

There has been for several years extensive modeling and simulation on the apparently simple problem of grain growth, however a lot of questions are still open. Several models have been used to simulate grain growth, for example, cellular automaton (CA), phase-field, Monte Carlo, Vertex and even finite element models. Among these, the vertex model distinguishes itself for the clarity of the underlying physics which are used. In the present chapter, a brief introduction of the different methods used for the simulation of the grain growth is presented. Finally, the vertex model, which is used in the present dissertation, will be introduced in detail.

2.2 Modeling and Simulation

Modeling (we refer to the mathematical modeling of physical systems) is the art of imitate and describe the nature by means of mathematical equations. The main purpose of the modeling is to isolate a part of the universe in order to analyze it and obtain a better understanding of the processes occurring within this space. However, because the nature is complex, some level of abstraction is indispensable [3]. This abstraction is what we call a model.

Bellomo and Preziosi [34] gave a strict definition of a mathematical model. They define a model using a generalized state variable concept. The definition and selection of the independent and the dependent variables, the evolution equation, and the physically related parameters are necessary. The model then can be defined as the equation or the set of equations, whose solution provides the time-space evolution of a physical system. The equation that defines the mathematical model can also be called the state equation. Figure 2.1 shows schematically the modeling process, which in accordance with our definition starts from the observation of a phenomenon and continues with the description of the nature through the model finishing with the validation and utilization of the same.

There is a gap between the definition of the model (which finishes after the formulation of the mathematical model) and the analysis and validation of the model. This gap exists because the formulation of the model does not take into account the method or methods for the solution of the governing equations. However, in modern materials science most models are rather complex and the state equations normally consist of coupled differential equations which should be solved correspondingly.

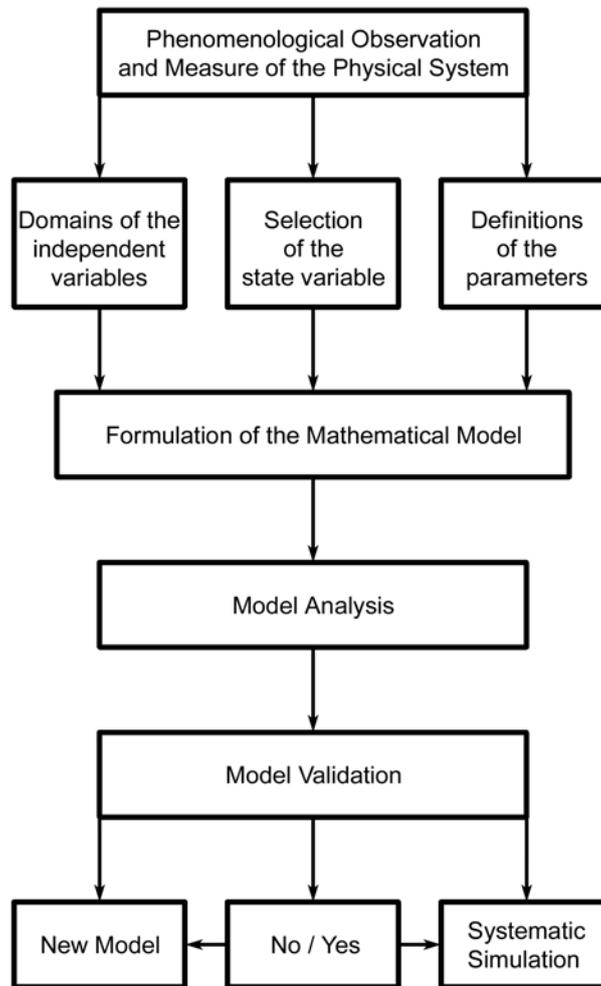


Figure 2.1. Flow chart of the modeling process [34].

Because the analytical solution of such systems is practically impossible, the only alternative left is the use of numerical methods to solve the governing equations and overcome the gap between model formulation and model analysis. However, the utilization of numerical methods introduces also the concept of exactitude of the numerical model. This occurs because the numerical model is not exactly identical to the analytical one. The exactitude of the numerical models depends among others on the truncation, series expansion, discretization, statistical, ergodic, and programming errors [3]. The validation of the model can be accomplished, even in complex models, by the derivation of analytical solutions of simple cases and the comparison with the numerical prediction. Nevertheless, the best validation of a model (analytical or numerical) will always be the direct comparison with the natural phenomena, which the model tries to describe.

Recapitulating, numerical modeling implies the solution of the analytical model by means of numerical methods. This procedure is called sometimes simulation. However, both terms are normally used indiscriminately. There is not a clear and well defined limit, which indicates where the modeling stops and where the simulation starts. The discrepancy in the utilization of both concepts arises from this lack of definition.

A numerical model is, however, still a model. It means that the principal objective of it is the description of the nature, independent of the method chosen for the solution of the state equations. In other words, if there is a clear boundary between analytical modeling and simulation the same boundary must be valid for the numerical modeling. Numerical modeling comprises, then, only the model formulation together with the necessary methods for the solution of the state equations, nothing more nothing less. In contrast, simulation is the mere application of the model to a well defined physical system in order to extract the response of the dependent variables under certain conditions. In fact, Ashby [35] classified simulation as the study of the dynamic response of a modeled system by subjecting the model to inputs, which represent (simulate) real events.

2.3 Grain growth models

Numerous models have been developed for the simulation of the grain growth. Most of them fall in three categories, Monte Carlo, Phase Field and Vertex models. Models based on cellular automata [36, 37], finite element [38] and even molecular dynamics [39, 40] have been also used to a lesser extent. In the present section, we will review briefly the most used models for the simulation of the grain growth. The vertex model will be explained in detail in this chapter.

2.3.1 Monte Carlo Potts Model

The name Monte Carlo originates from the usage of random numbers similar to those coming out of roulette games [41] in this model. The name was coined by Metropolis [42] based on this fact. For the simulation of grain growth a variant of the original Monte Carlo model is used, this variant is called the Monte Carlo-Potts model and was used for the first time by Anderson [43], precisely, for the simulation of grain growth.

In the Monte Carlo-Potts model the space is discretized in a lattice (Fig. 2.2), where each point of the lattice belongs to a particular grain (i.e. the grain is the “state” of the lattice point). The grain boundaries are not defined explicitly but they can be found where two lattice points with different states meet. Correspondingly, triple lines (points in 2D space) and quadruple junctions (only in 3D space) are defined in the same way. The energy of the system is given by the Hamiltonian of the discrete microstructure. The lattice points surrounded by points of the same state do not contribute to the total energy of the system and only those points which have a neighbor of a different state will increase the energy (i.e. grain boundaries).

The integration step can be described as follows [44]:

1. A lattice point l_i is probabilistically selected, l_i has already an orientation or state Q_{old} , which is called *old state*.
2. A new state (orientation) for l_i is assigned from the remaining $(Q-1)$ states; Q is the total number of different states in the system.
3. The Hamiltonian and therefore the energy, induced by the change of the state, are calculated.
4. The difference in energy ΔE between the new and the old state is calculated.

5. If ΔE is negative (i.e. reduction of the free energy of the system) the change is accepted automatically, however if the change of state represents an increase of the energy of the system ($\Delta E > 0$), the change can still be accepted but only with a certain probability that is described by a Boltzmann factor. The decision step is done in accordance with the conventional Metropolis Monte Carlo algorithm [42].

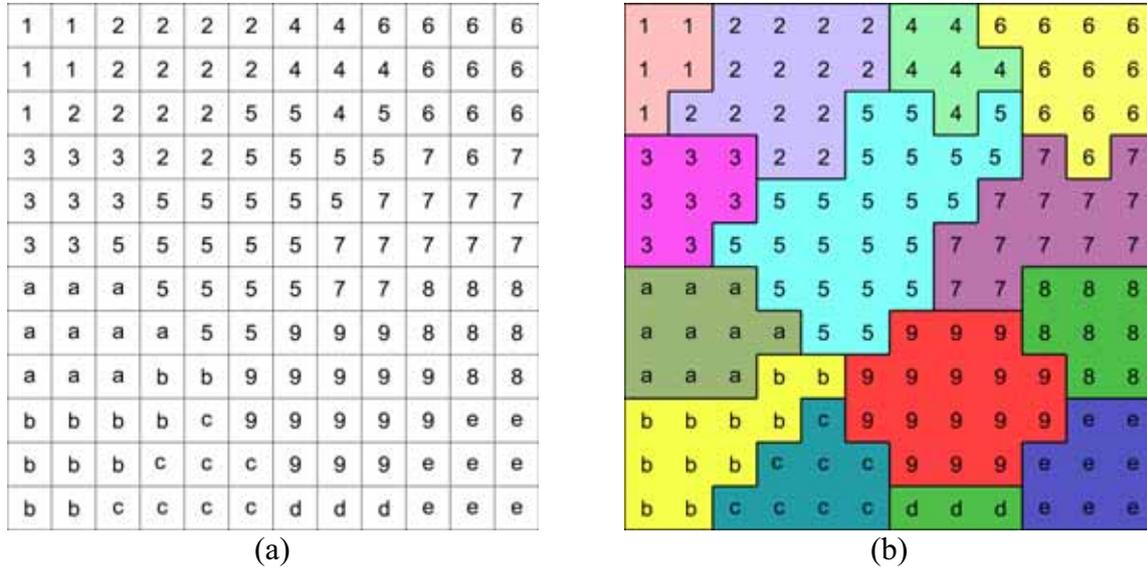


Figure 2.2. Discretization of a microstructure according to the Monte Carlo Potts model, each lattice point has an assigned state. The lattice points possess also certain energy according to the orientation of their grain.

2.3.2 Phase Field Model

In the phase field model, a continuous microstructure is represented by variables known as *order parameters*. For example, if we consider a simple system where only two phases exist, let say, a matrix and precipitates. It is possible to define a single *order parameter* η , which describes continuously the system. The matrix is represented then by $\eta=1$, whereas the precipitates by $\eta=0$, the interface between the matrix and the precipitates is represented by the gradient of both phases ($0 < \eta < 1$). For the simulation of grain growth, the discretization of the polycrystal is more complex, because the whole microstructure can not be described using a single *order parameter*, in this case it is necessary to use the same number of *order parameters* as different oriented grains exist in the polycrystal. Figure 2.3 shows an easy example of the discretization of a polycrystal for the simulation of the grain growth, each grain is represented by an individual order parameter whereas each cell can now have different *order parameters*. The grain boundaries, in fact, are formed by the spatial variation of the *order parameters* of the cells.

The evolution of the microstructure is given by the variation of the free energy functional with respect to the *order parameters*

$$\frac{\partial \eta}{\partial t} = M \frac{\partial g}{\partial \eta}, \quad (2.1)$$

where M is the mobility and g is the free energy functional as a function of the *order parameter*. At constant T and P , g takes typically the form [45]

$$g = \int_V [g_0(\eta, T) + \varepsilon(\nabla \eta)^2] dV, \quad (2.2)$$

where V and T represents the volume and temperature respectively. The second term in this equation $\varepsilon(\nabla \eta)^2$ is given by the gradient of the *order parameters* and hence introduces the grain boundary energy because this term is non-zero only for the interfaces (see Fig. 2.3).

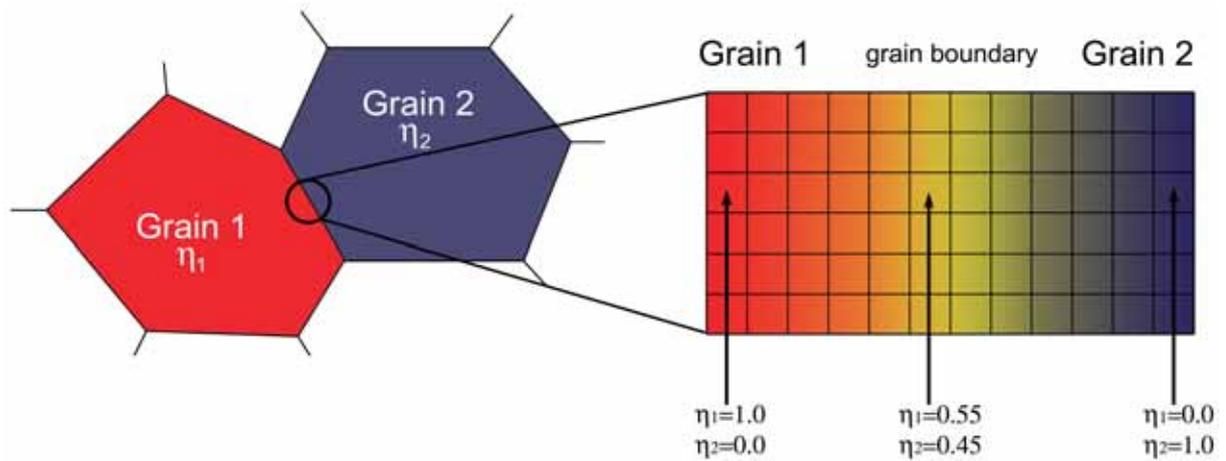


Figure 2.3. The discretization of the microstructure according to the phase field model [46].

For the phase field model, the construction of the free energy functional is crucial; this function must be defined to reflect the underlying physics of the phenomenon to be modeled [47].

2.3.3 The Vertex Model

The vertex model was first introduced by Kawasaki et al. in 1989 [48] for the simulation of cellular patterns. The basic idea behind this model is that the minimization of the free energy can be achieved exclusively by the motion of the triple junctions (called vertices by Kawasaki [48]). As a result, the curvature of the grain boundaries is not considered (Fig. 2.4a). The equations of motion are of dissipative character, it means that the total free energy of the system (potential energy) is dissipated by the motion of the vertices. The equations of motion for the vertices can be derived from the Lagrange equation

$$\frac{\partial R}{\partial v} = -\frac{\partial v}{\partial r}, \quad (2.3)$$

where the term in the left side represents the dissipation of the energy through the motion of the vertices whereas the term in the right side is the potential energy.

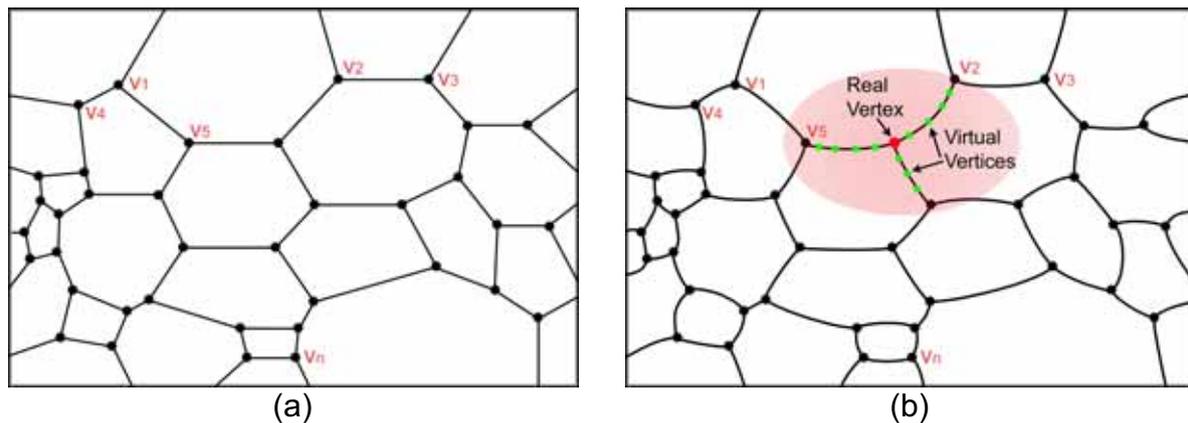


Figure 2.4. (a) The discretization of a microstructure after Kawasaki and (b) after Weygand [49]. Weygand as opposed to Kawasaki considered the curvature of the grain boundary by the introduction of so-called virtual vertices along the boundaries.

Weygand in 1998 [49] modified the original model by Kawasaki by allowing the curvature of the grain boundaries through the introduction of additional points (virtual vertices) along the grain boundary (Fig. 2.4b). The equations of motion for both kinds of vertices are calculated in the same manner as in the Kawasaki approach.

Other variations of these models consider straight grain boundaries but introduce an artificial curvature to the calculation of the velocities of the vertices to overcome the error introduced by the flat grain boundaries. In these models, the local equilibrium at the triple junctions is superimposed and used for the calculation of a factor that artificially introduces the curvature to the motion equations of the triple junctions [50].

Following the approach of Weygand, some models utilize virtual vertices along the grain boundary but the displacement of the triple junctions and virtual vertices is computed from the local curvature [50-53].

All these models are also called network models, because the discretization of the microstructure is achieved by means of a topological network of connected structural elements. In the case of the pure vertex model, these elements are exclusively the triple junctions whereas in Weygand's [49] and front-tracking models discrete grain boundaries are considered as a part of the network.

2.4 Simulation Method –A Vertex Model Approach–

In this section, it will be detailed the implementation of a 2D vertex model. The model is very flexible and capable to consider a large variety of parameters that affect the grain boundary motion and hence grain growth. The effect of some of these parameters on the grain boundary migration and grain growth evolution will be analyzed in further chapters.

The model is based on the network models [48,49], and uses a front-tracking approach [54]. One of the requirements of such methods is the discretization of the microstructure in a topological network of connected elements. For these reason, two different elements are considered: the triple junctions (the intersection point of three 2D grain boundaries) and grain boundaries, which are further segmented in a similar way to dislocation simulations found in the literature [55]. The grains are conformed

by the collection of boundaries and triple junctions surrounding them; they keep the information about the crystallographic orientations.

2.4.1 Equations of motion

Each element is considered to have a different equation governing its motion. First we will consider the case of the grain boundaries. A grain boundary moves with a velocity given by

$$v = m_{gb} p, \quad (2.4)$$

where m_{gb} is the grain boundary mobility and p is the driving force. For the general case when more than one driving force is applied to the grain boundary the velocity reads

$$v = m_{gb} \sum_i^n p_i. \quad (2.5)$$

The mobility is here considered to be a unique property of the grain boundary and therefore is not included within the sum. However, as shown in recent experimental investigations [56-59] on grain boundary migration in bicrystals under a stress field, the mobility can depend on the magnitude of the driving force induced by the stress (the mechanism for this phenomenon is not discussed here, but the dependency of the mobility on the character of the driving force is considered an exception). If this is the case, the mobility needs to be included also within the sum.

Because the capillary driving force is intrinsic for the grain growth phenomenon, it is possible to expand the sum as follows

$$v = m_{gb} T\kappa + m_{gb} \sum_i^{n-1} p_i = m_{gb} \kappa \left(\gamma + \frac{\partial^2 \gamma}{\partial \phi^2} \right) + m_{gb} \sum_i^{n-1} p_i, \quad (2.6)$$

κ is the curvature of the grain boundary and T is the line tension which is given by the sum of the grain boundary energy and the second derivative of the same with respect to the boundary inclination angle. It is noted that the boundary energy and mobility include their dependency on grain boundary misorientation. The energy dependence on the inclination angle is considered also in T .

Fig. 2.5 depicts a discretized boundary and the variables used for the calculation of Eq. (2.6) are also indicated. To define explicitly Eq. (2.6) is needed only the curvature of the grain boundary. The curvature can be calculated from the local geometry at each point b_i along the grain boundary with the help of the two immediately adjacent points b_{i-1} and b_{i+1} [55] (see appendix A). The path vector or tangential vector is determined. This vector describes the position of a discretizing point of the grain boundary with respect to the global coordinate system. In Fig. 2.5, the components of this vector are illustrated by \dot{x} and \dot{y} . Since the tangential vector is known, the components of the normal velocity can be easily calculated from this vector, the normal velocity is then given by

$$\vec{v}_n = \begin{pmatrix} -\dot{y} \\ \dot{x} \end{pmatrix} m_{gb} \kappa \left(\gamma + \frac{\partial^2 \gamma}{\partial \varphi^2} \right). \quad (2.7)$$

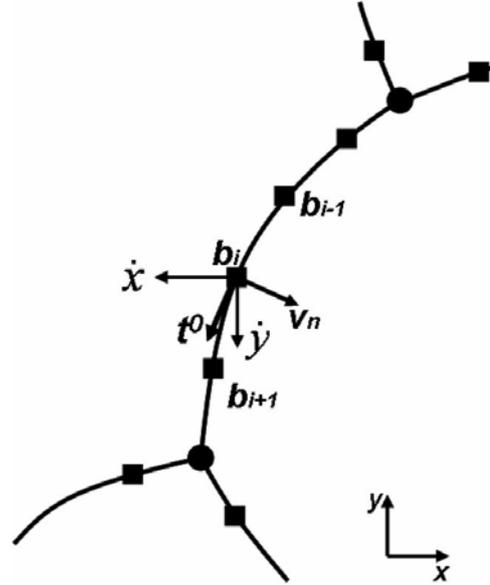


Figure 2.5. A discretized boundary is shown, t_0 represents the tangential vector to the boundary line at the point b_i , v_n is the normal velocity, \dot{x} and \dot{y} are the trajectory vectors along the boundary.

The motion equation of the triple junction can be calculated in a very similar way. The velocity of the triple junction is obtained from the equilibrium of forces existing at the triple junctions, which is given by the three adjoining grain boundaries and by the possible additional forces acting on the triple junction, the velocity can be defined as

$$\vec{v}_{tj} = m_{tj} \left(\frac{\vec{F}_{gb}}{\Delta s} + \sum_i^n \vec{P}_i \right), \quad (2.8)$$

where

$$\vec{F}_{gb} = \sum_i^n \left(\gamma + \frac{\partial^2 \gamma}{\partial \varphi^2} \right)_i \cdot \begin{pmatrix} \dot{x} \\ \dot{y} \end{pmatrix}_i = \sum_i^n T_i \cdot t_i^0, \quad (2.9)$$

m_{tj} is the triple junction mobility, Δs is the distance between the triple junction and the first discretizing point of an adjacent grain boundary (Fig. 2.6). Eq. (2.9) is the summation of the line tensions over the adjacent boundaries. Eq. (2.8) considers also the sum of the possible additional driving forces. The strict application of Eq. (2.8) will lead to the equilibrium of forces at triple junctions, if the dihedral angles between grain boundaries have a value of 120° then no motion of the triple junction will occur. However as discussed in the first chapter, the motion of the curved grain boundary introduces automatically the disequilibrium of forces that consequently leads to the motion of the triple junctions. It should be noted that in this model the motion of the triple junctions is not artificially superimposed in order to attain the equilibrium as in

other models [52, 53]. The equilibrium at triple junctions will only be attained if the necessary conditions for this exist.

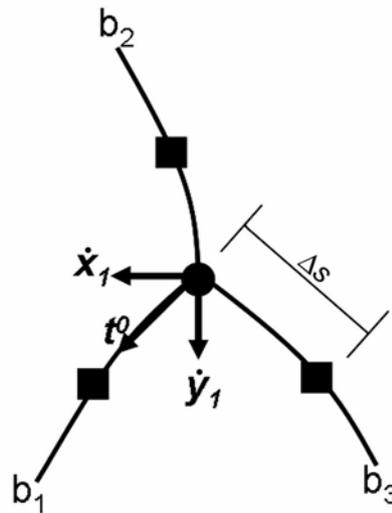


Figure 2.6. Variables used for the calculation of the triple junction velocity.

2.4.2 Topological Transformations

The principal disadvantage of the network models is that the topological transformations that take place during grain growth evolution must be incorporated by a set of analytically determined topological rules [60, 61] that need to be implemented in the model.

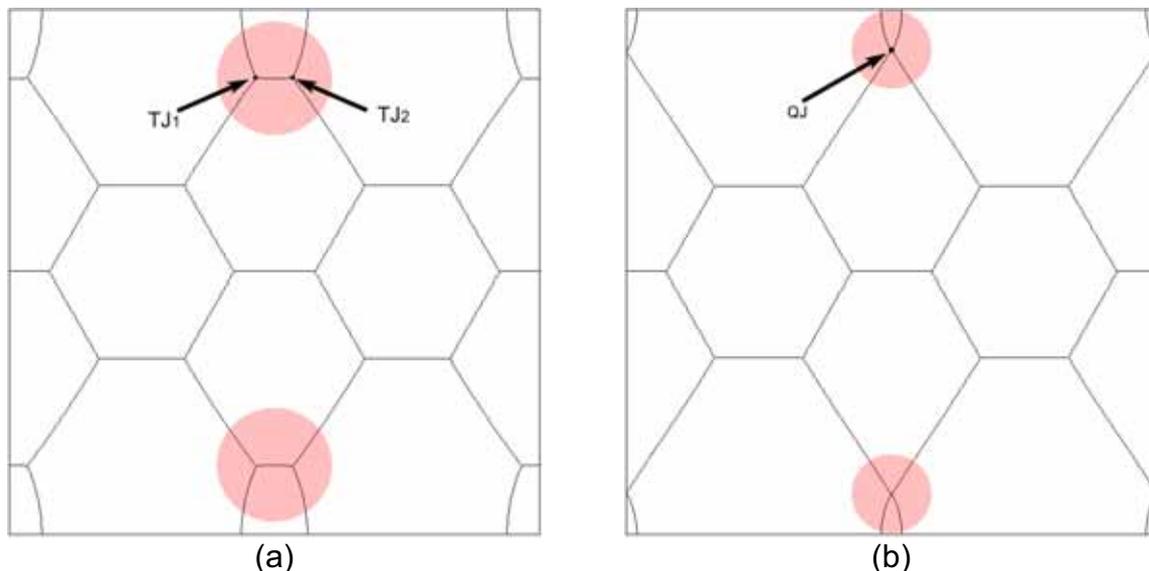


Figure 2.7. Grain growth evolution in a simple geometry, in (a) the disappearing grain boundary is highlighted whereas in (b) the quadruple junctions which are formed after the collision of the triple junctions as a result of the boundary annihilation.

In order to understand better the necessity to implement the topological transformations, let analyze a simple case. Fig. 2.7 shows two snapshots of the evolution of a simple microstructure during the course of grain growth. In the first figure (Fig. 2.7a) two grain boundaries (highlighted) migrate in the direction of their

center of curvature producing the shortening of the length of the boundary between the triple junctions TJ_1 and TJ_2 . The eventual disappearance of the grain boundary (Fig. 2.7b) causes the collision of the two triple junctions which were connected to the grain boundary forming a quadruple junction QJ (four grain boundaries meeting at one point). Since a quadruple junction is energetically unstable, it will split again into two triple junctions.

In the nature, this is managed simply by the rearrangement of the atoms that will always choose the less energetic configuration (i.e. two triple junctions). The problem is similarly managed by the Monte Carlo and phase field models. In the Monte Carlo model, a quadruple junction is represented by a zone with four different states and therefore the probability of one arbitrary cell to change to another state increases, the change of state is done automatically and is inherent to the model. Something similar happens in the phase field model. The quadruple junction zone will be characterized by a high gradient and thus the interchange energy of the cells within the zone increases and causes the rapid variation of the *order parameters* until the quadruple junction zone disappears.

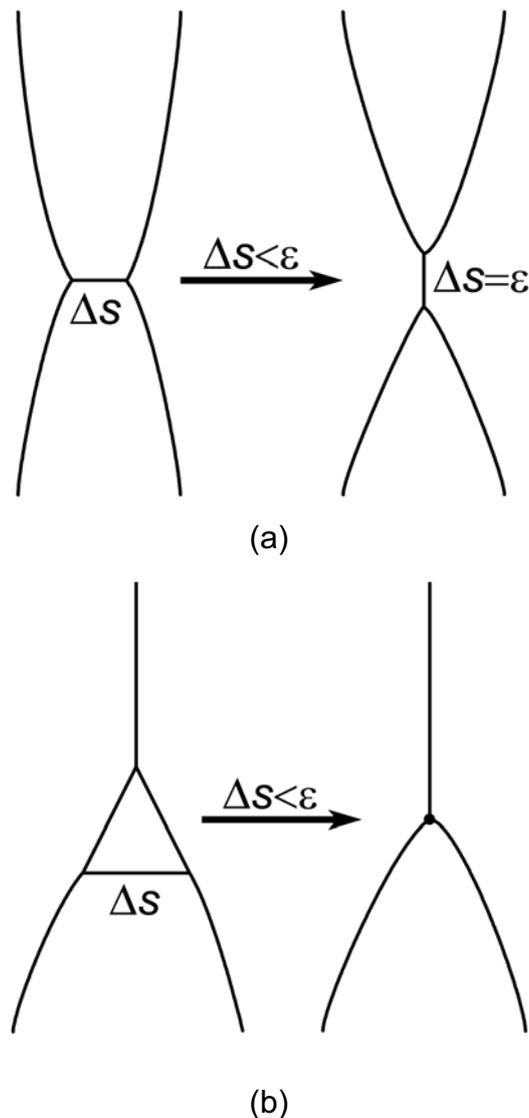


Figure 2.8. Topological transformations; (a) neighbor switching (T1) and (b) triangle elimination (T2). If Δs is smaller than ϵ then the transformation occurs.

Because in the network models only connected points compose the microstructure, the disappearance of a boundary means that the distance between two triple junctions approaches zero, when this occurs the network needs to be *reconnected* in order to minimize the free energy. The process occurs in two well defined steps: (a) quadruple junction formation (boundary collapsing) and (b) handling of the eventual split of the quadruple junction. For the implementation of 2D Vertex models, normally only two topological operations are considered [48]: neighbor switching operation (Fig. 2.8a) (usually denoted as T1) and triangle elimination (T2) (Fig. 2.8b). These operations are triggered when the distance Δs between triple junctions reaches a certain predefined critical value ε . The operation T2 is, in fact, not necessary because it can be achieved by the successive application of T1. However, this operation is normally implemented because it reduces the complexity of the model whereas the topology of the network remains intact.

It should be noted that T1 introduces a non-physical factor by avoiding completely the natural formation of quadruple junctions. Usually, such junctions are unstable and split automatically into two triple junctions and a new boundary. However, under anisotropic conditions, where the energies of the grain boundaries can greatly vary this might not be the case.

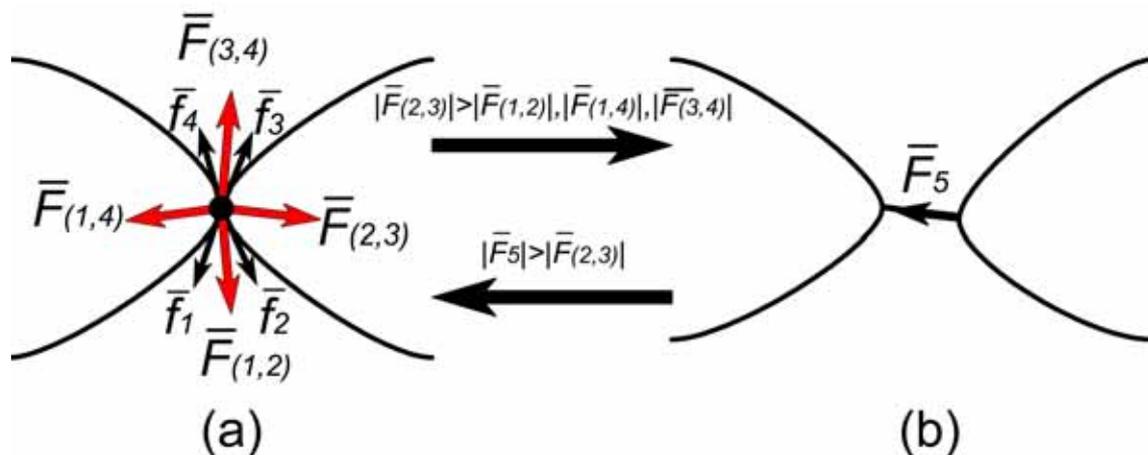


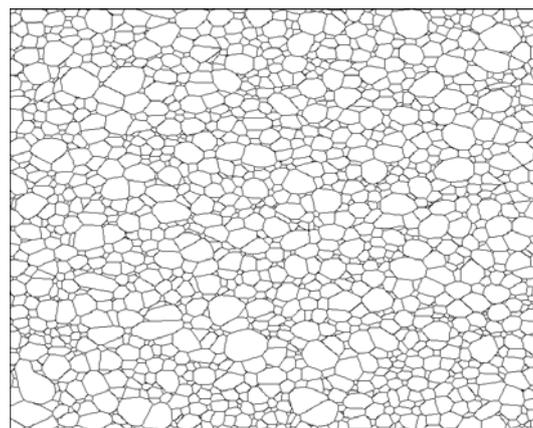
Figure 2.9. (a) A quadruple junction is allowed to form, the forces $\vec{f}_1, \vec{f}_2, \vec{f}_3, \vec{f}_4$ and $\vec{F}_{ij} = \vec{f}_i + \vec{f}_j$ are calculated; (b) if the split of the quadruple junctions leads to an increase in the free energy of the system the quadruple junction is the stable configuration.

To overcome this problem in the present model, the formation of the quadruple junctions is allowed and the split takes place only if it leads to a reduction of the total free energy of the system. The procedure is as follows, once that the quadruple junction is formed the forces \vec{f}_i exerted at the junctions by each grain boundary are calculated. The largest sum of the forces of two consecutively adjacent grain boundaries, denoted as \vec{F}_{ij} , allows to determine the direction of the rip. However, if the formation of the new grain boundary leads to an increase in the free energy of the system the quadruple junction is considered stable. This procedure is schematically shown in Fig. 2.9.

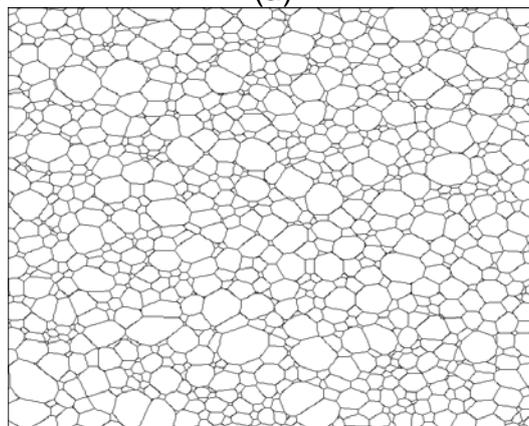
2.5 Validation of the Model

2.5.1 Grain Growth Kinetics

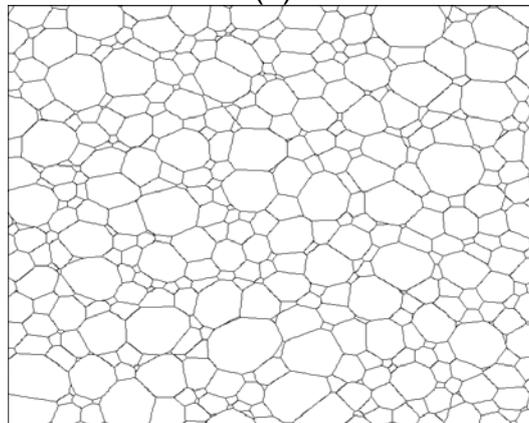
In order to determine the validity of the model, the outcome from the simulations were compared with classical theories on grain growth. For this purpose, a microstructure, comprised of 20000 grains, was constructed by means of a Voronoi tessellation [62, 63]. To give a rough impression of the simulations, Fig. 2.10 shows the evolution of the microstructure for increasing time.



(a)



(b)



(c)

Figure 2.10. Evolution of the simulated microstructure for $t_a < t_b < t_c$.

The simulations yield a scaling behavior which is characterized by parabolic kinetics, where the mean grain size increases with $t^{1/2}$. The time evolution of the normalized mean area is presented in Fig. 2.11, the linear fit is given by the equation

$$\langle A(t) \rangle = \langle A(0) \rangle + 1.4m_{gb}\gamma t. \quad (2.10)$$

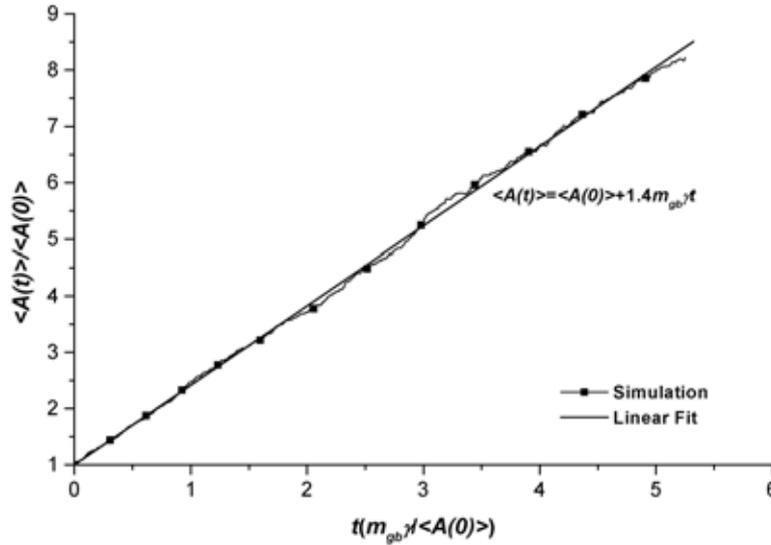


Fig. 2.11. Evolution of the mean grain area $\langle A \rangle$ with time. The simulated grain growth kinetics shows parabolic behavior.

2.5.2 Comparison with the von Neumann-Mullins Relation

The von Neumann-Mullins relation [64, 65] is a reference frame for the simulation of 2D grain growth, since it relates the growth rate of a grain in a polycrystal with the number of sides (topological class) of a definite grain. For the calculation of the relation, it is necessary to assume isotropic conditions, it means that the energy and mobility of the triple junctions are constant, and also the triple junctions are considered not to drag the grain boundary motion. Under these conditions the dihedral angle will take a value of 120° .

For the determination, let consider an arbitrary grain with an area S (Fig. 2.12). After certain time dt the grain boundaries will migrate a certain distance given by vdt , where v is the grain boundary velocity (Eq. (2.4)). The change of the area with respect to the time is, correspondingly, the contour integral of the product of the boundary velocity and the derivative of the boundary length dL

$$\frac{dS}{dt} = -\oint v dL, \quad (2.11)$$

the migration of the grain boundaries is exclusively curvature driven and can be substitute with Eq. (2.5)

$$\frac{dS}{dt} = -m_{gb}\gamma \oint \kappa dL. \quad (2.12)$$

If we consider now that every element dL of the grain boundary has a tangential vector with an angle φ , it is possible to define the curvature as the variation of the angle φ with respect to the perimeter of the grain boundary L

$$\kappa = \frac{d\varphi}{dL}, \quad (2.13)$$

therefore

$$\frac{dS}{dt} = -m_{gb}\gamma \oint d\varphi. \quad (2.14)$$

The integral of Eq. (2.14) in a continuous close curved will result in 2π , however, while the grain boundaries can be considered continuous curves, the grain itself can not (a grain is comprised by the union of continuous curved segments –grain boundaries–). At every triple junction the continuity of the grain shape is interrupted by the next grain boundary. The abrupt change is characterized by the turning angle β , because the energy is equal for all grain boundaries, the value of this angle corresponds to $\pi/3$, as seen in Fig. 2.12. The angular change from boundary to boundary must be subtracted from 2π ; with this, we obtain the final expression

$$\frac{dS}{dt} = -m_{gb}\gamma \left(2\pi - \frac{n\pi}{3} \right) = \frac{\pi}{3} \cdot m_{gb}\gamma (n-6). \quad (2.15)$$

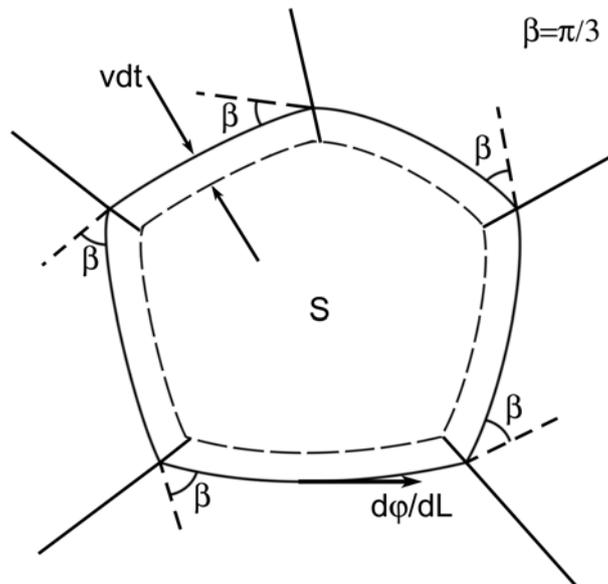


Figure 2.12. Parameters used for the determination of the von Neumann-Mullins relation.

Equation (2.15) relates the rate of change of the grain area to only the topological class n of the grain, n is the number of triple junction by which a grain is enclosed. It can be noted that grains with more than 6 sides will grow whereas grains with less will shrink.

In Fig. 2.13, the simulated rate of change of the grain area S is plotted as a function of the topological class n . The linear fit of the simulations has a slope of $1.0452m_{gb}\gamma$ while the slope of the von Neumann-Mullins relation is approximately $1.047m_{gb}\gamma$. The accuracy of the model is attributed to the clear interpretation of all physical parameters, and to the introduced method to handle the topological transformations. It can be observed that the largest deviation are found for the grains with only three sides ($n=3$). This occurs because these grains reach very small sizes and the curvature of their grain boundaries can not be properly represented. Such grains disappear almost instantly, affecting the statistics for the grains within this topological class.

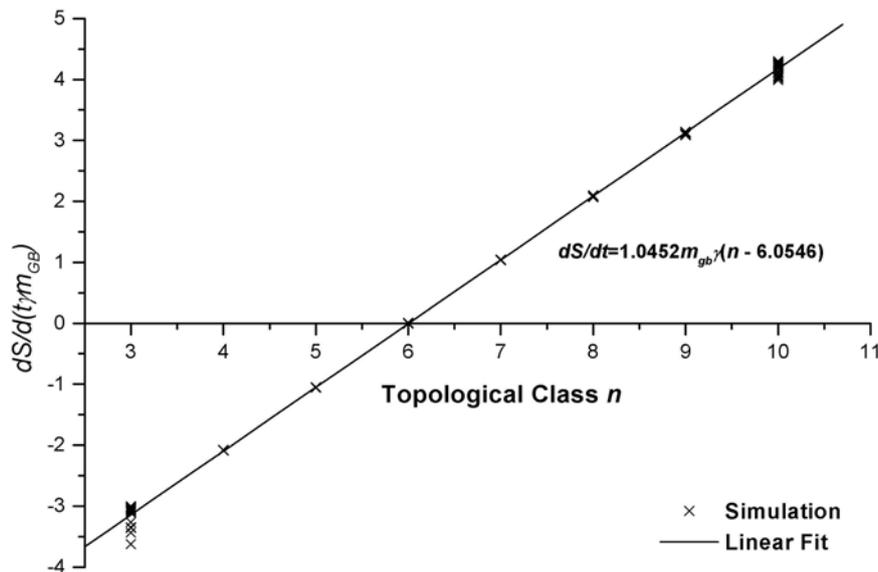


Figure 2.13. The comparison of the simulation results with the theoretical von Neumann-Mullins relation.

2.5.3 Grain Size Distribution

The microstructure of a material provides important information about the state of the material, distribution of the components (phases), and also hints about the physical or mechanical properties which can be expected from the material. For these reasons, the analysis and understanding of the microstructure is indispensable.

The microstructure of a material can be experimentally obtained by sectioning three-dimensional samples into two-dimensional planes. Examples of typical two-dimensional (simulated) microstructures in a polycrystal are given in Fig. 2.10. The microstructures which can be found during grain growth can be characterized basically by the mean grain size and its evolution with time. However, a uniform grain size is normally not expected, instead the grain sizes fluctuate along the mean grain size and can be described by a statistical distribution function. The grain sizes obtained experimentally can be represented by a lognormal distribution function, which is given by

$$f(D)dx = \frac{1}{\sqrt{2\pi\sigma}} \cdot \frac{1}{D} \exp \left[-\frac{1}{2} \left(\frac{\ln(D/D_m)}{\sigma} \right)^2 \right] dx, \quad (2.16)$$

where D is the grain size, D_m the mean grain size and σ the standard deviation.

In Fig. 2.14, the histogram of the grain size measured in a titanium sample after recrystallization is compared with the lognormal distribution function (Eq. 2.16). It can be observed that the grain sizes follow very well the theoretical function. Lognormal distributions can be normally found in processes where the independent variable can be obtained from the product of many small independent factors, for example the sizes of sand grains can be considered to be the product of the interactions between them (these interactions occurs randomly depending on many factors like number of neighbouring sand grains, wind presence, etc.). However, the fact that the grains of a polycrystal are lognormal-distributed lacks of a strict scientific justification, several attempts have been done trying to derive the same dependency from elementary premises but so far, none has been completely successful.

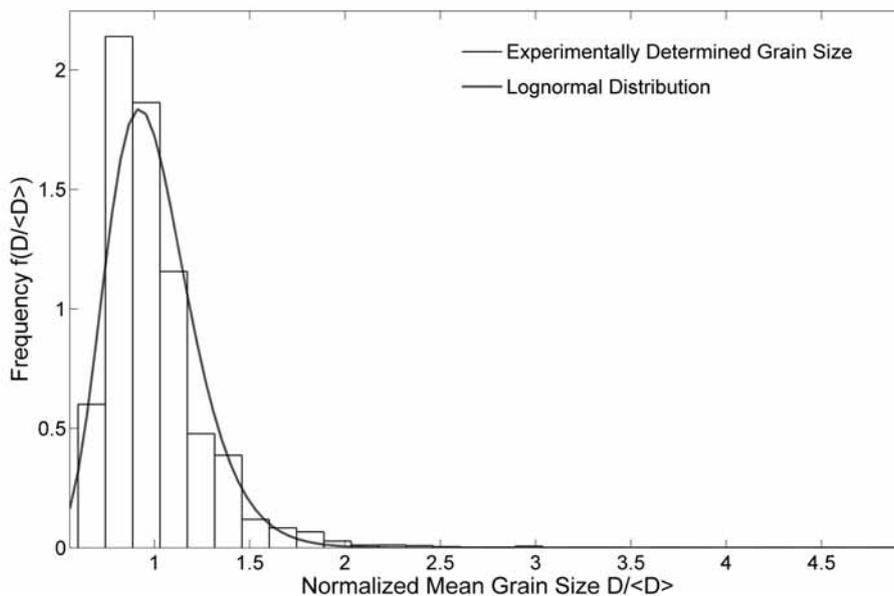


Figure 2.14. The histogram corresponds to the measured mean grain size in a pure titanium sample after recrystallization. The experimental grain size distribution can be fitted with the lognormal distribution.

Hillert [66] introduced a statistical model of grain growth by using some aspects of the method of Lifshitz and Slyozov [67] for coarsening of particles (Ostwald ripening) for the derivation of a fundamental grain size distribution. The grain size distribution derived by Hillert has been, however, never experimentally verified. In the same tone, other distributions have been proposed [68, 69]. These distributions function to some extent but there is not still a unified and clear derivation of a proper grain size distribution.

The grain size distributions obtained from simulations in isotropic conditions are normally characterized by their time invariance during grain growth (so called, self-similarity). If a model shows this behavior, it is said that the model reaches scaling

behavior. In Fig 2.15 the simulated grain size distribution is shown, it can be observed that despite the decreasing number of remaining grains the normalized grain size shows the same behavior. The distribution function which fits better the simulations is the Weibull function, this function is correlated with the gamma function and has been found to fit well some experimental results [69]

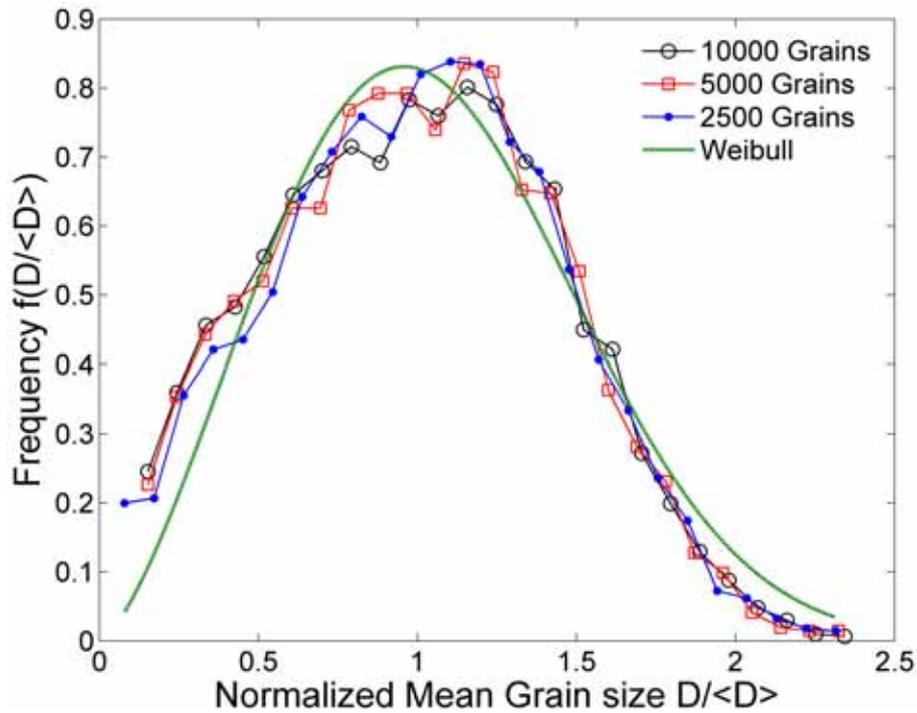


Figure 2.15. Simulated grain size distribution, the scaling regime which is characterized by the invariance of the distributions functions with time is shown. The simulated distributions can be well fitted by means of the Weibull distribution.

Chapter 3

Influence of a Magnetic Field on Grain Growth

3.1 Introduction

Grain growth is intimately related to the grain boundary migration and therefore is susceptible to the same factors which affect the movement of the grain boundaries. For example, in Chap. 1 we learned the different factors that cause grain growth stagnation and that all of them are related to some kind of impediment on the motion of the grain boundary. In a similar way, the different driving forces for the boundary migration may affect the evolution of the grain boundary. Nevertheless, the order of magnitude of the driving forces is normally completely dissimilar. For instance, the order of magnitude of the capillary driving force is of about 10^{-2} MPa [9] whereas for the magnetic driving force is approximately 10^{-4} MPa (for Bismuth, $H=10^7$ A/m). Due to this tremendous difference, it is difficult to think that other driving forces can affect grain growth evolution. For example, in recrystallization, the driving force provided by the deformation is much higher than the capillary driving force, therefore the curvature of the grain boundaries cannot practically affect the boundary movement during recrystallization (in fact, the grain boundaries migrate against its curvature indicating how diminutive the capillary driving force is for this phenomenon).

The effect of magnetic fields during the processing of materials has been extensively studied. In recrystallization and grain growth, this effect has been researched since 1949 [70] in iron-based alloys, however, the investigations are normally restricted to ferromagnetic materials [71]. Non-ferromagnetic materials are normally overlooked because the effect of a magnetic field in these materials has been considered negligible.

However, in recent experiments [72-74] carried out in non-ferromagnetic Bismuth and Zink bicrystals, it was found that a magnetic field can exert a sufficient driving force to produce the motion of the grain boundaries. Experiments in non-ferromagnetic polycrystalline samples [75, 76] also showed that magnetic annealing can relevantly modify the texture evolution. All these investigations evince the importance of the development of simulation models capable to reproduce this phenomenon.

3.2 The Magnetic Driving Force

It is well known that the anisotropy of any physical property can be used as a source for a driving force. It is necessary only to create a difference in free energy across the

grain boundary to produce the required driving force. This can be achieved, for example, by the application of a stress field to a material with an anisotropic Young's modulus or by the application of a magnetic field to a material with anisotropic magnetic susceptibilities.

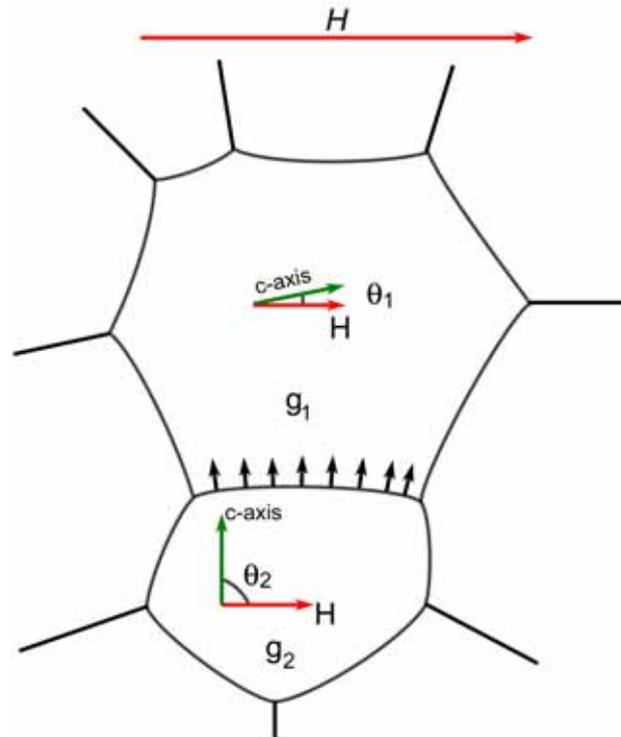


Figure 3.1. The magnetic driving force for a grain boundary is simply given by the difference in the magnetic induced free energy of the neighboring grains. The grain g_1 has a high magnetic free energy (when $\theta \rightarrow 0$, $p_m \rightarrow \max.$) whereas g_2 has a low energy, this leads to a driving force in the grain boundary in direction of the most energetic grain.

In the case of a magnetic anisotropic material the driving force is given by the difference in magnetic induced free energy of both crystals along a grain boundary. The magnetic free energy of one crystal reads [77]

$$E_m = \frac{1}{2} \mu_0 H^2 \chi, \quad (3.1)$$

where μ_0 is the vacuum permeability of the free space, H is the magnetic field strength and χ is the magnetic susceptibility of the crystal. The driving forces in a grain boundary with neighboring grains g_1 and g_2 (Fig. 3.1) can be written as

$$p_m = E_2 - E_1 = \frac{\mu_0 H^2}{2} (\chi_2 - \chi_1). \quad (3.2)$$

According to elementary crystallography the magnetic susceptibility of an uniaxial crystal can be written as $\chi = \chi_{\perp} + \Delta\chi \cos^2 \theta$, where $\Delta\chi$ is the difference in parallel χ_{\parallel} and perpendicular χ_{\perp} susceptibility, θ is the angle between the c -axis and the magnetic field. Substituting into Eq. (3.2) leads to

$$P_m = \frac{1}{2} \mu_0 \Delta \chi H^2 (\cos^2 \theta_2 - \cos^2 \theta_1). \quad (3.3)$$

To consider the magnetic driving force in the simulations it is only necessary to introduce explicitly Eq. (3.3) into Eq. (2.6) and (2.9), the velocity of the grain boundary can be calculated as follows

$$v = m_{gb} \kappa \left(\gamma + \frac{\partial^2 \gamma}{\partial \varphi^2} \right) + m_{gb} P_m, \quad (3.4)$$

because the capillary and the magnetic driving force have the same direction (not necessarily the same sense) and recalling the variables of Fig. 2.5, the velocity of each discretizing point along the grain boundary is given by

$$v = \begin{pmatrix} -\dot{y} \\ \dot{x} \end{pmatrix} m_{gb} [T\kappa + (E_2 - E_1)] = \begin{pmatrix} -\dot{y} \\ \dot{x} \end{pmatrix} m_{gb} \left[T\kappa + \frac{\mu_0 \Delta \chi H^2}{2} (\cos^2 \theta_2 - \cos^2 \theta_1) \right]. \quad (3.5)$$

The velocity of the triple junction is also slightly affected by the magnetic driving force. In the equation of the triple junctions (Eq. (2.9)), the magnetic driving force applied on the immediately adjoining segments of the grain boundaries at the triple junction needs to be considered, then the velocity of the triple junctions reads

$$\vec{v}_{ij} = m_{ij} \left\{ \frac{\vec{F}_{gb}}{\Delta s} + \sum_i^n \left[\frac{\mu_0 \Delta \chi H^2}{2} (\cos^2 \theta_2 - \cos^2 \theta_1) \right] t_i^0 \right\}. \quad (3.6)$$

3.3 Texture Evolution in Magnetically Annealed Titanium

Molodov et. al.[78] investigated the evolution of polycrystalline titanium during magnetic annealing. They found that a magnetic field effectively affects the evolution of the texture dramatically. The experiments were carried out in samples with different degrees of deformation. Two symmetrical peaks (Fig. 3.2) in the $\{0002\}$ pole figure characterize the deformation texture of titanium. These peaks spread around the orientations $\{\varphi_1=0^\circ, \Phi=35^\circ, \varphi_2=0^\circ\}$ and $\{\varphi_1=180^\circ, \Phi=35^\circ, \varphi_2=0^\circ\}$.

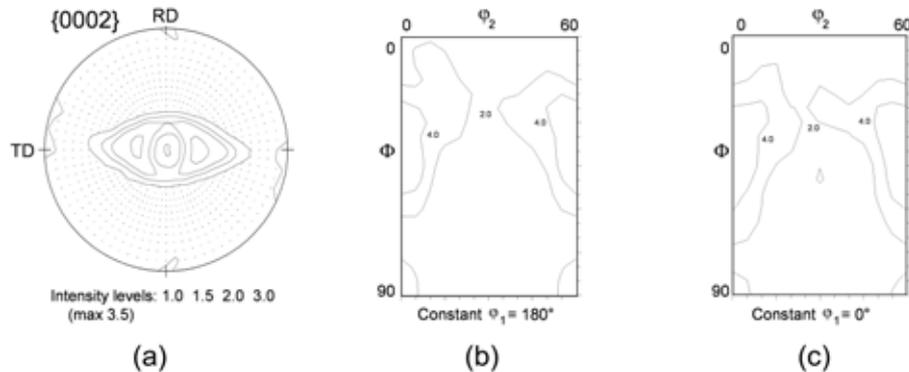


Figure 3.2. Texture of 75% deformed titanium after reduction by rolling: (a) $\{0002\}$ pole figure, ODF sections at (b) $\varphi_1=180^\circ$ and (c) $\varphi_1=0^\circ$ [79].

After the rolling, the samples were first annealed 15 minutes without magnetic field and then magnetically annealed under field strength of 17 T at 750°C for different times. The direction of the magnetic field was selected in such a way that the grains with orientations close to the texture component $\{\varphi_1=0^\circ, \Phi=35^\circ, \varphi_2\}$ possess a high magnetic free energy (*c*-axis perpendicular to magnetic field). After 240 minutes magnetic annealing the texture has considerably changed since the intensity of the component $\{\varphi_1=0^\circ, \Phi=35^\circ, \varphi_2\}$ has evidently weakened. This is attributed to the higher rate of disappearance of those grains with a higher magnetic free energy.

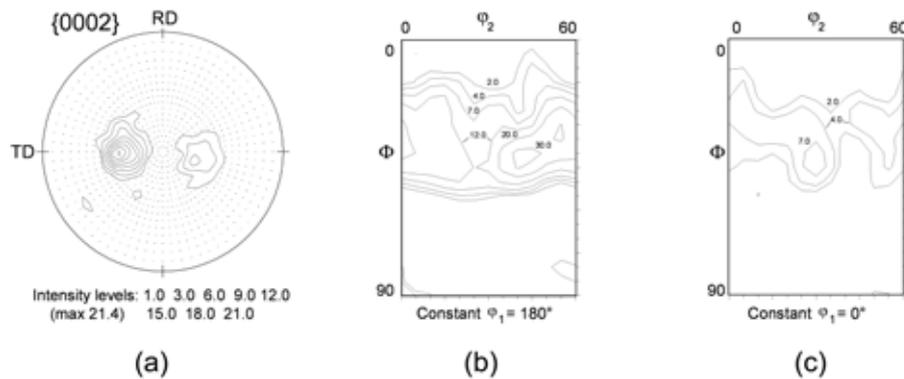


Figure 3.3. Texture after 240 minutes magnetic annealing, the weakening of the disfavored component is evidently.

3.4 Computer Simulations

In order to corroborate the hypothesis that the changes in the microstructure and texture were caused by the introduction of the magnetic field during the grain growth, computer simulations were performed. For this purpose, the polycrystalline microstructure obtained from EBSD measurements (Fig. 3.4a) was discretized for its use in the simulations. For the discretization of the microstructure, an algorithm was implemented that tracks and connects the triple junctions and grain boundaries of the microstructure through the difference of orientation between points and thus delivers the topological network that the model utilizes. The results of this discretization can be seen in Fig. 3.4b, which consists only of connected points forming grain boundaries whereas the EBSD mapping consists of single orientations and there is neither explicit discrimination of grains nor grain boundaries.

The model requires as input the information about the grain boundary energy and mobility, the orientation of the grains, the magnetic field and the initial microstructure. There is, so far, not reliable data on grain boundary energy and mobility for titanium, for this reason, these parameters were chosen to be constant for the entire simulation with values of $\gamma=0.3 \text{ J/m}^2$ and $m_{gb}=1 \times 10^{-10} \text{ m}^4 \text{ J}^{-1} \text{ s}^{-1}$. In turn, the used magnetic field strength was of 17.4 T. The other constants for the calculation of the magnetic driving force are respectively the difference in magnetic susceptibility for titanium $\Delta\chi=1.18 \times 10^{-5}$ and the permeability of the free space $\mu_0=4\pi \times 10^{-7} \text{ N/A}^2$. The microstructure and orientation of the grains were taken from the EBSD mappings (initial texture is shown in Fig. 3.6a), as described previously.

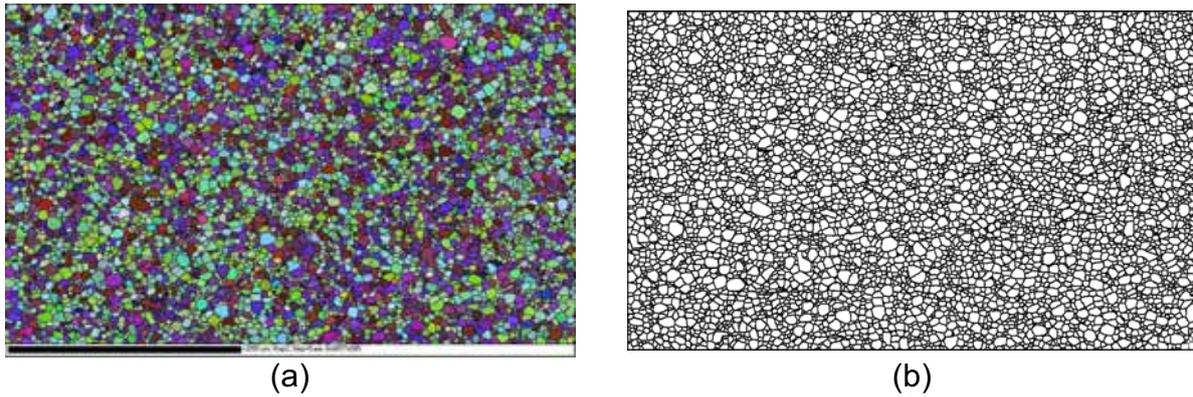


Figure 3.4. (a) Experimentally determined microstructure by means of orientation microscopy corresponding to the initial state before the magnetic annealing and (b) the same microstructure in its discrete form for the simulation.

The orientation of the magnetic field mirrors the conditions used in the experiment, as shown in Fig. 3.5. The magnetic field is perpendicular to the rolling direction (RD) whereas the transverse direction is tilted 32° with respect to the magnetic field. Because both component are symmetrical, it is expected that the grains with orientation near the component $\{\varphi_1=180^\circ, \Phi=35^\circ, \varphi_2\}$ have an additional driving force for the growth. Since their c -axes are nearly parallel to the magnetic field and thus have a smaller magnetic free energy in comparison with the component $\{\varphi_1=0^\circ, \Phi=35^\circ, \varphi_2\}$ whose c -axes are nearly perpendicular.

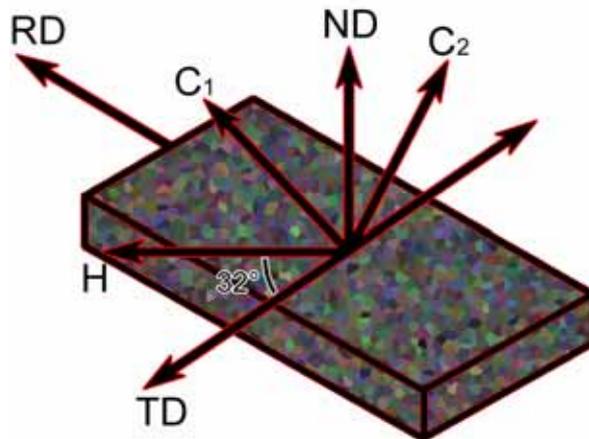


Figure 3.5. Spatial orientation of the cold-rolled sample with respect to the magnetic field H ; C_1 stands for the texture component $\{\varphi_1=180^\circ, \Phi=35^\circ, \varphi_2\}$ and C_2 for $\{\varphi_1=0^\circ, \Phi=35^\circ, \varphi_2\}$; ND/RD/TD are the normal/rolling/transverse direction respectively.

3.4.1 Texture and Microstructure Evolution

It should be noted, however, that the simulation results can only be compared qualitatively with the experimental ones. This is caused by two main factors, the lack of real data for the boundary energy and mobility and the fact that the experiments are performed in 3D samples whereas the simulation are 2D. Nevertheless, the simulations allow the possibility to draw general and qualitative predictions of the effect of the magnetic field on the microstructure evolution.

The texture obtained from the simulation shows a very good agreement with the experimental results. The intensity of the component $\{\varphi_1=0^\circ, \Phi=35^\circ, \varphi_2\}$ decreases

with increasing time (Fig. 3.6c), in absence of the magnetic field the texture, as expected, shows no relevant changes in its evolution with time for the same annealing time (Fig. 3.6b).

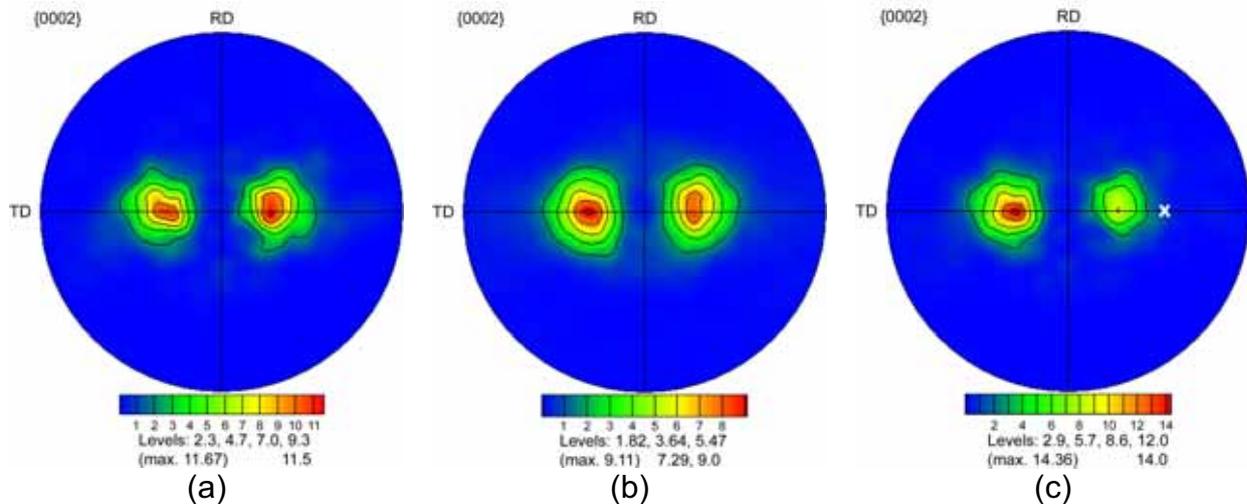


Figure 3.6. (a) $\{0002\}$ pole figure for 75%-rolled Ti sheet sample after annealing at 750° for 15 min; (b) and (c) - simulated pole figures after subsequent 10 min annealing at 750°C for a 2D Ti-polycrystal without field (b) and subsequent 20 min. in a magnetic field of 17.4 T (c) (field direction is indicated by a white cross).

The grains with orientations near to the favored component ($\{\varphi_1=180^\circ, \Phi=35^\circ, \varphi_2\}$), depending on their surroundings, have an additional driving force for their growing. Because the grains with higher magnetic energy disappear, the additional magnetic driving force decreases with time and after sufficient time the magnetic field has no further effect.

The measurement of the individual orientation by means of orientation microscopy provides the opportunity to analyze the evolution of the microstructure and its relationship with the fraction of grains which assemble a particular texture component. Since the magnetic driving force for an arbitrary grain depends on its environment, the distribution of the grains with different orientations within the microstructure is very relevant. In Fig. 3.7a, the EBSD mapping of the microstructure is shown, the grains belonging to the component $\{\varphi_1=180^\circ, \Phi=35^\circ, \varphi_2\}$ are depicted in red whereas the grains of the component $\{\varphi_1=0^\circ, \Phi=35^\circ, \varphi_2\}$ in green.

Despite some clustering of grains with the same orientation, it can be observed that the grains of both components tend to distribute themselves essentially homogenous. For this reason, the effect of the magnetic field is also expected to be homogenous. After the application of both annealing treatments (conventional and magnetic) the grains are distributed distinctly depending on the conditions of the annealing. The magnetically annealed sample shows a higher fraction of grains with orientation within the favored component $\{\varphi_1=180^\circ, \Phi=35^\circ, \varphi_2\}$ (Fig. 3.7b and 3.7d) whereas the sample annealed conventionally presents essentially the same quantity of grains of both components (Fig. 3.7c and 3.7e) which is the same condition found in the original sample before the treatments (Fig. 3.7a). The good agreement of the simulation with the experimental results can also be observed. It must be only stressed that the time of the simulation does not (and cannot, at least for 2D simulations) correspond with the real annealing time. The simulations provide,

however, qualitatively the same result which validates the simulation model for its application in the simulation of grain growth in a magnetic field.

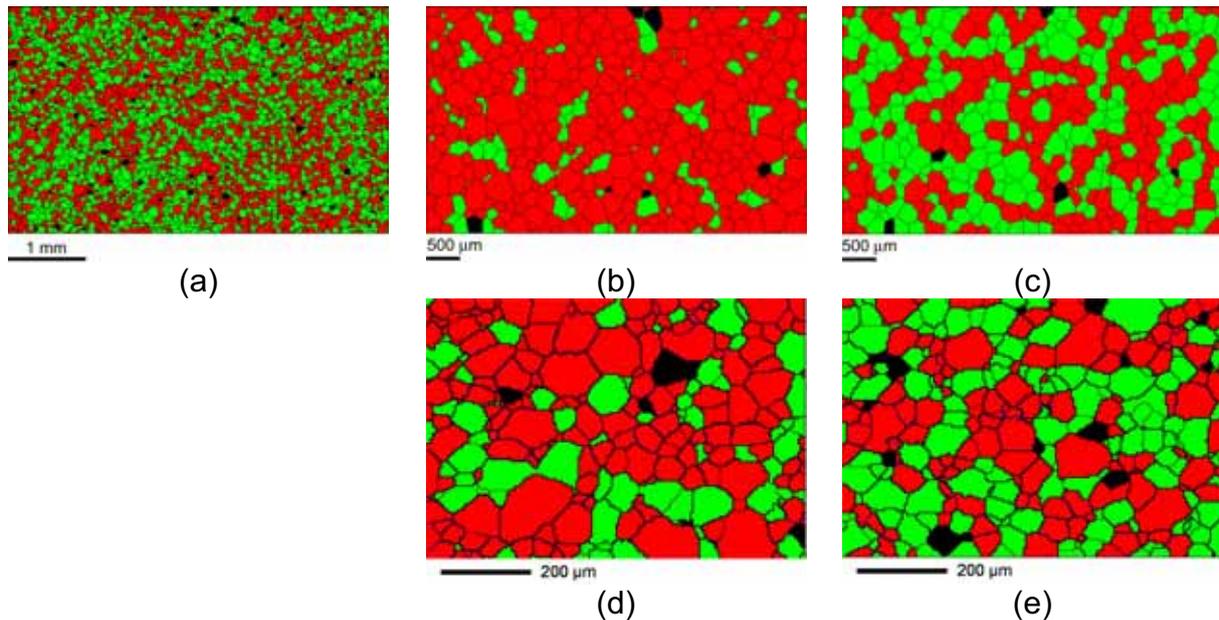


Figure 3.7. The simulated evolution of the grain fraction of the favored (red) and disfavored (green) component; (a) shows the original microstructure, the grain fraction of both components is practically the same. After 10 min. of magnetic annealing the microstructure is dominated by the favored grains (b), whereas without magnetic field for the same time (c) no significant difference can be found from the original condition. The same can be observed in the samples obtained experimentally (d)-(e) [79, 80]. The component $\{\varphi_1=180^\circ, \Phi=35^\circ, \varphi_2\}$ is depicted in ■, whereas $\{\varphi_1=0^\circ, \Phi=35^\circ, \varphi_2\}$ in ■ and other orientations in ■ respectively.

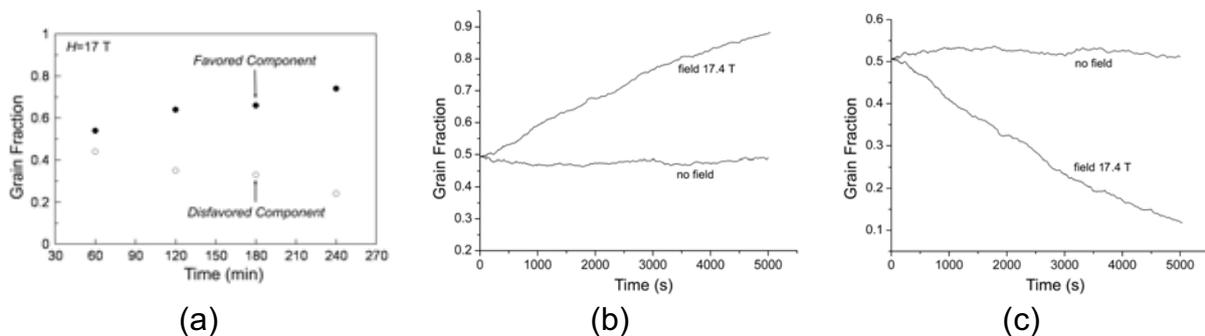


Figure 3.8. Grain fraction of the favored and disfavored components; (a) the evolution with time of experimental grain fraction for both components during magnetic annealing, (b) grain fraction evolution for the favored and disfavored (c) component during conventional and magnetic annealing.

In Fig. 3.8 the evolution with time of the grain fraction of the favored and disfavored component is shown. Consequently the amount of grains of the component $\{\varphi_1=0^\circ, \Phi=35^\circ, \varphi_2\}$ decreases apparently linear with time whereas the amount of the other component correspondingly increases, this effect was observed in both, experiments (Fig. 3.8a) and simulations (Figs. 3.8b and 3.8c). In contrast, during conventional annealing the grain fraction of both components remains practically constant with time which indicates that the grain growth is now exclusively driven by the reduction of the grain boundary surface.

3.4.2 Influence of the Magnetic Field on Grain Growth Kinetics

As seen in previous sections, the introduction of an additional driving force for the grain boundary migration affects effectively the evolution of the texture during the magnetic annealing, as result of the faster shrinking rate of the highly energetic grains. For this reason, it can be thought that the overall kinetics of the sample is affected as well. However, the relationship between the dynamic behavior of the mean grain size and the effect of the magnetic field is not easy to establish because the magnetic driving force is dependent on time, texture, morphology of the sample and spatial distribution of the grains. The initial grain size before the annealing plays an additional role, then for very small grain sizes, the capillary driving force might be much larger than the magnetic one and, as a result, have practically no influence. In order to analyze all these possibilities, the kinetics of the grain growth was studied by means of computer simulations.

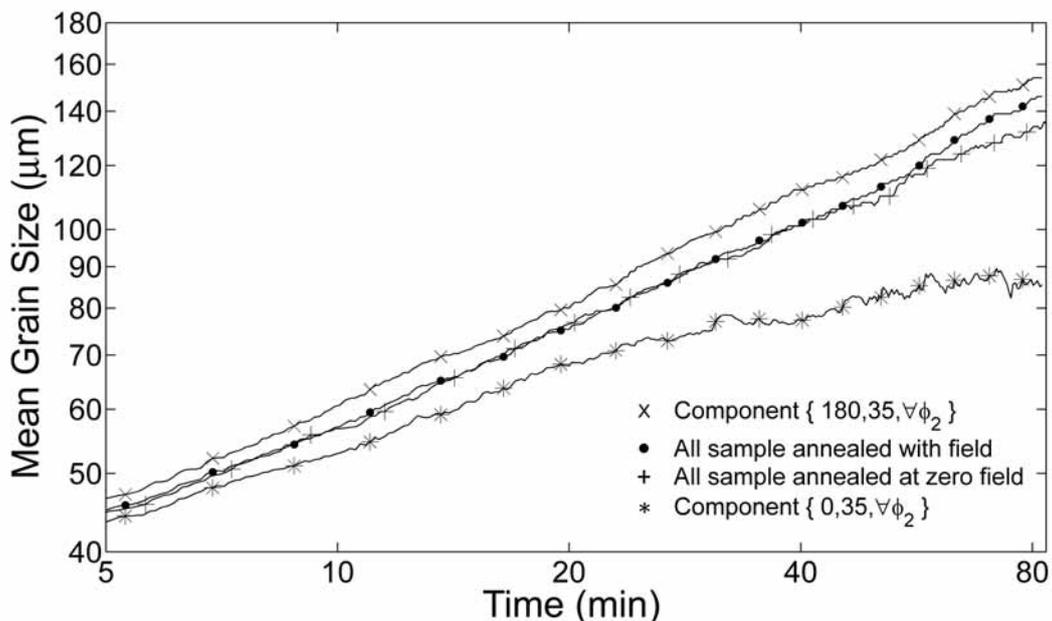


Figure 3.9. Simulated kinetics of the experimental setup given in Fig. 3.5. The overall kinetics for the conventional and magnetic annealing does not show any significant difference, this is caused by the compensation of the kinetics of the favored component with the kinetics of the disfavored component.

In Fig. 3.9, the results of the simulated kinetics obtained with the experimental conditions seen in Fig. 3.5 are presented. The kinetics obtained from all the grains, for the conventional and magnetic annealing, seems to be the same, no major difference between can be observed. This can be also appreciated in Figs. 3.7d and 3.7e, after the annealing treatments, the mean grain size does not change significantly.

However, if the kinetics of the diverse texture components is analyzed in detail, the difference becomes evident. For instance, the kinetics of the favored component is much higher than the kinetics of the disfavored component and the overall kinetics. The kinetics of the disfavored component presents also an interesting feature, at the beginning of the annealing, the curve for this condition seems to evolve linearly (Fig. 3.9) but after some time (approx. at 30 min) the kinetics becomes slower and the curve does not show further linearity. This occurs because grains of the opposite

component surround mainly the still existing grains of this component and thus the magnetic driving force affects decisively their growth.

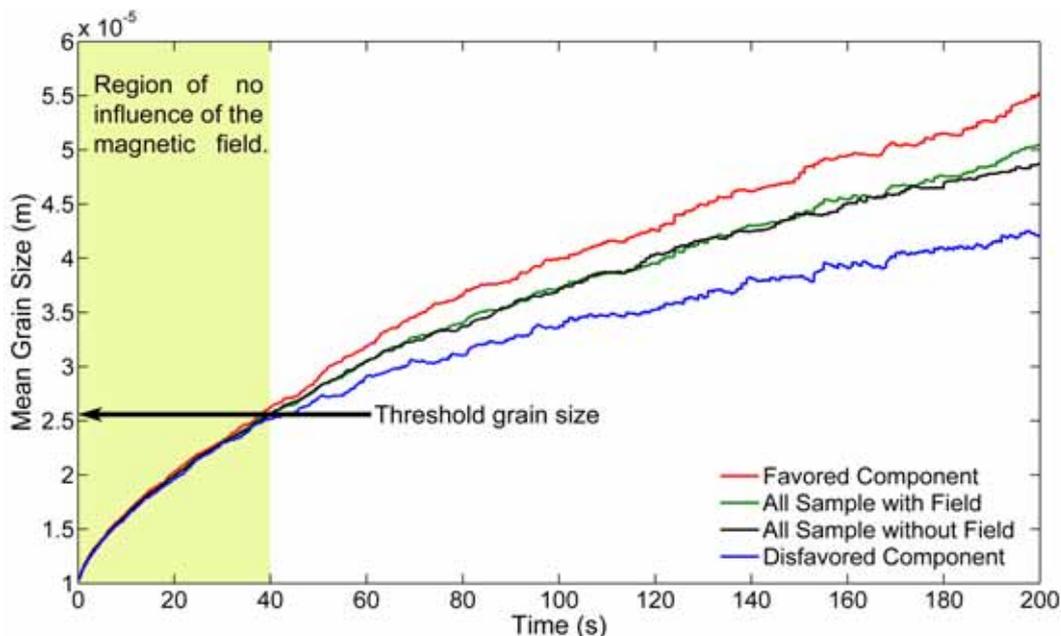


Figure 3.10. Simulated grain growth kinetics for a sample with an initial mean grain size of only 10 μm .

Due to the nature of the influence of the magnetic field, the existence of a threshold grain size is expected. In Fig. 3.10 the simulated kinetics of a sample with an initial grain size of 10 μm is plotted, all other parameters for the simulation were not changed. It is evident that the magnetic field does not affect the kinetics of the grain growth until a certain value of the mean grain size is reached. The kinetics of the favored and disfavored component (shaded region of Fig. 3.10) can not be indistinctly separated and present practically the same behavior as the kinetics of the entire sample.

3.4.3 Von Neumann-Mullins Relation during Magnetic Annealing.

As a consequence of the analysis of the previous section, it is also expected, the von Neumann-Mullins relationship not to be valid during magnetic annealing. In Fig. 3.11 the rate of area change for the favored component at different annealing times is shown and compared with theoretical von Neumann-Mullins relation. For the sake of simplicity, simple linear fits were selected to model the simulation data owing the fact that the real dependency of the grain-area rate change is unknown.

The area change rate, taken after 10 minutes of annealing, shows the largest deviation with respect to the theoretical relationship. This occurs because at early stages of the thermal treatment, the grains of both components are distributed homogeneously (Fig. 3.7a), their grain fractions are similar (Fig. 3.8b-c) and thus the grains of the favored component experiment a maximal advantage for their growth.

With the decrease in number of the disfavored grains the clustering of the favored grains is promoted and as consequence the evolution of the grains becomes slowly dominated by the capillary driving force (i.e. curvature driven grain growth). This

behavior is reflected also in Fig. 3.11, which shows that after subsequent annealing the area change rate of the favored component approaches the von Neumann-Mullins relationship. It can be noted that the simulation data after 80 minutes deviates only slightly from the von ideal von Neumann-Mullins relation. The curve for the disfavored grains after 10 minutes of magnetic annealing can also be observed in Fig. 3.11. A negative growing rate for grains with $n=6$ is evident, the curve is shifted to lower growing rates reflecting the influence of the magnetic field.

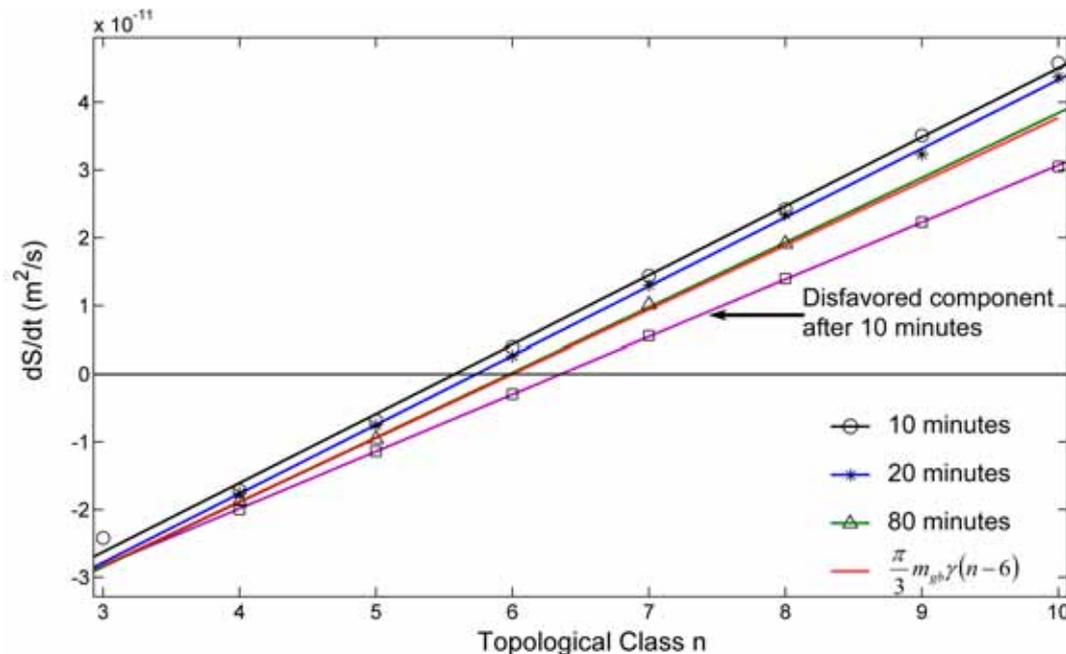


Figure 3.11. Grain-area rate with time in dependency on the topological class for the favored and disfavored component, the data were taken directly from the simulation at different times.

One would be tempted to derive an equivalent equation to the von Neumann-Mullins relation with consideration of the magnetic field. However, this task is practically impossible due to the stochastic nature of the magnetic driving force. Since the magnetic driving force change heterogeneously, the equilibrium angle at triple junctions deviates from $\pi/3$ and cannot be subtracted from result of the integration of Eq. (2.14). Another complication for the determination of the analytical equation arises from the dependency of the magnetic force on time, as seen in a previous section, because the disfavored grains disappear gradually, the influence of the magnetic field decreases accordingly, resulting in a completely new set of turning angles that should be rested from Eq. (2.14).

3.5 Magnetic Annealing in a Sample with Randomly Oriented Grains

In previous sections, it was effectively demonstrated that a magnetic field can affect the evolution of the texture and kinetics during grain growth in a strongly textured sample. However, it still remains open if the same occurs in samples mildly textured or even with randomly oriented grains. If the magnetic field is capable of affecting the evolution of grain growth even in this kind of samples, then it can be used to *engineer* materials magnetically by massively eliminating undesired texture components or promoting the growth of some selected grains, which would be the base of

magnetically tailored materials. In the current section, it will be analyzed the general case of a sample with randomly oriented grains.

Considering only a grain of the sample, the average magnetic driving force exerted at this grain can be expressed as the difference between the magnetic free energy of the grain and the average magnetic free energy resulting from the neighboring grains

$$\bar{P}_m = \frac{1}{2} \mu_0 \Delta\chi H^2 \left(\cos^2 \theta - \frac{\sum_i^n \cos^2 \theta_i}{n} \right), \quad (3.7)$$

where n is the number of grain boundaries enclosing the grain. For a crystalline aggregate with randomly oriented grains, the distribution of the angles between the c -axis and the magnetic field is given by [81]

$$F(\theta) = \frac{1}{2} \sin \theta, \quad (3.8)$$

the average magnetic driving force can be expressed then as [80]

$$\bar{P}_m^{random} = \frac{1}{2} \mu_0 \Delta\chi H^2 \left(\cos^2 \theta - \frac{1}{2} \int_0^\pi \sin \theta \cos \theta d\theta \right) = \frac{1}{2} \mu_0 \Delta\chi H^2 \left(\cos^2 \theta - \frac{1}{3} \right). \quad (3.9)$$

For a $\Delta\chi > 0$, the grains with $\theta < 54.73^\circ$ will be favored for growth independently of the direction of the field. Naturally, this condition can only be attained as long as the orientations of the grains remain random distributed. However, we can conclude that even in a sample with randomly oriented grains, there will always be grains with an energetic advantage for their growth and thus the sample will become textured during the magnetic annealing.

Despite that initially the grains with $\theta < 54.73^\circ$ will be favored for their growth irrespectively of the field direction, the latter is decisive for the final texture of the sample. Taking into account the direction of the magnetic field, the distribution of the magnetic energy for random orientations can be determined. In Fig. 3.12, such distribution is shown for the cases when the field is directed parallel to the direction z_0 (Fig. 3.12a) and when the field is directed parallel to the direction y_0 (Fig. 3.12b).

In both cases, it is evident that for some orientations, the magnetic energy is much higher and therefore grains with these orientations will have a disadvantage for their growth indistinctly of their spatial location in the polycrystal. Since the formation of clusters of similar orientations is not very probable: grains with orientations in the red zone will be surrounded by at least one grain of the blue zone and be consumed more rapidly by this grain (Fig. 3.12).

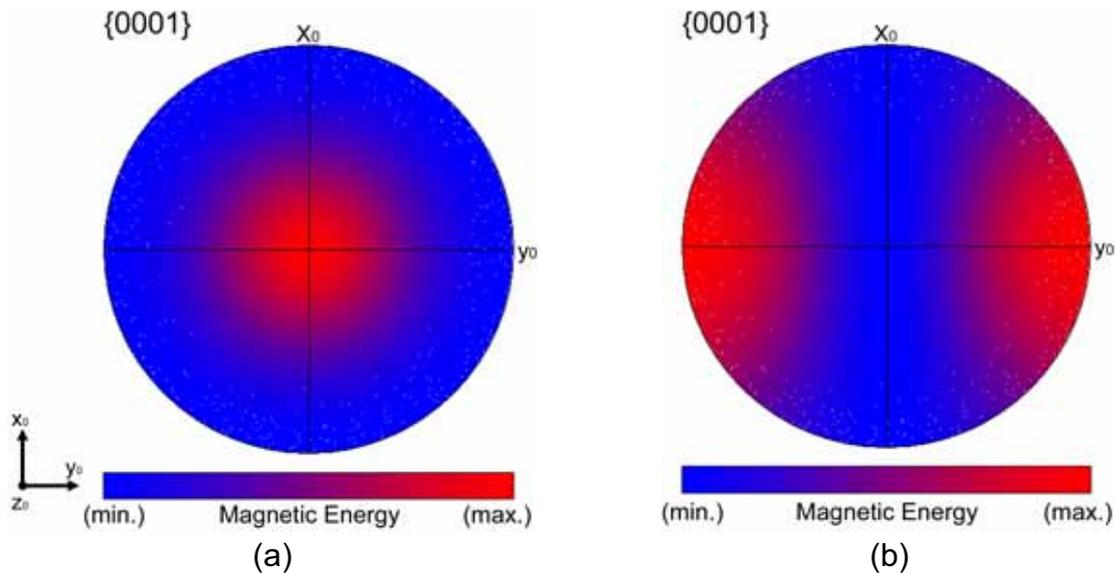


Figure 3.12. Distribution of the magnetic energy in the spherical space given a permanent direction of the field, in (a) the field is parallel to the direction z_0 (perpendicular to the paper plane) and in (b) parallel to the direction y_0 .

3.5.1 Orientation and Simulation Details

In order to demonstrate the validity of the previous assumptions, computer simulations were performed using the microstructure described in section 2.5. A random orientation distribution was imposed in the microstructure, while others parameters for the simulation (γ , m_{gb} and H) were not changed. Two different directions for the magnetic field were used, $[001]$ and $[010]$, both represented as unit vectors of the general vector $[x_0, y_0, z_0]$. Both directions correspond to the cases shown in Fig. 3.12.

The algorithm to generate a random orientation distribution is critical, because if simple random numbers are assigned to $\{\varphi_1, \Phi, \varphi_2\}$, due to the symmetry of the spherical space, the selection of random orientations from uniform distributions will lead to the clustering near the poles of the sphere ($\{0001\}$ pole figure for the hexagonal geometry). In order to avoid this complication a special algorithm is necessary. This algorithm and some useful tools for the easy and fast calculation of mis- and disorientations are explained in detail in appendix B.

The accuracy of the used algorithm can be appreciated in Fig. 3.13, where the pole figure of the obtained orientations and the corresponding misorientation distribution can be seen. The pole figure (Fig. 3.13a) shows that the clustering of orientations is relatively infrequent; this is reflected by the very low maximal intensity (about 1.2). In concordance with this result, the corresponding misorientation distribution of the grain boundaries in the sample (bars in Fig. 3.13b) agrees almost perfectly with the theoretical prediction (solid line in Fig. 3.13b) demonstrating the random character of the orientation distribution.

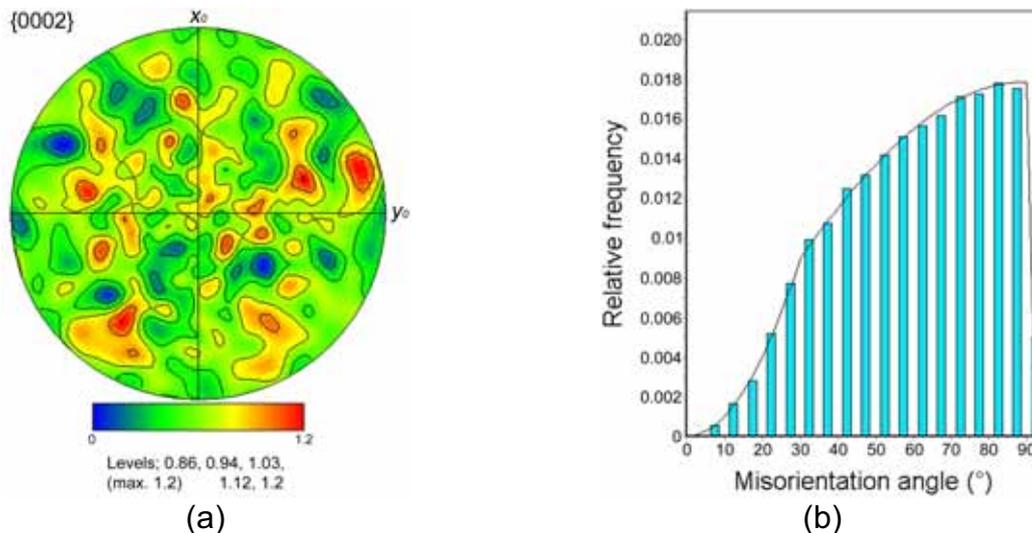


Figure 3.13. (a) $\{0002\}$ pole figure for a sample with an absolute random texture and (b) the corresponding misorientation distribution, the solid line represents the theoretical distribution function.

3.5.2 Texture Evolution

The simulation results showed that the magnetic field determines the final texture after the magnetic annealing. When the field is directed parallel to the z_0 -axis, the grains with orientation near to the component $\{\varphi_1, 90, \varphi_2\}$ experiment a lower magnetic energy (Fig. 3.12a) than the grains with other possible orientations in the polycrystal. For this reason, during the magnetic annealing, these grains have an advantage for their growth and are expected to consume the more energetic grains.

After only 15 minutes of magnetic annealing, the most energetic grains have already disappeared (Fig. 3.15a for t_1), the center of the pole figure has now the minimal intensity and the sample presents a significant texture. According to the color scale, the intensity shows an increasing gradient in the outward direction of the pole figure that corroborate that the grains with the lowest energy grow at expense of the others.

The texture becomes sharper with increasing time (Fig. 3.15a). This occurs because the magnetic energy is a continuous function of the spatial orientation of the crystallites, and therefore, there is not a limiting value where the energy suddenly drops to zero (discontinuities). In fact, taking as reference the center of the pole figure, it can be said that the magnetic energy decreases monotonically as the crystal orientation deviates from the center of the pole figure. Naturally, the only orientations with a zero magnetic energy will be those which lie precisely at the border of the pole figure i.e. with the orientation $\{\varphi_1, \Phi=90, \varphi_2\}$. In a hypothetically infinite polycrystal, normal grain growth (i.e. curvature driven), under these conditions of magnetic annealing, can only take place when all the remaining grains possess an orientation in the interval $\{\varphi_1, \Phi \equiv 90, \varphi_2\}$.

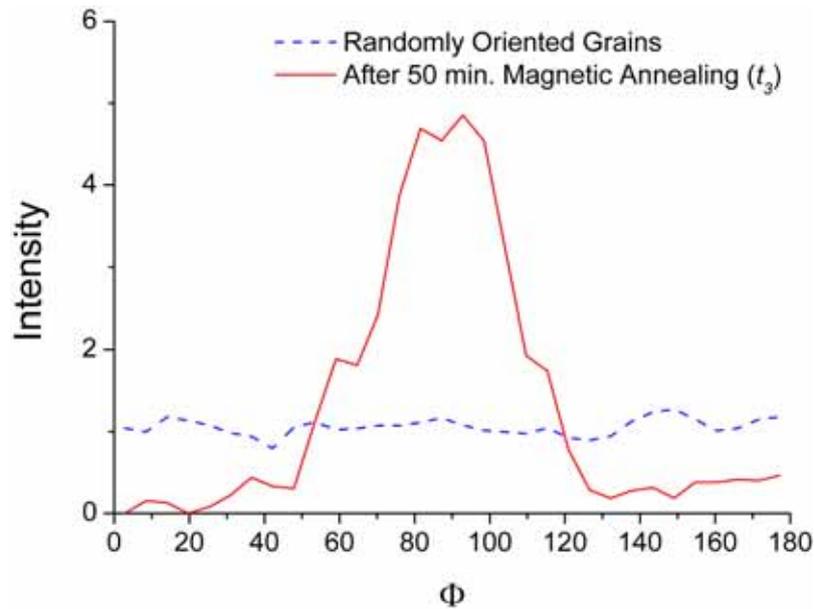


Figure 3.14. Comparison of the pole intensity for the sample with randomly oriented grains (t_0) with the magnetically annealed sample after 50 minutes, the direction of the sample corresponds to the vector [001]. Evidently, after the annealing the sample has a very sharp texture.

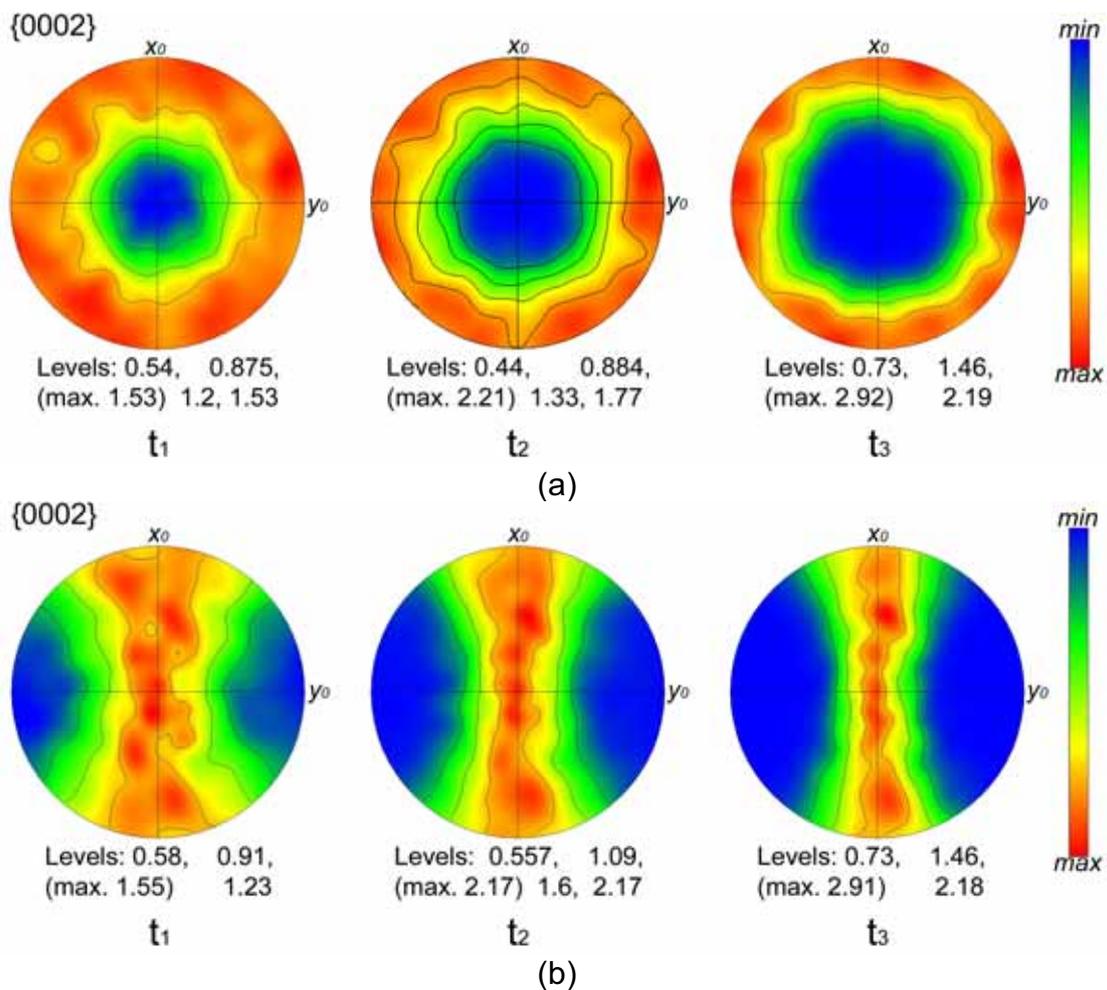


Figure 3.15. Texture evolution with time in a sample with randomly oriented grains with magnetic field (a) oriented parallel to the z_0 -axis (perpendicular to plane x_0y_0) and (b) oriented parallel to y_0 -axis (perpendicular to plane x_0z_0) with $t_3 > t_2 > t_1$.

The texturization of the sample can be corroborated by the plot of the texture intensity (Fig. 3.14) as a function of the Euler angle Φ . The values of the Euler angles φ_1 and φ_2 are irrelevant because the intensity is homogenous for all Euler angles for the case of a sample with random orientations. In the case of the magnetically annealed sample, the intensity shows only variation for Φ , as consequence of the magnetic annealing which leads to the disappearance of the grains with orientations different than $\{\varphi_1, \Phi=90^\circ, \varphi_2\}$. The intensity of the sample with random orientations is shown to be constant for all the range of Φ , furthermore, the intensity is very low. In contrast, the intensity of the sample which was annealed 50 minutes presents a high peak precisely at $\Phi=90^\circ$, the intensity of this peak is also much higher than the maximal intensity of the sample with randomly oriented grains.

In the case when the field has an orientation indicated by the unit vector $[010]$, the favored grains have an orientation given by the components $\{90^\circ, \Phi, \varphi_2\}$ and $\{\varphi_1, 0^\circ, \varphi_2\}$ in the Euler space. As in the previous case, after some time the sample becomes textured and with increasing time, the intensity of the orientations of the favored grains raises as well (Fig. 3.15b).

3.5.3 Grain Fraction Evolution

The sharpening of the texture is the result of the decrease of the grain fraction of the disfavored component with time. Unlike the case of titanium, where the initial texture was very sharp and the initial grain fraction similar, the grain fraction of both grain subsets is now clearly dissimilar. The favored grains are only about 35% of the grains at the beginning of the annealing (Fig. 3.16) whereas the rest corresponds to grains of the disfavored component. This leads to a similar but slightly different behavior of the evolution of the grain fraction with time with respect to the grain fraction evolution for the sample with a very sharp initial texture (Fig. 3.8).

The principal feature which can be drawn from this picture is that apparently there are two different regimes of the grain fraction evolution. The first regime is characterized by a high slope and takes place approximately in the time interval of 5-40 minutes. The slope is directly related to the magnetic driving force which experiment the grains in this stage. As the favored grains occupied only 35% of the polycrystal and due to the random character of their spatial distribution, it can be supposed that they are mainly surrounded by grains with an energetic disadvantage and thus will grow much faster at expense of the disfavored grains, which leads to the eventual intersection of both grain fractions.

In accordance with the decreasing number of disfavored grains, the favored grains come gradually into contact with grains that possess also a low magnetic energy and therefore their kinetics slows down which is reflected also in the deceleration of the grain fraction of the favored grains. The second regime starts when grains of the same energetic class dominate the microstructure, this occurs after approximately 40 minutes of magnetic annealing when the grain fraction of the disfavored grains is about 0.3.

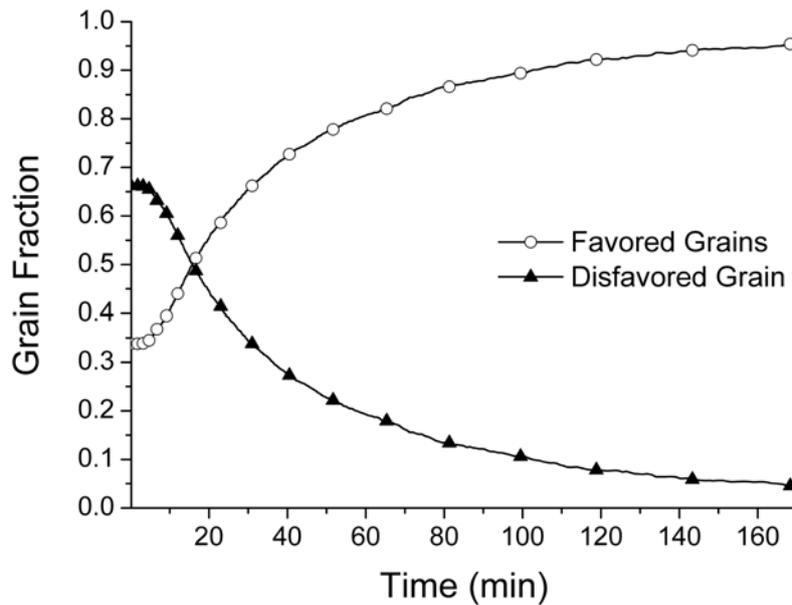


Figure 3.16. Computed grain fractions as a function of the annealing time for different grain subsets; favored grains subset $\{\varphi_1, \Phi=90, \varphi_2\}$ and disfavored $\{\text{all other grains}\}$.

3.5.4 Effect of the Magnetic Field on Grain Size Distribution and Topologic Arrangement of the Grains

As demonstrated in sec. 2.5.3, during normal grain growth under isotropic conditions, the grain size distribution is characterized by its time invariance. However, in presence of a magnetic field, the invariance cannot be guaranteed due to the enhanced growth of some grains at expense of the others.

The next example comprises the grain size distributions for the sample magnetically annealed with a field direction $[001]$. With this setup the grains with orientations $\{\varphi_1, \Phi=90, \varphi_2\}$ experiment a negative mean magnetic driving force $\bar{p}_m < 0$ whereas the remaining grains a positive one. This can be interpreted, in terms of the grain size distribution, as a displacement of the mean grain size of the favored and disfavored grains to greater and smaller values respectively and thus as an overall displacement of the grain size distributions.

As stated in sec. 2.5.3, the initial grain size of the used microstructure is normal distributed. Therefore, the corresponding initial distributions for the favored and disfavored grains are also normal, as shown in Fig. 3.17a. When the magnetic field is applied, the influence of it can be immediately seen after only 10 minutes of annealing. As mentioned previously, the distribution of the favored grains is shifted to the right side with respect to the mean grain size of the whole sample ($D/\langle D \rangle = 1$). In contrast, the distribution corresponding to the disfavored grains is displaced to the left side. Since most of the disfavored grains have a smaller size than the sample average, they have an additional disadvantage besides the one caused by the magnetic field because grains with smaller sizes are more prone to shrink (since $\kappa \propto 1/D$).

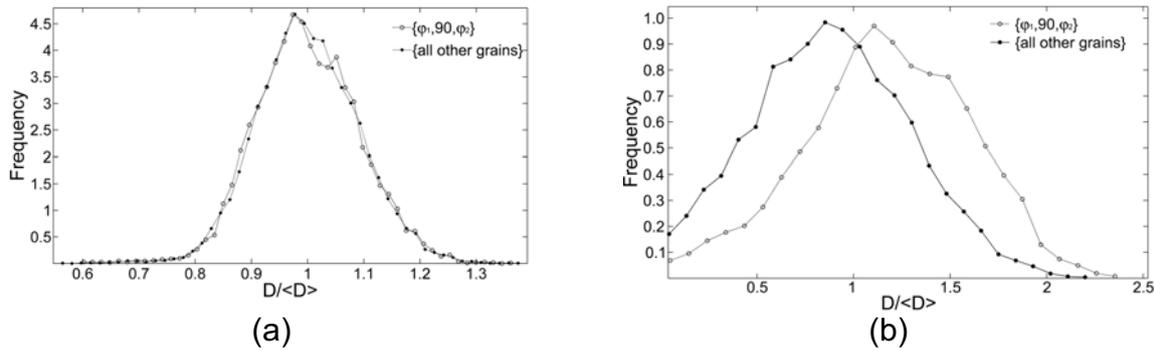


Figure 3.17. Grain size distributions for grains with low $\{\varphi_1, 90^\circ, \varphi_2\}$ and high $\{\text{all other orientations}\}$ magnetic energy. In this example the magnetic energy is oriented along the z_0 -direction, (a) initial distribution at $t=0$ and (b) distributions after only 10 minutes magnetic annealing.

The question now is whether the magnetic field can affect other characteristics of the microstructure. So far, the magnetic field has proven to affect effectively the texture and the grain growth kinetics. However, due to the nature of the magnetic driving force, the effect on the kinetics tends to dissipate as the microstructure becomes dominated by the grains with the lowest magnetic energy and thus the growth advantage is lost. For this reason, a noticeable modification of the morphology occurs only in the interval where the magnetic field influences determinedly grain growth.

For a strict analysis of the morphology, some objective criteria are needed, such as the grain size distribution function or the topological class distribution function. As in the case of the grain-size distribution function, the experimentally determined and simulated topological class distribution functions are different in some aspects. The experimental distribution reaches, normally, a maximum near the topological class $n=5$ [82, 83] whereas the simulated distribution reaches a maximum at $n=6$, which is the expected for a topological network. This difference arises because the experimental distributions are measured from 2D sections of three-dimensional samples whereas in the simulations the grain growth takes place exclusively in two-dimensional space. Nevertheless, the topological class distribution, in contrast to the size distribution, corresponds to a lognormal distribution for both cases (experimental and simulated).

In the present case, the simulated topological class distribution during conventional annealing reaches a maximum at $n=6$ (Fig. 3.18a), as expected. When a magnetic field is applied, the maximum can still be seen at $n=6$, however, the number of grains within this topological class decreases considerably (about 5%) (Fig. 3.18a). This results in a slight broadening of the distributions. It can be seen that there are more grains of all other topological classes with exception only of $n=6$, as result of the failing of the von Neumann-Mullins Equation.

In Fig. 3.18b, the distributions of the topological class for the favored and disfavored grains are shown. It can be seen that the distribution for the disfavored grains is displaced slightly to the left, whereas, exactly the opposite can be seen in the distribution corresponding to the favored grains. The displacement of the topological class distributions is in accordance also with the displacement of the distribution for the grain size. For instance, the grain size distribution of the disfavored samples is displaced clearly to smaller sizes and for this reason, it is expected, that grains with these conditions possess a lower topological class, which actually occurs.

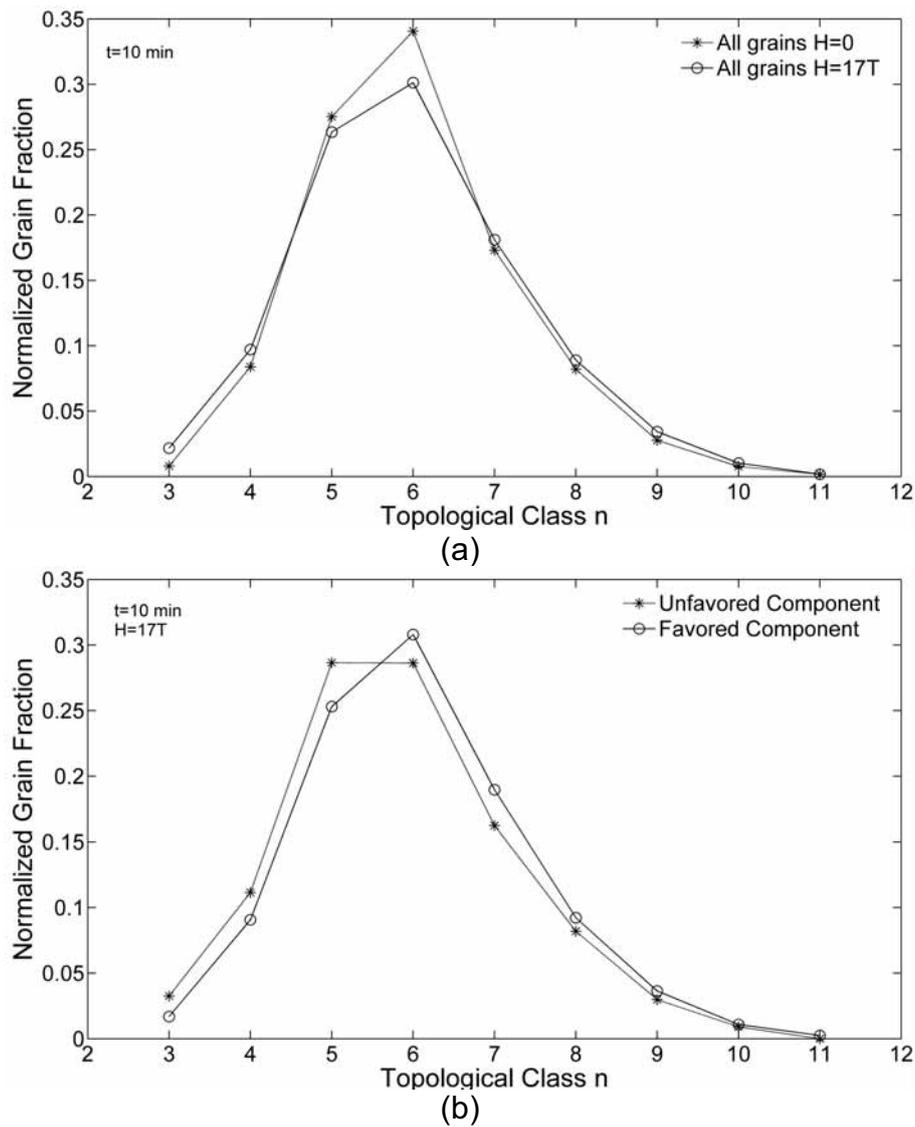


Figure 3.18. Normalized grain fraction as a function of the topological class for (a) the whole sample during magnetic and conventional annealing and (b) only during magnetic annealing but for the favored and disfavored grains.

Chapter 4

The Vertex Model, Grain Boundary Junctions and Grain Boundary Migration

4.1 Introduction

Grain boundary migration is one of the unresolved fundamental problems of the materials science. The interest in this topic arises from the fact that this phenomenon underlies a wide range of microstructural evolution processes, such as, recrystallization and grain growth and hence, is determinant for the physical, chemical and mechanical properties of materials. Extensive investigation in the field has been performed by measuring the mobilities in polycrystals, normally during recrystallization and grain growth. However, the extensive information provided by these investigations was useful only to certain extent and mainly only for the system in which the mobility was measured. Due to the nature of the experimental setups, only the average mobility could be obtained and therefore the correlation between the property (grain boundary mobility) and structure cannot be established. Additionally, the isolated effect of temperature, pressure, impurity content on the motion of specific grain boundaries cannot be studied by these methods.

Recently, fundamental results have been obtained by studying the motion of individual grain boundaries from bicrystal experiments [84-91]. As the bicrystal represents an isolated system, the dependency of the motion on determined factors (crystallography, impurity content, etc) can be straightforwardly established. For this reason, the bicrystal method for the determination of the (reduced) mobility has become, nowadays, the standard.

Besides, the previously mentioned factors that affect grain boundary motion. The triple junctions have been found [92-95] to influence grain boundary motion, as well. Naturally, investigations for the determination of the dependency of the grain boundary motion on this variable have been carried out in tricrystalline samples with very simple geometries. Despite the simplicity of the specimens, the existing methods [8, 9] for their manufacture require substantial experimental effort for the obtaining of tricrystals with the required quality.

Nevertheless, this problem is not present if the investigations are performed by means of computer simulations, since the geometry can be arbitrarily defined and the grain boundary character is predefined simply by setting the orientation of the neighboring grains. For this purpose, simulation models, normally in the microscopic

spatial scale (e.g. molecular dynamics), have been used to determine diverse effects on grain boundary mobility [96]. In a minor scale, mesoscopic models have been used for similar purposes [97]. The contempt for such models occurs because they make use necessarily of the boundary mobility and energy and thus rely on the data obtained either experimentally or by more fundamental simulation methods. However, the grain boundaries (as explained in Ch. 1) are complex structures depending on many factors, which cannot be always neglected during experimentation (e.g. grain boundary stiffness [98], external crystal surface [8], dependency of the mobility on boundary inclination [98, 99], etc.). It is precisely at this point, where mesoscopic simulations models can be used to understand better the underlying physics of these phenomena.

Regardless that the vertex model considers only the fundamental equations governing the boundary migration, it has been scarcely used for the simulation of simple grain boundary migration and preferably, and normally only, used for the simulation of topological networks despite that the model allows to study individually all factors and dependencies involved in the course of grain boundary migration.

In the present chapter, the vertex model is used in very simple geometries to explain fundamental problems found during grain boundary and triple junction migration. The theoretical basis of the motion of connected grain boundary systems and triple junctions is introduced. The examples in this chapter evince the flexibility and efficacy of the model.

4.2 Grain Boundary Systems with Triple Junctions

A triple junction, as defined in Sec. 1.4.1, is the intersection of a triple line with the plane or the point where three two-dimensional grains meet (Fig. 4.1). The triple junctions are the points where the grain boundaries interact with each other. They have well defined physical properties, such as line tension γ^j [100, 101] and mobility m_{ij} [102]. The motion of the triple junctions during the course of microstructure evolution occurs under the action of the grain boundaries energies and the line tension of the junction [9] and is given by

$$v_{tj} = m_{tj} \left(\sum_i^n \gamma_{gbi} \vec{t}_i - \frac{\gamma^j \vec{r}}{\|\vec{r}\|^2} \right), \quad (4.1)$$

where v_{tj} is the triple junction velocity, the vector \vec{t} is the tangential vector to the grain boundary which is also parallel to the line of the junction. The vector \vec{r} is the radius of curvature at a determined point of the triple line. If the influence of the line tension can be neglected, Eq. (4.1) reduces to

$$v_{tj} = m_{tj} \sum_i^n \gamma_{gbi} \vec{t}_i, \quad (4.2)$$

which is, in principle, equal to Eq. (2.8). Eq. (4.2) considers the sum of the grain boundaries energies that intersect at the same line, however, n (number of adjoining boundaries) is typically equal to three. More than three grain boundaries might

intersect along a line. However, since these configurations are energetically unstable, they will subsequently split up into several triple junctions.

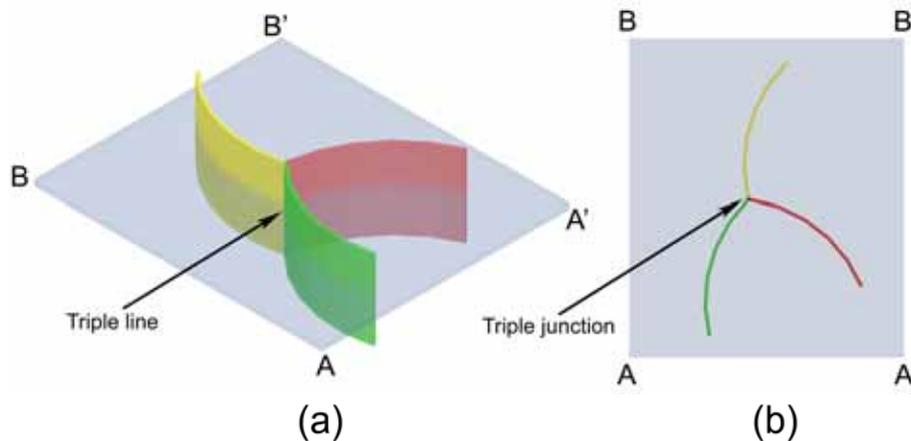


Figure 4.1. (a) Triple line and cutting plane (AA'-BB'); (b) the intersection of the three-dimensional triple line with the plane results in a two-dimensional triple junction.

4.3 Triple Junction Motion

It is commonly believed that triple junctions cannot affect grain boundary motion and that their role is reduced to maintain the thermodynamic equilibrium during grain boundary migration. However, in recent years, several experimental and theoretical investigations have demonstrated that these elements can drag grain boundary motion [94, 95, 103] because their motion can involve additional energy dissipation and thus have a finite and definite mobility [102].

The study of the kinetic properties of such system is only possible in the course of steady-state motion. However, the steady-state motion can be achieved in very few configurations. Since the driving force for the motion of the system is still the curvature of the boundaries, the required independency with time of the driving force depends necessarily on the geometry of the configuration and thus the range of possible configurations is restricted to those which fulfill the geometrical requirements. In the present chapter two different configurations will be considered, the first being a tri-crystalline system (Fig. 4.2) which has been achieved experimentally [92] and the second, being a system, which can be only theoretically considered due to the required boundary conditions of the system (Fig. 4.3) [9].

4.3.1 Grain Boundary Shape and its Correlation with the Steady-state Motion of a Tricrystalline System

In the following, a grain boundary system and a triple junction, as shown in Fig. 4.2, will be considered. The system is supposed to have grain boundary energies and mobilities independent of the grain boundary misorientation. Under such conditions, the normal velocity v_n of the grain boundary is given by the product of the mobility m_{gb} , energy γ and the curvature κ of the grain boundary, as follows

$$v_n = m_{gb} \gamma \kappa, \quad (4.3)$$

where the curvature of any two-dimensional curve explicitly reads

$$\kappa = -y''[1 + (y')^2]^{-3/2}. \quad (4.4)$$

The displacement velocity of the grain boundary in the x-direction can be easily calculated as

$$v_n = v_x \cos \varphi = v_x \cdot \frac{y'}{(1 + (y')^2)^{1/2}}. \quad (4.5)$$

Combining Eq. (4.3), (4.4) and (4.5) yields the differential equation

$$y'' = -\frac{v_x}{m_{gb}\gamma} y' [1 + (y')^2], \quad (4.6)$$

which provides the shape of the grain boundary depending on the used boundary conditions for its solution. According to the geometry of Fig. 4.2, the boundary condition of the current problem are: $y(0) = 0$, $y(\infty) = a/2$ and $y'(0) = \tan \theta$. The solution of Eq. (4.6) delivers

$$y(x) = \zeta \arccos\left(e^{-x/\zeta + C_1}\right) + C_2, \quad (4.7)$$

where

$$\begin{aligned} \zeta &= \frac{a}{2\theta}, \\ C_1 &= \frac{1}{2} \ln(\sin \theta)^2 \end{aligned} \quad (4.8)$$

and

$$C_2 = \zeta \left(\frac{\pi}{2} - \theta \right), \quad (4.9)$$

the meaning of the variables, a and θ are clear from Fig. 4.2. Finally, working out the boundary velocity in the x-direction in Eq. (4.6), substituting Eq. (4.7) in (4.2) and simplifying the resulting expression, the steady-state velocity of the system can be expressed as [9]

$$v_x = \frac{2\theta m_{gb}\gamma}{a}. \quad (4.10)$$

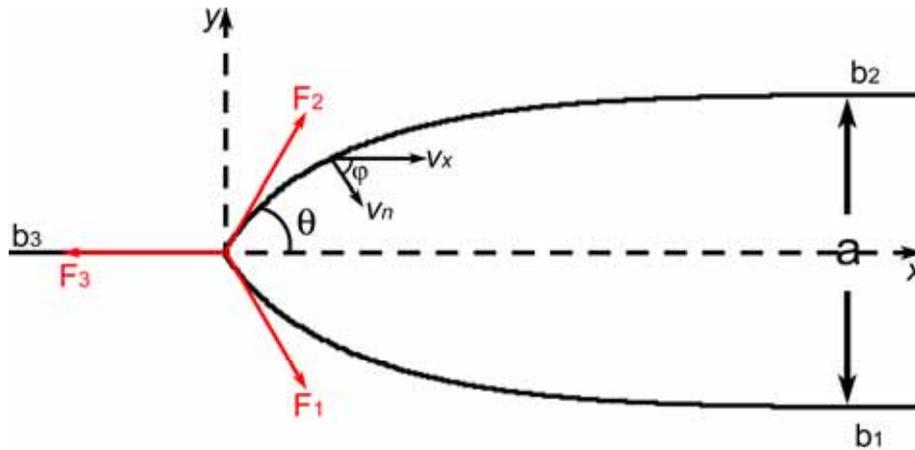


Figure 4.2. Geometry of the grain boundary system with triple junction.

The previous equation demonstrates that the steady-state motion of a boundary system with a triple junction is indeed possible but the description of the influence of the latter element on the evolution of the system is still lacking. In order to consider it, the equilibrium of forces at the triple junction needs to be taken into account. The force P acting at the triple junction can be determined from the sum over the surface tensions of the grain boundaries meeting at the triple junction

$$\vec{P} = \vec{F}_1 + \vec{F}_2 + \vec{F}_3. \quad (4.11)$$

Due to the symmetry of the forces, the force acting at the junction is reduced only to the x -component and thus the magnitude of the force P reads

$$P = 2\gamma \cos \theta - \gamma = \gamma(2 \cos \theta - 1). \quad (4.12)$$

The evolution in steady-state of the system requires the force P to be equal to $P = v_{ij} / m_{ij}$, and consequently the velocity of the triple junction is given by

$$v_{ij} = m_{ij} P = m_{ij} \gamma \cdot (2 \cos \theta - 1). \quad (4.13)$$

If the triple junction does not drag the evolution of the system, the force P is correspondingly equal to zero (if $m_{ij} \rightarrow \infty$ then $P \rightarrow 0$) and the equilibrium angle will be $\theta_{\infty} = 60^\circ$. It should be noted that under this circumstance the dihedral angle 2θ would correspond exactly to 120° .

Since v_x (Eq. (4.10)) and v_{ij} (Eq. (4.13)) have to be identical, it is possible to define a dimensionless parameter which determines the steady-state value of the angle θ and therefore the influence of a finite triple junction mobility on the evolution of the system.

$$\frac{2\theta}{2 \cos \theta - 1} = \Lambda_{ij} = \frac{m_{ij} a}{m_{gb}}. \quad (4.14)$$

If the quadruple junction is perfectly mobile, then $\Lambda_{ij} \rightarrow \infty$ and $\theta \rightarrow 60^\circ$, which is the equilibrium angle. In contrast, if the triple junction moves slowly and drags the migration of the grain boundary then $\Lambda_{ij} \rightarrow 0$ and $\theta \rightarrow 0$.

4.3.2 Effect of a Finite Triple Junction Mobility on the Evolution of a Multigranular System ($n > 6$)

A second system in which the motion occurs in steady-state is shown in Fig. 4.3. Unlike the configuration of Fig. 4.2, which can be used to conduct experimental investigations, the present configuration can only be theoretically considered. Nevertheless, this configuration is very useful because it helps to understand the influence of finite triple junction mobility on the growth of grains with a topological class larger than six, as will be shown in a further section.

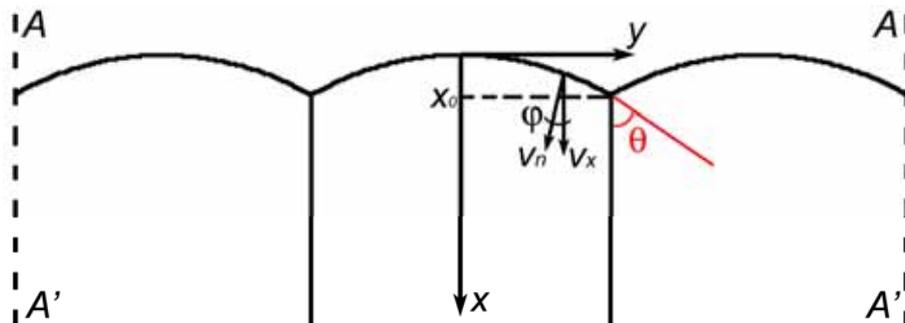


Figure 4.3. The motion of the triple junction of the grain boundary system takes place in steady-state. The dotted lines indicate the needed periodicity of the system in the y -direction, the equivalent to this would be an infinite system, which repeats itself in the same y -direction.

The shape of the curved grain boundary for the present configuration is defined by the solution of Eq. (4.6) but with a different set of boundary conditions, namely, $y'(0) = \infty$, $y'(x_0) = \tan \theta$ and $y(0) = 0$. Under these conditions the shape of the moving grain boundary is given by

$$y(x) = -C \arccos\left(e^{x/C}\right), \quad (4.15)$$

where

$$C = \frac{x_0}{\ln \sin \theta}. \quad (4.16)$$

The meaning of the angle θ and the distance x_0 can be seen in Fig. 4.3. The displacement velocity of the grain boundary is calculated in the same way as for the previous configuration (substituting Eq. (4.15) in (4.6) and further simplification); the steady-state velocity results

$$v_x = -\frac{m_{gb}\gamma}{x_0} \ln \sin \theta. \quad (4.17)$$

The motion of the triple junction occurs under the action of the surfaces energies of the three meeting grain boundaries, the triple junction velocity can be expressed as

$$v_{tj} = m_{tj} \gamma (1 - 2 \cos \theta). \quad (4.18)$$

Combining Eq. (4.17) and Eq. (4.18), we arrive to the expression of the dimensionless parameter similar to Eq. (4.14)

$$-\frac{\ln \sin \theta}{1 - 2 \cos \theta} = \Lambda_{tj} = \frac{m_{tj} x_0}{m_{gb}}. \quad (4.19)$$

When the kinetics are dominated by the grain boundary mobility ($\Lambda_{tj} \gg 1$) the angle θ tends to 60° whereas when the triple junction determines the kinetics ($\Lambda_{tj} \ll 1$) the angle tends to 90° which is fully equivalent to the flattening of the grain boundaries. This has deep repercussions on the von Neumann-Mullins equation because the equilibrium angle at triple junction is also affected by a finite triple junction mobility, this effect will be treated in a subsequent section.

4.3.3 Validation and Verification of the Equations for the Effect of a Finite Triple Junction Mobility on the Evolution of a Grain Boundary System

To validate the equations introduced in the previous section and verify the applicability of the vertex model when the triple junction mobility is finite, vertex model simulations were performed. Fig. 4.4 shows the grain assembly that reproduces the configuration shown in Fig. 4.2. The initial configuration can be seen in Fig. 4.4a, it can be noted that the initial geometry differs deeply from the required configuration. The system requires relaxing in order to reach the equilibrium geometry (Fig. 4.4b). During the simulation of this configuration, the angle θ and the time evolution of the surface of the grain were recorded as a function of time and Λ_{tj} .

The time evolution of the area is shown in Fig. 4.5, for large Λ_{tj} [$\infty, 5$] the area is evidently linear with time. For intermediate and low values of Λ_{tj} (5,0] the area dependency on time seems not to be linear. It might be thought that the evolution of the system does not takes place in steady-state for this regime. However, the plot of the area rate of change (Fig. 4.6) demonstrates that the steady-state motion of the grain boundaries is reached but at different times, this delay in time depends on Λ_{tj} , the lower the value of Λ_{tj} , the larger the delay. For instance, in the interval $\Lambda_{tj} = [\infty, 5]$ the relaxation time is very short and the constant area rate of change \dot{S} is reached very quickly, whereas in the interval $\Lambda_{tj} = (5, 0]$, the constant \dot{S} takes place after evidently much larger times. This can be explained by the fact that the area, which needs to be swept by the grain boundary in order to reach the steady-state configuration, increases with decreasing Λ_{tj} and thus the relaxation time increases. Additionally, during this stage the displacement velocities of the triple junction and grain boundaries are different, which leads to the nonlinearity of the grain area with time. Nevertheless, the most prominent consequence of the finite mobility of the triple junction is the slowing down of the grain growth kinetics. As seen in Fig. 4.5, for the lowest triple junction mobility the system requires about four times more time to

sweep the same area (i. e. the triple junction slows down the evolution of the system).

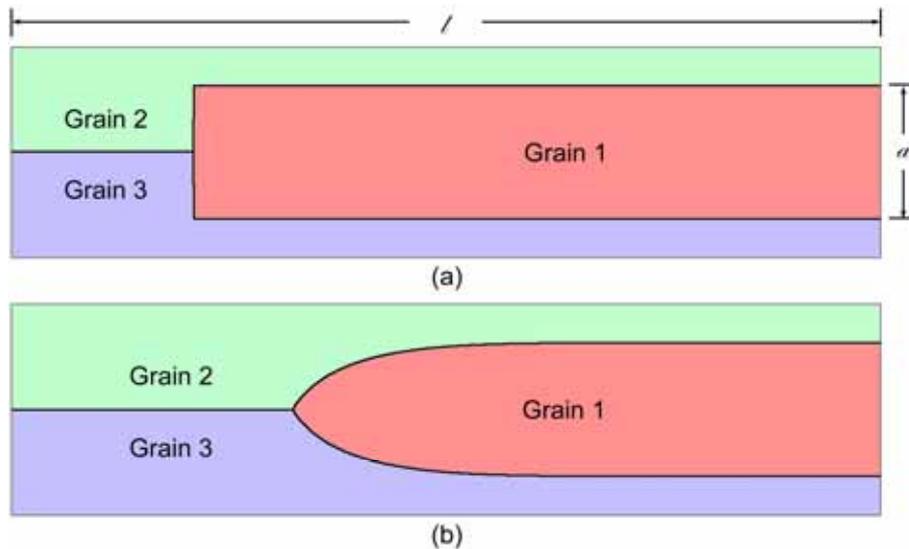


Figure 4.4. (a) Grain configuration used for the simulations of the configuration given in Fig. 4.2 at time t_0 and (b) after relaxation, when the steady-state motion occurs.

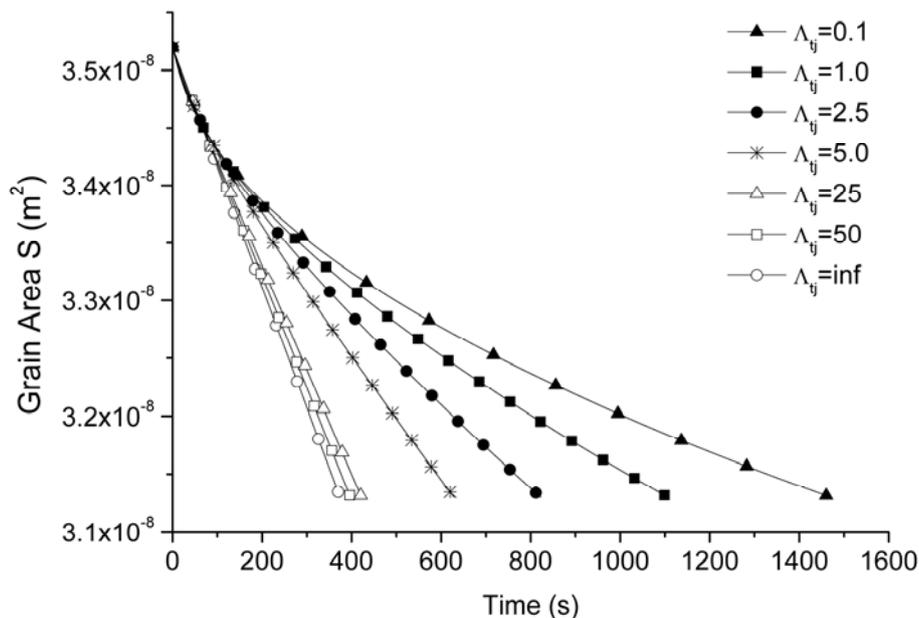


Figure 4.5. Evolution of the kinetics of the system shown in Fig. 4.4 for different triple junction mobilities.

The curve for \dot{S} (Fig. 4.6) shows that a perfect steady-state motion of the system is not attained, the value of \dot{S} reaches an almost constant value but a slightly non-constant dependency on time can still be observed. The explanation for this is found in one of the boundary conditions used for the integration of Eq. 4.6. The dimension a (grain size) is only attainable at the infinite according to Eq. 4.6, in order to attain a perfect steady-state motion this condition must be reproduced in the computer simulations, condition that is practically impossible. For this reason, a small dependency on time is introduced. The nonlinear dependency on time of the grain area is more evident for smaller Λ_{tj} because with the decrease of the angle θ , the finite length l (Fig. 4.5) needs forcibly to be increased in order to avoid the reduction

of the length a that takes place when the grain boundary is curved in the vicinity of l . The initial ratio l/a used in the simulation was constant and equal to $l/a=20$, thus the introduced error manifests itself more clearly for lower Λ_{tj} .

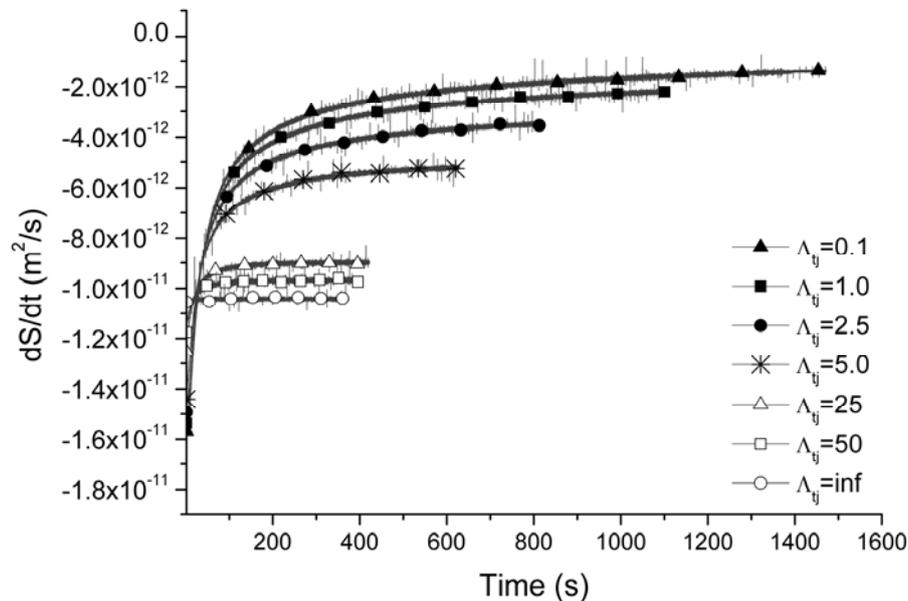


Figure 4.6. Area rate of change in dependency of time and triple junction mobility, certain time is needed before the steady-state motion can be achieved. However, a perfect steady-state motion is not attained.

One of the first effects of a finite triple junction mobility can be seen in the shape of the evolving grain boundaries. Eq. (4.14) predicts that the decrease of the triple junction mobility leads to the change of the equilibrium angle θ and consequently to the modification of the shape, since $y(x)=f(\theta)$. Fig. 4.7 illustrates the change of the shape and equilibrium angle as a function of Λ_{tj} . Experimental investigations in pure zinc tri-crystals have also confirmed that a change of the grain boundary shape, attributable to the triple junctions, occurs during annealing at different temperatures (Fig. 4.8) [92].

It has been so far demonstrated that the steady-state motion of a system of grain boundaries and a triple junction is possible. Additionally by means of the computer simulations the kinetics of the grain growth under the influence of a finite triple junction mobility was determined for the configuration corresponding to $n < 6$. To corroborate the case when $n > 6$, the geometry shown in Fig. 4.9 is used. This geometry reproduces exactly the configuration used for the derivation of Eq. (4.19), for these simulations periodical boundary conditions were used, as indicated in Fig. 4.3. In a similar manner to the previous case, the grain boundaries at the beginning of the simulation are flat and thus some relaxation time is required until they become curved and the motion proceeds in steady-state (Fig. 4.10). Despite the necessity of a relaxation time no major influence can be seen in the results. This is in part due to the initial configuration which possess boundaries closer to the equilibrium angle for low Λ_{tj} , i.e. $\theta=90^\circ$ and in part because for this case the quality of steady-state motion does not depend on the size of the simulation box at all.

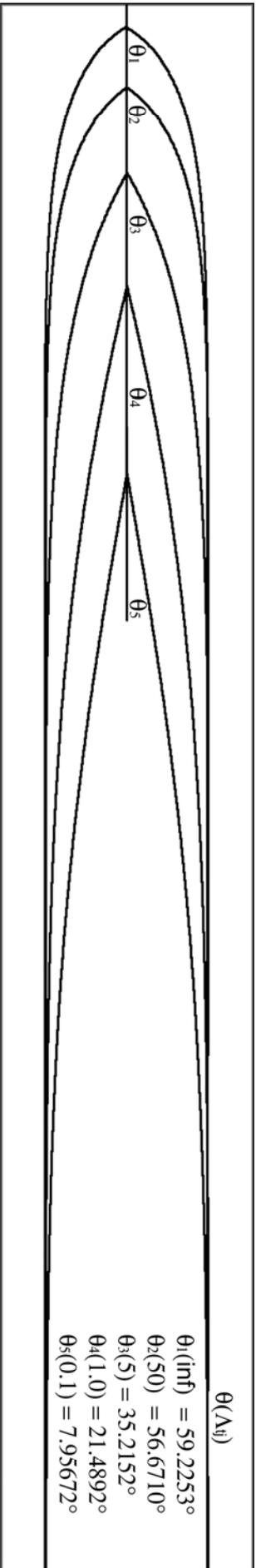


Figure 4.7. Steady-state grain boundary shapes and equilibrium angle for different triple junction mobilities.

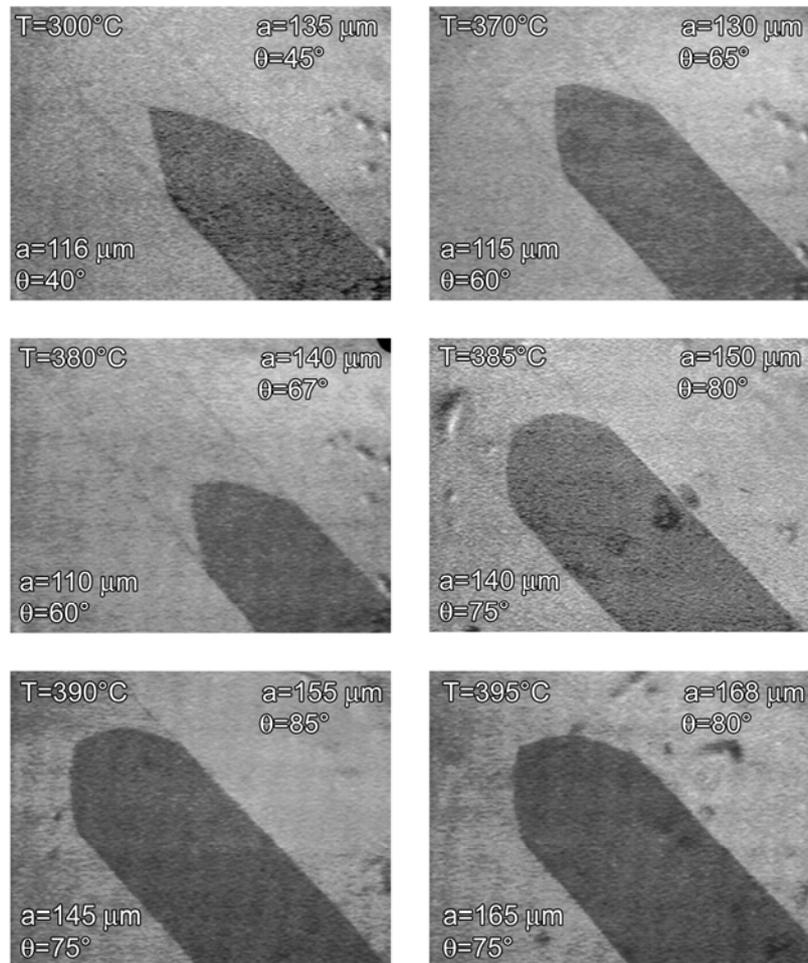


Figure 4.8. Experimental shapes [9].

The time evolution of the grain area (grain 1 in Fig. 4.9) is evidently linear, a decreasing finite triple junction mobility drags the grain growth in a similar way as in the case for $n < 6$. The shape of the grain boundaries and the equilibrium angle of the steady state motion are also influenced by the triple junctions. The flattening of the initially curved grain boundaries can be clearly seen in Fig. 4.11.

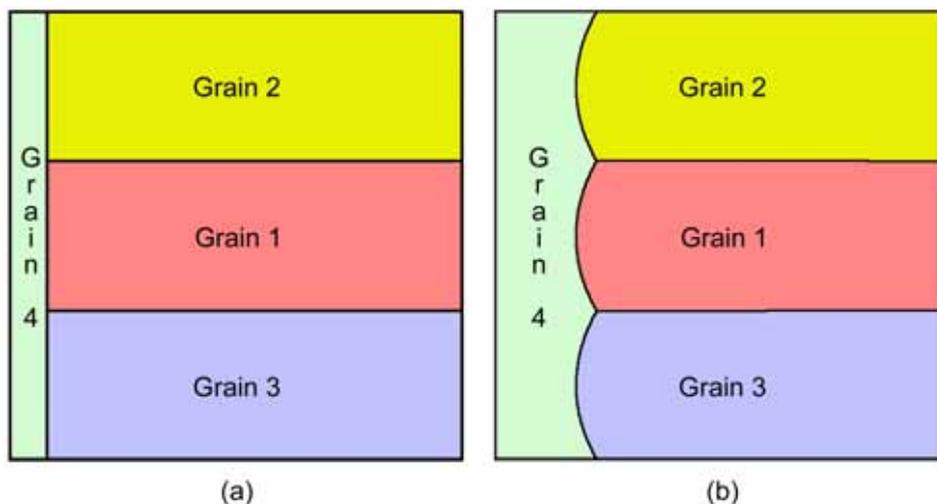


Figure 4.9. (a) Grain configuration used for the simulations of the configuration given in Fig. 4.3 at time t_0 and (b) after relaxation, when the steady-state motion occurs.

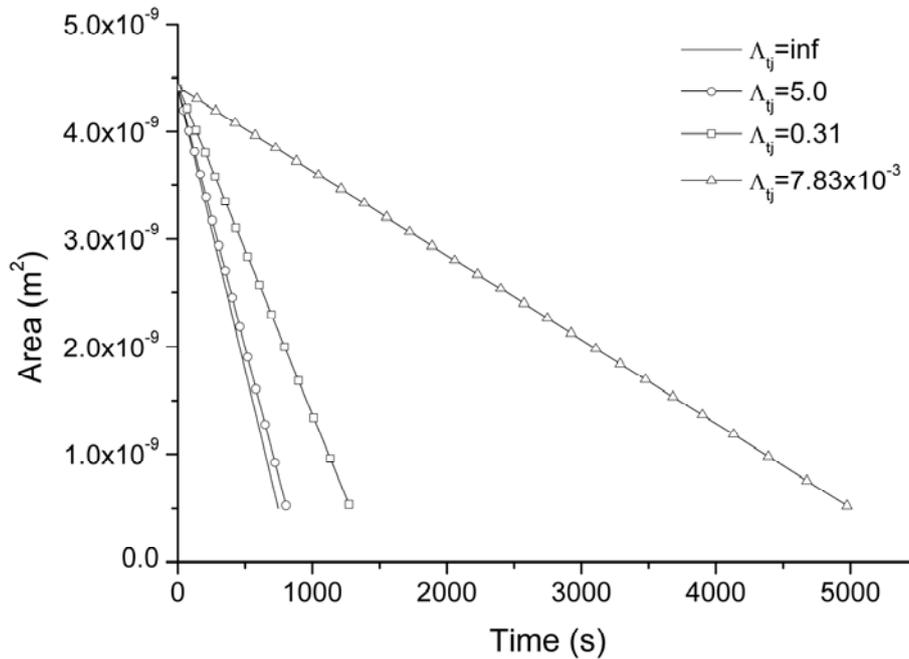


Figure 4.10. Evolution of the kinetics for the grain 1 in the configuration shown in Fig. 4.7, the steady-state motion is achieved almost immediately; the area of the grain as a function of time is evidently linear.

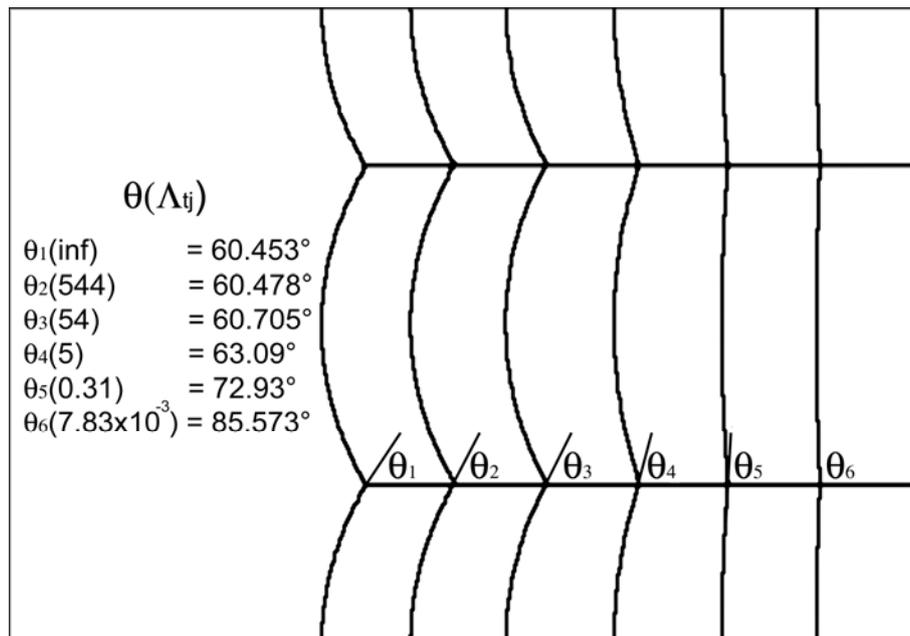


Figure 4.11. Steady-state shape and equilibrium angle for different mobilities ($n > 6$).

The change of the shape and equilibrium angle are a good indicator that triple junctions affect grain growth evolution, the magnitude of the effect can be estimated from the kinetics, but none of these results provide a validation for the simulation model. In order to demonstrate that the simulation results fully agree with the theoretical equations derived in the preceding section, the equilibrium angle θ has been plotted as a function of the triple junction mobility Λ_{tj} (Fig. 4.12) for both simulation cases, $n < 6$ and $n > 6$. In this plot, the lines represent the theoretical equations whereas the points were calculated with Eq. (4.14) and (4.19) from the angles which were taken directly from the simulations. The simulation results agree very well with the theoretical considerations, the deviations from the theoretical line

lie in the expected range error of the simulation method. Recalling that the vertex model uses straight-line segments to represent a continuous grain boundary, one can note that the error in the calculation of the angles will depend on the number of the segments that are being used to break down the grain boundary during a simulation. Nevertheless, despite the deviations, the simulation results show an outstanding agreement with the theoretical predictions. This point is very important because it validates both, the simulation model and the theoretical predictions. For the simulation model is particularly relevant because it means that the model can be used to simulate polycrystals with a finite triple junction mobility. In the next section, we will refer briefly to this point.

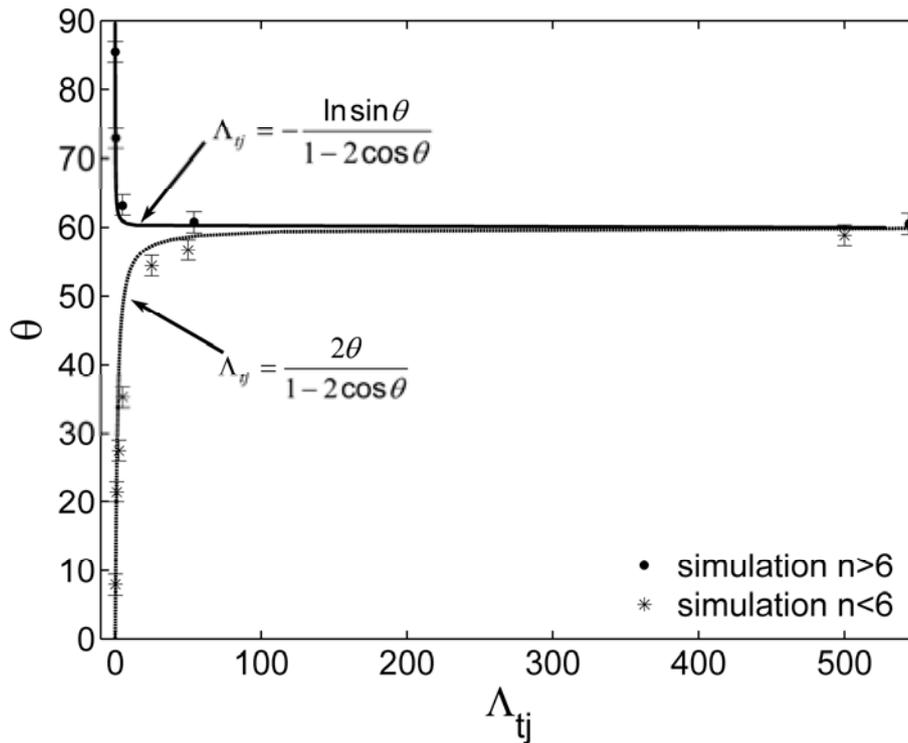


Figure 4.12. Comparison of the simulation results with the theoretical relationships given in Eq. (4.14) and (4.19).

4.3.4 Effect of a Finite Triple Junction Mobility on the Evolution of a 2D Polycrystal

The effect of a finite triple junction mobility on the evolution of a polycrystal has been in detail investigated [94]. It has been shown that grain boundary migration affected by triple junctions can be considered as motion of grain boundaries with mobile defects, in such a way that the area rate of change of the grains is given by [104]

$$\dot{S} = \frac{m_{gb}\gamma}{1 + \frac{1}{\Lambda_{tj}}} [2\pi - n(\pi - 2\theta)]. \quad (4.20)$$

Evidently, there will be two different expressions for the area rate of change depending whether the topological class is less than or more than 6. A finite triple junction mobility changes the value of the dihedral angle, in the case of $n < 6$, this angle decreases whereas in the case of $n > 6$ the angle increases. Since the

magnitude of the angle θ depends solely on Λ_{ij} it is possible to find the relationship between the \dot{S} and Λ_{ij} . First let consider the case when $n < 6$, by expanding the cosine function in Eq. (4.14) by its series equivalent, it is possible to work out the angle θ as follows [94]:

$$\theta = \frac{\sqrt{3}\pi\Lambda_{ij}}{6 + 3\sqrt{3}\Lambda_{ij}}, \quad (4.21)$$

and combining with Eq. (4.20) results in

$$\dot{S} = \frac{m_{gb}\gamma\pi}{3\left(1 + \frac{1}{\Lambda_{ij}}\right)} \left(n \frac{6 + \sqrt{3}\Lambda_{ij}}{2 + \sqrt{3}\Lambda_{ij}} - 6 \right). \quad (4.22)$$

If the triple junction mobility is infinite, Eq. (4.22) will convey the classical von Neumann-Mullins relationship. Eq. (4.22) shows that a zero growing rate is not anymore an exclusive function of the topological class.

In a similar manner, it is possible to work out θ from Eq. (4.19) ($n > 6$). The value of θ for this case reads

$$\theta = \frac{\pi}{3} - \frac{\ln \sin \frac{\pi}{3}}{\sqrt{3}\Lambda_{ij}}, \quad (4.23)$$

and the rate of change of the grain area for $n > 6$ can be expressed as

$$\dot{S} = \frac{m_{gb}\gamma\pi}{3\left(1 + \frac{1}{\Lambda_{ij}}\right)} \left[n \left(1 + \frac{6 \ln \sin \frac{\pi}{3}}{\pi\sqrt{3}\Lambda_{ij}} \right) - 6 \right]. \quad (4.24)$$

This expression becomes identical to the von Neumann-Mullins relation for an infinite triple junction mobility, as in the case for $n < 6$.

Gottstein, Ma and Shvindlerman [94] demonstrated the validity of these expressions using the vertex model and determined the effect of triple junctions on the grain growth kinetics. Fig. 4.13 shows the kinetics of the grain growth when is dominated completely by the motion of the triple junctions in comparison with the normal grain growth kinetics. It can be observed that grain growth is strongly dragged, for details refer to [28, 94].

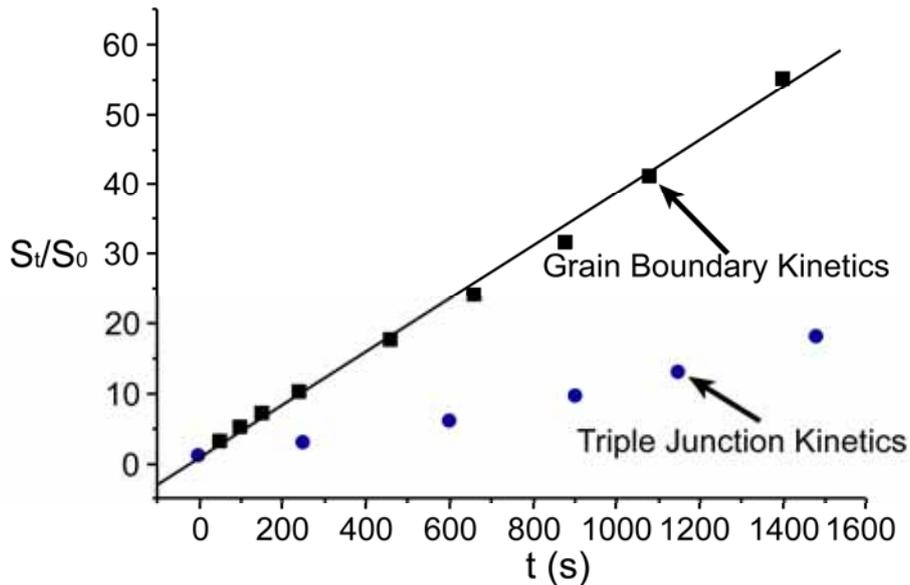


Figure 4.13. Triple junction- and grain boundary-grain growth kinetics [28].

4.4 Grain Boundary Motion and Dependency of the Boundary Energy on Inclination Angle

The physical properties of the grain boundaries depend on the eight parameters that describe the grain boundary. In particular, the mobility and the grain boundary energy are particularly sensitive to them. Normally, only the dependency of these properties on the misorientation angle is considered. This is in part due to the lack of reliable data for dependencies that are more complex and partially to the belief that other dependences do not affect grain boundary migration. In particular, the dependency of the grain boundary energy and mobility on grain boundary inclination is normally neglected, not without reason then in many cases, the boundary inclination does not strongly affect the migration of the grain boundaries [8, 98]. Moreover, molecular dynamic simulations have also shown that the shape of a U-shaped grain boundary is consistent with an isotropic reduced mobility [199].

Nevertheless, the neglect of the influence of this parameter has led in the past to the misinterpretation of results [97]. Therefore, it is clear that in some cases its influence cannot and must not be ignored. In the present section, it is shown that the vertex model can be used for the simulation of grain boundary migration when the dependency on inclination of the grain boundary energy is considered. The vertex simulations were used in conjunction with molecular static simulations for the understanding of the faceting of grain boundaries in Aluminum bicrystals.

4.4.1 Modification of the Vertex Model for the Consideration of the Inclination Dependency

In the vertex model, the influence of the inclination angle on the grain boundary migration needs to be explicitly implemented. The velocity of a migrating grain boundary is given by the product of the grain boundary mobility, curvature and the

sum of the grain boundary energy and its second derivative with respect to the inclination angle φ

$$v = m_{gb} \kappa \left(\gamma + \frac{\partial^2 \gamma}{\partial \varphi^2} \right). \quad (4.25)$$

The principal effect of the inclusion of the term $\frac{\partial^2 \gamma}{\partial \varphi^2}$ is the faceting of the grain boundaries (see Fig. 1.7). Since sharp steps normally characterize the transition between different facets, it should be noted that the curvature at these points, where a facet change occurs, is undefined. For this reason, utilization of Eq. (4.25) for the calculation of the velocity will introduced an error to the computation of the velocities during the simulation. To overcome this difficulty, it is possible to use, instead of the curvature, the sum of the forces, which are exerted at the discretizing points of the grain boundary, and to translate the second derivative of the energy with respect to the inclination angle into forces applied at the discretizing points. Eq. (4.25) transforms then into

$$v = m_{gb} \left[\frac{(\vec{F}_1 + \vec{F}_2)}{\Delta s_{12}} + \sum_i^n \frac{M_i(\varphi)}{\Delta s_i} \right] \approx m_{gb} \left[\gamma(\vec{u}_1 + \vec{u}_2) / (\Delta s_1 + \Delta s_2) + \sum_i^n \frac{M_i(\varphi)}{\Delta s_i} \right], \quad (4.26)$$

where the sum of the unit vectors defines the direction of the motion, the vector \vec{u} is defined as

$$\vec{u}_i = \frac{\vec{s}_i}{\|\vec{s}_i\|}, \quad (4.27)$$

and the torque $M(\varphi)$ is the first derivative of the energy with respect of the inclination angle

$$M(\varphi) = \frac{d\gamma}{d\varphi}. \quad (4.28)$$

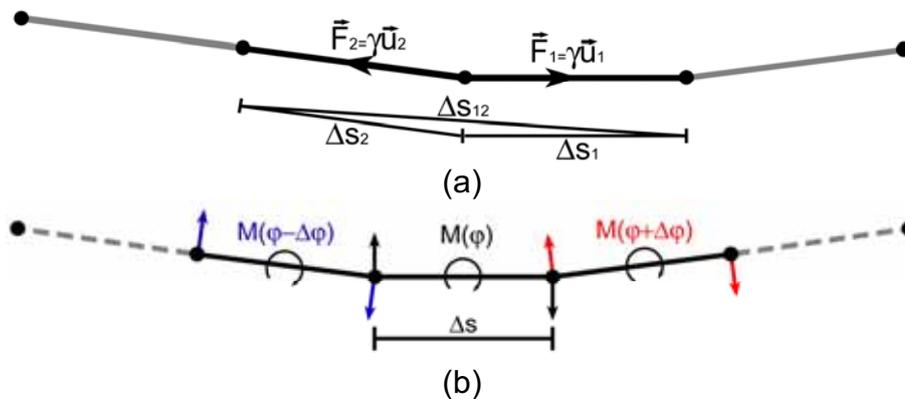


Figure 4.14. (b) Schematic representation of the forces at a discretizing point of a grain boundary; (b) each rigid segment of grain boundary senses a torque due to the anisotropy of the grain boundary energy with the inclination angle, which can be substituted by a par of forces and then apply as forces at the discretizing points.

Eq. (4.26) is completely equivalent to Eq. (4.25) but with the advantage that by avoiding the calculation of the curvature no error in the calculation of the grain boundary stiffness is introduced. For a demonstration of the equivalence of both equations, refer to [105].

The equation for the motion of the triple junctions (Eq. (2.8)) remains practically the same with only the inclusion of the three forces produced by the torques of the three adjoining grain boundaries.

4.4.2 Case of Study - Faceting of $\langle 100 \rangle$ Tilt Grain Boundaries

The next example is remarkable because it involves the utilization of three different investigation methods, as well as the linking between microscopic and mesoscopic simulation models. This situation represents an excellent opportunity to demonstrate that by the simultaneous application of different simulation and experimental techniques a better understanding of materials science problems can be accomplished.

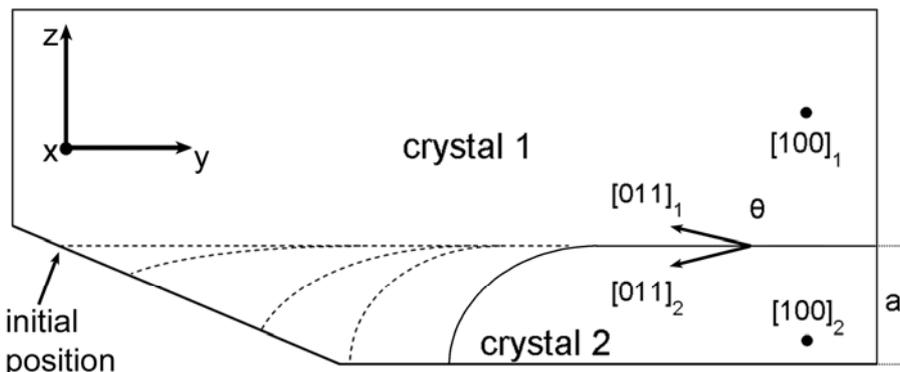


Figure 4.15. Bicrystal geometry of the experimental samples [98].

The motivation for the investigation arose from experimental observations of grain boundary faceting during the annealing of aluminium bi-crystalline samples with a $\langle 100 \rangle$ symmetrical aluminium grain boundary. The geometry of the sample corresponded to a quarter-loop. The crystallography and the geometry of the bicrystal is shown in Fig. (4.15). The samples had different misorientation angles and lay in the range of $8^\circ - 24^\circ$ and were annealed in the temperature window of $350^\circ\text{C} - 640^\circ\text{C}$. The behaviour of the motion of the grain boundaries was inconsistent. For example, the grain boundary with a misorientation angle of 8.4° showed no motion at all, even at high temperatures ($0.97T_m$). The principal observed feature was the faceting of the grain boundaries. In general, from the experimental results, it can be summarized that with increasing misorientation angle and temperature the faceting of the grain boundaries decreased. For instance, the grain boundary annealed at 600°C with a misorientation angle of 14.3° did not show facets, however, the same sample annealed at lower temperatures showed clearly faceting. An exact description of the experimental setup and the results can be found in [98].

The faceting was attributed to the anisotropy of the grain boundary energy with respect to the spatial position of the grain boundary (i.e. inclination angle) but single experimental results cannot provide enough evidence to demonstrate this

hypothesis. For this reason, molecular static simulations were carried out in order to determine firstly if such anisotropy exists. The simulation method is extensively described in [106]. In the present contribution, only the principal characteristics of the model will be mentioned.

4.4.2.1 Molecular Static Simulations

The simulation method utilizes an adapted 12-6 Lennard-Jones (LJ) pair potential for the calculation of the interaction energy between aluminum atoms

$$V^{LJ}(r_{ij}) = \alpha \left[\left(\frac{r_e}{r_{ij}} \right)^{12} - \left(\frac{r_e}{r_{ij}} \right)^6 \right], \quad (4.29)$$

where r_{ij} is the distance between neighboring atoms and r_e is the cutoff distance at which the interatomic potential is equal to zero, α is the depth of the potential well. The parameters r_e and α can be calibrated according to requirements. For the case of the present simulations, they were adjusted to the elastic constant and the bulk modulus for aluminium. The obtained values were, correspondingly, $\alpha=0.17$ eV and $r_e=2.561$ Å.

The construction of the grain boundary was achieved by simple generation of two identical FCC cubic lattices that were subsequently rotated with respect to each other along a common axis until the desired misorientation and inclination angles were acquired. By discriminated removal of superfluous atoms the grain boundary is finally built up [98]. As an example, Fig. 4.16 shows the two-dimensional projection of a $14.3^\circ \langle 100 \rangle$ grain boundary created with the method here described.

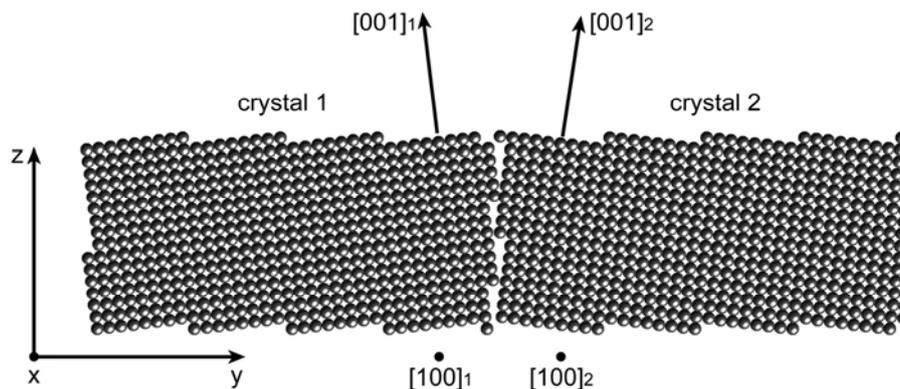


Figure 4.16. Two-dimensional projection of the atomic arrangement of a $14.3^\circ \langle 100 \rangle$ grain boundary [98].

Once the bicrystal is formed, the calculation of the energy at a temperature of 0 K can be performed. For this, the bicrystal is fully relaxed by means of the steepest gradient algorithm [106] and the minimal boundary energy can be easily calculated as

$$\gamma_{gb} = \frac{\left(\sum_{i=1}^N E_i \right) - N \cdot E_{coh}}{A}, \quad (4.30)$$

which is simply the subtraction of the total cohesive energy ($N \cdot E_{coh}$) for a perfect crystal under an absolute zero temperature from the sum of the potential energy E_i over all atoms of the system N . This quantity is finally divided by the effective grain boundary area A (which in practice is the area of the plane of the simulation box parallel to the grain boundary). It should be noted that the energy calculated in this way reflect only the minimal energy for the perfect bicrystal (perfect in the sense that there are not more defects involved besides the grain boundary) and not the local equilibrium grain boundary energy. The latter can be achieved by small variations of the configuration through vacancy segregation at locations where the local hydrostatic pressure is highest [106]. It was necessary to analyzed over 500 different configurations for each calculation. The configuration that provided the minimal energy was then chosen. Finally, the grain boundary energies for higher temperatures were computed using the approach of LeSar et al. [106, 107].

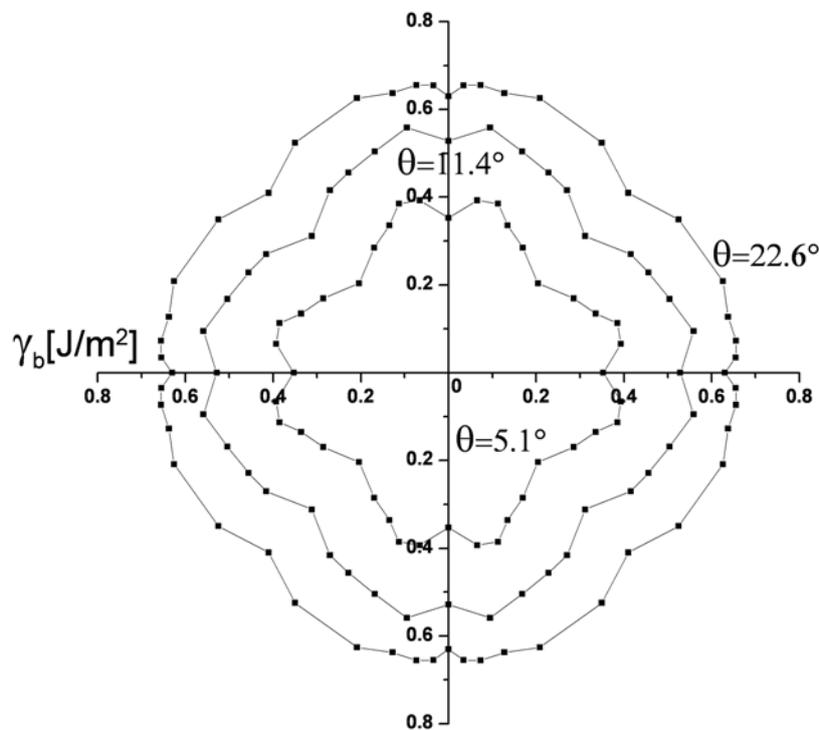


Figure 4.17. Polar plot of the grain boundary energy as function of the inclination angle for different misorientation angles [98].

The results of the simulation for different misorientation angles for a temperature of 0 K are summarized in Fig. 4.17. With respect to the misorientation angle, it can be observed that the anisotropy of the grain boundary energy with the inclination angle decreases for increasing misorientation. The plot corresponding to a misorientation of 5.1° present sharp cusps for the inclinations angle of 0° and 45° , the same cusps can still be seen in the other plots, which correspond to higher misorientation, but the dept of the cusps evidently decreases. For instance, the plot for a misorientation angle of 22.6° shows an almost circular shape, reflecting the more isotropic dependency of the energy on inclination angle. A similar effect can be observed with respect to the temperature. For the same misorientation angles and different temperatures, a softening of the curves and thus a decrease in the anisotropy can be observed.

The molecular static simulations demonstrate that the $\langle 100 \rangle$ tilt-grain boundary has an anisotropic energy with respect to the inclination angle but the simulations cannot predict if the effect of the anisotropic energy is large enough to produce the faceting of a mesoscopic grain boundary. For this reason, it is necessary to link the results of the molecular static simulations with a model capable to translate the outcomes to the mesoscopic scale.

4.4.2.2 Vertex-Model Simulations of Grain Boundary Migration

The simulation model has been extensively explained in Ch. 2. In order to simulate the anisotropy of the boundary energy with the inclination angle, the modifications described in section 4.4.1 were accomplished. For the simulations, instead of the quarter-loop geometry of the grain boundary, the geometry of a so-called island grain (circular grain embedded into a grain of different orientation) was selected because such geometry allows studying all possible inclination angles. The data about the dependency of the grain boundary energy on inclination and misorientation angle was used as input for the simulation model. Despite that the grain boundary mobility can also depend on the spatial orientation of the grain boundary, in the present simulations it was assumed constant. The reasons behind this are principally the lack of appropriate data and also the difficulty of measuring this property, even by means of simulations.

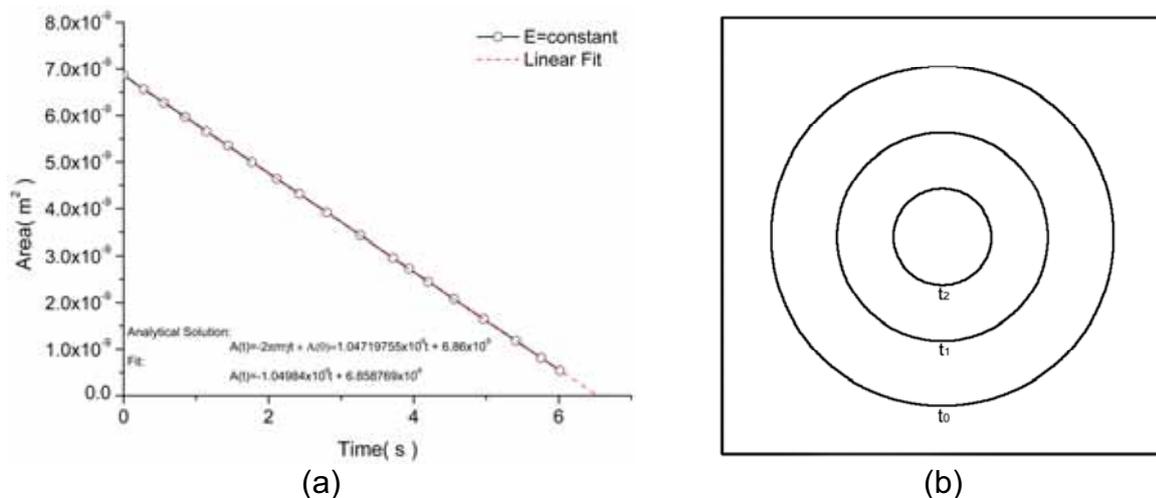


Figure 4.18. Evolution of an island-grain for a constant grain boundary energy. The energy is isotropic with respect to the inclination angle. For this case the kinetics of the grain growth can be analytically derived, (a) shows the comparison of the simulation results with the analytical solution whereas (b) shows the evolution of the grain at three different times $t_0 < t_1 < t_2$.

The purpose of this section is to demonstrate that the vertex model can simulate grain boundary evolution and grain growth when the energy is anisotropic with respect to the boundary spatial position. For this reason, the results delivered by the molecular static model will be used as input for the vertex model, however, only the results for 0 K and 500 K will be analyzed. The input can be fed into the vertex model in form of a list of inclination angles and corresponding energy or in form of a continuous mathematical function. If the data is introduced in the first manner, the program extrapolates the values that cannot be found directly in the list, for the present simulations, only linear extrapolation was used, but more complex extrapolation algorithms are available as well. The data extracted from the molecular

static simulation was fitted and the resulting functions were used to simulate grain boundary migration.

In order to verify the exactitude of the vertex simulations, simulations were first carried out using isotropic grain boundary energy. In this case, the kinetics of the grain growth for the island-grain can be analytically derived. The area A of the island-grain as a function of time t is given by the equation

$$A(t) = -2\pi m_{gb} \gamma_{gb} t + A(0) \approx 1.047 \times 10^{-9} t + 6.86 \times 10^{-9}, \quad (4.31)$$

for the present case, the simulation results delivered the following relation

$$A(t)_{fit} = -1.0498 \times 10^{-9} t + 6.859 \times 10^{-9}. \quad (4.32)$$

Evidently, the agreement is very good and indicates the applicability of the model to the current problem. With respect to the grain boundary shape, as expected, the grain remains circular during the whole simulation. Fig. 4.18b shows the evolution of the grain at three different times, in all cases the shape corresponded to a perfect circle.

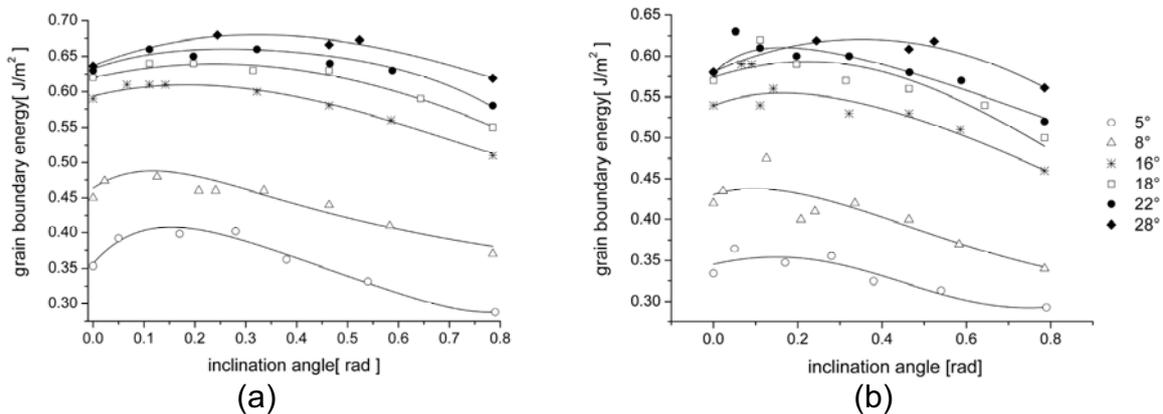


Figure 4.19. Simulated grain boundary energy as a function of inclination angle in Cartesian coordinates, the lines represent the fitting functions whereas the dots are the energies calculated with the molecular static method; (a) 0 K; (b) 500 K.

When the energy is inclination anisotropic, the situation changes radically, the shape of the island-grain is not circular any longer. The grain boundary has now clearly facets that correspond to the minima of the energy. According to Fig. 4.17, two minima can be appreciated, at 0° and 45° . In general, these minima are present in all the curves but the difference in magnitude between the minima decreases as the misorientation angle and the temperature increase.

The decrease of the difference between minima is reflected in the shape of the evolving grain boundary. For example, in Fig. 4.20a, the grain boundary shows only faceting for an inclination angle of 45° (with the corresponding symmetry) whereas no facet at 0° could form. As the misorientation angle increases, the facet for 0° becomes firstly visible and subsequently its length increases. At the beginning, this facet is inexistent because the energy for this facet is much higher than the energy for 45° and thus solely the 45° facets can achieve the minimal energetic state for the evolution of the configuration. Since the difference in energy between both states decreases, the minimal energetic configuration is result of the coexistence of both

facets. In the figure corresponding to a misorientation of 28° , the difference is practically zero and the length of the facets for 0° and 45° is almost the same.

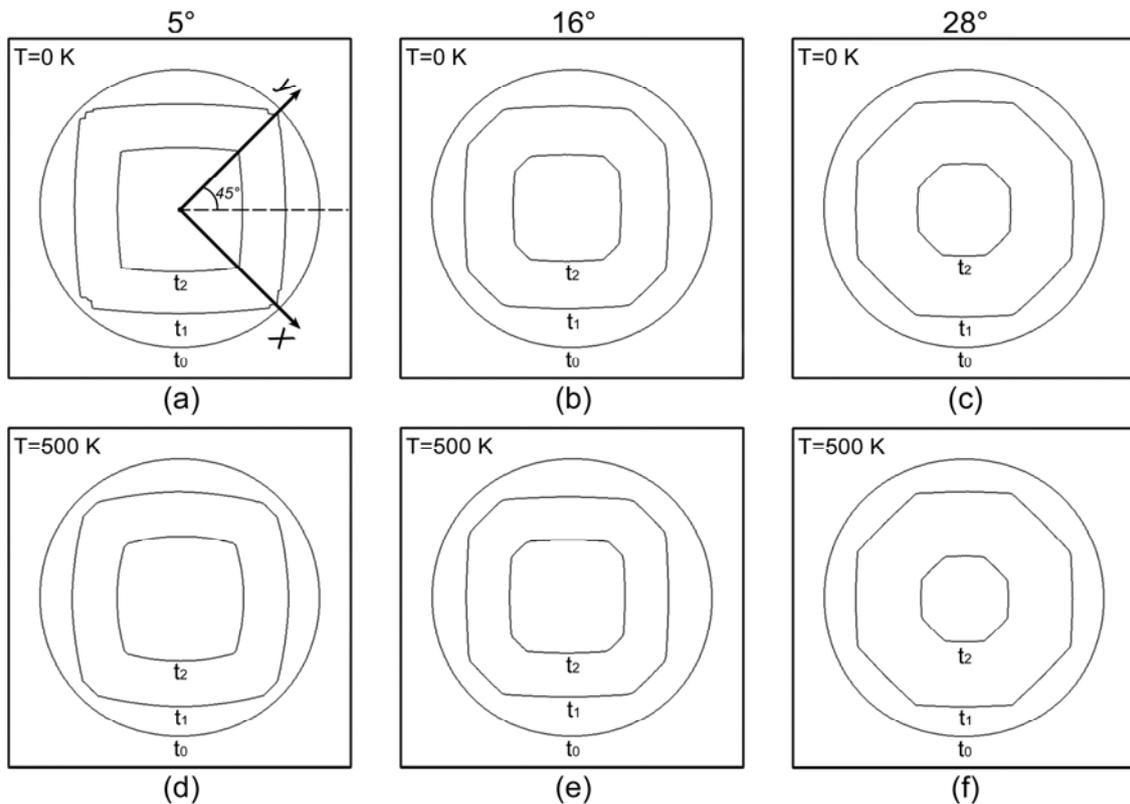


Figure 4.20. Simulated grain boundary shape for 5° , 16° and 28° misorientation angle. (a)-(c) were simulated using the curves corresponding to $T=0\text{K}$ and (d)-(f) with the curves for $T=500\text{K}$.

The grain does not attain a circular shape, even at high temperatures and misorientations, because, as shown by the curves of Fig. 4.19, the energy is still anisotropic and hence the 0° and 45° minima still determine the shape of the evolving grain. This deviates from the experimental observations. However, it does not contradict or invalidate the hypothesis that the faceting of the grain boundary is due to the anisotropy of the grain boundary energy with the inclination angle. On the contrary, the simulations corroborate this hypothesis. The deviations are explained on the basis that during experimentation other factors can also affect the facet formation and in the fact that for the simulation, the anisotropy of the grain boundary mobility with the inclination angle was not taken into account, which can eventually modify the conditions for the formation of the facets.

Chapter 5

3D Grain Growth Vertex Model

5.1 Introduction

Grain growth is a three-dimensional phenomenon and thus can only be fully considered in this space. Two-dimensional abstractions of the phenomenon are necessary because the mathematical complexity of the problem in 3D space is rather high. In order to properly describe grain growth in three dimensions, not only the full dependency of the boundary properties on the eight parameters that describe a grain boundary but also the 3D topology of the polycrystal needs to be considered.

Modeling and simulation of 3D grain growth are essential tools for the investigation of this phenomenon, since the three-dimensional experimental observation of polycrystals is difficult and normally restricted to few grains with modern techniques. Several three-dimensional models have been developed for the simulation of grain growth. All of them have advantages and disadvantages but among them, the Vertex model stands out for the clarity of the physics underlying it. Nevertheless, the principal disadvantage of this model is the high grade of programming skills necessary for its implementation. In the present chapter, the 3D Vertex model and the details for its implementation are presented.

5.2 3D Vertex Model

The simulation method is based on a vertex model that considers a front tracking approach [48, 49, 108-113]. In such approach, only the grain boundary is discretized whereas the grain interior is not. The grain is considered as the volume enclosed by certain grain boundaries and keeps the information about its crystallographic orientation. Fundamental stages of the simulation and modeling process are the creation of a microstructure for the simulation, the method for the grain boundary discretization, the formulation of the equations for the boundary motion and the topological transformations that take place as result of the minimization of the free energy through the disappearance of the grain boundaries. In the present section, all of these stages will be explained in detail.

5.2.1 Microstructure Generation

The generation of the microstructure is crucial for every simulation model. In 2D, the problem is relatively simple and the microstructure can be obtained even from

experimental sampling by means of techniques like optical, electronic and orientation microscopy and the further digitalization of the information. Nevertheless, in 3D the problem is more complicated since there are very few three-dimensional observation techniques, so far. Furthermore, the only existing methods allow merely the analysis of very small volumes of a sample and thus it is not representative of the whole sample.

The alternative to three-dimensional sampling is the reconstruction of a 3D microstructure from numerous successive two-dimensional slices of the sample (serial sectioning) [114]. The necessary effort for this task is, nevertheless, enormous if the acquisition is conducted by conventional techniques. Fortunately, 3D orientation microscopy has recently become available facilitating this task and the simultaneous development of algorithms capable to interpret the information and convey it in adequate forms has made possible the successful reconstruction and digitalization of three-dimensional microstructures. However, the information provided by these methods normally discriminates the grain boundaries (and thus it does not provide the microstructure as a topological network) and discretize the grains as small pieces of volume with an assigned orientation. For several simulation models such as cellular automata, phase field models, Monte-Carlo models, etc, this information is sufficient because they require the discretization of the volume, precisely through small volume elements. Conversely, for the Vertex model, this information is not adequate because, as will be explained in a subsequent section, the Vertex model demands the discretization of the grain boundaries. However, adequate algorithms for the identification of the grain boundaries are more complicated and require more computational efforts.

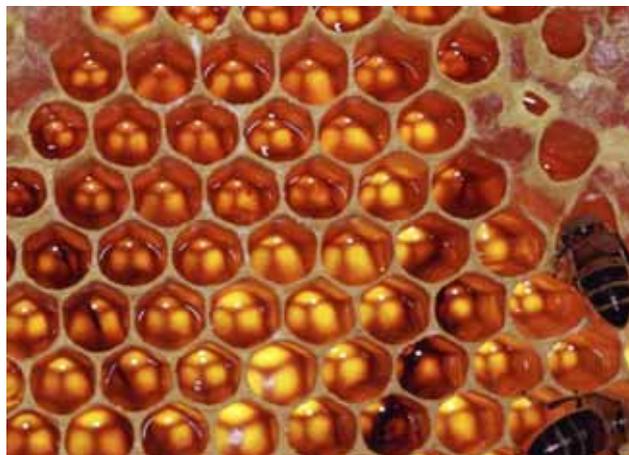


Figure. 5.1. Natural tessellation, the honeycomb pattern is a tessellation found in the nature. This tessellation is bounded by the physical constrains of the beehive.

The numerical alternative is the use of tessellations. A tessellation (sometimes also called mosaic) is a regular arrangement of polygons (2D) (regular in the sense that there are no gaps or overlaps between the elements of the tessellation), polyhedra (3D) or polytopes (n -dimensional) that a determined space comprises. A tessellation can be bounded or unbounded depending on the spatial boundary conditions. There are several tessellations in the nature (a polycrystal itself is an excellent example) in Fig. 5.1, as an example, a honeycomb pattern is shown [115].

For the simulation of grain growth, the so-called Voronoi tessellation can be usually found in the literature [44, 48, 49]. This kind of tessellations is simple and provides

the necessary information for the simulation of grain growth i.e. about the topological network. However, despite its simplicity, the numerical implementation for the algorithm that constructs the tessellation are either complicated or slow, and frequently both. For a detail descriptions of the different methods for the constructions of Voronoi tessellation and other topics on computational geometry refer to [62, 63].

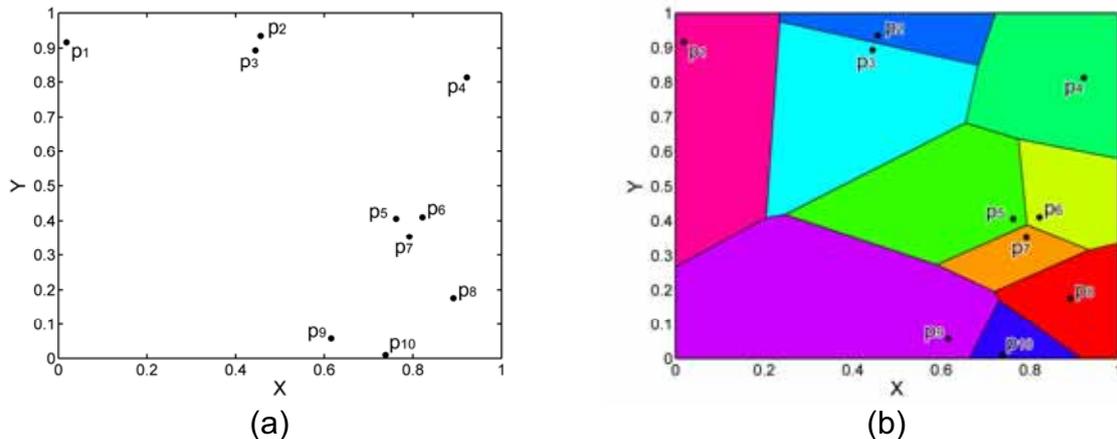


Figure 5.2. (a) Sites for the Voronoi tessellation and (b) the corresponding Voronoi diagram.

The concept of Voronoi tessellation is, in fact, more than a century old [116]. The formal definition is rather simple, given a defined (not necessarily finite) space S and letting $P=\{p_1, p_2, \dots, p_n\}$ be a set of points within S , where the points are called partition sites. The partition of the space is formed by assigning every point to its nearest site. All those points assigned to p_i form the *Voronoi region* $V(p_i)$, which is also called *Voronoi polygon* (only in 2D and in a bounded space). $V(p_i)$ consist of all the points at least as close to p_i as to any other site, explicitly

$$V(p_i) = \{x : |p_i - x| \leq |p_j - x| \forall j \neq i\}. \quad (5.1)$$

Evidently, the sites compete for the biggest region possible. The points where the region of influence of the sites overlaps form the limit for each Voronoi region: in 2D this limit is a line whereas in 3D is a surface, the collection of all these limits forms the *Voronoi diagram*. In Fig. 5.2, a two-dimensional Voronoi tessellation is shown, this tessellation was formed by ten sites in a bounded space S (Fig. 5.2a). Each site has influence over a limited region of the space S , the region is limited by straight lines that form polygons (Fig. 5.2b). An example of 3D Voronoi tessellation can be seen in Fig. 5.3.

In materials science, it is possible to identify a Voronoi region with a grain and the Voronoi diagram with the grain boundaries. It can be noted that this method delivers the topology of the tessellation and, therefore, is optimal for its utilization in the generation of an input for the Vertex model. The principal problem with the Voronoi tessellation is that it delivers an arbitrary grain size distribution. A discretional selection of the sizes of the cells is not possible. To overcome this difficulty, some modifications to the original method for the calculation of the Voronoi tessellation have been proposed [44, 117]. In summary, the Voronoi tessellation is an excellent alternative for the generation of microstructure for the simulation; with the actual stand, it is possible to produce even discretional grain size distributions.

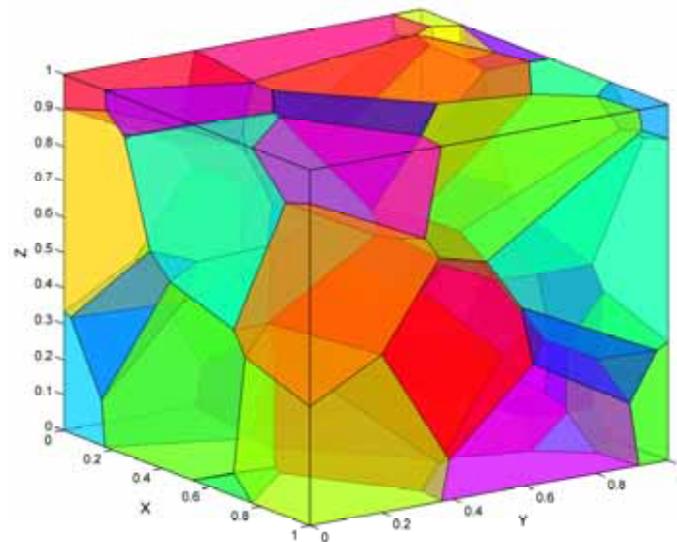


Figure 5.3. 3D Voronoi tessellation.

5.2.2 Discretization of the Grain Boundaries

The grain boundaries (internal interfaces) are discretized in triangular facets; for the vertices of these facets, the forces and velocities are calculated. While in the two dimensional case, the structural elements that conform the microstructure are the grain boundary and the triple junctions, in the three-dimensional case, an additional element needs to be added, namely, the quadruple junction. A quadruple junction is the geometrical point where four grains meet. In addition, the other two elements require a three-dimensional description. It means that for the current case a grain boundary is represented by a surface and the triple junction has now its real character as a line (for the sake of clarity, in the following, this element will be referred as triple line). All these elements and the kind of discretization are represented in Fig. 5.4.

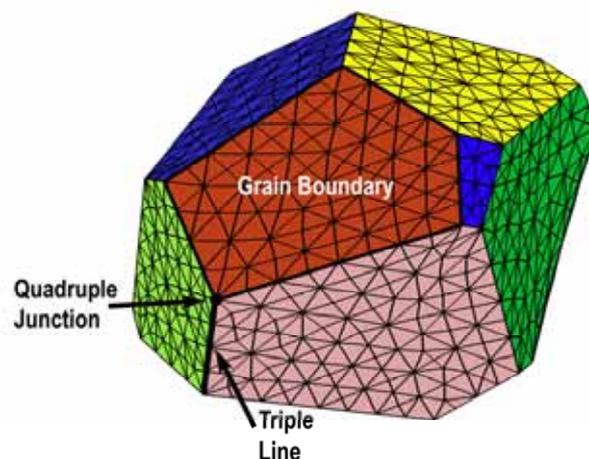


Figure 5.4. Discretized boundaries of a grain and their junctions with adjacent grains.

The procedure for the discretization depends on the kind of the provided initial input. Such input should at least deliver the spatial localization of the grains (center of mass), the grain boundaries enclosing it and the coordinates of the vertices

conforming the grain boundaries. If some of this information lacks, the construction of the microstructure becomes impossible. Nevertheless, supposing that this information is existent, the first step is to discretize the grain boundaries in triangular facets. The choice of the triangle as the minimal surface element is due to the fact that this geometrical element is the only one whose surface lies on the same plane (i.e. all of its points of the triangle are coplanar). The selection of other surface elements is possible but the calculation of velocity of the elements and the topology are more complicated because for complex geometries some of the points of the discretizing element might be non-coplanar.

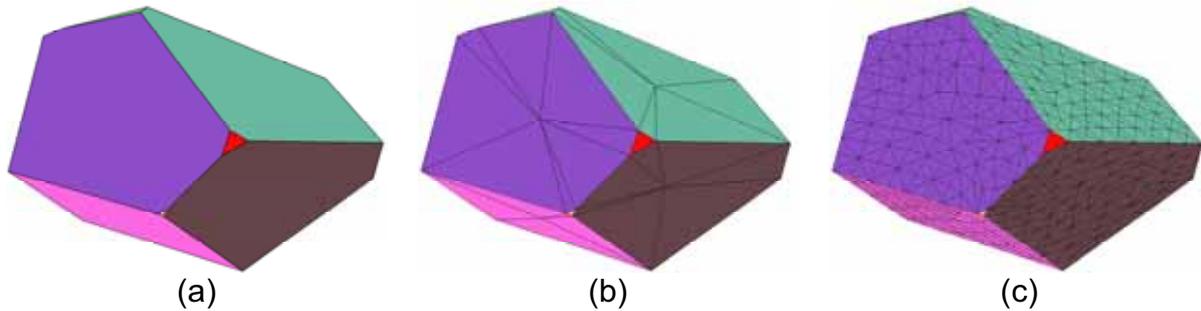


Figure 5.5. Sequence of the discretization procedure; (a) original polyhedron, (b) grain after the introduction of the first triangular facets and (c) after the sequential segmentation.

The grain boundaries are first discretized by the segmentation of the sides of the polyhedra that are delivered by the Voronoi tessellation. For this, it is necessary to calculate first the geometric centroid of the grain boundaries in order to construct the triangular facets. In Fig. 5.5a, a polyhedron as delivered by the Voronoi tessellation is shown, after the calculation of the geometrical centroid and the setting of the initial triangular facets, the same polyhedron can be observed in Fig. 5.5b. Fuchizaki et al. [110] and Weygand et al. [111] used a similar method for the discretization of the grain boundaries in their original works on 3D grain growth simulation. However, the subdivision of the grain boundaries in only these triangular facets cannot represent adequately the curvature of the grain boundaries and hence the error introduced to the calculation of the forces and velocities increases.

To overcome this problem, the recursive and continuous segmentation in further triangular facets is introduced. A minimal length Δs of the edges of the triangular facets is first defined. This length is not only necessary for the discretization of the grain boundaries but it is also required to trigger the topological transformations. The procedure for the segmentation of the facets is rather simple, whenever the distance between two vertices is larger than twice Δs , a new vertex in the middle of the segment is introduced, the facets attached to the edge are then split in two. The procedure is repeated until all edges have a length of about Δs . In fig. 5.6, an example of the procedure is schematized. In this example, an arbitrary grain boundary, whose shape corresponds to a regular hexagon, is discretized in triangular segments that are formed with the edges of the hexagon and the geometric centroid of the hexagon (Fig. 5.6a). Since the length of all edges is clearly larger than twice Δs , a new vertex (denoted by 1 in Fig. 5.6b) is introduced in one of the edges of the grain boundary. Correspondingly, the facet is sectioned into two new triangles (dotted line from 1 to the centroid), the same operation is repeated for all edges (2 and 3). Thereafter, the diagonals from the centroid to the vertices of the edges are split (4 and 5) and finally the first edge introduced at the beginning of the segmentation procedure is sectioned (6). The repetition of the process leads to the discretization of

the grain boundary as shown in Fig. 5.6c. The length of all edges is now very close to Δs . The procedure here described is only one possibility of the multiple potential segmentation procedures. However, the result is in any case similar (Fig. 5.5c).

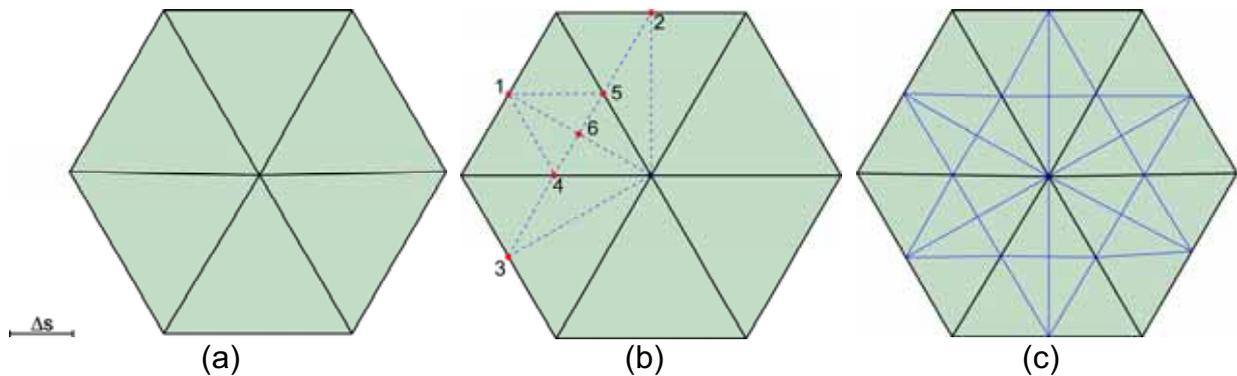


Figure 5.6. (a) Arbitrary grain boundary after initial discretization, (b) the distance between two points cannot be larger than twice the pre-defined critical distance Δs and (c) result after the segmentation of the edges of the facets and the facets themselves in new facets. The original edges are represented in black whereas the new introduced edges in blue.

5.2.3 Equation of Motion

The forces at vertices arise from the surface tensions of the triangular facets that adjoin the respective vertex. Figure 5.7 shows a vertex and the facets surrounding it. The force F_{f_1} due to the shaded facet f_1 on the vertex P_0 is given by

$$\vec{F}_{f_1} = \frac{\gamma_{gb}}{2} \cdot \frac{\vec{s}_0 \times (\vec{s}_1 \times \vec{s}_0)}{\|\vec{s}_1 \times \vec{s}_0\|}. \quad (5.2)$$

where γ is the grain boundary energy, and $\vec{s}_0, \vec{s}_1, \vec{s}_2$ are the edge vectors in the facet, which are fully determined by the position of the vertices (P_0, P_1 and P_2) conforming the facet (Fig. 5.7).

The sum of the forces over all facets surrounding the vertex leads to the net force

$$\vec{F}_{sum} = \frac{\gamma_{gb}}{2} \cdot \sum_{i=1}^n \frac{\vec{s}_{0i} \times (\vec{s}_{1i} \times \vec{s}_{0i})}{\|\vec{s}_{1i} \times \vec{s}_{0i}\|}. \quad (5.3)$$

where n is the total number of facets adjoining at P_0 . The velocity of the vertex reads

$$v = m_{eff} \cdot \vec{F}_{sum} = \frac{1}{D_f} \cdot \vec{F}_{sum}, \quad (5.4)$$

m_{eff} is the effective mobility of the vertex and D_f is the drag factor, which is defined as

$$D_f = \frac{A_n}{m_{gb}} + \frac{ds}{m_{dl}} + \frac{l}{m_{qp}}. \quad (5.5)$$

m_{gb} , m_{tl} , and m_{qp} are the grain boundary, triple line and quadruple junction mobilities, respectively, ds is the mean distance between adjacent vertices over a triple line, and A_n is the projected area of the surrounding facets onto the direction of motion.

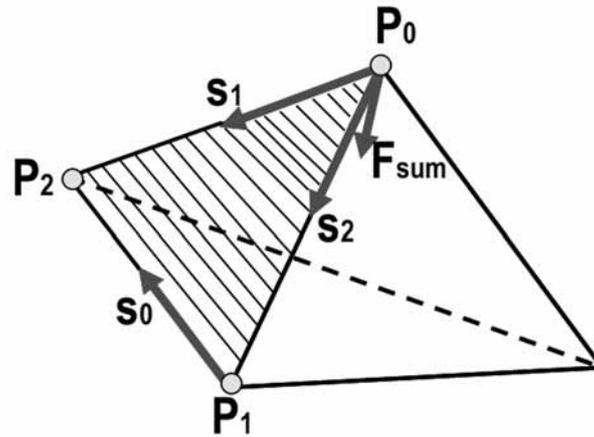


Figure 5.7. The velocity of a point is calculated from the local geometry of the facets adjoining it.

5.2.4 Topological Transformations

Topology is a concept that is foreign in the materials science; it is normally only introduced in the study of the topological properties of cellular patterns [48, 108] and by extension in the study of topology evolution in grain growth. In Ch. 1, the basic concepts of the topology of 3D polycrystals (topological network) were introduced. However, the notion of topology was limited to the number of structural elements that comprises a polycrystal.

Johann Benedict Listin introduced the term topology in 1847, however, one of the first topological results is found in a Leonhard Euler's paper of 1736 on *The seven bridges of Königsberg* [118]. The basic notions introduced in Ch. 1 on the topology of a polycrystal are due also to Euler. It means that the fundamental topology used in materials science is more than two centuries old.

Nevertheless, the importance of the topology, at least, for the grain growth is evident. Grain growth is, after all, a process of topological decay [12]. The comprehension of the definition of topology can bring a better understanding of its importance in this physical phenomenon, as topology is the mathematical study of the properties that are preserved through deformation, twisting, and stretching of objects. Evidently, during grain growth the individual crystals are subjected to deformation (though not in the mechanical sense). Due to the deformation, the topological properties of the grains change during the course of grain growth. The grains lose faces (grain boundaries), edges (triple lines) and vertices (quadruple junctions). The Euler formula (Eq. (1.14)-(1.16)) of the unbounded state indicates that the lost of any element affects necessarily the quantity of the other two elements. The fundamental operation during grain growth that triggers a change in the topology of the polycrystal is the lost of a triangular grain boundary (however is not the only event that triggers a topological transformation). When the triangular grain boundary collapses, the edges shared with other grains are destroyed, at this precisely instant the Euler formula for the unbounded state is not longer valid, because the collapsing of the grain boundary produces an edge with more than three grain boundaries and thus Eq. (1.14)-

Eq.(1.16) cannot be fulfilled. Consequently, the topological order needs to be restored. For this, new triangular grain boundaries are created and edges with multiple adjoining grain boundaries are reconnected until Eq. (1.14)-(1.16) are completely fulfilled.

The restoration of the topology during grain growth implies that the connectivity of the structural elements of the polycrystal must remain intact during the microstructure evolution. For instance, a quadruple junction links four grains, six grain boundaries and four triple lines, a triple line connects three grains, three grain boundaries and two quadruple junctions. If some element has a different connectivity, the elements surrounding it must be reordered until the natural connectivity is reassured. This reordering is called *topological transformation*.

Doubtless, the most difficult part in the implementation of the Vertex Model is the realization in the program of the topological transformations. In Ch. 2, the necessity of implementing such transformations was explained, as well as the indispensable topological transformations that take place during the evolution of 2D microstructures. In the three-dimensional case, the complexity sensibly increases due mainly to the increment of the possible cases that can occur during microstructure evolution.

Nevertheless, the basic transformations are well documented [61] and their implementation has succeeded to certain extent [109-111]. There are a finite number of transformations only if the energy of the grain boundaries is constant (isotropic energy). In the contrary case, the possible transformations will depend on the possible combinations of the energies of the grain boundaries attached to an edge that introduces a decrease in the free energy of the system. In an anisotropic system, the Euler formula is not anymore valid since multiple junctions can be stable even only instantly.

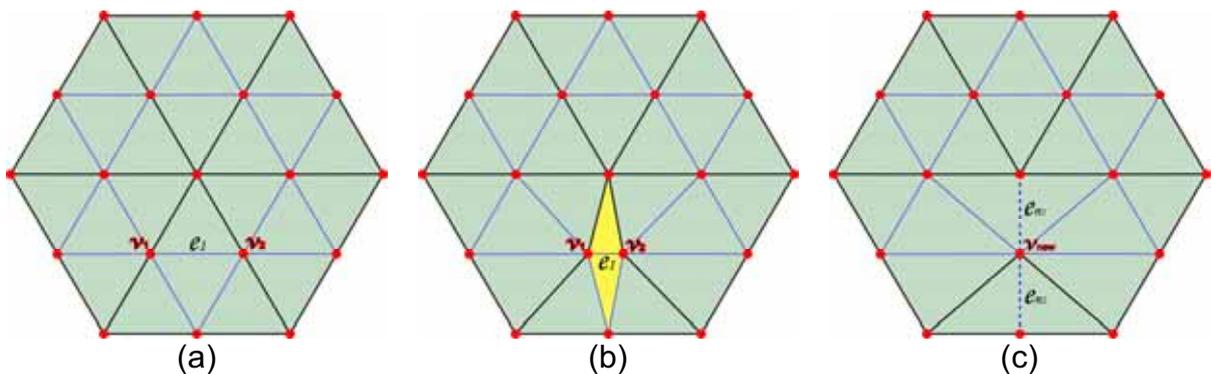


Figure 5.8. Elimination of a facet that possesses an edge with a length less than $0.5\Delta s$; (a) initial grain boundary, (b) the distance between two is less than $0.5\Delta s$ and (c) grain boundary after the elimination of the short edge and thus the adjoining facets.

As mentioned previously, a criterion established on basis of the minimal length Δs triggers the facet elimination, which in turn, triggers the topological transformations. The facet elimination is the fundamental process not only for the topological transformations but also for the boundary area reduction. To explain this procedure, we will refer to Fig. 5.8a, which shows again a surface with a hexagonal regular shape that is discretized in small regular triangles. In the same figure, let vertices v_1 and v_2 be attached by an edge e_1 on a triangular facet. Due to the action of the forces at the vertices v_1 and v_2 , they approach to each other (Fig. 5.8b); the distance

between them becomes then closer than $0.5\Delta s$, which is the condition that triggers the facet elimination. Since the edge between v_1 and v_2 will be eliminated, also the attached facets to the edge have to be removed. In the current case, only two facets are involved (highlighted in yellow in Fig. 5.8b). Respectively, if the considered edge lies in a triple line, then three facets are to be considered. A vertex v_{new} located at the mean length of e_1 replaces the vertices v_1 and v_2 (i.e. the length of the edge e_1 is zero), the attached facets disappear and are replaced by the edges e_{n1} and e_{n2} (dotted lines in Fig. 5.8c). A topological transformation triggers when the facet elimination meets determined conditions, which alter the topology of the system.

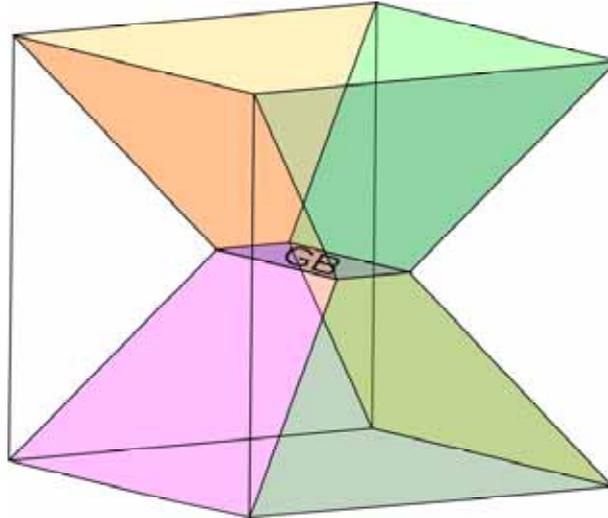


Figure 5.9. For the demonstration of the topological transformations, a small system is used, six grains fill the shown cube, in the figure only two of them are shown but the remaining grains fill completely the space.

In order to make clear the topological transformations that take place, the grain system shown in Fig. 5.9 will be employed. Fig 5.9 is a volumetric cubic section around a rectangular grain boundary (denoted by GB) of a bigger system. In the cube, there are six grains; however, only two of them and their boundaries are observed. The topology of this system follows the Euler formula and is correct for isotropic conditions.

For the explanation of the first topological transformation, let now consider only the grain boundaries shown in Fig. 5.10 of the system and let be the length of the edge e_1 between vertices v_1 and v_2 shorter than $0.5\Delta s$. Since the requirements for the facet elimination meet, the removal of edge e_1 occurs. After the elimination, the grain boundaries, attached previously to the vertices v_1 and v_2 , adjoin now vertex v_{n1} (Fig. 5.10c). The topology of the resulting configuration is not correct, since nine grain boundaries adjoin a single vertex (however, in Fig 5.10c only six grain boundaries are shown).

In Fig. 5.10b, the planar section perpendicular to the grain boundary GB at the edge e_1 is shown. After the elimination of the edge, the two-dimensional section (5.10b) shows that a 2D quadruple junction is formed. In the two dimensional case, this junction is energetic unstable and must split into two triple junctions, as explain in Ch. 2.

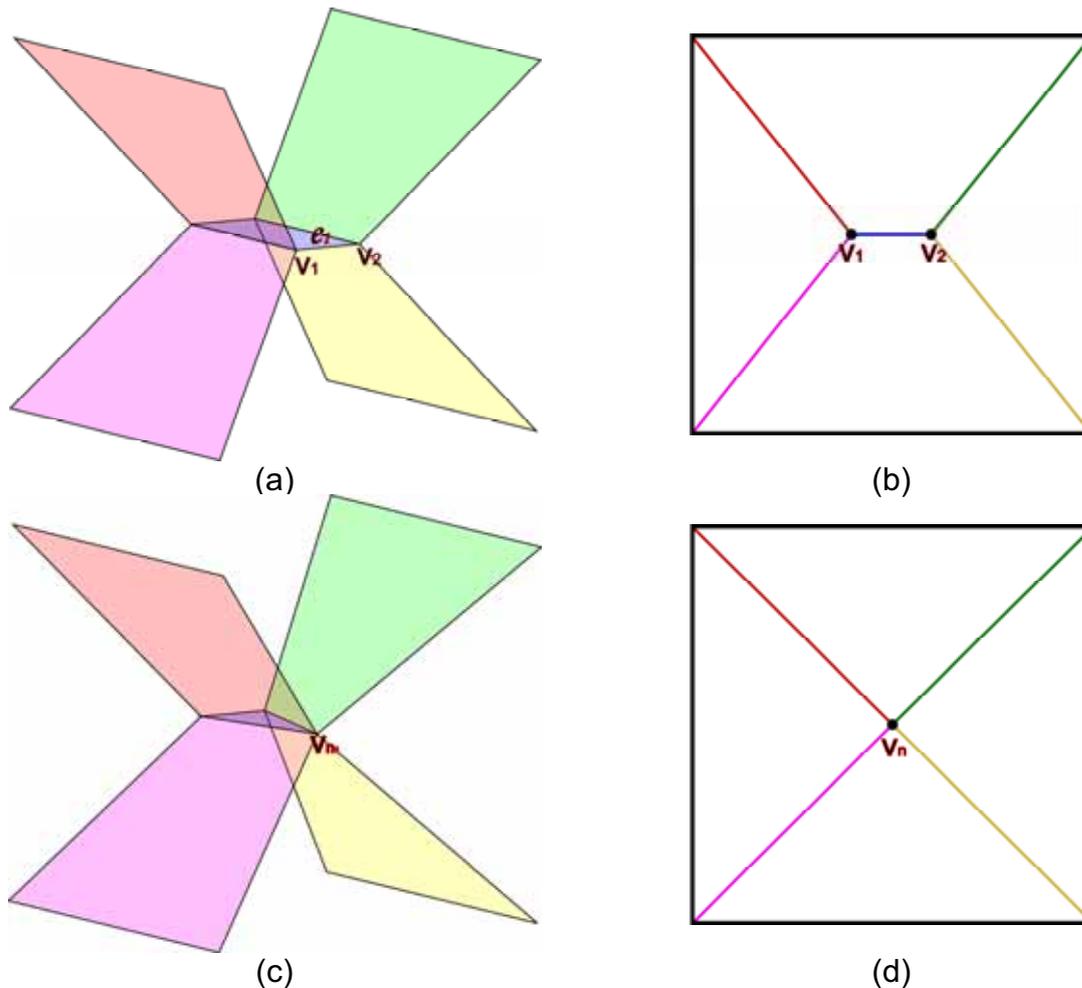


Figure 5.10. Grain boundary arrangement for the explanation of the topological transformation, (a) original configuration and (b) two-dimensional equivalent. After the deletion of edge e_1 the configuration converts into (c), which is the 3D equivalent of a 2D quadruple point (d).

The three-dimensional case is similar, under isotropic conditions, a vertex can only be adjoined by six boundaries; more than six boundaries lead to the energetic instability of the junction and to the further splitting of it into more stable configurations. In the case presented in Fig. 5.10c, in order to re-attain the energetic stability and the correct topology, a new triangular grain boundary needs to be introduced and the boundaries previously attached to the multiple junction need to be reconnected. Once the new grain boundary is introduced, the topology recovers its correct state again. Only a single triangular facet with vertices v_{n1} , v_{n2} and v_{n3} forms the new boundary (Fig. 5.11a).

Since a completely new grain boundary forms, it can be thought that this 3D topological transformation is equivalent to the 2D ripping of the quadruple point, which occurs after the collapsing of one boundary in 2D. However, it must be noted that in the 3D case there is no grain boundary disappearance, the boundary loses only one edge. Moreover, no quadruple line was created. In fact, the creation of a new grain boundary in 3D occurs only after two quadruple junctions collide into one (i.e. a grain boundary loses an edge) and do not occur after the collapsing of a grain boundary. Nevertheless, the collapsing of a grain boundary triggers another topological transformation, which will be explained in the following.

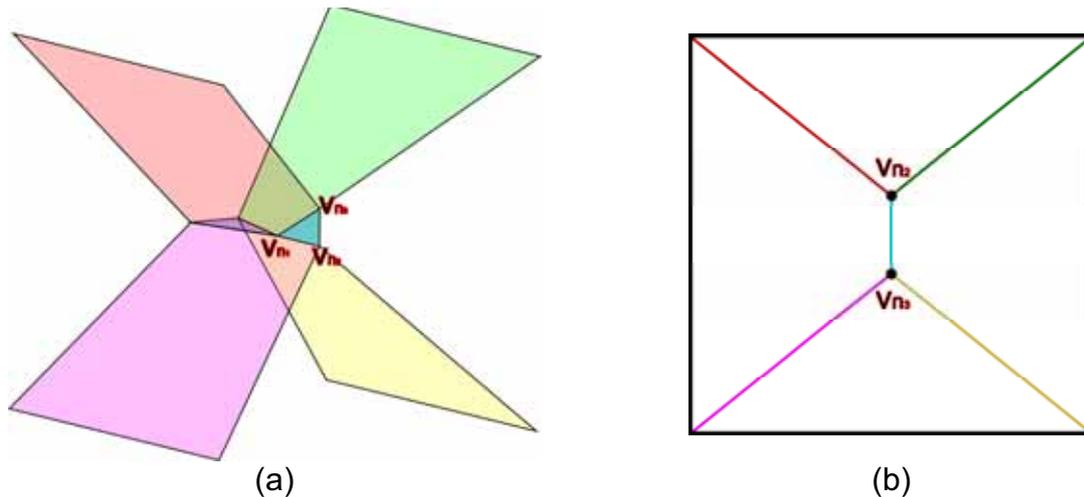


Figure 5.11. Introduction of a previously inexistent grain boundary in order to attain the energetic stability and the correct topology after the formation of the configuration shown in Fig. 5.10c. The new grain boundary and the vertices created to form the triangular facet (a) and (b) two-dimensional equivalent.

For the next topological transformation, we will depart from the configuration of Fig. 5.12a, which is the configuration delivered by the previous topological transformation. In contrast with the former, in the current case, the edge e_2 (v_a, v_b) meets the requirements for the facet elimination ($e_2 < 0.5\Delta s$).

The two-dimensional section (Fig. 5.12b) shows the situation; a grain boundary collapses and an unstable quadruple junction forms. The 2D sections show no difference with respect to the previous case, an edge collapses, a quadruple point appears and a “new grain boundary” must be introduced to correct the topology and regain the energetic stability.

Nevertheless, the 3D diagram shows a different situation. The elimination of edge e_2 causes the collapsing of the original grain boundary GB. After this, a quadruple line forms (Fig. 5.12b) and the topology does not follow the Euler formula since more than three grain boundaries adjoin a line, eight boundaries meet at a single point (v_n) in one extreme of the quadruple line and in the other extreme, only five boundaries adjoin a vertex (v_m).

In order to repair the topology, it is necessary to rip the quadruple line and form stable triple lines, just like in 2D. However, in 3D, this is not anymore achieved by the introduction of a new grain boundary but by the introduction of one or more triangular facets that complement the existing grain boundary and rip the quadruple line in two quadruple junctions and three triple lines (though one already existed in the form of the quadruple line). Fig. 5.13a shows the result after the insertion of the triangular facets for the splitting of the quadruple line. The 2D section shows the similarity with the two-dimensional topologic transformation.

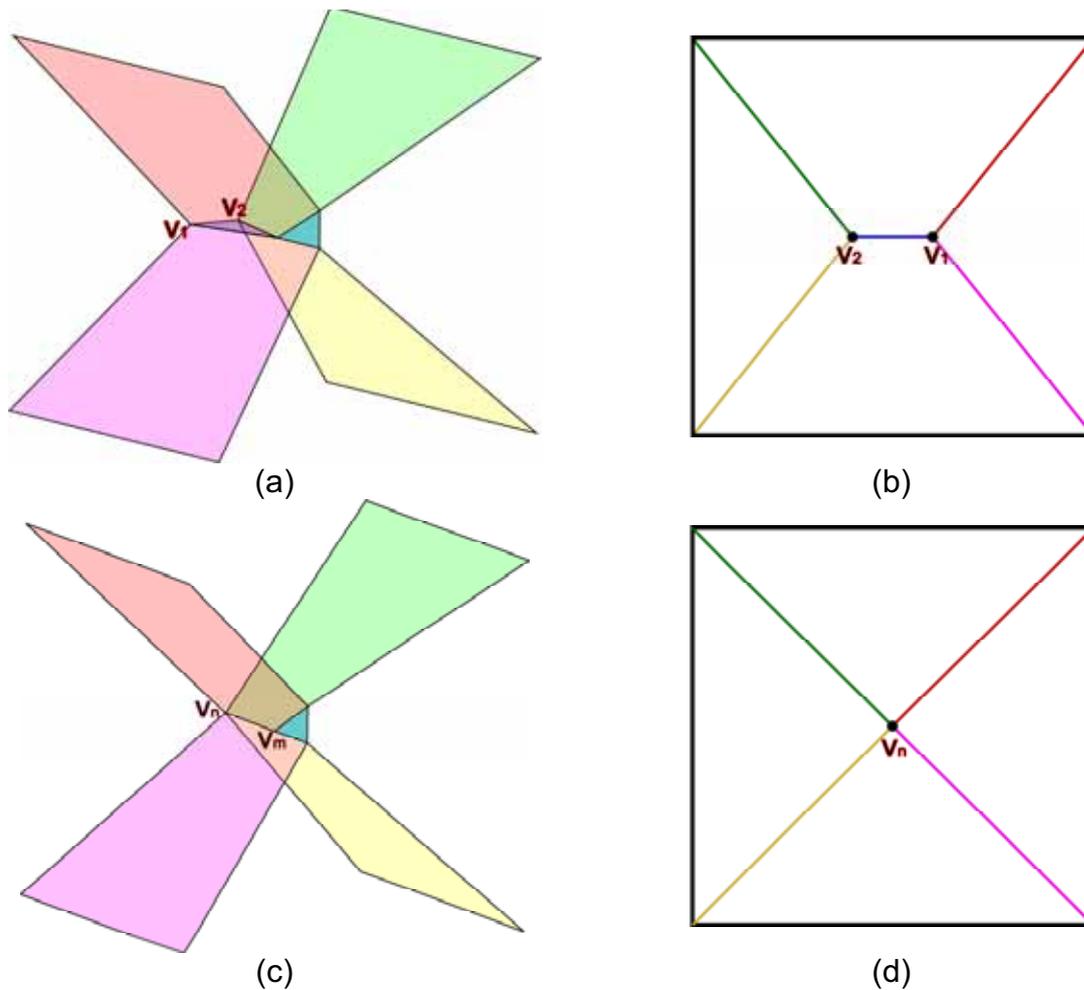


Figure 5.12. Collapsing of a grain boundary; (a) initial configuration and (b) planar section perpendicular to the grain boundary at edge e_2 , (c) after the collapsing of the grain boundary a quadruple line forms, (d) the planar section shows the formation of a quadruple junction.

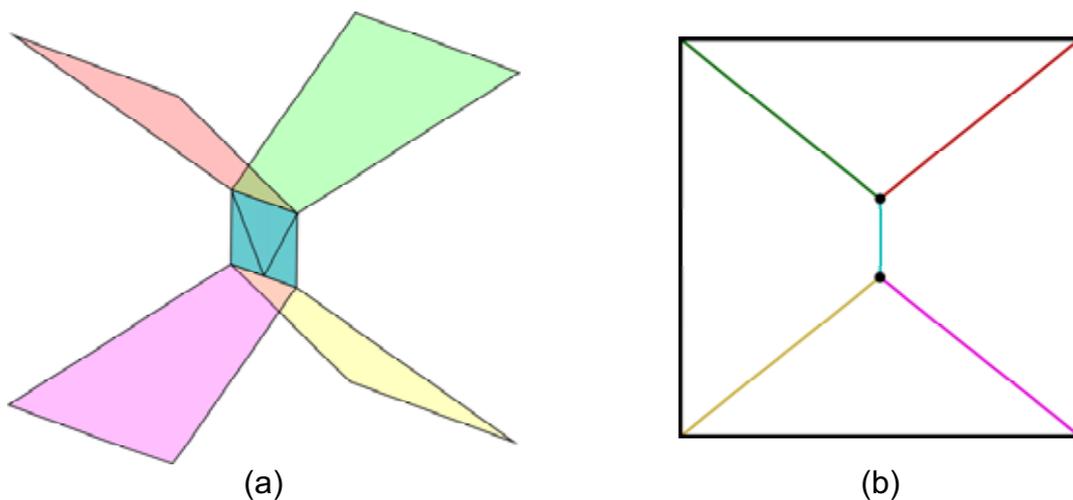


Figure 5.13. Topological transformation after the collapsing of a grain boundary and posterior quadruple line formation, since a grain boundary already existed, it is only necessary to introduce a triangular facet and connect it with the existing grain boundary; (a) 3D result and (b) 2D section.

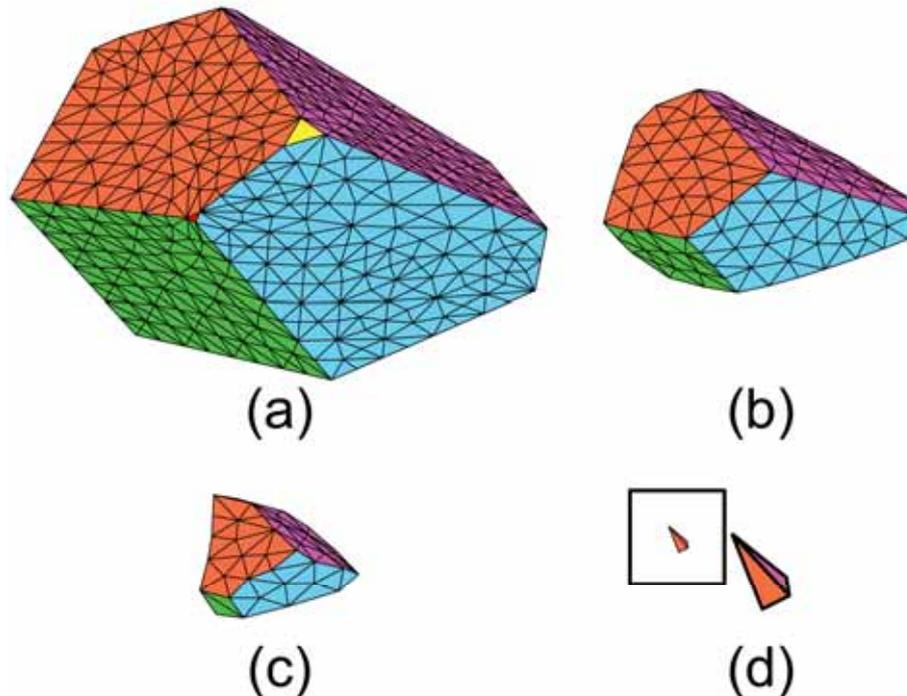


Figure 5.14. Shrinking grain at three different stages; prior to its disappearance, the grain resembles a tetrahedron; the real size of the grain is shown in the frame.

The last topological transformation is simple to explain, the only grain, which can collapse without affecting the topology, is the grain with a tetrahedral shape because its collapse leaves a natural quadruple junction. Grains with more than four sides can also instantly collapse as long as the volume is comparable to $(\Delta s)^3$. However, the collapsing of a grain with more than four sides leaves a multiple junction and thus an incorrect topology. The treatment of such junctions is more complicated since their topological properties (number of grains and boundaries adjoining it) depend on the state of the grain prior to collapsing and thus very infrequently the procedure to treat such a junction is the same.

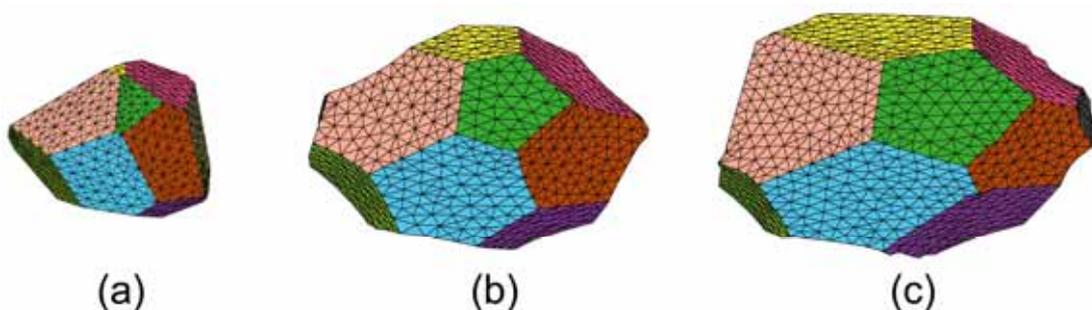


Figure 5.15. Growing grain from the simulations

The basic topological transformations were implemented in the program, and the result of them can be partially appreciated in Fig. 5.14 and 5.15. The grains for these figures were taken from a simulation performed on the polycrystal depicted in Fig. 1.8.b. Fig. 5.14 shows four different stages of the shrinking of a grain.

At the beginning of the simulations, the grain boundaries are still flat (Fig. 5.14a). After some time the grain boundaries become curved, the curvature of the grain boundaries is convex and thus the grain shrinks. In the last stage (Fig. 5.14d), preceding its collapsing, the grain shrinks until it achieves a tetrahedral form. The

real size of the grain in this last stage is shown in the black frame in Fig. 5.14d. In contrast, in Fig. 5.15, a growing grain is depicted; three different stages of its growth can be appreciated, during the growing of the grain, new grain boundaries are formed.

Chapter 6

Grain Boundary Junctions Revisited

6.1 Introduction

A polycrystalline aggregate is a system composed of grains, grain boundaries, triple lines and quadruple junctions. This system forms a topological network with a specified number of elements. For a long time, it was assumed that the only element affecting grain boundary migration was the grain boundary itself. Triple lines and quadruple junctions were not taken into account because these elements were believed not to drag grain boundary motion. However, in recent years several theoretical and experimental studies [103, 119, 120] have demonstrated that triple lines can have kinetics different from the adjoining grain boundaries, i.e. triple lines can possess a finite mobility, and therefore can drag grain boundary motion. The first experimental investigations were conducted only in a narrow range of geometrical configurations which allow a steady state motion of a system of connected boundaries [92]. Later on, experimental and theoretical investigations on polycrystalline samples indeed confirmed the dragging effect of triple lines [94].

Whereas the experimental study of triple lines can be easily conducted in quasi-2D systems quadruple junctions are true 3D features and hence their study can be only accomplished in 3D space which is difficult to do by experiments on metals, since metals are opaque. As a first attempt to address this problem, Gottstein and Shvindlerman [121] introduced a new concept, which would permit the study of a finite quadruple junction mobility in a special grain assembly. In the current chapter, this concept is extended and the effect of a finite quadruple junction mobility on grain growth is explored by means of computer simulations.

6.2 Three-sided Grain Configuration

In [121], the four grains assembly outlined in figure 6.1 was proposed. The main feature of this configuration is that one of the four grains has only three boundaries as depicted by the enclosing triple lines shown in Fig. 6.1. In such configuration the motion of the connected boundary system proceeds under the action of the triple line tension γ and is assumed to occur in steady-state. The dimensionless parameter describing the influence of the quadruple junction is given by

$$\Lambda_{qp} = \frac{m_{qp}a}{m_{tj}} = \frac{2\theta_1}{2\cos\theta_1 - 1}, \quad (6.1)$$

where m_{qp} is the quadruple junction mobility, m_{tl} is the triple line mobility, θ_1 is the angle at the tip of the triple lines at the quadruple junction, and a is the grain size (Fig. 6.1). Obviously the effect of a finite quadruple junction mobility is reflected by the change of the angle θ_1 . For a perfectly mobile quadruple junction $\Lambda_{qp} \rightarrow \infty$ and $\theta_1 \rightarrow \pi/3$, whereas for a very low quadruple junction mobility $\Lambda_{qp} \rightarrow 0$ and $\theta_1 \rightarrow 0$.

The steady-state motion of such a configuration can occur only when the shrinkage of the three-sided cross section proceeds much more slowly than the displacement of the quadruple junction.

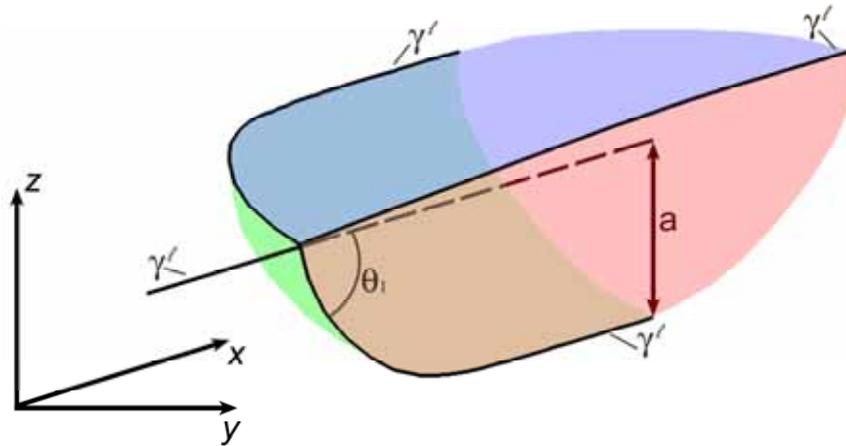


Figure 6.1. Grain assembly proposed in [121] for the determination of the dimensionless parameter Λ_{qp} .

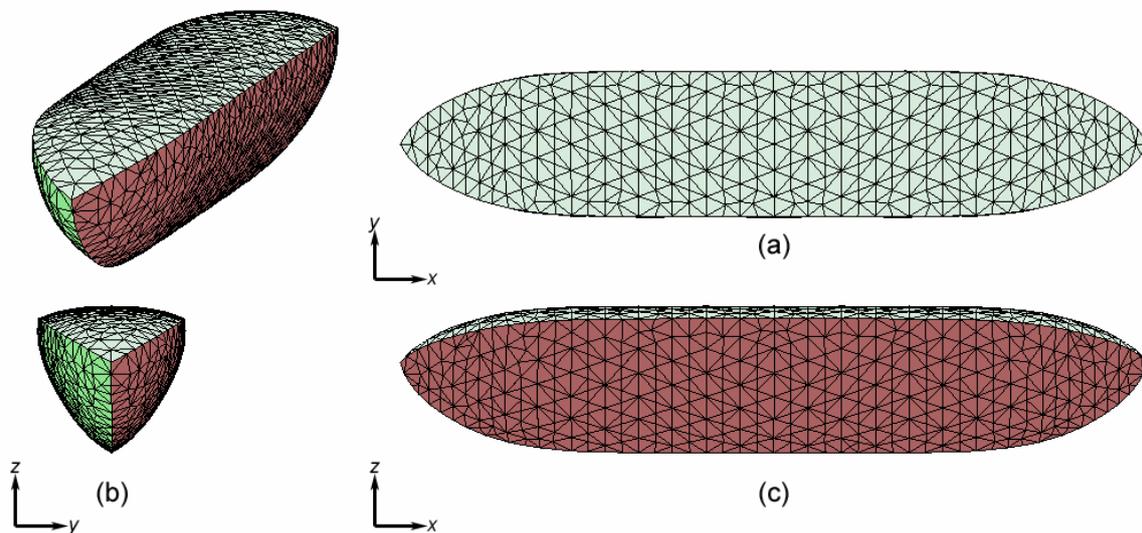


Figure 6.2. Geometry of the three-sided grain shown in Fig. 1, (a) top view, (b) front view and (c) lateral view.

6.2.1 3D Vertex Simulation

For the simulations a 3D vertex model was used. A description of the model and its implementation can be found in chapter 5 as well as in [122]. The geometry of the three-sided grain used in the simulations is shown in figure 6.2; it perfectly matches the configuration shown in Fig 6.1. As stated in the previous section the shrinkage of

the cross section should not contribute to the volume change of the grain, in order to maintain the geometry for the displacement of the quadruple junctions. To check the validity of this assumption the computed net displacements of the triple line and the quadruple junction are plotted in Figure 6.3a for the case of an infinite quadruple junction mobility m_{qp} . Contrary to expectations the magnitude of the triple line displacement is not negligible. In fact, the velocity of both junction elements is not very different (Fig. 6.3b); the triple line velocity is only approximately 3-4 times slower than the quadruple junction velocity. In fact, if the three-sided grain is very long (a prerequisite for Eq. (6.1)), the cross section and hence the whole grain vanishes even before the two quadruple points meet. The necessary condition that the volume change is essentially dominated by the motion of the quadruple junction – if the shrinkage of the cross section can not be avoided – can only be achieved for very small m_{tl} , when the shrinkage of the cross section is dominated by triple lines kinetics. In this case the grain boundaries are virtually flat, which would severely restrict the kinetic range where the investigation can be carried out.

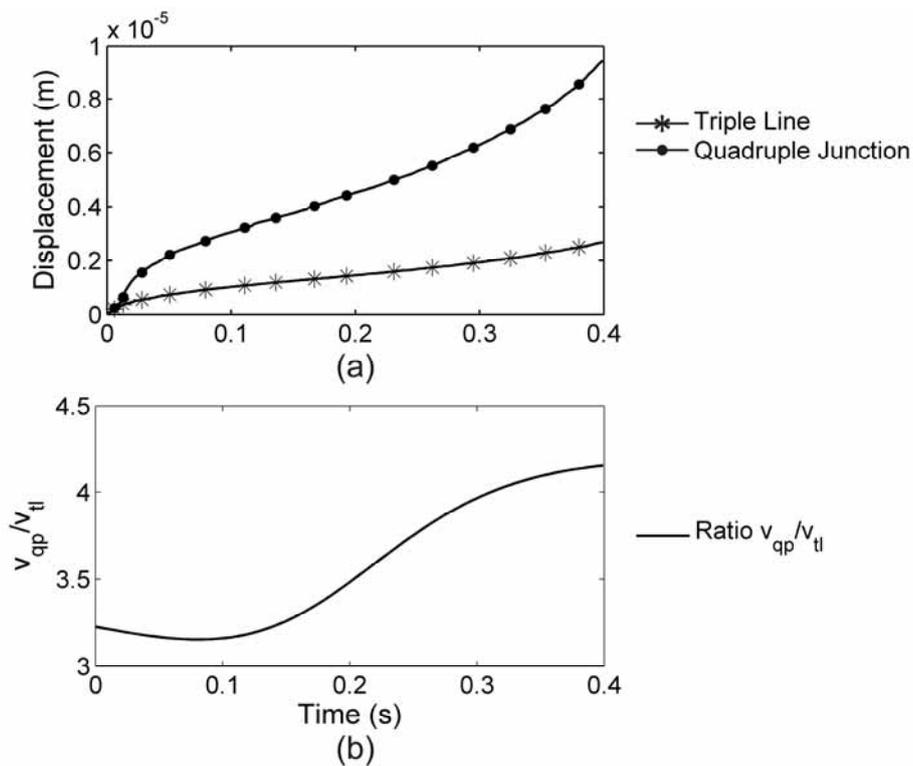


Figure 6.3. Triple line and quadruple junction displacement (a); ratio of quadruple junction to triple line velocity (b).

6.3 Steady-state Quadruple Junction Motion

The cross section of the previous configuration corresponds to a three-sided grain, which is subjected to a high shrinking rate. By contrast, for a steady-state quadruple junction motion a cross section, which neither grows nor shrinks, is needed. The von Neumann-Mullins law [65] predicts that this can only be fulfilled by a grain with a six-sided cross section. Furthermore, to make sure that the dihedral angle between adjacent boundaries remains 120° is necessary that the system consists only of regular hexagons (Fig 6.4a), i.e. the cross section plane should be filled by regular hexagons. The corresponding 3D grain assembly is an arrangement of hexagonal

prisms (Fig. 6.4b). It is noted that in the front and the back of the hexagonal prisms two more grains are connected to the system, in order to generate intergranular quadruple junctions.

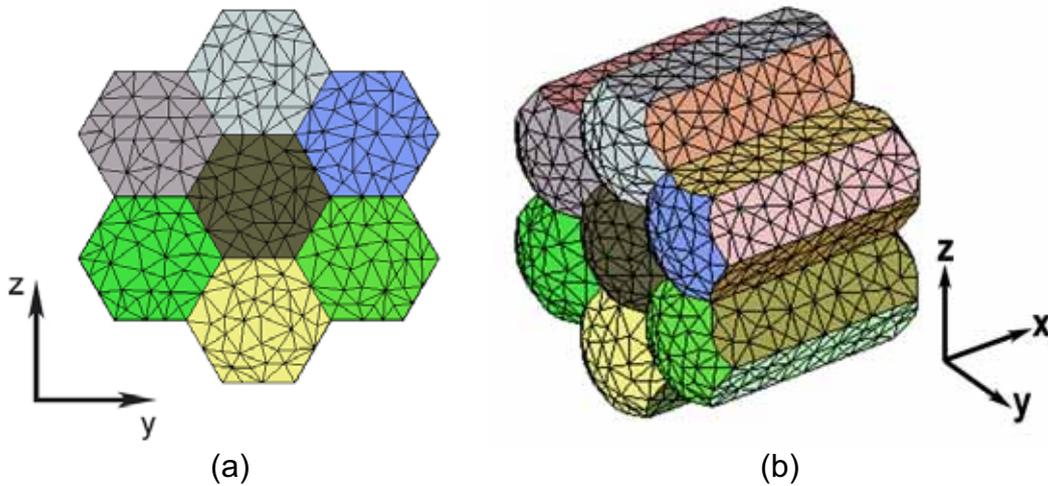


Figure 6.4. (a) Cross section of the used grain assembly, it is composed of regular hexagons and the dihedral angles are 120° . For this reason no shrinkage or growth of the cross section occurs; (b) the special grain assembly allows a steady-state motion of the quadruple points. Only the first layer of grains adjoining the central grain is shown, however, there are more hexagonal grains filling the space (plane y - z) while in the x direction, in front and in the back of the configuration, two more grains, whose shape is irrelevant, adjoin the hexagonal grains.

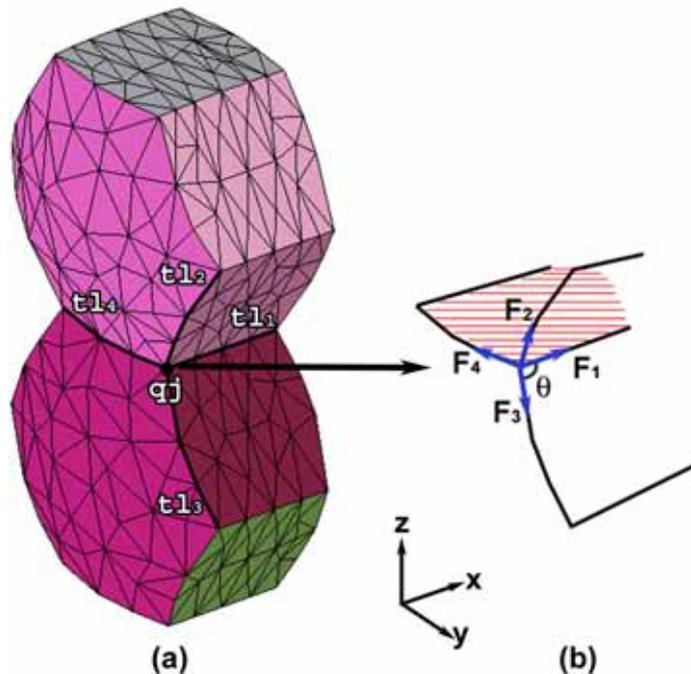


Figure 6.5. Geometry of four triple lines (tl) meeting at the quadruple junction (qj).

6.3.1 Equations of Motion

As in the configuration shown in Fig. 6.1, the motion proceeds under the action of the triple junction line tension γ^j , which can be negative or positive. Fig. 6.5a shows two grains of the configuration as well as the grain boundaries meeting at a quadruple junction. The condition for steady-state motion of the system is that the line tensions

of all triple lines at the quadruple junction have the same sign. Configurations which are formed by triple lines with line tension of different sign are possible as well, however, in such condition, configurations with steady-state motion are unlikely to exist.

From Fig. 6.5a it is possible to extract the geometry of the triple lines meeting at their point of intersection. The forces acting on the quadruple junction due to the triple junction line tensions are depicted in Fig. 6.5b. θ denotes the angle between adjacent triple lines on the same grain boundary. The force P acting on the quadruple junction can be determined from the sum over the line tension of all triple lines meeting at the quadruple junction

$$\vec{P} = \vec{F}_1 + \vec{F}_2 + \vec{F}_3 + \vec{F}_4. \quad (6.2)$$

For the used geometry the sum is reduced to the sum of the components in x -direction of the line tension. Due to the symmetry of forces at the quadruple junction the sum of forces in the y - and z -direction, respectively, are zero. Hence,

$$P = \gamma^l (1 + 3 \cos \theta). \quad (6.3)$$

Then, the velocity of the quadruple junction reads

$$v_{qp} = m_{qp} P = m_{qp} \gamma^l (1 + 3 \cos \theta). \quad (6.4)$$

The equilibrium angle at zero force on the quadruple point is easily calculated. It corresponds to the tetrahedral dihedral angle $\theta_\infty = \arccos(-1/3) \approx 109.47^\circ$.

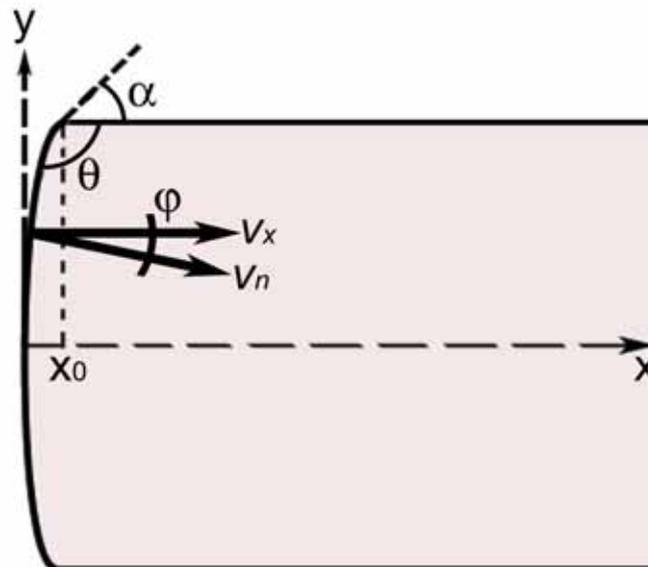


Figure 6.6. Shape of the grain boundaries and definition of the variables used for the derivation of the equation of motion.

Taking into account the shape of the grain boundaries, the problem can be comprehensively described. In Fig. 6.6 the grain boundary shaded in Fig. 6.5b is shown with a new coordinate system. The variables used for the derivation of the equation of motion are also shown.

The velocity of a moving triple line is given by

$$v_n = m_{tl} \gamma^l \kappa, \quad (6.5)$$

where

$$\kappa = -y'' [1 + (y')^2]^{-3/2}, \quad (6.6)$$

represents the curvature of the triple line. The horizontal steady-state velocity v_x of the system is related to the normal velocity v_n as follows

$$v_n = v_x \cos \varphi = v_x \frac{y'}{(1 + (y')^2)^{1/2}}. \quad (6.7)$$

Combining Eqs. (6.5), (6.6) and (6.7) yields the differential equation

$$y'' = -\frac{v_x}{m_{tl} \gamma^l} y' [1 + (y')^2], \quad (6.8)$$

which needs to be solved under the boundary conditions $y(0) = 0$, $y'(x_0) = \tan \alpha$, $y'(0) = \infty$, and $\alpha = \pi - \theta$.

The length x_0 and the angle α are clear from Fig. 6.6, $y(x)$ is the shape of the triple line obtained by integration of Eq. (6.8) and given by:

$$y(x) = -\frac{x_0}{\ln \sin \alpha} \arccos \left[e^{\left(\frac{x}{x_0} \right) \ln \sin \alpha} \right]. \quad (6.9)$$

Finally, the velocity v_x of steady-state motion of the triple line is equal to

$$v_x = -\frac{m_{tl} \gamma^l}{x_0} \ln \sin \alpha. \quad (6.10)$$

Since v_x (Eq. (6.10)) and v_{qp} (Eq. (6.4)) have to be identical, this defines the dimensionless parameter Λ_{qp} which characterizes the influence of a finite quadruple junction mobility on grain boundary migration.

$$-\frac{m_{tl} \gamma^l}{x_0} \ln \sin \alpha = m_{qp} \gamma^l [1 + 3 \cos \theta], \quad (6.11)$$

$$\frac{m_{qp} \cdot x_0}{m_{tl}} = \Lambda_{qp} = -\frac{\ln \sin \alpha}{1 + 3 \cos \theta}. \quad (6.12)$$

Substituting α by θ we obtain the final expression in terms of this angle,

$$\Lambda_{qp} = -\frac{\ln \sin(\pi - \theta)}{1 + 3 \cos \theta} = -\frac{\ln \sin \theta}{1 + 3 \cos \theta} = \frac{m_{qp} \cdot x_0}{m_{tl}} \quad (6.13)$$

If the quadruple junction is perfectly mobile, then $\Lambda_{qp} \rightarrow \infty$ and $\theta \rightarrow 109.47^\circ$, which is the equilibrium angle. In contrast, if the quadruple junction moves slowly and drags the migration of the grain boundary then $\Lambda_{qp} \rightarrow 0$ and $\theta \rightarrow \pi/2$.

6.3.2 Effect on Grain Microstructure Evolution

From Eq. (6.13) it is clear that the angle θ is completely defined by the dimensionless parameter Λ_{qp} , which, in turn, does not only depend on the triple line and quadruple junction mobilities but also on the grain size, x_0 . It is noted that the term x_0 is not the grain size itself but is directly related to it. This is relevant because it indicates that, as in the case of triple line drag, the effect of quadruple junctions increases with decreasing grain size.

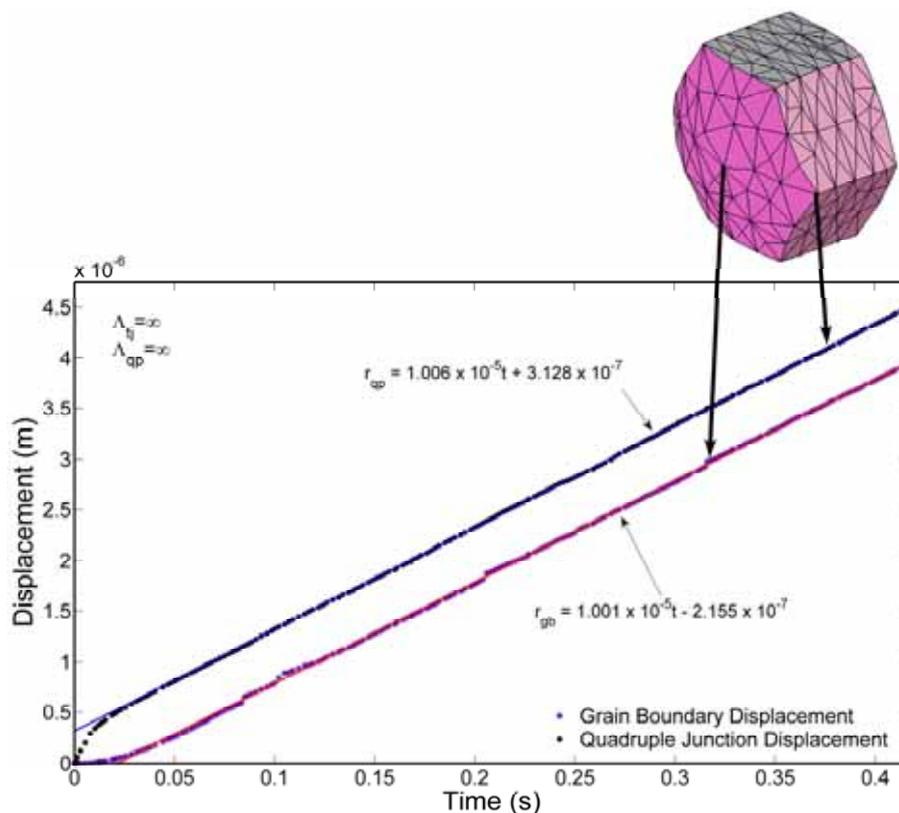


Figure 6.7. Displacement of grain boundary and quadruple junction vs. time. The triple line and quadruple junction mobilities were considered to be infinite. Both lines are practically parallel indicating a steady-state motion of the configuration. The grain indicates the points where the displacements were taken from.

In order to demonstrate that the motion of the configuration attains a steady-state motion, two simulations under extreme conditions were performed. For the first simulation triple line and quadruple junction mobilities were considered infinite. By contrast, for the second simulation an extremely low quadruple junction mobility was used ($\Lambda_{qp} = 1.2 \times 10^{-3}$).

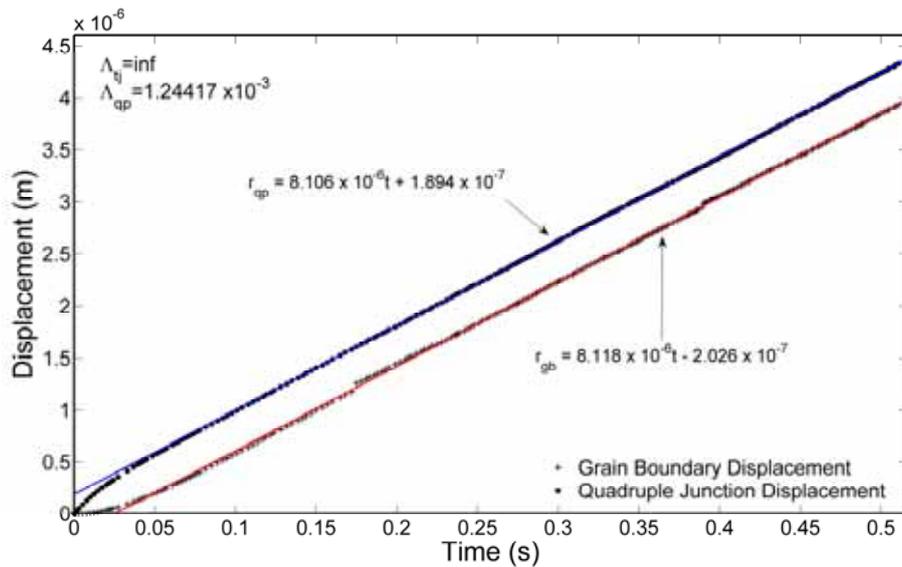


Figure 6.8. Grain Boundary and quadruple junction displacement vs. time for very low quadruple junction mobility. Steady-state motion also occurs for this condition.

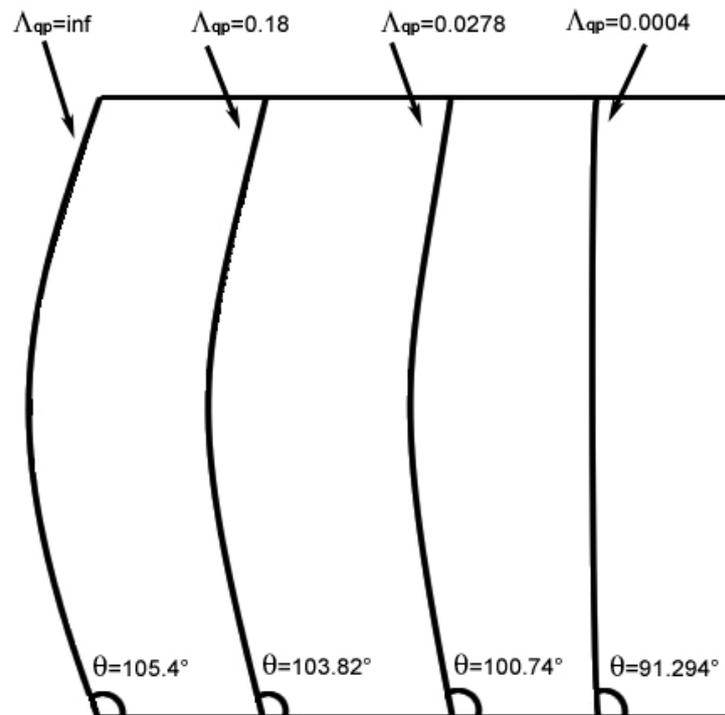


Figure 6.9. Shape of the triple lines for different values of Λ_{qp} . Minor deviations from the theoretical angles can be attributed to the discretization used in the simulations.

Figure 6.7 shows the displacements of the grain boundary and the quadruple junction as a function of time for the first case ($m_H = \infty$, $m_{qp} = \infty$). The displacement was taken directly from the simulations. Initially all the boundaries were flat; after a short time the boundaries became curved and the motion proceeded in steady-state. Minor jitters are only the artifacts of the simulations [122]. The displacement of both considered elements is linear with time, the velocities of grain boundary and the quadruple junction are practically the same, i.e. both lines have the same slope.

As expected, the motion also proceeds in steady-state when Λ_{qp} is very low, as shown in Fig. 6.8. The displacement is also linear in time, and both velocities are almost equal. Evidently the proposed grain configuration also attains a steady-state behavior in the course of time.

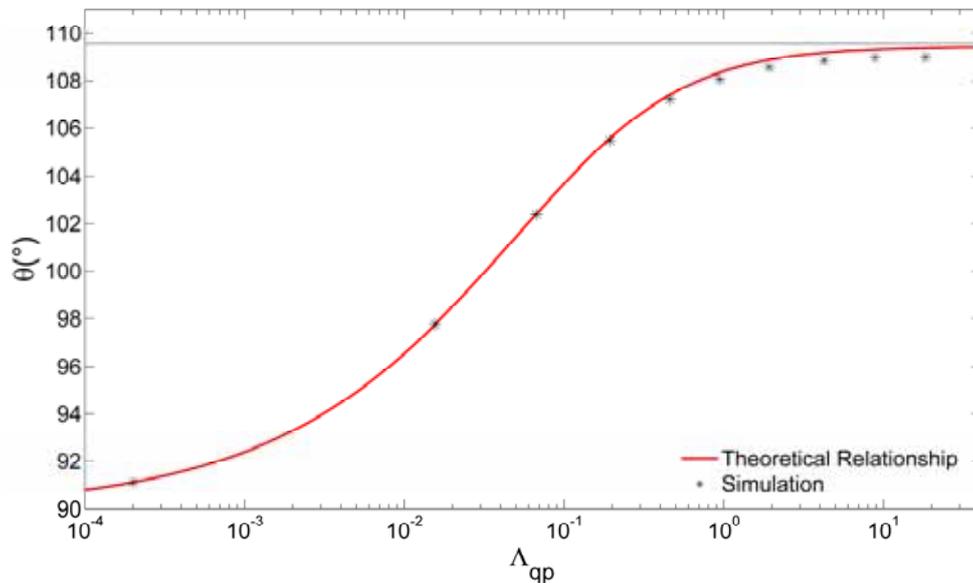


Figure 6.10. Comparison of the function θ vs. Λ_{qp} and simulation results.

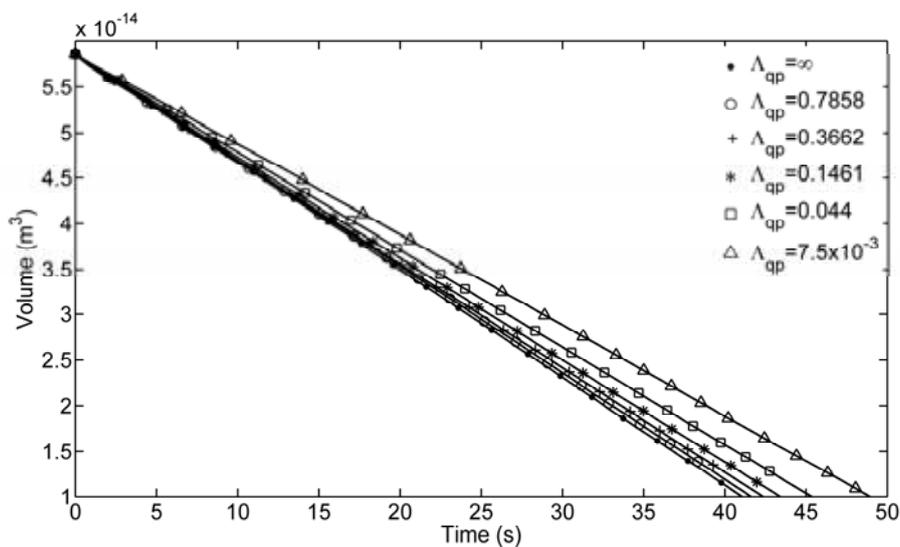


Figure 6.11. Grain volume vs. time for different Λ_{qp} .

One effect of a finite quadruple junction mobility can be seen in the shape of the grain boundary. The triple lines delimiting the boundary become flat as a result of the decrease of Λ_{qp} (Fig. 6.9). Eq. (6.13) predicts that the effect of Λ_{qp} is reflected by a change of the angle θ , however this also impacts the curvature of the triple lines and hence, the shape of the grain boundary. The geometry of the triple lines in figure 6.9 was taken directly from the simulations. The steady-state angles obtained from the simulations agree very well with the theoretical curve (Eq. (6.13)), as shown in Fig. 6.10.

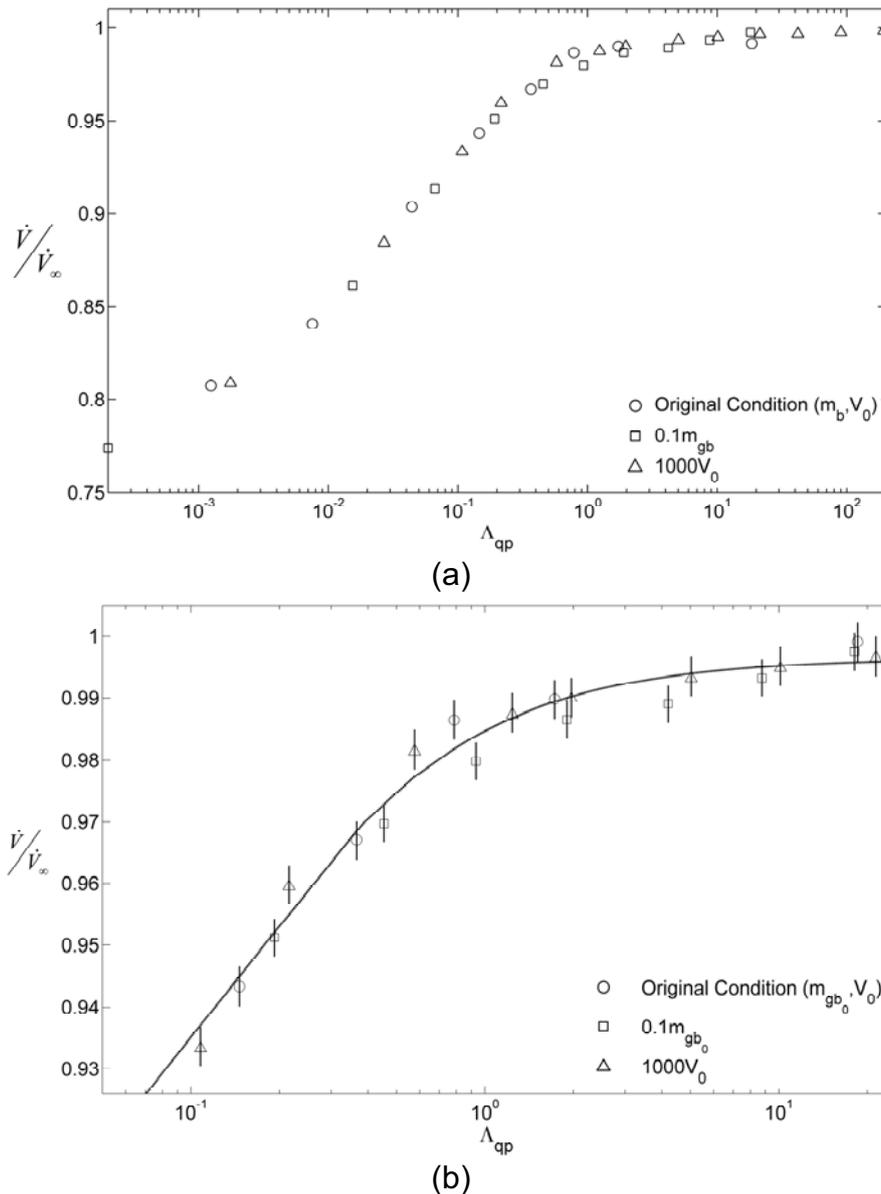


Figure 6.12. Relative volume change rate as a function of Λ_{qp} . Three different conditions are shown: (o) original condition; (\square) grain boundary mobility reduced by a factor 10, and (Δ) the grain volume increased by a factor 1000; (b) magnification of Fig. 12a for low and medium values of Λ_{qp} .

Qualitatively, a finite quadruple junction mobility can modify the geometry of the evolving configuration. However, for a quantitative description it is necessary to evaluate the grain size evolution as a function of Λ_{qp} . In Fig. 6.11, the grain volume as a function of time is shown for different values of Λ_{qp} . A small but evident retardation of the kinetics can be observed with decreasing Λ_{qp} . This becomes more obvious in Fig. 6.12, where the relative volume change rate $\left(\frac{\dot{V}}{\dot{V}_\infty}\right)$ is plotted (\dot{V}_∞ is the volume change rate when $\Lambda \rightarrow \infty$). Apparently, $\left(\frac{\dot{V}}{\dot{V}_\infty}\right) \rightarrow 1$ when $\Lambda_{qp} \rightarrow \infty$. By contrast, when $\Lambda_{qp} \rightarrow 0$, $\left(\frac{\dot{V}}{\dot{V}_\infty}\right)$ approaches zero. This behavior is expected because the volume change rate is indirectly a function of θ , Λ_{qp} , or $\dot{V} = f(v_{qp}) = f(\theta(\Lambda_{qp}))$.

Fig. 6.12 demonstrates the scaling behaviour of the model. Three simulations with very different simulation parameters are compared. The first simulation assumed a certain value of m_{b0} and V_0 . In a second simulation the grain boundary mobility was one order of magnitude lower than m_{b0} , whereas the third simulation assumed a volume 1000 times larger than V_0 . No significant differences in the relative volume change rate among the three conditions are found. Fig. 6.12b shows the same graph but restricted to the low and intermediate range of Λ_{qp} , for a more accurate comparison. The small variations of the different simulations are below the uncertainty range.

6.4 Effect of a Finite Triple Line Mobility on the Evolution of the 3D Grain Assembly

Due to the small size and the low frequency of quadruple junctions, it is expected that their effect on grain growth should be smaller in comparison, for example, to triple lines, which occupy a much larger volume and occur more frequently. In this section the effect of triple lines on the kinetics of the same 3D configuration will be briefly analyzed.

In figure 6.13, the grain volume as a function of annealing time is presented. Here m_{qp} was considered infinite, while m_{tl} was varied to achieve different regimes of Λ_{tl} . The retardation of the kinetics by a finite m_{tl} is evident. It can be observed that in the large and intermediate ranges ($\Lambda_{tl}=[\infty, \sim 1]$) the volume decreases linearly with time. This means that the motion of the grain boundary network occurs under steady-state conditions.

However, for values of $\Lambda_{tl} \ll 1$ the linearity is lost. Under such conditions the kinetics become triple line dominated, because the original curved grain boundaries become flat and the dihedral angles at triple lines deviate from the equilibrium angle (120°). At first glance, the effect of triple lines is more pronounced than the effect of quadruple junctions.

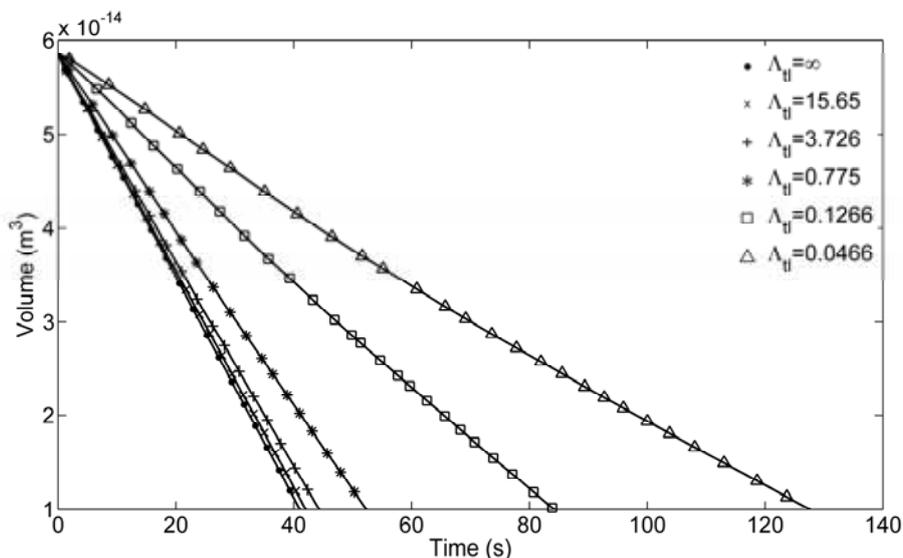


Figure 6.13. Grain volume as a function of time for different values of Λ_{tl} .

6.4.1 Effect on Grain Microstructure Evolution

The comparison between triple line and quadruple junction kinetics serves to better understand the phenomenology of grain growth, especially in nanocrystalline materials. However, for the considered grain arrangement such comparison has to be restricted to the regime of large and intermediates values of Λ_{tl} , because as shown in Fig. 6.13, for low values of Λ_{tl} , the system does not show steady-state motion. Thus, in the following we assume $\Lambda_{tl}, \Lambda_{qp} > 5$.

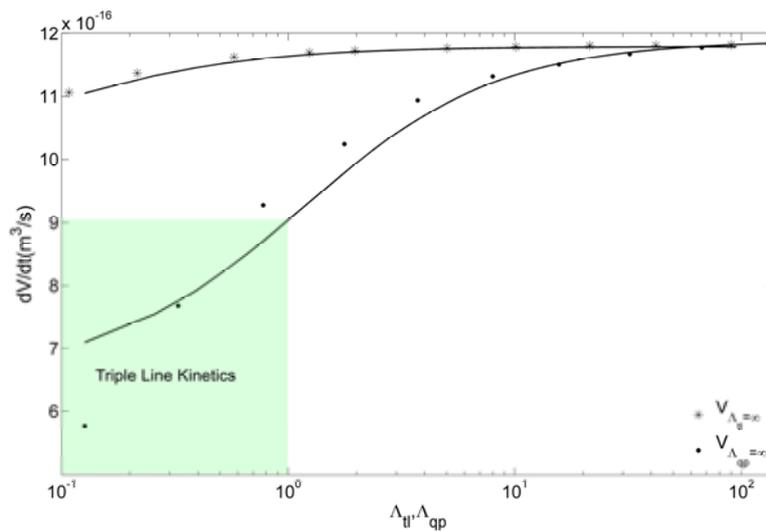


Figure 6.14. Volume change rate, for (*) Λ_{qp} is varied while Λ_{tl} is held infinite and for (•) Λ_{tl} is varied whereas Λ_{qp} is held infinite.

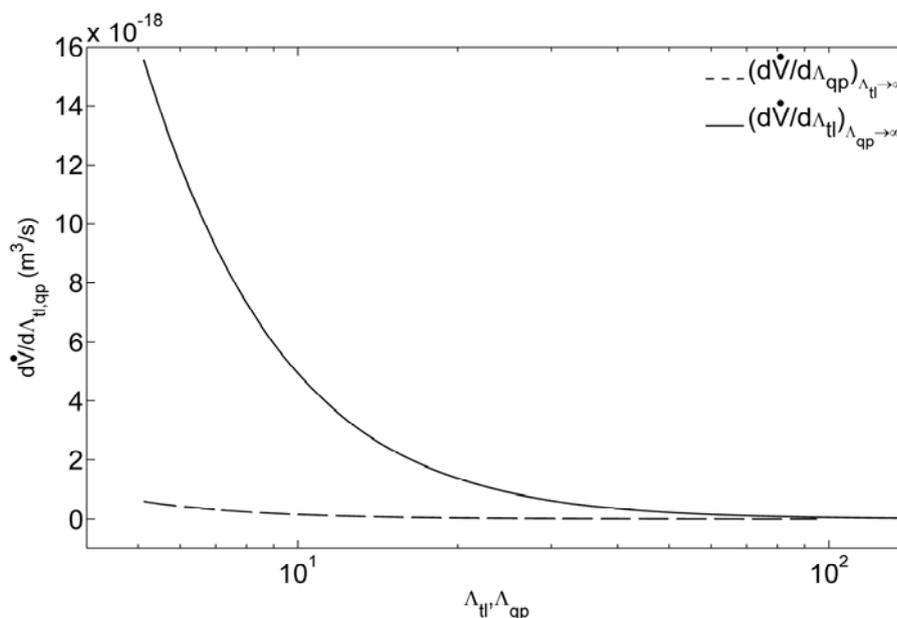


Figure 6.15. The rate $\frac{d\dot{V}}{d\Lambda_i}$ ($i=tl,qp$) as a function of Λ_i .

The volume change rate as a function of triple line and quadruple junction mobility (Fig. 6.14) suggests that for $\Lambda_{tl}, \Lambda_{qp} > 100$ the drag effect is practically constant. However, for the intermediate regime ($5 < \Lambda_{tl}, \Lambda_{qp} < 100$) the triple lines seem to drag

boundary motion more effectively than quadruple junctions as reflected by a much lower volume change rate for $\Lambda_{tl} = \Lambda_{qp}$.

For intermediate values of Λ_{tl} , Λ_{qp} the differences in $\dot{V}(\Lambda)$ are markedly pronounced, because $\dot{V}(\Lambda)$ is more sensible to a change of Λ_{tl} than of Λ_{qp} . The derivatives of the volume change rate with respect to Λ_{tl} and Λ_{qp} reveal that $(d\dot{V}/d\Lambda_{tl})_{\Lambda_{qp} \rightarrow \infty}$ increases faster with decreasing Λ_{tl} than $(d\dot{V}/d\Lambda_{qp})_{\Lambda_{tl} \rightarrow \infty}$ with decreasing Λ_{qp} (Fig. 6.15). In essence, triple lines drag grain boundary motion more effectively than quadruple junctions contrary to predictions of other authors [123].

6.5 Comparison with Theoretical Predictions

6.5.1 Analytical Description of the Volume Rate of Change

The von Neumann-Mullins relation gives a general and physically transparent description of the growth of a definite grain in a polycrystal. The main advantage of this relation is its precise topological nature: a grain with topological class $n > 6$ will grow while grains with $n < 6$ will shrink. All attempts to derive a 3D analogue [124-126] were successful only to a certain extent.

Recently, MacPherson and Srolovitz [127] introduced the n -dimensional equivalent to the von Neumann-Mullins law. The MacPherson-Srolovitz relation (Eq. (14)) considers two terms, the mean width $L(D)$ of a given domain D (grain) and the length of the edges $e(D)$ (triple lines) of the same domain.

$$\frac{dV}{dt} = -2\pi m_{gb} \gamma \left(L(D) - \frac{1}{6} e(D) \right), \quad (6.14)$$

where m_{gb} is the grain boundary mobility and γ is the grain boundary energy. $L(D)$ and $e(D)$ are defined as follows

$$L(D) = \frac{1}{2\pi} \sum_i^n \beta_i e_i, \quad (6.15)$$

$$e(D) = \sum_i^n e_i'' . \quad (6.16)$$

The term $e(D)$ is simply the length of the triple lines of a given grain, whereas the term $L(D)$ reflects the local variation of the surface with respect to a fixed reference. The normal to each element dS of the surface characterizes its spatial orientation, which may be different from the orientation of other elements surrounding dS . Its difference to an adjacent element across a junction of length e_i is denoted by the angle β , also known as the turning angle. In particular the orientation difference β across a triple line corresponds to the external dihedral angle as established by the

surface tensions of the adjoining grain boundaries. Another interesting feature of this term is that it introduces implicitly the curvature of the surface.

6.5.2 Comparison of the Simulation Results with the MacPherson-Srolovitz Equation

The special configuration which was introduced in section 6.3 of this chapter makes it possible to determine analytically all the terms of Eq. (6.14). In Fig. 6.16, one grain of the configuration is shown. Two new variables, a and d , define the dimensions of the grain; d is the length of the longitudinal triple lines while a is the length of the triple lines of the hexagonal cross section. The curvature of the triple line is included in a .

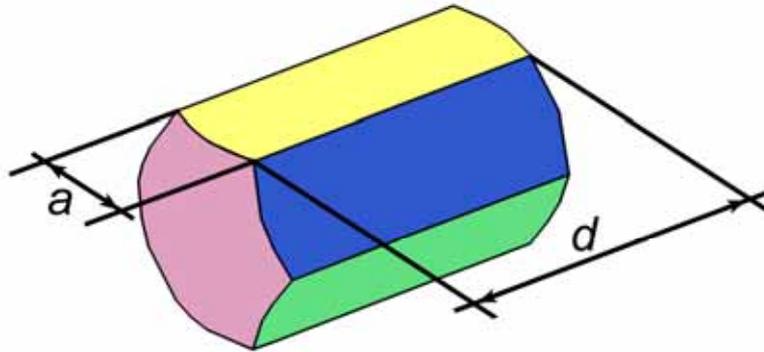


Figure 6.16. One grain of the special grain assembly and the dimensions a and d .

The term $e(D)$ for this grain reads

$$e(D) = \sum_i^n e_i'' = 6d + 12a, \quad (6.17)$$

and the term $L(D)$ is given by

$$L(D) = \frac{1}{2\pi} \sum_i^n \beta_i e_i = \frac{1}{2\pi} \left(2L_k + \frac{1}{3} \pi \cdot 6d + \frac{1}{3} \pi \cdot 12a \right) = \frac{L_k}{\pi} + d + a, \quad (6.18)$$

where L_k is the unknown mean width of the two curved faces of the grain. Because all other grain boundaries are flat, $\beta = 0$ and thus, their surface does not contribute to the mean width.

Combining Eqs. (6.17) and (6.18) with Eq. (6.14) the volume change rate can be determined

$$\frac{dV}{dt} = -2\pi m_{gb} \gamma \left(\frac{L_k}{\pi} + d + 2a - d - 2a \right) = -2m_{gb} \gamma L_k. \quad (6.19)$$

The volume change rate for the considered configuration depends exclusively on the term L_k which represent the only curved grain boundaries in the configuration. Since the configuration moves in steady-state, $\dot{V} = \text{const}$. This prediction was examined by

computer simulations. The 3D-vertex simulations rendered independently the parameters needed for the MacPherson-Srolovitz relation [127] and \dot{V} .

Figure 6.17 shows the calculated parameters $L(D)$ and $e(D)$ taken directly from the geometry of the considered grain. If the grain evolves in steady-state the curves $L(D,t)$ and $e(D,t)$ have to be parallel to yield $\dot{V} = \text{const.}$ in Eq. (6.14). According to Fig. 6.17 this condition is evidently fulfilled. Also, the value of the volume change rate calculated according to Eq. (6.14) agrees perfectly with the simulation results (Fig. 6.18).

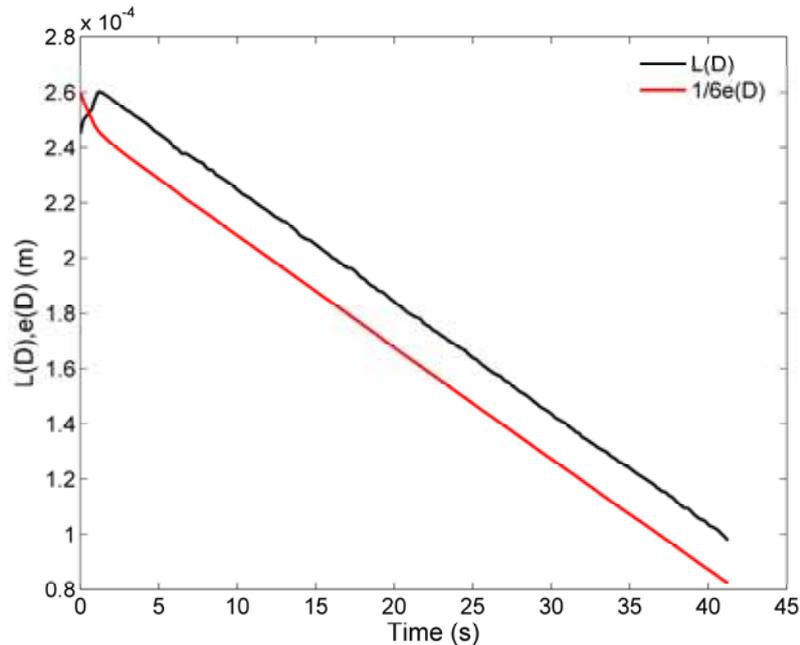


Figure 6.17. The temporal evolution of the parameters $L(D)$ and $e(D)$.

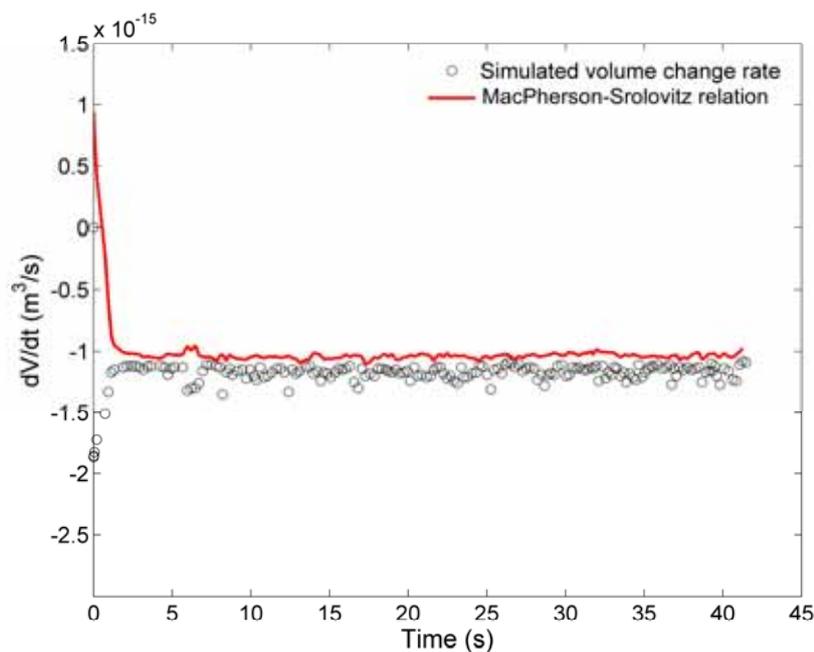


Figure 6.18. Comparison of dV/dt as obtained from simulations and calculated using Eq. (6.14).

The observed small deviation is attributed to the calculation of the parameter $L(D)$ which is very sensitive to the size of the mesh.

Another important question is whether the MacPherson-Srolovitz relation holds for the general case when the driving force is not constant (i.e. the curvature depends on time). We can use the configuration shown in Fig. 6.2 to investigate the problem. As demonstrated in sec. 6.2.1., this configuration does not evolve in steady-state. Correspondingly, the volume does not change linearly with time i.e. \dot{V} is not constant (Fig. 6.19).

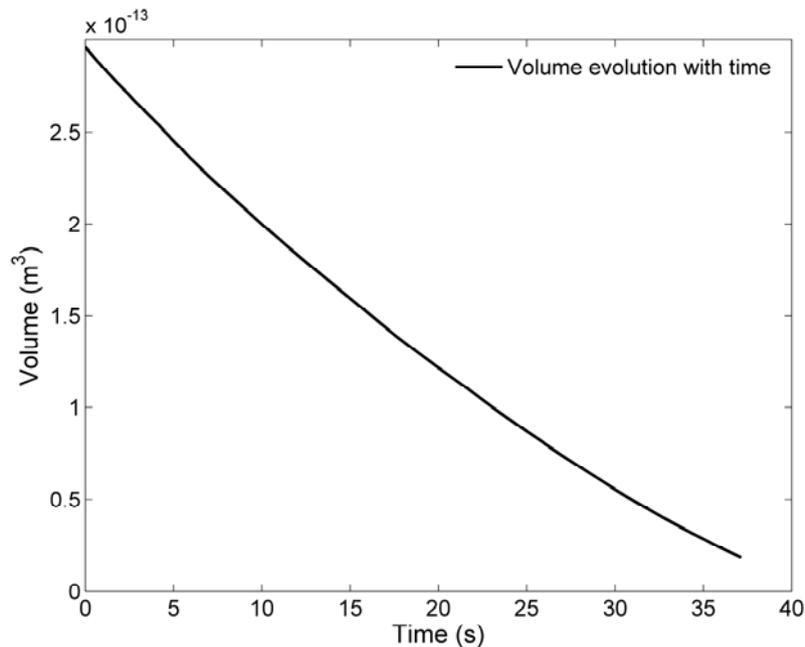


Figure 6.19. Simulated temporal evolution of the grain in Fig. 6.1.

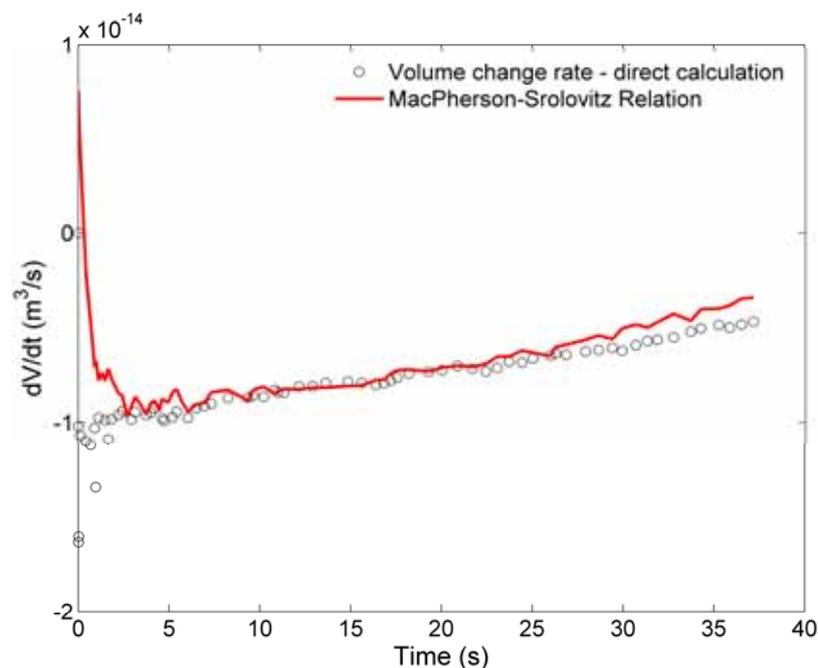


Figure 6.20. Comparison of theoretical predictions (Eq. (6.14)) and simulation results.

According to Fig. 6.20, the predictions of Eq. (6.14) agree very well with the volume change rate calculated from the data of Fig. 6.19. For long times, simulations and theory seem to diverge. However, this is caused by the decreasing number of triangular facets in the simulation as the grain shrinks which increases the error in the calculation of $L(D)$.

6.5.3 The Effect of a Finite Quadruple Junction Mobility on the MacPherson-Srolovitz Equation

One major effect of a finite quadruple junction mobility is a change of the curvature of the triple lines, which implicitly alters also the length of the triple lines. The total length of the triple lines $e(D)$ for the configuration shown in Fig. 6.16 is given by the sum of all triple line lengths a and d . If the horizontal triple lines are straight, the calculation of d is very simple, however, the determination of the length a becomes problematic because the triple lines of the hexagonal cross section are now curved. Nevertheless, Eq. (6.9) describes the shape of the triple line and can be used to calculate the triple line length. The length of any two-dimensional curve is given by

$$l = \int_{s1}^{s2} \sqrt{1 + \left(\frac{dy}{dx}\right)^2} dx. \quad (6.20)$$

Applied to Eq. (6.9) we obtain

$$l = \int_0^{x_0} \sqrt{1 + \frac{e^{2x/c}}{1 - e^{2x/c}}} dx = \int_0^{x_0} \frac{dx}{\sqrt{1 - e^{2x/c}}}, \quad (6.21)$$

where $c = x_0 / \ln \sin \alpha$. Integration leads to

$$l = \frac{x_0}{\ln \sin \alpha} \operatorname{arcsech} \sin \alpha = \frac{x_0}{\ln \sin \theta} \ln \left(\frac{1 + \sqrt{1 - \sin^2 \theta}}{\sin \theta} \right). \quad (6.22)$$

Accordingly, the length of the triple lines of the hexagonal cross section can be easily calculated as

$$a = 2l = \frac{2x_0}{\ln \sin \theta} \ln \left(\frac{1 + \cos \theta}{\sin \theta} \right). \quad (6.23)$$

By series expansion of Eq. (6.13) we find the angle θ as a function of Λ_{qp}

$$\theta = \frac{2\Lambda_{qp}}{3\Lambda_{qp} + \sqrt{\Lambda_{qp}(9\Lambda_{qp} + 2)}} + \frac{\pi}{2}. \quad (6.24)$$

While the length a strongly depends on Λ_{qp} , the term d does not, at least not directly. Actually d changes linearly with time

$$d = d_0 - 2v_{gb}t, \quad (6.25)$$

where d_0 is the length of the longitudinal triple line at $t=0$, v_{gb} is the velocity of the front and rear faces of the grain. This velocity depends naturally on Λ_{qp} but remains constant for $\Lambda_{qp}=\text{const}$. From the simulation it is possible to extract the dependency of the parameter a on Λ_{qp} and to test the validity of the derived equations. For this, the length a/x_0 from the simulations is compared with Eq. (6.23) (Fig. 6.21).

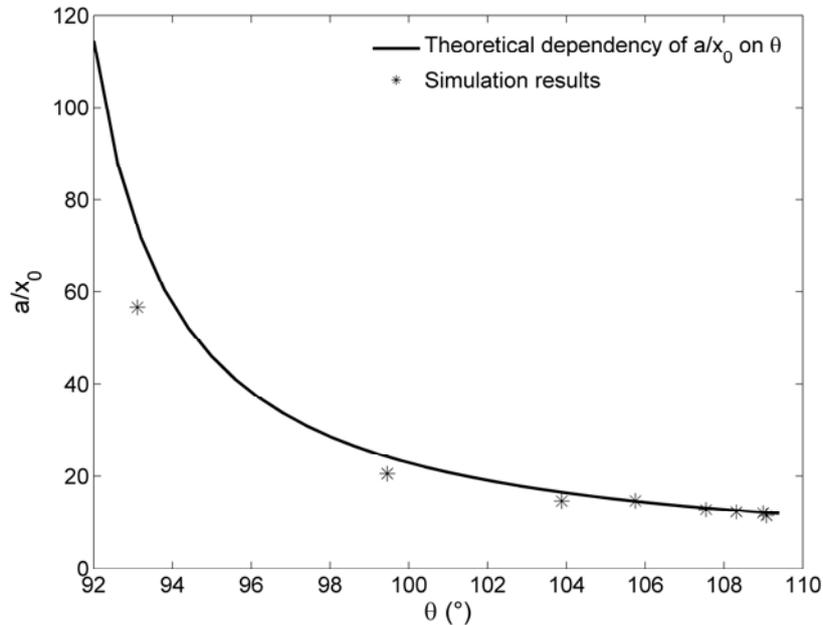


Figure 6.21. Dependency of the triple line length on the angle θ .

The triple line length as a function of Λ_{qp} is given in Fig. 6.22. Both dependencies of a/x_0 on θ and Λ_{qp} , confirm good agreement of the theoretical predictions and the simulation results.

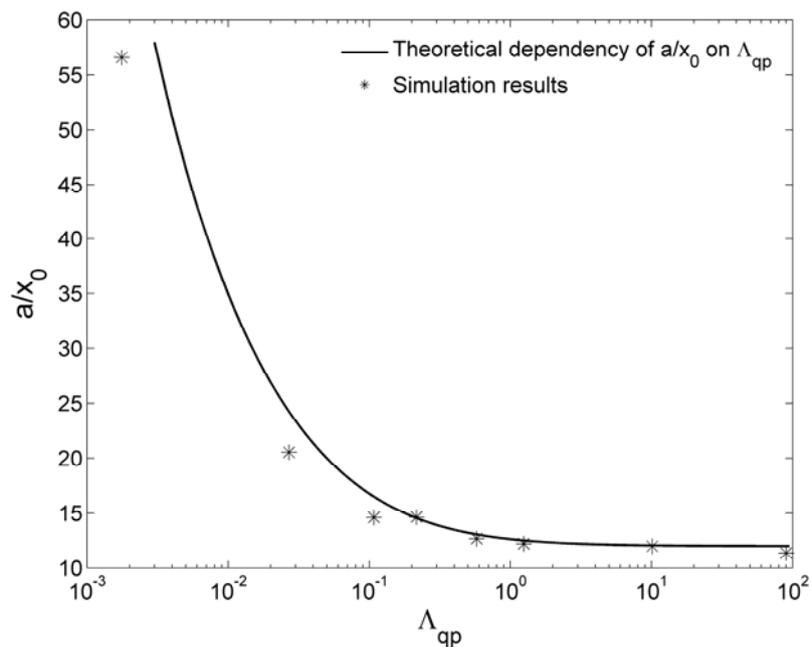


Figure 6.22. Dependency of a on Λ_{qp} .

It would be also desirable to know analytically the dependency of $L(D)$ on θ and Λ_{qp} . However, for the solution of this problem the velocity of the grain boundary needs to be related to the velocity of the triple lines. This introduces the ratio of grain boundary and triple line energies which is so far unknown.

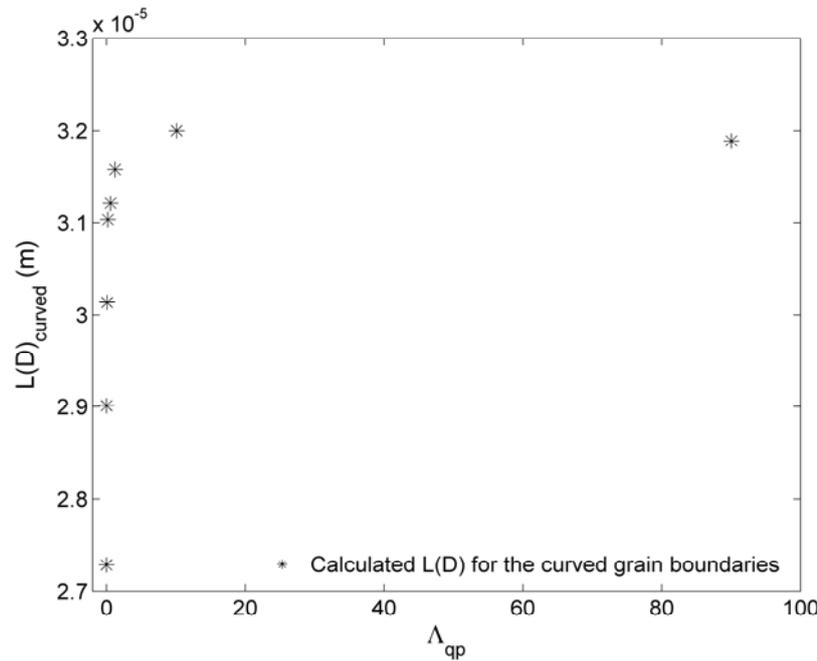


Figure 6.23. Dependency of $L(D)$ on Λ_{qp} for the curved grain boundaries of the special grain assembly shown in Fig. 6.5.

Nevertheless, from the simulations this dependency can be extracted. According to the definition of $L(D)$ the flat grain boundaries do not contribute to this term. Moreover, the turning angle of the longitudinal triple lines does not depend on Λ_{qp} . Only the curved grain boundaries and the turning angle of the triple lines at the cross section vary with changing Λ_{qp} . In Fig 6.23, $L(D)$ for the curved grain boundaries is shown as a function of Λ_{qp} . $L(D)$ increases rapidly for small $\Lambda_{qp} < 1$. In the intermediate range ($1 < \Lambda_{qp} < 20$) a transition occurs to a constant value of $L(D)$, which correspond to the curvature of the grain boundary at zero drag force.

Since the parameters $L(D)$ and $e(D)$ are affected by a finite quadruple junction mobility, it can be expected that a modified MacPherson-Srolovitz relation exists that takes the additional parameter Λ_{qp} into account like recently shown for the modification of the von Neumann-Mullins relation for a limited triple junction mobility in 2D grain growth [94,128]. Since both $L(D)$ and $e(D)$ are expected to depend on the junction mobility, a generalized MacPherson-Srolovitz relation will be of the form:

$$\frac{dV}{dt} = f(L(\Lambda_{qp}, \Lambda_{tl}), e(\Lambda_{qp}, \Lambda_{tl})). \quad (6.26)$$

Chapter 7

Summary

The objective of the present dissertation was to contribute in the elucidation of the phenomenon known as grain growth. Grain growth takes place after the completion of recrystallization in a polycrystal free of dislocations. The driving force for the grain boundary migration is the reduction of the free energy of the polycrystal through the reduction of the total grain boundary surface. Since decisive properties of the grain boundaries depend on the eight parameters that describe them, grain growth results in a very complex process, as well.

Due to the complexity of the phenomenon, complete theoretical abstraction is not possible. In order to overcome this problem, diverse simulation models have been developed with the purpose to study grain growth under controlled conditions. For this task, cellular automata, phase-field, Monte Carlo mode, Vertex models, etc. have been used. Among them, the Vertex model stands out for the clarity of the physics underlying the model.

The principal feature of the Vertex model is the kind of discretization that is used. The vertex model in its two dimensional variant uses points along the grain boundary and straight line segments between them to represent a continuous boundary. The triple junction is considered also as an individual discretizing element. Grain microstructure evolution occurs as result of the collective motion of the individual grain boundaries and triple junctions and their interaction. The velocity of the boundary is calculated at each discretizing point of the boundary from the local curvature and the intrinsic properties of the grain boundary (mobility and energy). The motion of the triple junction occurs under the action of the forces exerted by the adjoining grain boundaries at the junction.

The principal disadvantage of the model is the high level of programming skills required for its implementation. Since the model consists of a net of connected points, the topological transformations that take place during grain growth need to be handled by the program through the reconnection of the net. Despite the difficulty of its implementation, the model delivers remarkable results. The model has been compared with classical theories on grain growth and showed less than 1% deviation from the von Neumann-Mullins relation, and yielded a scaling behavior, which is characterized by parabolic kinetics, where the mean grain size increases with $t^{1/2}$, and by the invariability of the grain size distribution with time.

Additionally, the model has been successfully used for the simulation of grain growth under the effect of an extraneous driving force. As grain growth is product of the migration of the grain boundaries, the boundary area is the main driving force but not the only that can be exerted simultaneously. In fact, a gradient of any intensive

thermodynamic variable leads to a driving force. A magnetic field, for instance, causes an energetic gradient due to the magnetic anisotropy of hexagonal materials. In these materials, a driving force for the boundary migration appears when a difference in magnetic induced energy of both crystals along the grain boundary exists. Experimental observations in pure titanium demonstrated that the application of a magnetic field in a sample with an initial butterfly texture affect the evolution of the texture and grain growth kinetics, as well. The experimental investigation showed that the growth of one component of the texture was promoted whereas the growth of the other component was disadvantageous. However, due to the experimental setup, it was not possible to determine whether the affectation occurred during recrystallization or grain growth. The Vertex model effectively demonstrated that the magnetic field affects the texture evolution during grain growth, since it exerts an additional driving force to the grain boundaries of grains with a low magnetic energy promoting their growth. Further simulations in samples with randomly oriented grains showed that the magnetic field is capable to promote the growing or shrinking of desired or undesired components.

Besides grain boundaries, other structural elements can influence grain microstructure evolution, namely triple junctions. A triple junction is the point where three two-dimensional grain boundaries meet. Triple junctions have been proved to have a finite mobility and thus to affect grain boundary migration in connected systems, since the kinetics of the system depends on the velocity of the slowest element. The Vertex model was used to cross-validate theoretical considerations of the effect of a finite triple junction mobility in simple geometries of connected grain boundaries with triple junctions. In all cases, the Vertex model reproduced very well the theoretical expectations validating both the simulation model and the theory.

Simulation of simple geometries led to relevant results. The simulation of simple grain boundary migration requires straightforward setups. Simulation has the additional advantage that by this mean the preparation of an adequate sample is avoided. Probably, the main advantage of the utilization of simulation methods is that the effect of diverse variables can be studied separately under controlled conditions. For example, the effect of the anisotropy of the energy with respect of the inclination of the grain boundary was successfully studied by means of computer simulations. The simulations were performed with two different simulation techniques, molecular-static and Vertex model simulations and additionally corroborated by experimental observations in aluminum. This example is remarkable because linked microscopic and mesoscopic models.

The Vertex model is a notable model, but the complexity of the programming and implementation in 3D spaces is notably high, since the topological transformations that must be implemented, become more complex, as well as, the reconnection of the topological net after such events.

Simulation with the Vertex model in 3D space requires four stages. The first is the generation of the configuration to be simulated. This stage is achieved by diverse means; it can be obtain by the reconstruction of experimental samples by serial sectioning or by the utilization of mathematical techniques for the construction of spatial tessellations. The second stage involves the discretization of the grain boundaries. The third stage is the formulation of the equations of motion of the discretizing elements and finally the fourth involves the implementation of the

topological transformation and reconnection of the net. The last stage is the most difficult to accomplish.

The 3D Vertex model was used for the simulation of a special three-dimensional assembly, which permitted the study of the finite mobility of quadruple junctions. In analogy with triple junctions, quadruple junctions are the structural elements of a polycrystal where four grains meet. A special configuration, which permits the steady-state motion, was proposed. The simulations of this configuration showed that quadruple junctions can drag the grain boundary migration. However, simulation on the same configuration with a finite triple line mobility showed that triple lines drag more effectively grain growth than triple junctions. Finally, the simulations were compared to the MacPherson-Srolovitz relation that describes the volume change of rate of grains as a function of their metrics and topology. The results showed a very good agreement.

Abstract

Grain growth is the result of the collective migration of the grain boundaries of a polycrystal. Since grain boundaries are very complex elements, grain growth is complex as well. The mathematical description of the grain boundary requires four parameters in the two-dimensional case and eight parameters in the three-dimensional one. The evolution of the microstructure in the course of grain growth is determined by the grain boundary mobility and energy; both properties depend on all the parameters for the definition of the grain boundary. Since triple lines, quadruple points and chemical composition play an important role, grain boundary becomes even more complex.

The modeling of the grain growth requires the consideration of all the factors that affect grain growth. In the present dissertation, a Vertex Model for the simulation of two- and three-dimensional grain growth is implemented. The two-dimensional model was corroborated with classic basic theories on grain growth. Simulation on normal grain growth showed scaling behavior and a deviation of less than 1% when compared with the von Neumann-Mullins relationship. Furthermore, the model validated the theory on the finite mobility of the triple junctions from Gottstein and Shvindlerman and with this the model showed its applicability for the simulation of more complex granular aggregates with a finite triple junction mobility. The model also allows the use of experimental data. For instance, it was utilized for the reproduction of an experimental setting of magnetic influenced grain growth in pure titanium samples. The results of the simulation demonstrated that a magnetic field can determine the texture and grain growth kinetics of magnetic anisotropic metals.

Simulation can also help to understand unexpected experimental results. For example, it was explained by means of molecular static and vertex model simulation the faceting of certain grain boundaries in aluminum. For this purpose, the grain boundary energy was obtained from molecular-static simulation and subsequently used in Vertex simulation. The results showed that the faceting of the grain boundaries can be attributed to the anisotropy of the grain boundary energy with the inclination angle.

In turn, the 3D model was utilized to study the effect of the boundary junctions on three-dimensional grain growth. For this purpose a special configuration that allows the steady-state motion of the grain boundaries was used. The simulation results showed a very good agreement with the theoretical expectations and demonstrated that the finite mobility of the quadruple junctions can drag grain boundary migration. However, it was also found that triple lines drag more effectively grain growth.

Zusammenfassung

Kornwachstum ist das Resultat von der gemeinsamen Wanderung der Korngrenzen eines Vielkristalls. Dieses Phänomen ist sehr komplex, da die Korngrenzen selbst sehr komplizierte Elemente sind. Schon im zweidimensionalen Fall benötigt man vier Parameter zu ihrer geometrischen Definition, während in 3D acht Parameter zur Festlegung der Korngrenze notwendig sind. Die Entwicklung eines Gefüges während Kornwachstum wird durch die Korngrenzenmobilität und –energie bestimmt, wobei beide Korngreneigenschaften von allen Parametern zur Definition der Korngrenzen abhängen. Da Tripellinien und Quadrupelpunkte sowie ggf. die Zusammensetzung zusätzlich eine sehr wichtige Rolle spielen können, ist das Kornwachstum noch komplexer.

Die Kornwachstumsmodellierung benötigt die Betrachtung von allen Faktoren, die das Kornwachstum beeinflussen. In vorliegender Dissertation wurden ein zwei- und ein dreidimensionales Vertex Modell implementiert, das die Betrachtung all dieser Faktoren ermöglicht. Das zweidimensionale Modell wurde mit klassischen grundlegenden Theorien des Kornwachstums vollständig validiert. Die Simulation bestätigt das zeitliche Skalierungsverhalten und die von Neumann-Mullins Relation mit einer Abweichung von weniger als 1%. Weiterhin beweist das Modell die Theorie von Gottstein und Shvindlerman zur Auswirkung einer endlichen Beweglichkeit der Tripellinien. Da das Modell auch die Anwendung experimenteller Daten erlaubt, wurde es benutzt, um Experimente des magnetisch beeinflussten Kornwachstums in reinem Titan in Computersimulationen zu reproduzieren. Die Ergebnisse dieser Simulationen zeigen, dass ein Magnetfeld die Textur und die Kinetik des Kornwachstums in magnetisch anisotropen Metallen beeinflussen kann.

Simulationen können auch helfen, um experimentelle unerwartete Beobachtungen zu verstehen. Zum Beispiel wurde mithilfe der Vertex und Molekularstatik-Simulationen die Facettierung der gewissen Korngrenzen in Aluminium erklärt. Zu diesem Zweck wurde die Korngrenzenenergie aus Molekularstatik-Simulationen berechnet und im Vertex Modell für Skalen-übergreifende Simulationen verwendet. Die Ergebnisse zeigen, dass die Facettierung auf die Anisotropie der Korngrenzenenergie mit der Korngrenzenlage zurückgeführt werden kann.

Des Weiteren wurde das neu entwickelte dreidimensionale Vertex Modell zur Untersuchung des Einflusses von Tripellinien und Quadrupelpunkten auf die Korngrenzenwanderung benutzt. Zu diesem Zweck wurde eine spezielle Konfiguration vorgeschlagen und getestet, die die stationäre Bewegung der Korngrenzen erlaubt. Die Ergebnisse der Simulationen zeigen, dass Quadrupelpunkte die Korngrenzenwanderung und daher Kornwachstum hemmen können. Gleichwohl zeigen die Resultate auch, dass Tripellinien einen viel stärkeren Einfluss auf das Wachstum haben. Dreidimensionale Simulation bestätigten auch die MacPherson-Srolovitz Relation, die die Wachstumsrate einzelner Körner in Abhängigkeit geometrischer Merkmale der Körner beschreibt.

References

- [1] P. Haasen: Physikalische Metallkunde (1974), Chapter 3., 1. Edition, Springer.
- [2] G. Gottstein: Physikalische Grundlagen der Materialkunde, Chapter 7., 1. Edition, Springer.
- [3] D. Raabe: Microstructure Simulation in Materials Science, Chapter 1., 1. Edition, Shaker.
- [4] W.T. Read and W. Shockley, Phys. Rev., Vol. 78 (1950), pp. 275-289.
- [5] G. Friedel: Leçons de Crystallography, Paris, 1926.
- [6] G. Wulff, Z. Kristallogr. Mineral, Vol. 34 (1901), pp. 409.
- [7] G. Hosson et. al.: The Nature and Behaviour of Grain Boundaries, TMS-AIME, pp. 13.
- [8] V. A. Ivanov: On kinetics and thermodynamics of high angle grain boundaries in aluminium: Experimental Study on Grain Boundary Properties in Bi- and Tricrystals (2006), Dissertation, Chapter 1, RWTH-Aachen, Institut für Metallkunde und Metallphysik.
- [9] G. Gottstein, L. S. Shvindlerman: Grain boundary migration in metals (1999), CRC Press, USA.
- [10] L. Euler: Elementa doctrinae solidorum, *Novi comm. acad. scientiarum imperialis petropolitanae*, Vol. 4 (1752-1753), pp.109-160. Re-printed in *Opera*, Vol. 26, pp. 71-92.
- [11] C. S. Smith, Trans. Met. Soc. AIME, Vol. 175 (1948), pp. 15.
- [12] R. N. Rhines: Microstructology: Behaviour and Microstructure of Materials, Chapter 3, 1. Edition, Dr. Riederer Editions, Stuttgart.
- [13] P. A. Beck, J. C. Kremer, L. J. Demer and M. L. Holzworth, Trans. Met. Soc., AIME, Vol. 175 (1948), pp. 372.
- [14] P. A. Beck, J. Appl. Phys., Vol. 19 (1948), pp.507.
- [15] P. A. Beck, M. L. Holzworth and W. O. Manly, Trans. Met. Soc. AIME, Vol. 175 (1951), pp. 634.
- [16] J. E. Burke, Trans. Met. Soc. AIME, Vol. 180 (1949), pp. 73.
- [17] E. A. Grey and G. T. Higgins, Acta Met., Vol. 21 (1973), pp. 309.
- [18] E. N. da C. Andrade and D.A. Aboav, Proc. Roy. Soc., A, Vol. 291 (1966), pp. 18.
- [19] E. A. Grey and G. T. Higgins, Scr. Met., Vol. 6 (1972) 258.
- [20] O. K. Chopra and P. Niessen, Acta Met., Vol. 21 (1973) pp. 1451.
- [21] K. Lücke, K. Detert, Acta Met., Vol. 5 (1957), pp. 628.
- [22] K. Lücke, H. Stüwe, Acta Met., Vol. 19 (1971), pp.1087.
- [23] J. W. Cahn, Acta Met., Vol. 10 (1962), pp.789.
- [24] G. T. Higgins, Met. Sci. J., Vol. 8 (1974), pp. 143.
- [25] C. Zener, private communication to C. S. Smith, Trans. Am. Inst. Min. Engrs., Vol. 175 (1949), pp. 15.
- [26] P. Cotterill and P. R. Mould: Recrystallization and Grain Growth (1976), Chapter 9, 1. Edition, Surrey University Press.
- [27] J. Calvet and C. Renon, Rev. Met. (Paris), Vol. 57 (1960), pp. 347.
- [28] Y. Ma, Dissertation, RWTH-Aachen, Institut für Metallkunde und Metallphysik.
- [29] C. G. Dunn and J. L. Walter: Recrystallization, Grain Growth and Textures, ASM, Ohio.

- [30] J. E. Palmer, C. V. Thompson and H. I. Smith, *J. Appl. Phys.*, Vol. 62 (1987), pp. 2492.
- [31] C. V. Thompson: *Grain Growth in Polycrystalline Materials*, eds. Abbruzzese and Brozzo, *Trans. Tec. Publins.*, pp. 325.
- [32] F.J. Humphreys and M. Hatherly: *Recrystallization and Related Annealing Phenomena* (2004), Chapter 11, 2. Edition, Elsevier.
- [33] W. W. Mullins, *Acta Met*, Vol. 6 (1958), pp. 414.
- [34] N. Bellomo and L. Preziosi: *Modelling Mathematical Methods and Scientific Computation* (1995), Chapter 1, CRC Press, Florida, USA.
- [35] M. F. Ashby, *Mat. Sc. Techn.*, Vol. 8, pp. 102.
- [36] Y. Liu, T. Baudin and R. Penelle, *Scripta Mat.*, Vol. 34 (1996), pp.1679-1683.
- [37] J. A. Spittle and S. G. R. Brown, *Acta Met. Mater.*, Volume 42 (1994), pp. 1811-1815.
- [38] M.C. Demirel, A.P. Kuprat, D.C. George, B.S. El-Dasher, G.K. Straub, and A.D. Rollett, *Proceedings of the First Joint International Conference on Grain Growth*, Aachen, Germany (2001), Eds. G. Gottstein and D.A. Molodov, Springer Verlag, pp. 297-302.
- [39] V. Yamakov, D. Moldovan, K. Rastogi and D. Wolf, *Acta Mat.*, Vol. 54 (2006), pp. 4053-4061.
- [40] S. Xiao and W. Hu, *J. Cryst. Growth*, Vol. 286 (2006), pp. 512-517.
- [41] K. Binder and D. Stauffer in: *Applications of the Monte Carlo Method in Statistical Physics* (1987), Ed. K. Binder, Springer, pp. 1-33.
- [42] N. Metropolis, A. W. Rosenbluth, M.N. Rosenbluth, A. H. Teller and E. Teller, *J. Chem. Phys.*, Vol. 21 (1953), pp. 1087.
- [43] M. P. Anderson, D. J. Srolovitz, G. S. Grest and P. S. Shani, *Acta Met.*, Vol. 32 (1984), pp. 784.
- [44] D. Zöllner: *Monte Carlo Potts Model Simulation and Statistical Mean-Filed Theory of Normal Grain Growth* (2006), Dissertation, Otto-von-Guericke-Universität Magdeburg.
- [45] J. W. Cahn, *Trans. Met. Soc. AIME*, Vol. 242 (1968), pp. 167.
- [46] V. Tikare, E. A. Holm, D. Fan and L. -Q. Chen, *Acta Mat.*, Vol. 47 (1998), pp. 363-371
- [47] M. A. Miodownik, *J. Light Met.*, Vol. 2 (2002), pp. 125-135.
- [48] K. Kawasaki, T. Nagai, and K. Nakashima, *Phil. Mag. B*, Vol. 71 (1989), pp. 399.
- [49] D. Weygand, Y. Bréchet and J. Lépinoux, *Phil. Mag. B*, Vol. 78 (1998), pp. 329-352.
- [50] Cl. Maurice and F. J. Humphreys in: *Thermomechanical Processing in Theory, Modelling and Practice: [TMP]² Proceedings of an International Conference Organised in Celebratio of the 75th Anniversary of the Swedish Society for Materials Technology* (1996), Stockholm, Sweden.
- [51] H. J. Frost, C. V. Thompson, C. L. Howe, J. Whang, *Scr. Metall.* Vol. 22 (1988), pp. 65-70.
- [52] T.O. Sætre, N. Ryum in: *Modeling of Coarsening and Grain Growth* (1993), C.S. Pande and S.P. Marsh (eds.), *The Minerals, Metals & Materials Society*, Warrendale, pp. 281-294.
- [53] C. Maurice, F. J. Humphreys in: *ICGG-3: Third International Conference on Grain Growth* (1998), Pittsburgh, PA, USA. pp. 81-90.
- [54] D. Kinderlehrer, I. Livshits and S. Ta'asan, *SIAM J. Sci. Comput.*, Vol. 28 (2006), pp. 1694-1715.
- [55] V. Mohles, *Phil. Mag. A*, Vol. 81(2001), pp. 971.

- [56] M. Winning: Grain Boundary Mechanics (2007), 1. Edition, Cuvillier Ed., Göttingen, Germany.
- [57] M. Winning, G. Gottstein and L. S. Shvindlerman, *Mat. Sci. Eng. A*, Vol. 317 (2001), pp. 17-20.
- [58] M. Winning, G. Gottstein and L. S. Shvindlerman, *Acta Mat.*, Vol. 49 (2001), pp. 211-219.
- [59] M. Winning, *Acta Mat.*, Vol. 51 (2003), pp. 6465-6475.
- [60] V. E. Fradkov, M. E. Glicksman, M. Palmer and K. Rajan, *Acta Met. Mat.*, Vol. 42 (1994), pp. 2719-2727.
- [61] A. C. Ferro and M. A. Fortes, *Interf. Sci.*, Vol. 5 (1997), pp. 263-278.
- [62] J. O'Rourke: Computational Geometry in C (1998), Chapter 5, 2. Edition, Cambridge University Press.
- [63] M. de Berg, M. van Kreveld, M. Overmars and O. Schwarzkopf: Computational Geometry Algorithms and Applications (1998), Chapter 7, 2. Edition, Springer.
- [64] J. von Neumann in: Metals Interfaces (1952), American Society for Testing Materials, Cleveland, pp. 108.
- [65] W. W. Mullins, *J. App. Phys.*, Vol. 27 (1956), pp. 900-904.
- [66] M. Hillert, *Acta Met.*, Vol. 13 (1965), pp. 227-238.
- [67] I. M. Lifshitz and V. V. Slyozov, *J. Phys. Chem. Sol.*, Vol. 19 (1961), pp. 35-50.
- [68] C. Wang, G. Liu and X. Qin, *J. Mat. Sci. Lett.*, Vol. 22 (2003), pp. 473-475.
- [69] W. Fayad, C. V. Thompson and H. J. Frost, *Scripta Mat.*, Vol. 40 (1999), pp. 1199-1204.
- [70] R. Smolukowski and R. W. Turner, *J. Appl. Phys.*, Vol. 20 (1949), pp. 745-747.
- [71] T. Watanabe in: Recrystallization and Grain Growth (2001), G. Gottstein and D. A. Molodov (Eds.), Springer, pp. 11-20.
- [72] D. A. Molodov, G. Gottstein, F. Heringhaus and L. S. Shvindlerman, *Scripta Mat.*, Vol. 37 (1997), pp. 1207-1213.
- [73] D. A. Molodov, G. Gottstein, F. Heringhaus and L. s. Shvindlerman, *Scripta Mat.*, Vol. 46 (1998), pp. 5627-5632.
- [74] A. D. Sheikh-Ali, D. A. Molodov, H. Garmestani, *Appl. Phys. Lett.*, Vol. 82 (2003), pp. 3005-3007.
- [75] A. D. Sheikh-Ali, D. A. Molodov, H. Garmestani, *Scripta Mat.*, Vol. 46 (2002), pp. 857-862.
- [76] D. A. Molodov and A. D. Sheikh-Ali, *Acta Mat.*, Vol. 52 (2004), pp. 4377-4383.
- [77] W. W. Mullins, *Acta Met.*, Vol. 4 (1956), 421-432.
- [78] D. A. Molodov, P. J. Konijnenberg, N. Bozzolo and A. D. Sheikh-Ali, *Mat. Lett.*, Vol. 59 (2005), pp. 3209-3213.
- [79] D. A. Molodov, C. Bollmann, P. J. Konijnenberg, L. A. Barrales-Mora, V. Mohles, *Mat. Trans.*, in press.
- [80] D. A. Molodov, P. J. Konijnenbrg, L. A. Barrales Mora, *J. Mater. Sci.*, Vol. 41 (2006), pp. 7853-7861.
- [81] E. W. Weisstein in: Mathworld – a Wolfram web resorce, <http://mathworld.wolfram.com/SpherePointPicking.html>.
- [82] P. Feltham, *Acta Metallurgica*, Vol. 5 (1957), pp. 97-105.
- [83] V. Novikov: Grain Growth and Control of Microstructure and Textura in Polycrystalline Materials (1996), CRS Press, Florida, USA.
- [84] K. T. Aust and J. W. Rutter, *Trans. AIME*, Vol. 215 (1959), pp. 119.
- [85] K. T. Aust and J. W. Rutter, *Trans. AIME*, Vol. 215 (1959), pp. 820.
- [86] K. T. Aust and J. W. Rutter, *Acta Metall.*, Vol. 13 (1965), pp. 181.
- [87] R. C. Sun and C. L. Bauer, *Acta Metall.*, Vol. 18 (1970), pp. 635.
- [88] R. Viswanathan and C. L. Bauer, *Acta Metall.*, Vol. 21 (1973), pp. 1099.

- [89] M. S. Masteller and C. L. Bauer, *Scripta Metall.*, Vol. 10 (1976), pp. 1033.
- [90] E. M. Fridman, Ch. V. Kopetskii, L. S. Shvindlerman and V. Yu. Aristov, *Z. Metallk.*, Vol. 64 (1973), pp. 458.
- [91] E. M. Fridman, Ch. V. Kopetskii and L. S. Shvindlerman, *Z. Metallk.*, Vol. 66 (1975), pp. 533.
- [92] U. Czubyko, V. G. Sursaeva, G. Gottstein and L. S. Shvindlerman, *Acta Mat.* Vol. 46 (1998), pp. 5863-5871.
- [93] G. Gottstein, A. H. King and L. S. Shvindlerman, *Acta Mat.*, Vol. 48 (2000), pp. 397-403.
- [94] G. Gottstein, Y. Ma, L. S. Shvindlerman, *Acta Mat.*, Vol. 53 (2005), pp. 1535-1544.
- [95] D. Mattissen, D.A. Molodov, L.S. Shvindlerman and G. Gottstein, *Acta Mat.*, Vol. 53 (2005), pp. 2049-2057.
- [96] M. Upmanyu, D. J. Srolovitz, L. S. Shvindlerman and G. Gottstein, *Acta Mat.*, Vol. 47 (1999), pp. 3901-3914.
- [97] M. I. Mendeleev and D. J. Srolovitz, *J. Mater. Res.*, Vol. 17 (2002), pp. 234-245.
- [98] D. Kirch: In-Situ SEM Investigation of Individual and Connected Grain Boundaries in Aluminium (2007), Dissertation, RWTH-Aachen, Institut für Metallkunde und Metallphysik.
- [99] A. E. Lobkovsky, A. Karma, M. I. Mendeleev, M. Haataja, D. J. Srolovitz, *Acta Mat.*, Vol. 52 (2004), pp. 285-292.
- [100] J. W. Gibbs: *Collected Works* (1928), Longmans, Green and Co., New York, London, Toronto.
- [101] A. H. King in: *Boundaries and Interfaces in Materials: The Davis A. Smith Symposium* (1998), R. C. Pond, W. A. T. Clark, A. H. King, D. B. Williams (Eds.), TMS, Warrendale, Pa.
- [102] A. V. Galina, V. E. Fradkov, L. S. Shvindlerman, *Phys. Met. Metall.*, Vol. 63 (1987), pp. 165-168.
- [103] G. Gottstein and L.S. Shvindlerman, *Scripta Mat.*, Vol. 54 (2006), pp. 1065-1070.
- [104] G. Gottstein and L. S. Shvindlerman, *Acta Materialia*, Vol. 50 (2002), pp. 703-713.
- [105] V. Mohles: *Thermisch aktivierte Versetzungsbewegung in Kristallen auf der Grundlage von Simulationsrechnungen* (1997), Dissertation, Technische Universität Carolo-Wilhelmina zu Braunschweig, Ed. Shaker
- [106] E. Janot, *Titel* (2008), Dissertation, RWTH-Aachen, IMM.
- [107] R. LeSar, R. Najafabadi and D. J. Srolovitz, *Phys. Rev. Lett.*, Vol. 63 (1989), pp. 624-627.
- [108] Y. Enomoto, R. Kato, *Acta. Metall.*, Vol. 38 (1990), pp.765-769.
- [109] K. A. Brakke, *Exp. Math.*, Vol. 1 (1992), pp. 141-165.
- [110] K. Fuchizaki, T. Kusaba and K. Kawasaki, *Phil. Mag. B*, Vol. 71 (1995), pp.333-357.
- [111] D. Weygand, Y. Bréchet and J. Lépinoux, *Acta Mat.*, Vol. 46 (1998), pp. 6559-6564.
- [112] D. Weygand, Y. Bréchet and J. Lépinoux, *W. Gust, Phil. Mag. B*, Vol. 79 (1999), pp. 703-716.
- [113] D. Weygand, Y. Bréchet and J. Lépinoux, *Adv. Eng. Mat.*, Vol. 3 (2001), pp. 67-71.
- [114] S.-B. Lee, A. D. Rollett and G. S. Rohrer, *Mat. Sc. For.*, Vol. 558-559 (2007), pp. 915-920.
- [115] E. G. Klarreich, *American Scientist*, Vol. 88 (2000), pp. 152-161.

- [116] G. Voronoi, *J. fuer die Reine Angewandte Mathematik*, Vol. 133 (1907), pp. 97-178.
- [117] P. Richard, L. Oger, J. P. Troadec, A. Gervois, *Physica A*, Vol. 259 (1998), pp. 205-221.
- [118] L. Euler, *Comment. Acad. Sci. U. Petrop.* Vol. 8 (1736), pp. 128-140, Reprinted in: *Opera Omnia Series Prima*, Vol. 7 (1766), pp. 1-10.
- [119] V. A. Ivanov, D. A. Molodov, L. S. Shvindlerman and G. Gottstein: *Acta Mat.*, Vol. 52 (2004), pp. 969-975.
- [120] S. G. Protasova, G. Gottstein, D. A. Molodov, V. G. Sursaeva and L. S. Shvindlerman: *Acta Mat.*, Vol. 49 (2001), pp. 2519-2525.
- [121] G. Gottstein and L.S. Shvindlerman: *Scripta Mat.*, Vol. 52 (2005), pp. 863-866.
- [122] L.A. Barrales Mora, L.S. Shvindlerman, V. Mohles, G. Gottstein: *Mat. Sc. Forum*, Vol. 558 (2007), pp. 1051-1056.
- [123] Y. Bréchet and M. Militzer: *Scripta Mat.*, Vol. 52 (2005), pp. 1299-1303.
- [124] S. Hilgenfeldt, A.M. Krynik, S.S. Koehler, and H.A. Stone: *Phys. Rev. Lett.*, Vol. 86 (2001), pp. 2685-2688.
- [125] M.E. Glicksman: *Phil. Mag.*, Vol. 85 (2005), pp. 3-31.
- [126] P. R. Rios and M. E. Glicksman: *Acta Mat.*, Vol. 55 (2007), pp. 1565-1571.
- [127] R. D. MacPherson, D. J. Srolovitz: *Nature*, Vol. 446 (2007), pp.1053-1055.
- [128] G. Gottstein and L.S. Shvindlerman: *Scripta Mat.*, Vol. 10 (1998), pp. 1541-1547.
- [129] C. Runge, *Math. Ann.*, Vol. 46 (1895), pp. 167.
- [130] M. W. Kutta, *Z. für Math. u. Phys.* Vol. 46 (1901), pp. 435.
- [131] W. H. Press, B. P. Flannery, S. A. Teukolsky, and W. T. Vetterling, *Numerical Recipes in C: The Art of Scientific Computation* (1992), Chapter 16, 2. Edition, Cambridge University Press.
- [132] E. Fehlberg, *Computing (Arch. Elektron. Rechnen)*, vol. 6 (1970), pp. 61–71.
- [133] J. R. Cash, A. H. Karp, *ACM Transactions on Mathematical Software*, Vol. 16 (1990), pp.201-222.
- [134] V. Mohles and B. Fruhstorfer, *Acta Mat.*, Vol. 50 (2002), pp. 2503-2516.
- [135] V. Randle und O. Engler: *Introduction to Texture Analysis: Macrotexture, Microtexture and Orientation Analysis* (2000), Taylor & Francis Ltd.
- [136] H. Grimmer, *Acta Cryst. A*, Vol. 30 (1974), pp. 685-688.
- [137] D. C. Handscomb, *Canad. J. Math.*, Vol. 10 (1958), pp. 85-88.
- [138] R. Bonnet, *Acta Cryst. A*, Vol. 36 (1980), pp. 116-122.
- [139] H. Grimmer, *Acta Cryst. A*, Vol. 36 (1980), pp. 382-389.
- [140] H. Grimmer and R. Bonnet, *Acta Cryst. A*, Vol. 46 (1990), pp. 510-514.
- [141] K. Shoemake in *Proc. of SIGGRAPH* (1985), pp. 245-254.
- [142] J. J. Kuffner in *Proc. of the Intl. Conf. on Robotics and Automation* (2004), pp. 1-6.

Appendix A

Details of the Simulation Program

A.1 Programming

The core of the simulation program is an Ordinary Differential Equation (ODE) fourth-order Runge-Kutta integrator [129, 130] with an adaptive step size [131]. This method utilizes some parameters for the calculation of the solution of the first order differential equation, these parameters were originally set by Fehlberg [132] and subsequently modified by Cash and Karp [133]. The current program uses a set of parameters that were optimized by Mohles [105] and utilized for the simulation of dislocation dynamics [55, 105, 134].

The program is written using the object-oriented paradigm. The objects in the simulation are for the two-dimensional case: the grains, grain boundaries and triple junctions (also called vertices, sing. vertex). The grain boundaries are formed by an array of the elemental object *node* whereas the triple junction is itself an upper class of the node. The nodes keep only the information about their position $\{(x,y,z)_i\}$. The objects that formally enter into the integration routine are the triple junctions and the grain boundaries; each of them has its own differential equation (see Ch. 2). In the three-dimensional case, the objects are listed as follows: grains, grain boundaries, edges and vertices, again the *nodes* are a subclass of vertex. The edges are identified as a triple line only if three grain boundaries are attached to them, and correspondingly a vertex is considered as a quadruple junction only if four grains adjoin the vertex. In this case, only the vertices enter into the integration routine.

During the simulation, the integrator calls the routine that contains the differential equations of the integration elements (2D: triple junctions and grain boundaries, 3D: vertices). This routine calculates then from the vector $\{(x,y,z)_{i,t+\delta t}\}$ at the time $t+\Delta t$ the derivatives $\{(dx/dt,dy/dt,dz/dt)_{i,t+\delta t}\}$ which is returned to the integrator. After more of such callings for different values of $0\leq\delta t\leq\Delta t$, the integrator calculates the new position of the elements for the time $t+\Delta t$. After the completion of the integration routine, the output for the simulation can be generated, afterward the integrator is called again and the process is repeated until the conclusion of the simulation.

The vectors calculated in the differential equations at the time $t+\delta t$ and the time itself have not a physical meaning, they are only possibilities of the real solution. The real time step Δt and thus the real calculation is determined by error estimation (adaptive step size [132]) of the difference between calculations of different approximation orders and by the comparison with a provided error bound.

A.2 Curvature Determination From the Local Geometry

The algorithm for the calculation of the curvature of a discrete two-dimensional curve was taken from [105]. With this method, the first dy/dx and the second d^2y/dx^2 derivatives can be calculated and used for the depiction of the grain boundary.

The derivatives $\dot{x} = dx/ds$ and $\dot{y} = dy/ds$ are needed for the description of the tangential vector (\dot{x}, \dot{y}) . The driving force for the boundary migration operates in the normal direction to the tangential vector, which is given by the vector $(-\dot{y}, \dot{x})$. The curvature κ reads

$$\kappa = \frac{\dot{x} \cdot \ddot{y} - \dot{y} \cdot \ddot{x}}{(\dot{x}^2 + \dot{y}^2)^{3/2}} = \dot{x} \cdot \ddot{y} - \dot{y} \cdot \ddot{x} \quad (\text{A.1})$$

where \ddot{x} and \ddot{y} are the second parametric derivatives of the dependent and independent variables. Because $\dot{x}^2 + \dot{y}^2 = 1$, the equation can be simplified.

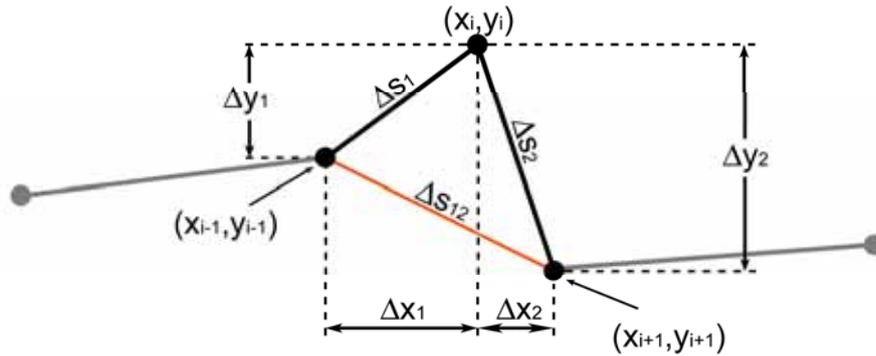


Figure A.1. Variables for the calculation of the curvature from the local geometry.

In Fig. A.1, the required variables for the calculation of the curvature are indicated, the meaning of the parameter is given in the following:

$$\Delta x_1 = x_i - x_{i-1} \quad (\text{A.2})$$

$$\Delta x_2 = x_{i+1} - x_i \quad (\text{A.3})$$

$$\Delta y_1 = y_i - y_{i-1} \quad (\text{A.4})$$

$$\Delta y_2 = y_{i+1} - y_i \quad (\text{A.5})$$

$$\Delta s_{1,2} = \sqrt{\Delta x_{1,2}^2 + \Delta y_{1,2}^2} \quad (\text{A.6})$$

$$\Delta s_{12} = \sqrt{(\Delta x_1 + \Delta x_2)^2 + (\Delta y_1 + \Delta y_2)^2} \approx \Delta s_1 + \Delta s_2 \quad (\text{A.7})$$

The second parametric derivatives read

$$\ddot{x} = 2 \frac{\Delta s_2 x_{i-1} + \Delta s_1 x_{i+1} - (\Delta s_2 + \Delta s_1) x_i}{\Delta s_1 \Delta s_2 (\Delta s_1 + \Delta s_2)} \quad (\text{A.8})$$

and

$$\ddot{y} = 2 \frac{\Delta s_2 y_{i-1} + \Delta s_1 y_{i+1} - (\Delta s_2 + \Delta s_1) y_i}{\Delta s_1 \Delta s_2 (\Delta s_1 + \Delta s_2)} \quad (\text{A.9})$$

Finally, the wanted variables are:

$$\Delta s_i = \frac{1}{2} (\Delta s_1 + \Delta s_2) \quad (\text{A.10})$$

$$\dot{x}_i = \frac{\Delta s_1}{\Delta s_{12}} \frac{\Delta x_2}{\Delta s_2} + \frac{\Delta s_2}{\Delta s_{12}} \frac{\Delta x_1}{\Delta s_1} \quad (\text{A.11})$$

$$\dot{y}_i = \frac{\Delta s_1}{\Delta s_{12}} \frac{\Delta y_2}{\Delta s_2} + \frac{\Delta s_2}{\Delta s_{12}} \frac{\Delta y_1}{\Delta s_1} \quad (\text{A.12})$$

$$\kappa_i = \dot{x}_i \cdot \ddot{y} - \dot{y}_i \cdot \ddot{x} \quad (\text{A.13})$$

Appendix B

On Quaternions, Rotations, Orientations and Disorientations

B.1 Orientations, Rotations and Quaternions

An orientation describes the spatial position of an object with respect to a reference frame. Orientations are also called angular positions. In the simple case of a vector, the direction cosines with respect to the reference describe the orientation of the vector. If the object is, for instance, a rigid body the orientation of the object is more complex to represent because only the position of the body given by a fixed point in the body and a reference frame (translation) are not enough since the body may still be rotated. The orientation of a rigid body has thus two components, a linear (translation) and an angular (rotation) position or orientation. The linear component is trivial because a translation is a simple operation and normally the reference frame is translated to the fixed point in the rigid body, which leaves the rotation, as the only needed descriptor for the orientation of the body; this is known as the Euler's rotation theorem.

A rotation is non-commutative transformation that describes the motion of a body around a fixed point. Rotations are difficult to represent because the topology of spatial rotations does not permit a smooth embedding in Euclidian three-dimensional space (considering a solid sphere in \mathbf{R}^3). Nevertheless, according to the Euler rotation theorem, any rotation may be described by only three angles, which are known, precisely, as the Euler's angles. The Euler's angles are probably the most used way to represent a rotation and thus an orientation. However, there are other forms to represent a rotation, namely, rotation matrix, axis-angle representation, Rodrigues vector, quaternions and Cayley-Klein parameters. All these representations have advantages and disadvantages, some can be better visualized or interpreted, others offer easiness of calculation or faster calculation, etc.

For the simulations, three different representations are used for different reasons, Euler's angle are employed because they are the standard used in orientation microscopy. The reader can note that also rotation matrixes are obtained from such measurements, however, rotation matrixes are a very bad choice because its usage is a waste of computational resources, both in memory and in velocity. Another representation considered is the axis-angle pair, which is very popular among researchers of grain boundary migration. The last offered alternative is the usage of quaternions. Quaternions offer the easies and faster calculation, however, they remain unpopular due to their difficult abstraction. Whereas, in the program, the user can select any of the alternatives to represent orientations and rotations, all the

calculations are performed using quaternions. In the following, the basic concept of the quaternions will be described, for an explanation of other orientation representations refer to [135]

Quaternions are a non-commutative extension of the complex numbers. William Rowan Hamilton first described them in 1843. A quaternion can be also seen as a vector in \mathbf{R}^4 . It has a real component and a vectorial component. Amusingly, due to their dual nature, quaternions have interesting properties. A quaternion has the general form:

$$q = q_0 + \vec{u} = q_0 + q_1i + q_2j + q_3k \quad (\text{B.1})$$

where q_0 is the real part and \vec{u} is the vectorial one. In analogy with complex numbers and contrarily to vectors in \mathbf{R}^3 , a quaternion has an inverse. For this reason, it is said that vectors in \mathbf{R}^4 can have an inverse. The sum of two quaternions $q = q_0 + \vec{q} = q_0 + q_1i + q_2j + q_3k$ and $r = r_0 + \vec{r} = r_0 + r_1i + r_2j + r_3k$ is defined as

$$q + r = (r_0 + q_0) + (r_1 + q_1)i + (r_2 + q_2)j + (r_3 + q_3)k \quad (\text{B.2})$$

For the calculation of the product of two quaternions, the introduction of some properties is first needed. The following axioms describe the basic properties of quaternions

$$i^2 = j^2 = k^2 = ijk = -1 \quad (\text{B.3a})$$

$$ij = k \quad (\text{B.3b})$$

$$jk = i \quad (\text{B.3c})$$

$$ki = j \neq ik = -j \quad (\text{B.3d})$$

Eq. (B.3) points out that the quaternion multiplication is not commutative. With these properties, we can now define the product as

$$qr = (q_0 + q_1i + q_2j + q_3k)(r_0 + r_1i + r_2j + r_3k) \quad (\text{B.4})$$

expanding the product in Eq. (B.4) and applying the equalities of Eq. (B.3a)-(B.3d) the product reads in \mathbf{R}^4 vectorial representation

$$qr = \begin{bmatrix} q_0r_0 - (q_1r_1 + q_2r_2 + q_3r_3) \\ q_0r_1i + q_1r_0i + (q_2r_3 - q_3r_2)i \\ q_0r_2j + q_2r_0j + (q_3r_1 - q_1r_3)j \\ q_0r_3k + q_3r_0k + (q_1r_2 - q_2r_1)k \end{bmatrix} \quad (\text{B.5})$$

Probably, this notation makes not much sense. However, it allows the simplification into a very interesting equation

$$qr = q_0r_0 - \vec{q} \cdot \vec{r} + q_0\vec{r} + r_0\vec{q} + \vec{q} \times \vec{r} \quad (\text{B.6})$$

The product of two quaternions involves both, the dot and the cross product of the vector part of the quaternion.

In analogy with complex numbers, the conjugate q^* of quaternion q is given by

$$q^* = q_0 - \vec{q} = q_0 - q_1i - q_2j - q_3k \quad (\text{B.7})$$

whereas

$$qq^* = q_0^2 + q_1^2 + q_2^2 + q_3^2 \quad (\text{B.8})$$

Now, in analogy with vectors, the quaternion has a length or norm

$$|q| = \sqrt{qq^*} = \sqrt{q_0^2 + q_1^2 + q_2^2 + q_3^2} \quad (\text{B.9})$$

We have now everything to define the inverse of a quaternion

$$q^{-1} = \frac{q^*}{|q|^2} \quad (\text{B.10})$$

A unit quaternion (i.e. $|q| = 1$) can be expressed as

$$q = \cos \frac{\theta}{2} + \sin \frac{\theta}{2} \vec{n} \quad (\text{B.11})$$

where the angle θ and the vector \vec{n} are to be identified with a rotation. For instance, let u be a quaternion with an scalar part equal to zero, such as $u = 0 + \vec{u}$, then the operation $u' = quq^*$ defines the rotation $rot(\theta, \vec{n})$ of the vector \vec{u} . There is a simple demonstration that the quaternions really represent a rotation, for those interested, it only needs the expansion of the product quq^* , the application of half angle formulas, simplification of the expression and finally the comparison with the Rodrigues's formula.

B.2 Mis- and Disorientations

A misorientation is the necessary rotation to bring two orientations together with respect to a general reference frame. Misorientation are used to represent grain boundaries because a grain boundary is the region where to crystals with different spatial orientations interact. A disorientation is by definition the misorientation with the minimal orientation angle and with a rotation axis located in the Standard Stereographic Angle. The discrimination is necessary because the misorientation between two rotations can lead to a rotation angle as high as 180° yet due to crystal symmetry two lattices cannot be different than a well defined limit, for example, for the cubic lattice, it cannot be different by more than $\sim 62.8^\circ$. The calculation of mis- and disorientation will be explained next.

For the calculation of the misorientation with quaternions, first is needed to express the two orientations in terms of quaternions, for the calculation, it will be assumed that the orientations are given in terms of Euler's angle or axis-angle representation. An orientation given in form of the latter with an angle θ and an axis expressed by \vec{n} has an equivalent quaternion q equal to:

$$q = \cos \frac{\theta}{2} + \vec{n} \cdot \sin \frac{\theta}{2} \quad (\text{B.14})$$

respectively, the quaternion can be expressed as an axis-angle pair as

$$\theta = 2 \arctan\left(\frac{|\vec{q}|}{q_0}\right) = 2 \arctan(q_0) \quad (\text{B.15})$$

and

$$\vec{n} = \frac{\vec{q}}{|\vec{q}|} \quad (\text{B.16})$$

The conversion from Euler's angle to quaternion is more complicated, nonetheless straightforward. Given the Euler's angles $(\varphi_1, \Phi, \varphi_2)$ the quaternion components read

$$q_0 = \cos\left(\frac{\Phi}{2}\right) \cos \frac{\varphi_1 + \varphi_2}{2} \quad (\text{B.17})$$

$$q_1 = \sin\left(\frac{\Phi}{2}\right) \cos \frac{\varphi_1 - \varphi_2}{2} \quad (\text{B.18})$$

$$q_2 = \sin\left(\frac{\Phi}{2}\right) \sin \frac{\varphi_1 - \varphi_2}{2} \quad (\text{B.19})$$

$$q_3 = \cos\left(\frac{\Phi}{2}\right) \sin \frac{\varphi_1 + \varphi_2}{2} \quad (\text{B.20})$$

The calculation of the misorientation is very simple, a misorientation quaternion m between two orientations, given by the quaternions p and q respectively, is

$$m = pq^{-1} \quad (\text{B.21})$$

where q^{-1} is the inverse of the quaternion q as defined in Eq. (B.10) and the product pq^{-1} is obtained with Eq. (B.6).

The quaternion m describes the orientation to bring the lattice of the crystal with orientation p in coincidence with the crystal with orientation q . The rotation angle is not necessarily the minimum. In order to calculate the minimal rotation angle and by extension the disorientation, a method, which varies depending on the crystal lattice, must be applied.

Let consider the cubic lattice. The cubically equivalent quaternions to $\pm m$ are obtained by arbitrary permutations and sign changes from one of the following six expressions [136]

$$\{m_0, m_1, m_2, m_3\} (= m) \quad (\text{B.22a})$$

$$\sqrt{2}\{m_0 + m_1, m_0 - m_1, m_2 + m_3, m_2 - m_3\} \quad (\text{B.22b})$$

$$\sqrt{2}\{m_0 + m_2, m_0 - m_2, m_1 + m_3, m_1 - m_3\} \quad (\text{B.22c})$$

$$\sqrt{2}\{m_0 + m_3, m_0 - m_3, m_1 + m_2, m_1 - m_2\} \quad (\text{B.22d})$$

$$\frac{1}{2}\{m_0 + m_1 + m_2 + m_3, m_0 + m_1 - m_2 - m_3, m_0 - m_1 + m_2 - m_3, m_0 - m_1 - m_2 + m_3\} \quad (\text{B.22e})$$

$$\frac{1}{2}\{m_0 + m_1 + m_2 - m_3, m_0 + m_1 - m_2 + m_3, m_0 - m_1 + m_2 + m_3, m_0 - m_1 - m_2 - m_3\} \quad (\text{B.22f})$$

The disorientation angle corresponds to the component with the maximal value among the 24 listed possibilities, for example, let $\sqrt{2}(m_1 + m_3)$ (Eq. B.22a) have the maximal value, the disorientation angle will be then $\theta = 2 \arccos \sqrt{2}(m_1 + m_3)$ and the possible rotation axes will be defined by the remaining three components on the same line, $\sqrt{2}[m_0 + m_2, m_0 - m_2, m_1 - m_3]$.

If the quaternion with the minimal rotation angle is defined by $M = M_0 + \vec{M}$, where M_0 is the maximum value among the 24 possibilities of Eq. (B.22) and \vec{M} is the vectorial part of the quaternion, which was formed by arbitrary ordering of the remaining three components of the selected quaternion (Eq. (B.22)), then the axis of $\pm M$ with $M_0 > 0$ lies in the standard stereographic triangle if $M_1 \geq M_2 \geq M_3 \geq 0$. The reordering of the components of \vec{M} in order to fulfill the previous inequality delivers the disorientation because, as defined by Handscomb [137], rotations with the smallest angle and an axis in the standard stereographic angle are called disorientations. For the cubic lattice, the conditions that a rotation must fulfilled, in order to be a disorientation, were described by Grimmer [136]

$$M_1 \geq M_2 \geq M_3 \geq 0 \quad (\text{B.23a})$$

$$M_1 \leq (\sqrt{2} - 1)M_0 \quad (\text{B.23b})$$

$$M_1 + M_2 + M_3 \leq M_0 \quad (\text{B.23c})$$

The selection of the disorientation for the hexagonal lattice is as easy as for the cubic lattice. Given a misorientation $m = m_0 + \vec{m}$ with components $\{m_0, m_1, m_2, m_3\}$,

Similar methods for the calculation of the disorientation for other elemental crystalline lattices can be found in [139-140].

B.3 Random Orientations

A naïve attempt for the generation of random orientation might try to sample uniformly each Euler angle independently. However, this results in a distribution that is biased toward the polar regions. In the program, an algorithm for the generation of uniformly distributed quaternions is used. The method is taken from [141].

The method utilizes three intermediate random variables in order to produce unit quaternions. The algorithm is shown in pseudo-code as follows [142].

Algorithm: Pseudo-code to generate uniformly distributed random quaternions.

Input: none

Result: uniform random quaternion $q = q_0 + \vec{u} = q_0 + q_1i + q_2j + q_3k$

$s = rand();$

$\sigma_1 = \sqrt{1-s};$

$\sigma_2 = \sqrt{s};$

$\theta_1 = 2\pi \cdot rand();$

$\theta_2 = 2\pi \cdot rand();$

$q_0 = \sigma_2 \cdot \cos \theta_2$

$q_1 = \sigma_1 \cdot \sin \theta_1$

$q_2 = \sigma_1 \cdot \cos \theta_1$

$q_3 = \sigma_2 \cdot \sin \theta_2$

return q

Lebenslauf

M. Sc. Luis Antonio Barrales-Mora

Persönliche Daten

11.22.1977 geboren in Mexiko Stadt, Mexiko
verheiratet, keine Kinder

Ausbildung

08.1996 - 12.2000 Luft- und Raumfahrttechnikingenieurwesen an der
IPN - Technische Hochschule, Mexiko Stadt
02.2001 - 06.2003 Master in Werkstoffwissenschaften an der IPN -
Technische Hochschule, Mexiko Stadt
04.2004 – 09.2007 Dissertation in Werkstoffwissenschaft an der
RWTH-Aachen

Beruflicher Hintergrund

04.2004 - 10.2007 Stipendiat/Mitarbeiter am Inst. für Metallkunde
und Metallphysik, RWTH-Aachen
seit 10.2007 Wissenschaftlicher Mitarbeiter am Institut für
Metallkunde und Metallphysik, RWTH Aachen

Wichtige Ehrungen

04.2004 - 10.2007 DAAD-Promotionsstipendium
07.2007 Distinguirter Nachwuchswissenschaftler bei der
dritten Konferenz über Rekristallisation und
Kornwachstum, Jeju, Korea
06.2008 Distinguirter Nachwuchswissenschaftler im
Rahmen der Exzellenzakademie
Materialwissenschaft und Werkstofftechnik
„Computational Materials Science – Grenzflächen
und grenzflächendominierte Prozesse“

